Chem Soc Rev

ROYAL SOCIETY OF CHEMISTRY

REVIEW ARTICLE

View Article Online
View Journal | View Issue

Cite this: *Chem. Soc. Rev.*, 2024, **53**, 9490

Extrinsically conducting MOFs: guest-promoted enhancement of electrical conductivity, thin film fabrication and applications

Rajat Saha * and Carlos J. Gómez García *

Conductive metal–organic frameworks are of current interest in chemical science because of their applications in chemiresistive sensing, electrochemical energy storage, electrocatalysis, *etc.* Different strategies have been employed to design conductive frameworks. In this review, we discuss the influence of different types of guest species incorporated within the pores or channels of metal–organic frameworks (MOFs) and porous coordination polymers (PCPs) to generate charge transfer pathways and modulate their electrical conductivity. We have classified dopants or guest species into three different categories: (i) metal-based dopants, (ii) molecule and molecular entities and (iii) organic conducting polymers. Different types of metal ions, metal nano-clusters and metal oxides have been used to enhance electrical conductivity in MOFs. Metal ions and metal nano-clusters depend on the hopping process for efficient charge transfer whereas metal-oxides show charge transport through the metal–oxygen pathway. Several types of molecules or molecular entities ranging from neutral TCNQ, I_2, and fullerene to ionic methyl viologen, organometallic like nickelcarborane, *etc.* have been used. In these cases, the charge transfer process varies with the guest species. When organic conducting polymers are the guest, the charge transport occurs through the polymer chains, mostly based on extended π-conjugation. Here we provide a comprehensive and critical review of these strategies to add electrical conductivity to the, in most cases, otherwise insulating MOFs and PCPs. We point out the guest encapsulation process, the geometry and structure of the resulting host–guest complex, the host–guest interactions and the charge transport mechanism for each case. We also present the methods for thin film fabrication of conducting MOFs (both, liquid–phase and gas–phase based methods) and their most relevant applications like electrocatalysis, sensing, charge storage, photoconductivity, photocatalysis,… We end this review with the main obstacles and challenges to be faced and the appealing perspectives of these 21st century materials.

Received 13th May 2024

DOI: 10.1039/d4cs00141a

rsc.li/chem-soc-rev

1. Introduction

Since 1999, after the discovery of MOF-5 by Yaghi *et al.*, metal–organic frameworks (MOFs) or porous coordination polymers (PCPs) have become the most studied functional materials in chemical science.[1–3] MOFs or PCPs, constructed using discrete metal ions or metal clusters as nodes and organic multi-topic ligands as spacers, have attracted significant attention not only due to their aesthetically beautiful architectures but also thanks to their large surface areas, chemically functionalized cavities, flexible skeletons and intriguing electronic properties.[4–6] Such structural characteristics make them potential functional materials for gas and solvent adsorption,[7] storage,[8] separation,[9] catalysis,[10] sensing,[11] drug delivery,[12] *etc.* Additionally, the almost infinite choice of organic bridging ligands and metal ions, with different oxidation states and coordination numbers, allows the modulation of their structures and properties in a controlled manner.[13–15]

In order to obtain advanced functionalities, different crystal engineering design principles, including both pre- and post-synthetic modifications of the basic building blocks, have been employed to convert simple MOF structures into more complex ones.[16–18] Such structural complexity can be achieved by the exchange of ligands or metal ions *via* post-synthetic methods[19,20] or by grafting extra functional units either on the metal atom[21] or on the ligand backbone.[22] Multifunctional MOFs have also been designed by using different types of ligands and guests in simple MOFs.[23] In this regard, the most promising design principle is the utilization of the inherent void space of MOFs to encapsulate different types of guest

---

Departamento de Química Inorgánica, Universidad de Valencia, Dr Moliner 50, 46100 Burjasot (Valencia), Spain. E-mail: Rajat.Saha@uv.es, carlos.gomez@uv.es

species that may modulate and create new functionalities different from those of the host MOF and the guest.[24–27]

In the last decade, electrically conductive MOFs and PCPs have gained much attention for their numerous applications in energy storage,[28,29] electrocatalysis,[30,31] chemiresistive sensing,[32,33] *etc.* However, the implication of MOFs in electronic and electrochemical applications is hindered by their low-charge transport properties. The poor overlap between metal d-orbitals and ligand donor p-orbitals results in weakly conducting or insulating materials.[34] Given the enormous opportunity offered by conducting MOFs, several strategies have been used to increase and modulate their electrical conductivity: (a) the use of ligands having soft donor atoms like S, P, Se, *etc.*, (b) the use of extended conjugated organic ligands, (c) the use of redox-active building blocks (metal ions and organic ligands), and (d) the incorporation of guest species within the pores/voids of the frameworks, *etc.*[35–43] Based on the electron conduction pathway, electrically conductive MOFs are categorized into two classes: (i) intrinsically conducting MOFs (ic-MOFs), in which electron conduction proceeds only through the metal–ligand backbone, and (ii) extrinsically conducting MOFs (ec-MOFs), where electron conduction is dependent on the guest species present in the host framework.

In order to control the electrical conductivity of ic-MOFs, researchers have shown that the utilization of soft donor-based organic ligands is a very promising strategy to enhance their conductivity thanks to a better metal–ligand overlap.[44,45] A nice example is MOF $[Cu_3(C_6S_6)]_n$, which contains an infinite [–Cu–S–] network and shows the highest reported conductivity for any MOFs.[46] Different research groups have utilized extended conjugated organic ligands like pyrene, coronene, *etc.* to develop in-plane charge transport. An example of this strategy is MOF PTC-Fe (PTC = 1,2,3,4,5,6,7,8,9,10,11,12-perthiolated coronene), which has a coronene core with S donor atoms and shows a high electrical conductivity.[47] The presence of mixed-valence metal ions can also improve the electrical conductivity. Thus, Long *et al.* have reported a billion-fold increase in the electrical conductivity of MOFs by using mixed-valence metal ions.[48] On the other hand, the Harris group has shown that the use of radical-based ligands can increase the overall charge transport properties of MOFs and PCPs.[49] Furthermore, defect healing can improve the intrinsic charge transport properties of MOFs.[50] The detailed structural analysis has allowed a significant improvement and development of ic-MOFs and PCPs in the last decade.

Unfortunately, the incorporation of guests within the channels or cavities of these ic-MOFs and PCPs to prepare ec-MOFs induces a loss of crystallinity of the MOFs in most cases,[51] rendering the study and development of ec-MOFs, in a rational way, very difficult. Nevertheless, there has been substantial growth in this field in the last few years.

Although a few review articles have focused on the guest-dependent electrical conductivity of MOFs, the major focus has been placed on intrinsically conducting frameworks.[28,31,34–36,52–59] From the structural point of view, the design of ic-MOFs has gained much attention, and, therefore, most of the reviews are centred on the structure–property relationship of these ic-MOFs, while for the guest-dependent conducting ec-MOFs, the focus has been mostly centred on TCNQ,[60] iodine,[61] polyiodides[62] and some conducting polymers.[63] However, to date, there have been no comprehensive reviews highlighting all the factors associated with the guest-dependent electrical conductivity of these ec-MOFs (Fig. 1).

Herein, we present an exhaustive review of the characteristics of the guest species that have been used by different research groups to enhance the charge transport properties of MOFs. We start with the charge transport mechanisms (band and hopping transport) operative for these MOFs and with the different charge transport pathways: (a) through bond,

Rajat Saha

Rajat Saha received his PhD from Jadavpur University, India, in 2013 on designing multifunctional MOFs and organic materials using crystal engineering techniques. He joined as an Assistant Professor at the Department of Chemistry, Kazi Nazrul University, Asansol, India, in 2016. His research interests have mainly centered on designing MOFs for versatile applications. Presently, he is working as a Maria Zambrano Postdoctoral Fellow at Universitat de Valencia, Spain. Now, he is working on conducting MOFs for their applications in spintronics and others.

Carlos J. Gómez García

Carlos J. Gómez García (Valladolid, Spain, 1964) received his PhD from the University of Valencia with the extraordinary doctoral award in 1991. After performing two post-doctoral stays at Rennes and Bordeaux (France), he joined the University of Valencia as an associate professor in 1993. In 1998 he was promoted as assistant professor and as full professor in 2007 at the Inorganic Chemistry department at the University of Valencia (after a national habilitation). Since 2014 he leads the Multifunctional Modulable Molecular Materials (M4) group. His main interests are magnetic and conducting MOFs and coordination compounds, including polyoxometalate-based materials for energy applications.

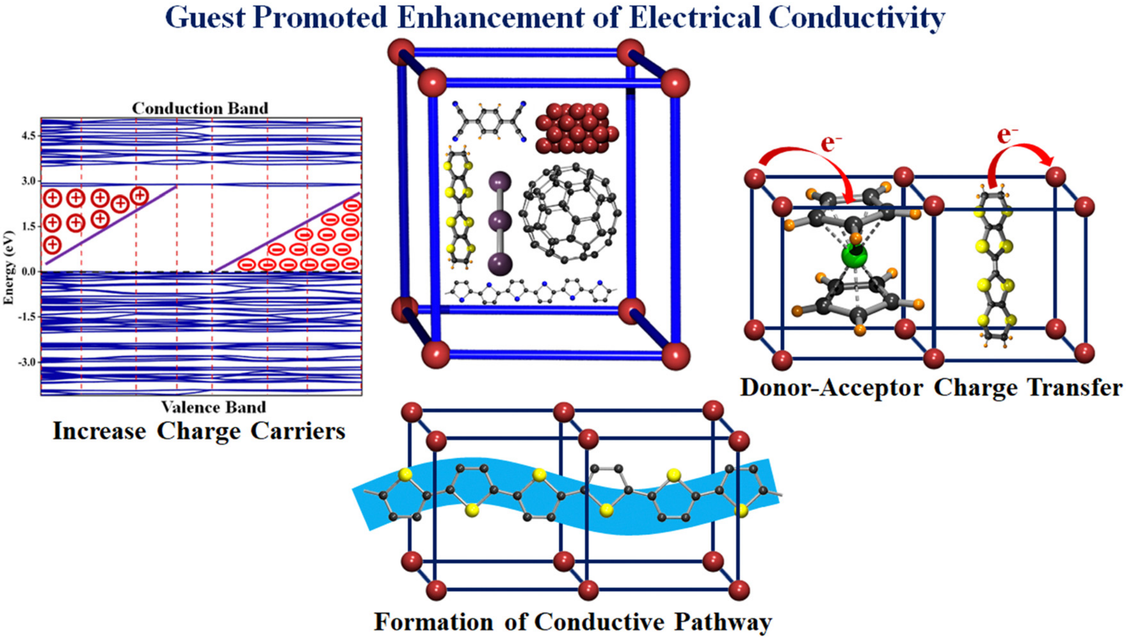

Fig. 1 Different mechanisms to promote and enhance electrical conductivity in porous MOFs/PCPs by encapsulation of different guest species.

(b) through layer, (c) through space, (d) redox hopping and (e) through guest. We then provide an overview of the formation of host–guest MOF structures through encapsulation of guest species by both *in situ* and post-synthetic modification methods. We present the principles that guide the choice of electroactive guest species to design ec-MOFs. Afterward, we show examples of guest-dependent electrical conductivity in MOFs revising all the guest species used to enhance charge transport in MOFs (organic[60] and inorganic[61] molecules and organic conducting polymers[63]). According to their composition, structure, host–guest interaction and charge conducting behaviour, we classify these guest species into three categories: (a) metal-based guests[35] (metal ions, metal nano-clusters and metal oxides), (b) molecule-based guests (TCNQ, iodine and polyiodides, ferrocene, fullerene, tetrathiafulvalene and its derivatives, metal–organic molecules, bromine, organometallic compounds, *etc.*) and (c) organic conducting polymer guests (such as PEDOT, PANI, PPy, PA and PTh) (Scheme 1). We discuss the different methods for the encapsulation of the guest species, the modification of the geometry of the framework after guest encapsulation, the charge transport pathway, the operative charge transport mechanism and the

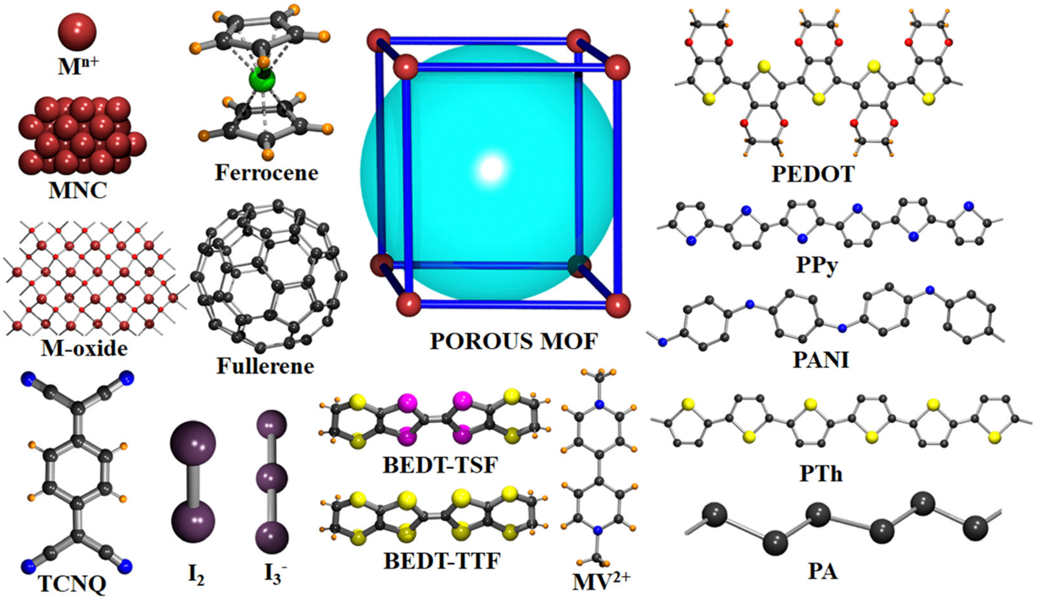

Scheme 1 Different types of dopants used to modulate the electrical conductivity of MOFs.

enhancement/change of electrical conductivity of the resulting guest-loaded host MOFs. Afterward, we discuss the different methods employed to develop thin films of MOFs to find out the most suitable ones for the extrinsically conducting MOFs. We have classified all the processes into two categories based on the medium used for the thin film preparation: (a) liquid phase processing (including exfoliation, electrochemical synthesis, interfacial method, epitaxial growth, *etc.*) and (b) gas phase processing (physical vapor deposition, atomic layer deposition and chemical vapor deposition). Then, we discussed different applications like electrocatalysis, sensing, charge storage, photoconductivity, photocatalysis, *etc.* using ec-MOFs. Finally, we have summarized the general aspects of this field, obstacles and perspectives. We have not considered those guest species which can't be accommodated within the pores of MOFs.

1.1 Transport mechanisms

Charge transport in conductive MOFs usually takes place through two types of mechanisms: (i) band-like and (ii) redox-hopping (Fig. 2).[64]

(i) Band transport occurs when the strong overlap between the metal and ligand orbitals of the MOFs generates continuous energy valence and conduction bands. The energy difference (E_g) between these bands defines their predictable electrical properties like metallic conductors (when both bands overlap and $E_g = 0$), semiconductors (when $E_g < 3.6$ eV), and insulators (when $E_g \geq 3.6$ eV).[65] For metallic conductors, both the conduction and valence bands merge and they show a decrease in conductivity with increasing temperature due to electron–phonon coupling which restricts the free movement of electrons in the band. In semiconductors, the electrical conductivity increases with increasing temperature due to the increase in charge carriers in the conduction band. For a classical semiconductor, the conductivity follows the Arrhenius law: $\sigma = \sigma_0 \exp(-E_a/kT)$ where E_a is the activation energy, which is equal to half of the band gap ($E_a = E_g/2$). In insulators, there should not be any change in the electrical conductivity when the temperature is varied.

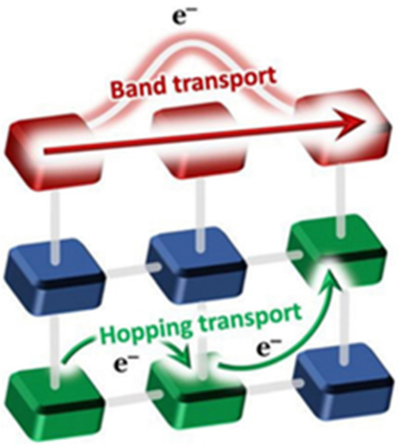

Fig. 2 Band-like and redox hopping conductivity mechanisms operating in MOFs. Reproduced with permission from ref. 64. Copyright 2019, Royal Society of Chemistry.

(ii) Hopping transport assumes that the charges are localized and "jump" through a phonon-assisted quantum tunnelling mechanism. In this case, the conductivity follows the equation $\sigma = \sigma_0 \exp[(-T_0/T)^{\alpha}]$, where $\alpha = 1/(1 + d)$ and d is the dimensionality of the conducting lattice. Thus, $\alpha = 1/4$ for three-dimensional (3D) lattices, as predicted by the Mott model.[66] In this case, the electron transport can be described as an exchange process between redox couples. In this hopping model, when the temperature increases, the electron delocalization increases, and, therefore, the conductivity also increases. The electrical conductivity can be defined by Mott's variable range hopping (VRH) theory (eqn (1)):

$$\sigma(T) = \sigma_0 \left(\frac{T_{\text{Mott}}}{T}\right)^{1/2} \exp\left(-\left(\frac{T_{\text{Mott}}}{T}\right)^{\gamma}\right) \quad (1)$$

with

$$T_{\text{Mott}} = \frac{16}{k_B N(E_F) {L_{\text{loc}}}^3} \quad (2)$$

where the VRH exponent (γ) is calculated from the dimensionality of the transport pathway: $\gamma = 1/(1 + d)$ and the values of γ are 1/4, 1/3 and 1/2, respectively, for three-, two- and one-dimensional systems. σ_0 is the conductivity at infinite temperature, k_B is the Boltzmann constant, T_{Mott} is the Mott characteristic temperature, $N(E_F)$ is the density of states at the Fermi level and L_{loc} is the localization length. Therefore, a material with a 3D, 2D or 1D electron conduction pathway will follow a linear dependence in the plot of ln $[{T_{\text{Mott}}}^{1/2}\,\sigma(T)]$ *vs.* $T^{-\gamma}$, with $\gamma = 1/(1 + d)$ and T_{Mott} can be calculated from the slopes of these plots. Although most MOFs are insulators, the number of semiconducting and even metallic MOFs is continuously increasing.[67] The mechanism used to explain the conductivity in these conducting MOFs is, in most cases, the band model, although the hopping model has also been used in some cases (Table 1).[68]

The electron conduction in both, ic-MOFs and ec-MOFs, proceeds through different pathways like through bond, through layer, through space and redox hopping.[35] However, electron transport may occur only through guest species in some ec-MOFs (as we will see later, there are many insulating MOFs that become conductive only when the guests are inserted). In through-bond transport, the metal–ligand overlap is the predominant factor in promoting the electron transport. Based on this transport idea, several ligands with soft donor atoms (S, P, Se, *etc.*) have been combined with different transition metal ions to construct conductive MOFs.[46] Following the electron transport in 2D materials like graphene, the design of conductive MOFs with extended π-conjugated organic ligands (like benzene, triphenylene, coronene, *etc.*) has gained much attention. Note that in these MOFs, the electron transport follows a through-plane pathway.[47] Interlayer π-interactions have also significant contribution in through-space charge transport for these 2D layered MOFs. The π-interactions operative between the aromatic core of organic ligands can transport

Table 1 Metal based guest-promoted enhancement of electrical conductivity of MOFs

MOF	Guest	Method[a]	σ_{MOF} (S cm^{-1})	$\sigma_{Guest@MOF}$ (S cm^{-1})	σ[b] mechanism	Ref.
Mg-MOF-74	$0.35LiO^iPr + 0.25LiBF_4$	PSM	—	3.1×10^{-4}	Hopping	69
Mg-MOF-74	$0.05LiBF_4$	PSM	—	1.8×10^{-6}	Hopping	69
Mg-MOF-74	$0.6LiO^iPr$	PSM	—	1.2×10^{-5}	Hopping	69
UiO-66	$Li\text{-}O^tBu$	PSM	—	1.8×10^{-5}	Hopping	70
$[Cu_2(BPY)_2(DSNDI)]$	$LiClO_4$	PSM	4.65×10^{-12}	2.3×10^{-6}	Hopping	71
$[Zn(OBA)(L)\cdot DMF]$	Cd^{2+}	PSM	5.8×10^{-6}	1.8×10^{-2}	Hopping	72
Rb-CD-MOF	AgNC	PSM	6.8×10^{-10}	3.1×10^{-9}	Hopping	73
NU-1000	AuNP	PSM	$\leq 10^{-12}$	5.2×10^{-7}	Hopping	74
NU-1000	SnO_2	PSM	$\leq 10^{-12}$	1.8×10^{-7}	BT	75

[a] PSM, post-synthetic method. [b] BT, band transport.

electrons through the MOF as well as through space. Encapsulation of aromatic guest molecules within the void space of MOFs can promote the through space charge transfer between the aromatic cores of the organic building blocks of the host framework.[35] Utilization of redox-active metal ions[48] or ligands[49] or guest species[62] may induce the charge transport within the framework thanks to the hopping of localized electrons between different redox active sites. Finally, the encapsulation of organic conductive polymers within the void space of host frameworks induces electron conduction in the MOF through the polymeric chains of the guest.[63] In some cases, the guest–guest interaction is also operative to conduct electrons within the host framework.

1.2 Host–guest MOFs

In MOF literature, a host–guest complex is defined as a chemical system made up of two or more subunits self-assembled together to form a super-molecular entity. In a host–guest complex, there is a control of the host–guest interactions and the guest (usually a molecule) is encapsulated within the continuous structure of the host.[76–78] Different types of intermolecular interactions like hydrophobic association,[79] hydrogen bonding,[80] electrostatic interactions,[81] metal coordination,[82] van der Waals forces,[83] π–π stacking interactions,[84] *etc.* have been found to stabilize the host–guest structure. Within the confined space of the host, the geometry, molecular orientation, supramolecular behaviour and subsequent properties of the guest molecules may be different from those in the bulk and gas phases. On the other hand, the structure-related functionalities of the host–guest complex can be modulated by changing the type and amount of the inserted guest. Different types of molecular systems having discrete inner cavities such as crown ethers,[85] cryptands,[86] cavitands,[87] calixarenes,[88] *etc.* have been designed for tailor-made functionalities through encapsulation of different types of guests.

Different well-established methods have been used by researchers to load guest molecules within the host MOFs. These methods can be grouped into two main categories: (a) templated *in situ* (TIS) and (b) post-synthetic modification (PSM).

In the TIS method, the guest species are mixed with the metal ions and the ligands during the MOF synthesis. The strong metal–ligand coordination interactions build the framework architecture around the guest molecules. The guest molecules remain in the channels and cavities anchored by weak interactions, coordinated to unsaturated metal centres or even connected to functional groups of the ligands. These guest molecules, as templates, may induce a different structure of the MOFs compared to the one obtained in the absence of these guest species. Such TIS synthesis allows the preparation of single crystals of guest-encapsulated host structures to study the host–guest interactions. This method also allows encapsulation of guests larger than the pore window of the framework that restricts the removal/insertion of the guests. Different electroactive molecules like iodine, TTF, *etc.* and monomers of different organic conducting polymers have been incorporated within the void space of MOFs by this method (Fig. 3).

Post-synthetic modification is a well-established method to change the basic structure of the synthesized MOFs to obtain desired functionalities. Different guest molecules or guest precursors can be inserted within the channels or pores of MOFs. Researchers have used different techniques for guest loading such as dissolving the guest in different solvents, adsorption of guests in the gas phase, ion exchange, *etc.* Encapsulation of guests through this PSM method depends on the size of the guest, pore window size of the host and host–guest interactions. Though this method is very easy to handle and used very often, it has several drawbacks: (i) loss of crystallinity during guest encapsulation, (ii) inhomogeneous distribution of the guests within the MOF channels and (iii) leaching. In several cases, post-treatment of encapsulated precursors to build the active guest species can damage the crystallinity of the frameworks.

Besides these two popular methods, another method namely grafting within the MOF architecture has also gained popularity. In this method, the framework is pre-functionalized either by using open metal sites or ligands having free functional organic sites, which are further utilized to load the guest species following the pre-functional sites. The accommodated guest species have been found to attach strongly to the free functional organic sites.

1.3 Principles for the choice of guests to design ec-MOFs

Electron conduction in MOFs may follow two different transport pathways: (a) through-bond and (b) through-space (Fig. 4).[35]

The through-bond charge transport implies the presence of infinite metal–ligand coordination interactions in the MOF to conduct electrons. A good d–p (σ or π) overlap between metal orbitals and ligand functional groups with well-matched energy

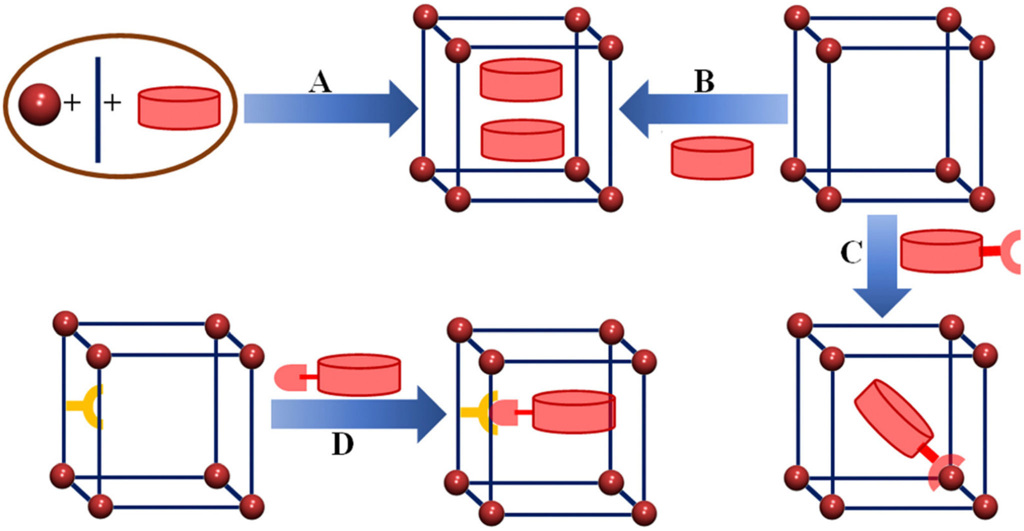

Fig. 3 Different encapsulation methods to prepare guest@host MOF structures: (A) template method, (B) post-synthetic encapsulation, (C) grafting on metal and (D) grafting on the ligand.

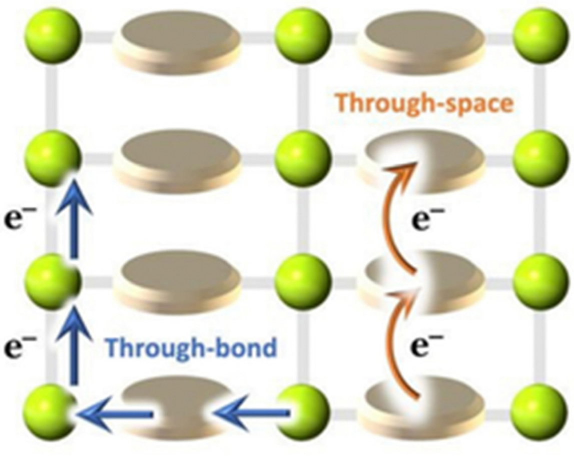

Fig. 4 Through-bond and through-space charge-transport pathways in MOFs. Reproduced with permission from ref. 64. Copyright 2019, Royal Society of Chemistry.

levels leads to small band gaps and high charge carrier mobilities. On the other hand, for the through-space charge transport, electron conduction occurs through the non-covalent π-interactions between highly conjugated planar organic moieties.

In contrast, for extrinsically conducting MOFs, electron conduction is dependent on the guest molecules and host–guest interactions. In the previous section, we have discussed the incorporation of guest species within the host MOFs where the host–guest binding may vary from covalent (including coordination) bonding to non-covalent interactions. Additionally, the incorporation of organic conductive polymers can show charge transport without any significant influence on the framework.

Based on this well-known host–guest interaction, the ec-MOFs can be designed following four different strategies: (i) MOF–guest coordination interactions: the encapsulated guest moieties can coordinate metal centres to promote the electrical charge transport pathway within the framework, as observed by Allendorf *et al.*, who have shown a 10^{10} times enhancement of the electrical conductivity of HKUST-1 through encapsulation of TCNQ.[89] The encapsulation of a secondary bridging moiety provides an alternative pathway for the charge transport for the weakly conducting or insulating MOFs through well-matched metal–guest orbital overlaps. After the first report, several groups have attempted to modify the charge transport behaviour of MOFs through encapsulation of different types of charge-carrying organic bridging ligands like TCNQ and related molecules.[90] (ii) Donor–acceptor interactions: the donor–acceptor interactions between the host MOF and guest moieties have been exploited to develop ec-MOFs. In this case, the guest moiety can be grafted on the metal–organic structure or within the void space. Hupp *et al.* have shown the enhancement of electrical conductivity through encapsulation of fullerene moieties within the void space of a MOF.[91] (iii) Extended π-interactions: the encapsulation of aromatic guest species may help to develop extended host–guest charge transport pathways.[92] (iv) Conducting polymers: organic conductive polymers like PPy, PANI, *etc.* can provide an independent conducting pathway and, therefore, the incorporation of organic conducting polymers within the void space of MOFs is an excellent strategy for developing ec-MOFs.[93,94]

2. Classification of guests to design extrinsically conducting MOFs

Electrical conductivity of a material is defined as the charge transport ability through the material and is characterized by both the charge carrier concentration and the charge carrier mobility. It is highly challenging to control the charge transport properties of MOFs. However, chemical modifications may modulate the electrical conductivity of the MOFs in a controlled way. In the present review, we focus only on the modulation of the electrical conductivity of MOFs by guest encapsulation within the channels or cavities *i.e.*, extrinsically conductive MOFs (ec-MOFs).

Self-assembly of carboxylate-containing organic ligands with metal ions results in poor metal–ligand overlap with large energy gaps and poor conductivity.[95] Additionally, the presence of inherent porosity cuts off the extended π-conjugation among the aromatic ligands of the framework. In this respect, encapsulation of electroactive guest species within the channels or cavities of these MOFs can build up an alternative charge transport pathway throughout the framework.[96] The charge transport of such guest-encapsulated MOFs follows two different mechanisms: (a) host–guest charge transfer interaction and (b) charge transport through the guest. The presence of discrete guests within the pores of MOFs may enhance the first mechanism resulting in an increase of the electrical conductivity through host–guest charge transfer interactions. In contrast, conducting polymers enhance the second mechanism since they provide extended conjugation assemblies throughout the MOF as a charge transport pathway.[97,98] In some cases, a guest–guest charge transfer interaction has also been found.[99] To date, many studies have been done on this topic and, herein, we summarize all these efforts to construct extrinsically conducting MOFs by guest insertion. Thus, in this review, we present the design of conductive MOFs based on the encapsulation of different types of guests within the voids or channels.

To date, several types of guest species like metal ions, metal nanoparticles, metal oxides, inorganic and metal–organic complexes, different organic molecules, halogens, anions, organic polymers and so on, have been accommodated within the void space of MOFs, following the dimension of the pores and understanding the host–guest interactions. In the present review, to discuss the modulation of electrical conductivity of porous MOFs through encapsulation of guest species, we have classified the guests into three categories: (i) metal-based guests, (ii) molecule-based guests and (iii) conducting polymers. This classification is based on their chemical composition, geometry, host–guest interaction and charge transport pathway.

In the first category, metal-based guests, we include metal ions, metal nanoparticles (MNPs) and metal-oxides, as the main component of these guests is the metal ion itself. Metal ions may be present in the pores either as a single metal ion or as a cluster attached to the framework by electrostatic interactions or coordination bonds. An example of this type is the incorporation of Cd^{2+} ions within a framework through $Cd^{2+}\cdots S$ interaction of the ligand.[72] MNPs may agglomerate within the pores of the MOFs through electrostatic interaction. Thus, Ag^+ ions can be loaded within the Rb-CD-MOFs through electrostatic interactions between the metal ions and hydroxide groups that also serve to reduce Ag^+ to form Ag-NPs.[73] In a similar way, metal-oxides can be incorporated into MOFs through electrostatic interactions with the hydroxide groups of the framework.[75] In the second group of guests, molecules and molecular entities, we will discuss different types of inorganic molecules like ferrocene, nickel(II)carbolide complexes, iodine/polyiodides, *etc.* as well as organic molecules like TCNQ, fullerene, TTFs, *etc.* These molecules or molecular entities have their own molecular structure and are loaded within the framework through different host–guest interactions, depending on the framework and the guest. Their charge transfer pathways may also vary with the guest. In the third group of guests, organic conductive polymers, we include well-known conductive organic polymers like PEDOT, PPy, PANI, *etc.* that have 1D structures formed by a purely organic backbone and interact with the host framework mostly through π-interactions.

2.1 Metal-based guests

Encapsulation of different metal-based guest species within porous MOFs has gained much attention in promoting different physical and chemical properties of the host framework. Thus, Bu *et al.* have demonstrated how the encapsulation in MOFs of different metal-based guest species can modulate their catalytic, sensing and luminescent properties.[24] Of course, metal-based guests have also been often used for the enhancement of electrical conductivity of MOFs. Based on their composition, we have classified these metal-based guests into three main sub-categories: (a) metal ions, (b) metal nano-particles (MNPs) and (c) metal oxides. Such metal-based guest species help to promote the charge transfer within the guest@host MOF through electrostatic interactions and a redox hopping mechanism.

2.1.1 Metal ions. Following the charge transport properties of ions, different functional materials have been designed for practical applications such as Li-ion batteries, solid fuel cells, proton transport, *etc.* Here, we will show the possibility of modulating and enhancing the charge transport properties of MOFs through encapsulation of metal ions.

Long *et al.* measured the electrical conductivity of the Li^+ doped Mg-MOF-74 formulated as $\{(LiO^iPr)_{0.35}(LiBF_4)_{0.25}(EC)(DEC)\}@Mg_2(dobdc)$ (Table 1) (H_4dobdc = 2,5-dihydroxybenzene-1,4-dicarboxylic acid, EC = ethylene carbonate and DEC = diethyl carbonate, Fig. 5).[69]

Mg-MOF-74 contains coordinatively unsaturated Mg^{2+} centres upon desolvation. Desolvated Mg-MOF-74 was immersed in a hot hexane solution of LiO^iPr for 2 weeks and the obtained material $(LiO^iPr)_{0.5}@Mg_2(dobdc)$ was immersed in a 1 M solution of $LiBF_4$ in 1 : 1 EC/DEC to obtain the compound $\{(LiO^iPr)_{0.35}(LiBF_4)_{0.25}(EC)(DEC)\}@Mg_2(dobdc)$. Electrical conductivity was measured by the two-probe contact method on pressed pellets. This compound shows an electrical conductivity of 3.1×10^{-4} S cm^{-1}, higher than that of the related compounds $\{(LiBF_4)_{0.05}(EC)_x(DEC)_x\}@Mg_2(dobdc)$ (1.8×10^{-6} S cm^{-1}) and $(LiO^iPr)_{0.6}@Mg_2(dobdc)$ (1.2×10^{-5} S cm^{-1}). Ethylene carbonate molecules and O^iPr^- anions coordinate to the Mg^{2+} sites which consequently allow the penetration of charge-compensating Li^+ ions within the channels. The Li^+ ions can easily move along the channels resulting in the

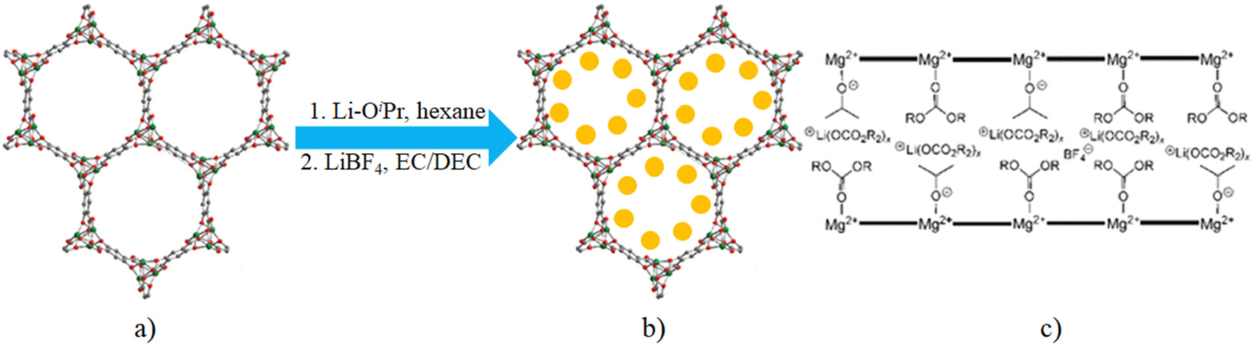

Fig. 5 (a) Structure of Mg-MOF-74. (b) Li^+ incorporation in Mg-MOF-74 (Li^+ = yellow balls). (c) Representation of a cross-sectional view along a channel of the solid [R = $CH_2–CH_2$ (EC) or CH_2CH_3 (DEC)]. Reproduced with permission from ref. 69. Copyright 2011, The American Chemical Society.

observed conductivity enhancement. These authors have also investigated the conductivity of LiOMe and LiOEt incorporated within Mg-MOF-74 but these are worse conductors than the other compounds.69 The same group has also reported an increase in the electrical conductivity of UiO-66 $\{[Zr_6O_4(OH)_4(BDC)_6]\}$ in a similar way. Dehydration of the framework creates open coordination sites on the Zr^{4+} ions by forming $\{Zr_6O_6\}^{12+}$ core units. Immersion of the dehydrated UiO-66 in a 1 M LiO^{t}Bu solution in THF at 353 K for 7 days leads to compound Li-O^{t}Bu@UiO-66 whose AC impedance measurement shows a conductivity of 1.8×10^{-5} S cm^{-1} at room temperature.[70]

Recently, Saha *et al.* have prepared a 2D neutral Cu(I)–sulfonate MOF using a NDI ligand functionalized with two sulfonate groups (NDIDS = 4,4′-(1,3,6,8-tetraoxobenzo[*lmn*]-[3,8]-phenanthroline-2,7(1*H*,3*H*,6*H*,8*H*)-diyl)-bis(2-hydroxy benzoic acid)), which can simultaneously bind guest Li^+ cations with the carbonyl groups and with the free sulfonate oxygen atoms and the perchlorate anions through anion–π interaction with the π-acidic NDI core. The impedance measurement shows that Li^+@MOF has 10^6 times higher conductivity (2.3×10^{-6} S cm^{-1}) than the undoped sample (4.65×10^{-12} S cm^{-1}).[71]

In the same year, the Morsali group showed an interesting case of modulation of the electrical conductivity of a porous framework through Cd^{2+} adsorption. Following the Cd^{2+} uptake capacity of the amine-functionalized UiO-66 framework, these authors prepared a MOF formulated as [Zn(OBA)(L)]·DMF (where L = 5,6-di(pyridin-4-yl)-1,2,3,4-tetrahydropyrazine and H_2OBA = 4,4′-oxybisbenzoic acid). The basic building block *N*1,*N*2-bis(pyridin-4-ylmethylene)ethane-1,2-diamine undergoes a C–C coupling reaction and forms L under the reaction conditions. Structural analysis shows that $[Zn_2(COO)_4]$ paddle-wheel units are connected by OBA ligands to form coordination layers which are further connected by L to form a 2-fold interpenetrated 3D framework containing channels decorated by amine groups (Fig. 6). The activated framework was soaked in an aqueous solution of $Cd(NO_3)_2$ for 10 min and the absorbed amount was determined by ICP analysis. The absorption capacity is 155 mg g^{-1}. Interestingly, the framework shows selective absorption of Cd^{2+} over Hg^{2+}, Pb^{2+}, Cd^{2+}, Zn^{2+}, Co^{2+}, Cr^{2+}, Fe^{2+} and Ca^{2+} under similar conditions. The unusual selective absorption of Cd^{2+} within the framework is proposed to be based on weak interactions between the absorbed Cd^{2+} with the amine and pyrazone groups of the ligand. The electrical conductivity of the framework increases from 5.8×10^{-6} S cm^{-1} to 1.8×10^{-2} S cm^{-1} after Cd^{2+} incorporation and the electrical conductivity is dependent on the amount of absorbed Cd^{2+} ions. The enhancement of electrical conductivity arises from the redox hopping between the dopant and the host framework.[72]

2.1.2 Metal nanoclusters (MNCs). Different research groups have explored the incorporation of metal-nanoclusters

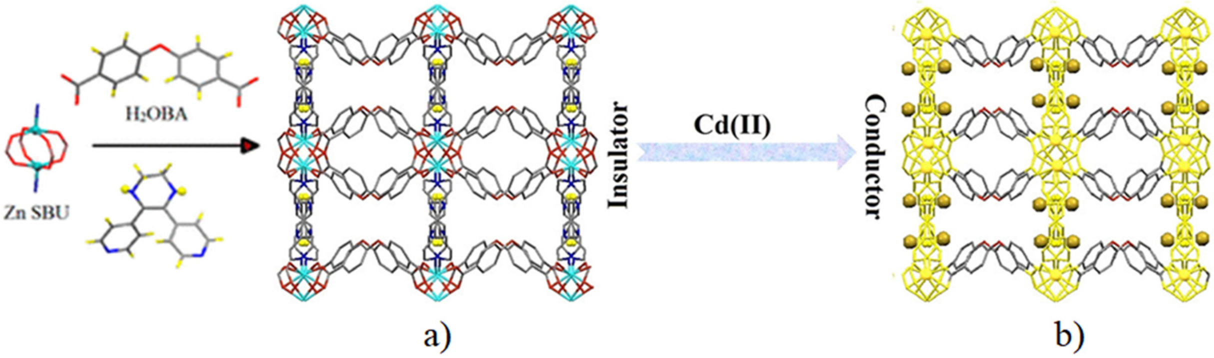

Fig. 6 (a) Representation of the 3D framework of MOF [Zn(OBA)(L)]·DMF formed by the interaction of the paddle-wheel $Zn_2(CH_3COO)_4$ secondary building unit, H_2OBA, and L ligand. (b) Possible pathway for electron transfer (yellow) of Cd@MOF. (The golden balls display the Cd^{2+} ions). Reproduced with permission from ref. 72. Copyright 2019, The American Chemical Society.

(MNCs) within the void space of MOFs. MNCs are well-known for their unusual physical and chemical properties such as high surface area, large charge density, electronic structure and chemical reactivity and, based on these, MNCs may show different functionalities such as heterogeneous catalysis, electrocatalysis, drug delivery, *etc.* Due to their high chemical reactivity, MNCs tend to agglomerate, form larger particles, or oxidize, with the concomitant loss of their unique properties. This is why the synthesis of MNCs with the desired size is a challenging task. In this context, the synthesis of MNCs within the confined space of MOFs is highly beneficial as it simultaneously helps to form MNCs with the desired size and protect them. MNCs are basically encapsulated within the pores of MOFs *via* PSM methods: introduction of metal salts within the pores of the MOFs and then chemical reduction. Herein, we present examples of MNCs inserted in MOFs that have led to an increase in the conductivity of the MOF. Such encapsulation of MNC promotes electron transfer through the redox hopping mechanism in most cases.

The first report, by Han *et al.*, showed an enhancement of the electrical conductivity of an insulator MOF, Rb-CD-MOFs, formed by reacting RbOH with γ-cyclodextrin (γ-CD).[73] Single crystals of the MOFs were immersed in an acetonitrile solution of $AgNO_3$. Ag^+ ions diffused within the channels of the MOF and were reduced by the –OH groups of the cyclodextrin molecules to form Ag nanoclusters (AgNCs). X-ray powder diffraction (XRPD) studies show that AgNC@Rb-CD-MOF does not lose any crystallinity while TEM analysis indicates that the size of the AgNC is ∼2 nm. N_2 adsorption study indicates that compound AgNC@Rb-CD-MOF has a high porosity, similar to the parent MOF. Two-probe electrical conductivity measurements show that the conductivity of this compound varies in the range of 6.8×10^{-10} to 3.1×10^{-9} S cm^{-1}, whereas the parent Rb-CD-MOF is an insulator. Furthermore, upon illumination, AgNC@Rb-CD-MOF shows a further 10^4 times enhancement of the electrical conductivity.[73] In this case, the charge transport occurs through the hopping mechanism (Fig. 7).

A similar strategy was used by Ma and co-workers to prepare AgNC@Pb-CD-MOF.[100] Pb-CD-MOF, prepared by reacting $PbCl_2$ with β-CD, was taken in ultrapure water and $AgNO_3$ was added to the solution. Ag^+ ions diffuse in the channels and are then reduced by the –OH groups of the β-CD moieties to form AgNCs. Impedance analysis shows that AgNC@Pb-CD-MOF shows better conductivity than the parent MOF Pb-CD-MOF, as the incorporation of AgNC has improved the electron transfer ability. AgNC@Pb-CD-MOF was further used for electroluminescent based immune-sensing.[100]

A significant enhancement of the electrical conductivity upon incorporation of AuNP within the pores of NU-1000 MOF has been recently reported by Saha and co-workers.[74] For the first time, they have loaded AuNPs within MOF pores by directly immersing NU-1000 MOF crystals in aqueous $AuCl_3$ solution overnight. The consequent reduction of Au^{3+} to Au-NPS was monitored by the naked eye colour change from bright yellow to orange. The reduction of infiltrated Au^{3+} ions was

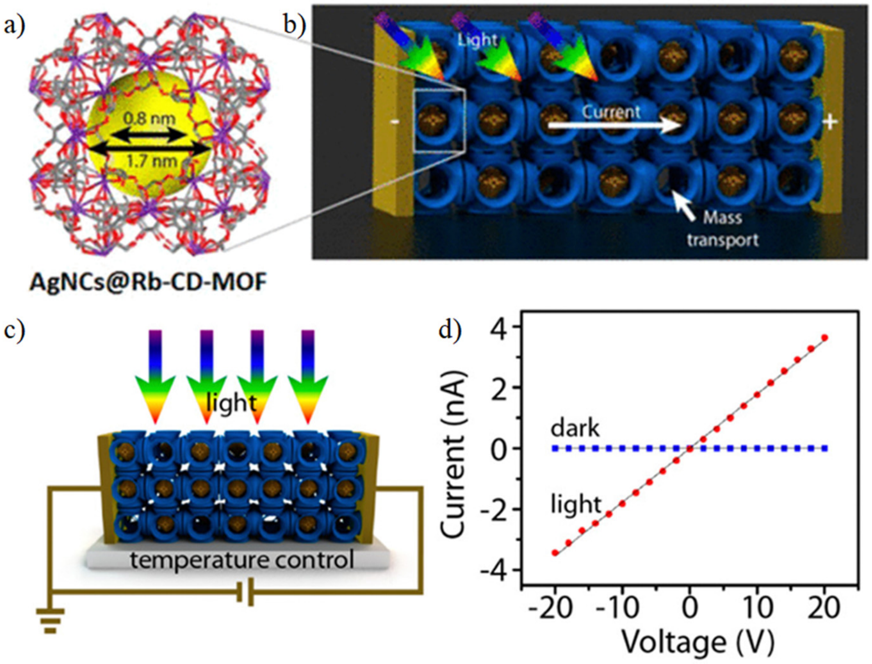

Fig. 7 (a) Unit cell content of an Rb-CD-MOF crystal synthesized from γ-CD and RbOH. The yellow sphere indicates a ∼1.7 nm cavity; the channels connecting the cavities are ∼0.8 nm wide. (b) Schematic representation of Ag nanoclusters deposited by immersing Rb-CD-MOF crystals in a CH_3CN solution of $AgNO_3$. Not all the cavities contain nanoclusters. (c) Experimental arrangement for measuring photoconductance of MOF crystals. (d) I–V characteristics of AgNC@Rb-CD-MOF crystals under light irradiation (630 mW cm^{-2}) and in the dark. The conductivities are, respectively, 1.8×10^{-8} and $\sim 2 \times 10^{-11}$ S cm^{-1}. Reproduced with permission from ref. 73. Copyright 2015, The American Chemical Society.

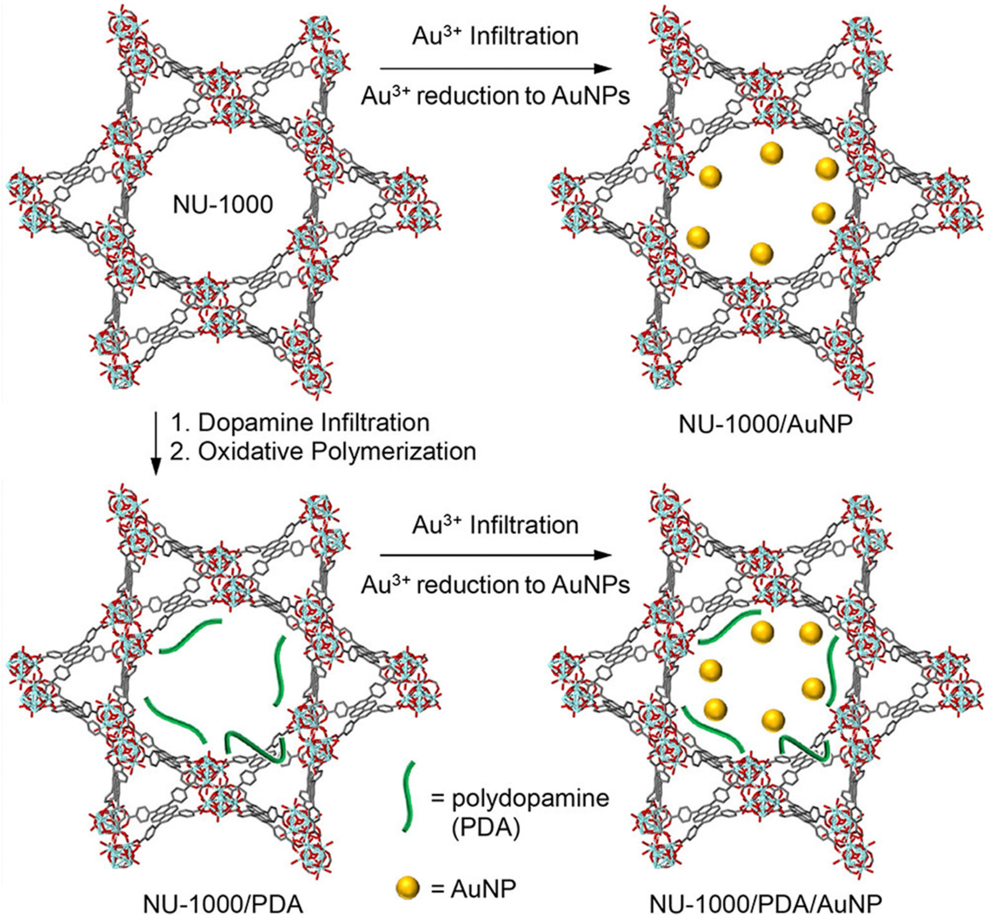

Fig. 8 Transformation of NU-1000 to AuNP@NU-1000, PDA@NU-1000 and (AuNP-PDA)@NU-1000 MOFs. Reproduced with permission from ref. 101. Copyright 2018, The American Chemical Society.

carried out by hydroxide groups of the $[Zr_6(\mu^3\text{-}O)_4(\mu^3\text{-}OH)_4(OH)_4(H_2O)_4]$ nodes of the framework (Fig. 8).

The formation of AuNP@MOF was characterized by XRPD analysis. In order to compare the formation of AuNP@MOF, they have also attempted to synthesize AuNP within the pores of NU-1000 MOF using a multi-step method developed by others.[101] This method implies (a) incorporation of dopamine monomers within the pores of the MOF, (b) polymerization of the dopamine monomers to obtain PDA within the MOF pore, (c) immersion of PDA@MOF in an aqueous solution of $AuCl_3$ and the consequent reduction of Au^{3+} by the hydroxide groups of the dopamine moieties to form (AuNP–PDA)@NU-1000 MOF. The XRPD analysis indicates the formation of AuNPs within the pores of the NU-1000 MOF without loss of any crystallinity, resulting in a similar MOF as the one synthesized directly without the help of dopamine. N_2 sorption studies indicate that the BET surface area of AuNP@NU-1000 MOF (1527 $m^2\ g^{-1}$) is higher than that of AuNP–PDA@NU-1000 MOF (715 $m^2\ g^{-1}$) but lower than the parent MOF (2215 $m^2\ g^{-1}$). These values clearly probe the loading of AuNPs and PDA within the pores of the framework.

Two-probe electrical conductivity measurements show similar room-temperature conductivities of 1.2×10^{-7} S cm^{-1} for AuNP@NU-1000 MOF and 5.2×10^{-7} S cm^{-1} for AuNP–PDA@NU-1000 (Fig. 9), both 10^4 times higher than that of the parent MOF ($\leq 10^{-12}$ S cm^{-1}). It is suggested that the charge hopping or tunnelling of electrons across the framework becomes more facile after the incorporation of AuNPs.[74]

Recently, Vilian *et al.* have inserted Pd-NPs into MIL-101(Cr) to obtain Pd@MIL-101(Cr), based on the interaction between the uncoordinated amine groups with the loaded Pd centres.[102] The synthesized MIL-101(Cr) MOF was soaked in an aqueous solution of $PdCl_2$ at room temperature for 8 h and afterward the solid was collected by centrifugation. Pd nanoparticles were formed by reduction using H_2 at 200 °C for 1 hour. Impedance analysis indicates that the charge transfer resistance (R_{ct}) of Pd@MIL-101(Cr) (384 Ω) is much lower than that of the parent MOF (1104 Ω).[102]

Gold nanoparticles have also been loaded, by Wang *et al.*, into the void space of an imidazole-based framework formulated as $[Zn_2(mim)_4(Hmim)(H_2O)_3]$ (ZIF-L) (Hmim = 2-methylimiazole, ZIF = zeolitic-imidazolate framework). The impedance analysis also shows that the charge transfer resistance of Au@ZIF-L is much lower than that of ZIF-L itself.[103]

Platinum nanoparticles can also be incorporated into three different UiO-MOFs (namely, UiO-66, UiO-67 and UiO-68), as

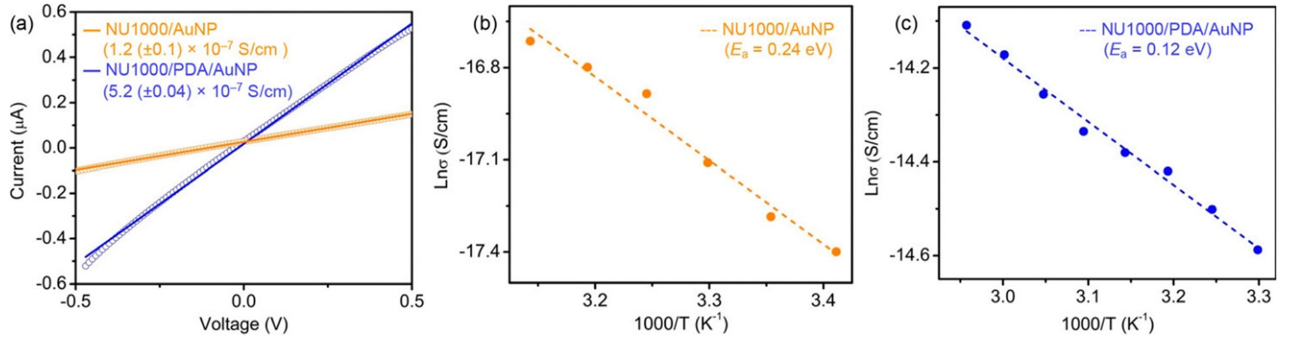

Fig. 9 (a) Representative *I*–*V* plots of AuNP@NU-1000 (orange) and (AuNP–PDA)@NU-1000 (blue). (b) Arrhenius plots of the temperature dependent conductivities of AuNP@NU-1000 (orange) and (AuNP–PDA)@NU-1000 (blue), showing their respective activation energies. Reproduced with permission from ref. 101. Copyright 2018, The American Chemical Society.

shown by Guo and co-workers.[104] The Pt-NPs were incorporated by *in situ* synthesis and characterized using TEM, XRPD, XPS and N_2 adsorption analyses. XRPD analysis shows that the crystallinity of UiO-66 and UiO-68 does not change upon loading with Pt-NPs while the crystallinity of UiO-67 is significantly damaged. Interestingly, Pt-NP@UiO-66 and Pt-NP@UiO-68 show better adsorption behaviours and larger surface areas than their parent frameworks. Impedance analysis indicates that the electron transfer ability increases significantly for all the frameworks after Pt-NP loading. The charge transfer resistance (R_{ct}) value increases as follows: Pt@UiO-66-2/GCE (2396 Ω), Pt@UiO-68-2/GCE (2677 Ω), UiO-66/GCE (3042 Ω), Pt@UiO-67-2/GCE (3379 Ω), UiO-68/GCE (4697 Ω) and UiO-67/GCE (5872 Ω).[104]

The host–guest structure, AgNC@ZIF-67, has been prepared by incorporating Ag^+ ions within the framework and consequent reduction by $NaBH_4$. Impedance spectroscopy shows that AgNC@ZIF-67 is a better conductor than ZIF-67 itself, indicating that the presence of AgNCs is an important factor for improving the conductivity of the material. Furthermore, the material was used for electrochemical glucose sensing.[105] Similarly, Dong *et al.* have developed a silver nanoparticle MOF: Ag@ZIF-67 that is more conductive than the pristine framework.[106]

Very recently, Ballav and co-workers have shown the possibility of tuning the electrical conductivity of the semiconducting MOFs $[Cu_3(HHTP)_2]$ and [Cu-TCNQ] through encapsulation of AgNPs.[107] Thin films of these MOFs and the corresponding AgNP@MOFs were prepared on fluorine-doped tin oxide (FTO) substrates through the layer-by-layer (LBL) method. The film thickness was monitored by the LBL cycles while the doping of AgNPs was varied with the exposure time in AgOAc solution. The formation of AgNP@MOFs was monitored using XRPD, FESEM, EDXS and XPS studies. The electrical conductivity measurements show that $[Cu_3(HHTP)_2]$ is a semiconductor with an electrical conductivity value of $\sim 10^{-6}$ S cm^{-1}. The conductivity value increases with the doping of AgNPs. Doping for 5 minutes can enhance the electrical conductivity by ~2 orders of magnitude, although it still remains semiconducting. In contrast, doping for 10 minutes and above results in AgNP@$[Cu_3(HHTP)_2]$ that shows a metallic behaviour with a conductivity value of $\sim 2 \times 10^{-1}$ S cm^{-1} at 300 K. On the other hand, the encapsulation of AgNPs within Cu-TCNQ in AgNP@Cu-TCNQ enhances its electrical conductivity by about 1000 times (from $\sim 7 \times 10^{-7}$ to $\sim 4.7 \times 10^{-4}$ S cm^{-1}), although it shows a semiconducting behaviour. These authors have demonstrated that the formation of large amounts of Ag(0)-NPs within $[Cu_3(HHTP)_2]$ is the main reason for such metallic conductivity of AgNP@$[Cu_3(HHTP)_2]$ while Ag(I)-TCNQ is formed in the case of Cu-TCNQ.[107]

2.1.3 Metal oxides.

Although very rare, a few attempts to modulate the electrical conductivity of MOFs have been performed through the incorporation of metal oxides within the pores. One of these few attempts, performed by Kung and co-workers,[75] showed a successful enhancement in the electrical conductivity of NU-1000 MOF through the incorporation of SnO_2 within the pores. As synthesized NU-1000 MOF was immersed in a hexane solution of $Sn(amd)_2$ (where amd = bis(*N*,*N*′-di-i-propylacetamidinato)), leading to the incorporation of the cationic $[Sn(amd)]^+$ complex by interaction with the hydroxide groups of the framework. After the first grafting cycle, a total of 4.3 Sn atoms were deposited on each node. A second cycle of grafting was carried out by an atomic layer deposition technique by replacing the amd^- ligand in the inserted $[Sn(amd)]^+$ complex using steam. After four consecutive cycles, a total of 24 Sn atoms were deposited per node and the XPS study shows that Sn is present in the +4 oxidation state (due to aerial oxidation of Sn^{II} to Sn^{IV}). X-ray single crystal structure analysis shows that the tin(IV) oxo-species are located between the nodes. Difference electron density (DED) analysis with samples obtained after three consecutive grafting cycles indicates the formation of SnO_2 chains along the crystallographic *c*-axis (Fig. 10). It also indicates the presence of tin(IV) oxo-species at the centre of the hexagonal pore. After loading of SnO_2 within the void space, the pore diameter decreases from 31 to 27 Å. N_2 adsorption studies indicate that the BET surface area decreases with increasing the loading of SnO_2 to 2100, 1410, 1130, and 680 m^2 g^{-1}, for pristine NU-1000, SnO_2@NU-1000 (1 cycle), SnO_2@NU-1000 (2 cycles), and SnO_2@NU-1000 (3 cycles), respectively (Fig. 11). Two-probe electrical conductivity

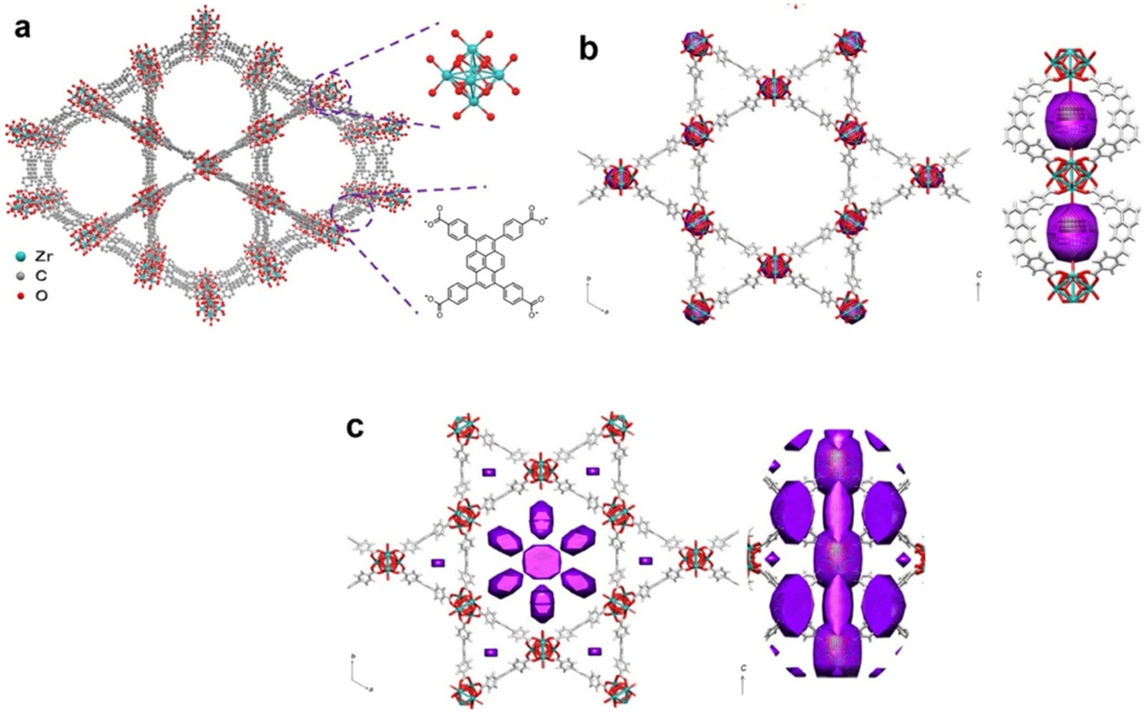

Fig. 10 (a) Top-view of the crystal structure of NU-1000. H-atoms are omitted for simplicity. DED maps of (b) SnO_2@NU-1000 (1 cycle) and (c) SnO_2@NU-1000 (3 cycles). The electron density of SnO_2 is presented in purple. Reproduced with permission from ref. 75. Copyright 2018, The American Chemical Society.

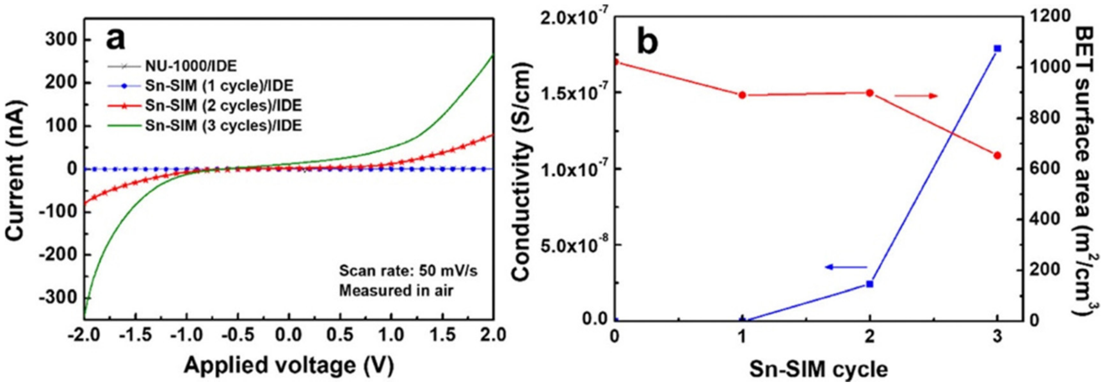

Fig. 11 (a) I–V curves of NU-1000/IDE, SnO_2@NU-1000 (1 cycle)/IDE, SnO_2@NU-1000 (2 cycles)/IDE and SnO_2@NU-1000 (3 cycles)/IDE, measured in air at room temperature. (b) Electrical conductivity and BET surface area of NU-1000, SnO_2@NU-1000 (1 cycle), SnO_2@NU-1000 (2 cycles), and SnO_2@NU-1000 (3 cycles). Reproduced with permission from ref. 75. Copyright 2018, The American Chemical Society.

measurements show that the conductivity of the SnO_2@NU-1000 MOF obtained after three cycles of grafting reaches 1.8×10^{-7} S cm^{-1} while the parent MOF is insulating (Fig. 11). Furthermore, the obtained material was used for hydrogen gas sensing.[75] The electron transport occurs through the tunnelling mechanism.

2.2 Molecule-based guests

Different types of electroactive molecules and molecular entities including TCNQ (7,7,8,8-tetracyanoquinodimethane), iodine, polyiodides, ferrocene, fullerene, tetrathiafulvalene and its derivatives, methyl viologen, *etc.* have been encapsulated within the channels of MOFs to induce and enhance conducting properties of the parent MOFs (Table 2). In most cases, the guest molecules are incorporated by post-synthetic methods within the voids of pre-synthesized MOFs, although, in some cases, guest molecules are used as templates and incorporated by *in situ* methods. The encapsulated guest species remain either attached to the metal/ligand framework by coordination/covalent linkages or within the voids through non-covalent interactions.

Such incorporation of electroactive molecules can induce or enhance the electrical conductivity by several mechanisms: (i) by creating a new electron conducting pathway throughout the framework thanks to the formation of covalent/

Table 2 Molecular guest-promoted enhancement of electrical conductivity of MOFs

MOF	Guest	Method	σ_{MOF} (S cm^{-1})	$\sigma_{\text{Guest@MOF}}$ (S cm^{-1})	σ mechanism	Ref.
HKUST-1	TCNQ	PSM	10^{-8}	7×10^{-2}	CT	89
$[Cu_2(AcO)_4(CuTPyP)_{1/2}]\cdot CHCl_3$	TCNQ	PSM	10^{-9}	10^{-6}	CT	90
$[Cu_2(TATAB)_3]\cdot 7.5H_2O$	TCNQ	PSM	9.8×10^{-12}	10^{-7}	CT	113
$[Zn_3(\text{DL-lac})_2(pybz)_2]\cdot 2.5DMF$	I_2	PSM	—	3.42×10^{-3}	D–A CT	117
$[Co^{II}{}_3(lac)_2(pybz)_2]\cdot 2.7\ I_2$	I_2	PSM	—	7×10^{-6}	D–A CT	118
$Cu[Ni(pdt)_2]$	I_2	PSM	10^{-8}	10^{-4}	D–A CT	119
$\{[Cu_6(pybz)_8(OH)_2]\cdot I^{5-}\cdot I^{7-}\}_n$	$I_5^- + I_7^-$	PSM	—	8.11×10^{-7}	D–A CT	120
$[Cu_6(pybz)_8(OH)_2]^-(I^-)_2\cdot 3.5CH_3OH$	I^-	PSM	—	8.04×10^{-9}	D–A CT	120
[Co-NDC]	I_2	PSM	—	1.88×10^{-6}	D–A CT	121
$[Co_{1.5}(BDC)_{1.5}(H_2bpz)]\cdot 0.5I_2\cdot DMF$	I_2	PSM	2.5×10^{-9}	1.56×10^{-8}	D–A CT	123
$[Tb(Cu_4I_4)(ina)_3(DMF)]$	I_2	PSM	5.7×10^{-11}	2.16×10^{-4}	D–A CT	124
$[V_2^{III}(OH)_2(L)]$	$I_2 + I_3^-$	PSM	1.7×10^{-10}	1.16×10^{-4}	D–A CT	125
Cu-TCNQ	I_2	PSM	10^{-5}	10^{-3}	D–A CT	126
$[Cd(NDC)_{0.5}(PCA)]\cdot G_x$	I_2	PSM	10^{-12}	10^{-7}	D–A CT	190
$[Eu_4(BPT)_4(DMF)_2(H_2O)_8]$	I_n^-	PSM	8.27×10^{-7}	2.71×10^{-5}	D–A CT	127
$[Zn_2(TTFTB)(H_2O)_2]$	I_n^-	PSM	1.6×10^{-9}	2.5×10^{-10}	D–A CT	128
$[Zn_3(ExTTFTB)_2(H_2O)_4]\cdot 6EtOH$	I_2/I^-	PSM	10^{-10}	10^{-6}	D–A CT	131
$(BEDT\text{-}TTF)_3[MnCr(ox)_3]$	BEDT-TTF	TEM	—	250	D–A CT	137
$(BEDT\text{-}TSF)_3[MnCr(ox)_3]\cdot CH_2Cl_2$	BEDT-TSF	TEM	—	1–23	D–A CT	138
$(BEDT\text{-}TTF)_x\ [MnRh(ox)_3]\cdot CH_2Cl_2$	BEDT-TTF	TEM	—	13	D–A CT	139
$(BEDT\text{-}TTF)_3[CoCr(ox)_3]$	BEDT-TTF	TEM	—	1	D–A CT	140
$(BEDS\text{-}TTF)_3[MnCr(ox)_3]$	BEDS-TTF	TEM	—	$<10^{-6}$	D–A CT	140
$(BEDS\text{-}TTF)_3[CoCr(ox)_3]$	BEDS-TTF	TEM	—	$<10^{-6}$	D–A CT	140
$(BET\text{-}TTF)_3[MnCr(ox)_3]$	BET-TTF	TEM	—	4	D–A CT	140
$(BET\text{-}TTF)_3[CoCr(ox)_3]$	BET-TTF	TEM	—	21	D–A CT	140
$(BEDT\text{-}TSF)_3[CoCr(ox)_3]$	BEDT-TSF	TEM	—	2.3	D–A CT	140
$(BMDT\text{-}TTF)_3[MnCr(ox)_3]$	BMDT-TTF	TEM	—	1.5	D–A CT	140
$(ES(1Se)\text{-}TTF)_3[MnCr(ox)_3]$	ES(1Se)-TTF	TEM	—	0.1	D–A CT	140
$(BEDO\text{-}TTF)_3[MnCr(ox)_3]$	BEDO-TTF	TEM	—	1.4	D–A CT	140
$(BEDT\text{-}TTF)_3[Cu(ox)_3]3H_2O$	BEDT-TTF	TEM	—	4	D–A CT	144
$(BEDT\text{-}TSF)_3[Cu(ox)_3]3H_2O$	BEDT-TSF	TEM	—	140	D–A CT	146
NU-901	C_{60}	PSM	10^{-3}	10^{-14}	D–A CT	91
$(TTFTB)_3[(Fe_3O)(H_2O)_2(OH)]_2$	C_{60}	PSM	3.7×10^{-11}	4.7×10^{-9}	D–A CT	151
HKUST-1	Ferrocene	PSM	10^{-14}	2×10^{-9}	D–A CT	166
NU-1000	$[Ni(L^1)_2]$	PSM	Insulator	2.7×10^{-7}	D–A CT	169
$[Zn_2(TCPB)(BPDPNDI)]$	MV^{2+}	PSM	6×10^{-7}	2.3×10^{-5}	D–A CT	92
$[Zn_2(TCPB)(BPDPNDI)]$	DFDNB	PSM	6×10^{-7}	3.5×10^{-6}	D–A CT	92
$[Zn_2(TCPB)(BPDPNDI)]$	DNT	PSM	6×10^{-7}	1.5×10^{-6}	D–A CT	92
Zn_2TTFTB	TCNE	PSM	10^{-7}	120×10^{-7}	D–A CT	202
Cd_2TTFTB	TCNE	PSM	20×10^{-7}	80×10^{-7}	D–A CT	202

L = biphenyl-3,3′,5,5′-tetracarboxylate; L^1 = dicarbollide; PSM = post-synthetic method; TEMP = template; CT = charge transport; D–A CT = donor–acceptor charge transfer.

coordination linkages between the metal centres, (ii) by developing a donor–acceptor (D–A) host–guest charge transfer pathway within the framework, and (iii) through guest–guest interactions.

In the first mechanism, the encapsulated guest acts as a bridge between metal centres and provides an alternative electron conduction pathway. It is obvious that the guest should be a good electronic conductor as TCNQ, which is a π-conjugated organic building block that may induce high conductivity through the formation of linkages between different metal centres of the MOFs. Similarly, the formation of polyiodide chains within the channels of MOFs can substantially enhance their electrical conductivity by formation of coordination bonds between metal centres and polyiodides. While the donor–acceptor (D–A) charge transfer interaction is a well-established phenomenon in co-crystals and has been used for applications in optoelectronic devices, it is less studied in MOFs. The formation of MOFs using metal–ligand coordination also reduces the electron density on the ligand backbone through the partial transfer of electron density from ligands to the cationic metal centres that act as electron acceptors. The incorporation of electron-rich guest species (iodides) within the voids/channels of MOFs produces donor–acceptor electron transfer pathways throughout the framework, inducing higher electrical conductivity. Again, the utilization of conjugated organic ligands for the synthesis of MOFs results in electron-rich skeletons, and therefore, the incorporation of electron acceptor molecules can also create D–A charge transfer pathways throughout the framework.

2.2.1 TCNQ. Tuning the electrical conductivity of porous MOFs through encapsulation of the redox active and conjugated guest molecule, 7,7,8,8-tetracyanoquinodimethane (TCNQ),[108] is an attractive and very used approach (Fig. 12). A thin film of the MOF $Cu_3(BTC)_2$ (also known as HKUST-1, where H_3BTC = benzene-1,3,5-tricarboxylic acid) on silica-coated silicon wafers was prepared by Allendorf *et al.*, and TCNQ was inserted by soaking it in a saturated TCNQ solution.[89] The presence of TCNQ within the pores of the

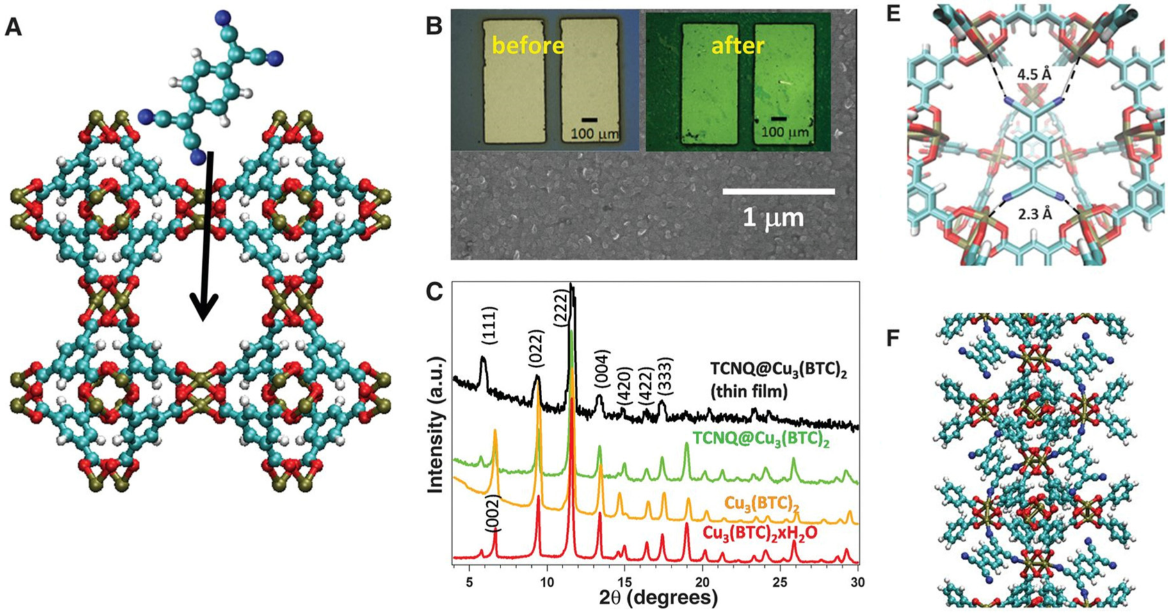

Fig. 12 Fabrication of conductive MOF thin-film devices and structural characterization. (a) TCNQ molecule shown above a $Cu_3(BTC)_2$ MOF; arrow points into the pore. Colour code: H = white, N = blue, C = cyan, O = red and Cu = light brown. (b) SEM image of a MOF-coated device; insets are optical images of devices before and after TCNQ infiltration. (c) XRD data for powder and grazing incidence XRD for a thin film. (e) Minimum-energy configuration for $TCNQ@Cu_3(BTC)_2$ obtained from *ab initio* calculations. (f) Possible configuration that would provide a conductive channel through the MOF unit cell. Reproduced with permission from ref. 89. Copyright 2014, The American Association for the Advancement of Science.

MOF was confirmed by the XRPD analysis, Rietveld analysis and adsorption studies. Both, the absorption and Raman spectral analysis indicate the presence of a charge transfer between the MOF and TCNQ and also the coordination of TCNQ to the Cu^{2+} centres (Fig. 12).

The presence of metal–ligand coordination-mediated charge transfer interaction increases the conductivity by about six orders of magnitude. HKUST is a poorly conducting MOF having a conductivity of 10^{-8} S cm^{-1} at room temperature while the electrical conductivity of TCNQ@HKUST-1 reached a value of 7×10^{-2} S cm^{-1} with an activation energy of 41 meV. *Ab initio* calculations indicate that TCNQ guest molecules cross linked the dimeric Cu paddlewheels within the MOF leading to strong electronic coupling between the dimeric Cu subunits.

Through-bond charge transport might be the cause of the increase in the conductivity of TCNQ@HKUST-1 (Fig. 13). This charge transport was confirmed by substituting TCNQ with its saturated analogue H_4TCNQ. H_4TCNQ@HKUST-1 shows a similar conductivity to HKUST-1 itself. This H_4TCNQ was unable to delocalize the carriers (Fig. 13). Later, Allendorf, Fischer and co-workers synthesized TCNQ incorporated HKUST-1 with the precise molecular formula $TCNQ_{1.0}@Cu_3BTC_2$ that shows an electrical conductivity value of 1.5×10^{-4} S cm^{-1}. They have also tried to provide insight on the location and binding of TCNQ within the MOF.[109] Thürmer *et al.* have encapsulated TCNQ within pre-deposited thin films of HKUST-1 on ITO. These TCNQ loaded HKUST-1 thin films show 10^{10} times higher electrical conductivity (10^{-1} S cm^{-1}) than the parent MOF (10^{-11} S cm^{-1}).[110] A similar study performed by Deep *et al.* showed that encapsulated TCNQ within the thin film of HKUST-1 on a gold-screen printed electrode has 10^9 times more conductivity than the host MOF.[111] In a third related study, Jung and co-workers showed a 10^7 times enhancement of the electrical conductivity (2.42×10^{-4} S cm^{-1}) through impregnation of TCNQ within thin films of HKSUT-1 obtained by solution shearing process.[112]

Vittal, Loh and co-workers have developed a conductive thin film of a MOF with inserted TCNQ. By changing the reaction conditions from simple mixing to slow solvent diffusion, they have synthesized nano-sheets of the 2D MOF $[Cu_2(AcO)_4(CuTPyP)_{1/2}]\cdot CHCl_3$ (H_2TPyP = 5,10,15,20-tetra-4-pyridyl-21*H*,23*H*-porphine) and transfer them to the substrate. The atomic force microscopy (AFM) study indicates the average thickness of the nano-sheets is about 70 nm. For electrical conductivity measurements, they also prepared thin films of the 2D MOF on silicon wafers and then TCNQ was incorporated within the thin films. The resultant TCNQ@2D-MOF shows 10^3 times higher conductivity than the parent MOF (10^{-9} S cm^{-1}). They have demonstrated that the charge transfer interaction between the host and TCNQ guest molecules is the main reason behind such an increment in the electrical conductivity.[90]

Recently, Shiozawa *et al.* have prepared thin films of TCNQ@Co-MOF-74 on glass substrates following the previous results. They observed that thin films of TCNQ@Co-MOF-74 are more conductive than the parent Co-MOF-74 (insulating in nature), although they are less conductors than TCNQ@HKUST-1 since TCNQ cannot build a conductive pathway within the honeycomb structure of Co-MOF-74 in contrast to HKUST-1.[113]

TCNQ has also been incorporated within the voids of the 3D MOF $[Cu_2(TATAB)_3]\cdot 7.5H_2O$ (where H_3TATAB = 4,4′,4″-((1,3,5-triazine-2,4,6-triyl)tris(azanediyl))tribenzoic acid) by Xu *et al.*[114]

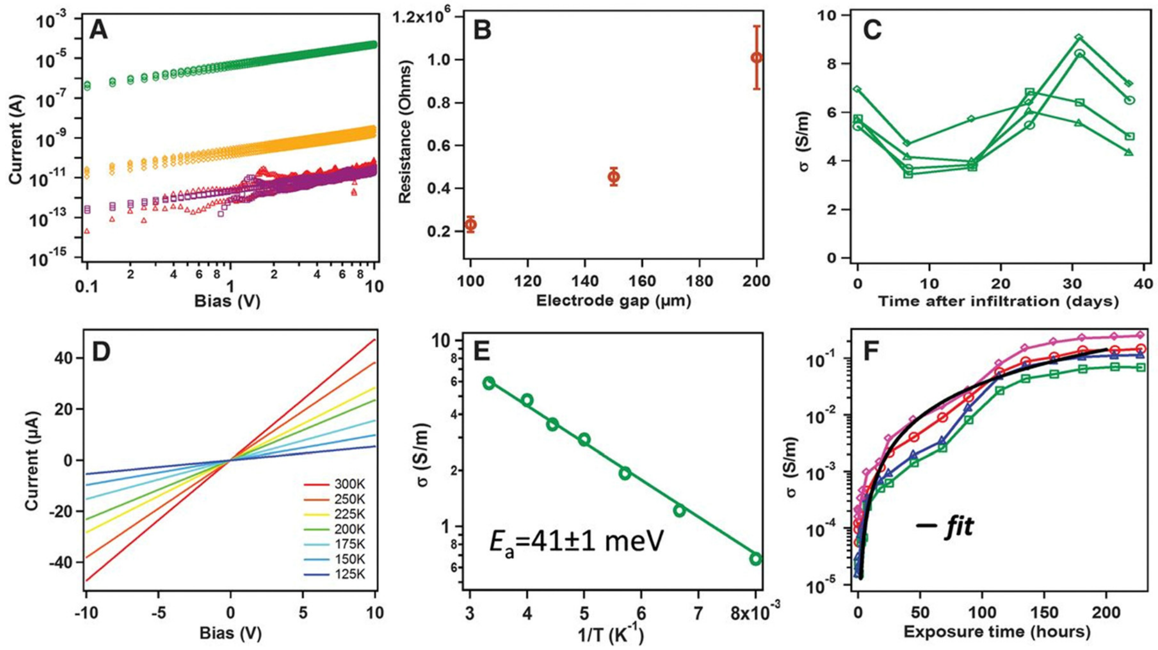

Fig. 13 Electronic transport characteristics of MOF thin film devices. (a) *I*–*V* curves before (red) and after insertion of TCNQ (green), F_4-TCNQ (gold), or H_4-TCNQ (purple). (b) Channel-length dependence of conductivity for TCNQ-infiltrated devices; error bars denote standard deviations. (c) Stability of conductivity over time for several devices. (d) *I*–*V* curve temperature dependence. (e) Arrhenius plot of the conductivity. (f) Conductivity *versus* exposure time for several devices. The black line is a fit to percolation theory, $\sigma = 4 \times 10^{-6}\,(t - 0.5)^2$, where *t* is exposure time. Reproduced with permission from ref. 82. Copyright 2014, The American Association for the Advancement of Science.

The TCNQ@MOF has 10^4 times higher conductivity than the parent MOF. These authors have demonstrated that the insertion of the unoccupied molecular orbitals of TCNQ molecules into the HOMO–LUMO gap of the MOF formed a charge transport channel within the 3D MOF, facilitating the conduction of electrons.[114]

A significant enhancement of the electrical conductivity has been recently reported by Sindhu and Ballav by depositing HKUST-1 on TCNQ-doped HKUST-1.[115] Pure MOF HKUST-1 thin film shows an electrical conductivity of 10^{-8} S cm^{-1} and the encapsulation of TCNQ increases the conductivity to 10^{-3} S cm^{-1}. The deposition of HKUST-1 on TCNQ@HKUST-1 shows a further enhancement of the conductivity.[115]

2.2.2 Iodine and polyiodides. Due to the redox active behaviour, large size and high electron density of iodine – the encapsulation of iodine and polyiodides into MOFs has gained much interest.[116] The incorporation of I_2 within the pores of MOFs can increase the electrical conductivity thanks to two different mechanisms: (i) an increase in the intermolecular interactions between I_2 and aromatic pore walls and (ii) a charge transfer transition between I_2 and the framework through an n–σ* host–guest charge transfer.

Zeng *et al.* have shown the possibility of tuning the electrical conductivity of $[Zn_3(\text{DL-lac})_2(pybz)_2]\cdot 2.5DMF$ (where DL-lac = lactate and pybz = 4-pyridine benzoate) through I_2 loading within the 1D channels (∼11 × 10 Å) by soaking the MOF in a cyclohexane solution of I_2 (Fig. 14). The electrical conductivity of I_2@MOF is 3.42×10^{-3} S cm^{-1} along the channels and 1.65×10^{-4} S cm^{-1} in the direction perpendicular to the channels. Both values are much higher than those of the pristine MOF (7×10^{-6} S cm^{-1}). The authors demonstrated that the donor–acceptor interaction between the loaded I_2 and the aromatic pore walls is the reason for conductivity enhancement.[117] They have also tuned both the electrical and magnetic properties through the incorporation of I_2 within the channels of $[Co^{II}{}_3(lac)_2(pybz)_2]\cdot 3DMF$ (where pybz = 4-pyridyl benzoate and lac = D- and L-lactate). Iodine incorporation has been done by soaking single crystals of the desolvated framework within a saturated solution of I_2 in DMSO/H_2O (v/v = 1 : 1) or in cyclohexane. The DMSO:water solution leads to the partially oxidized framework $[Co^{III}Co^{II}{}_2(pybz)_2(lac)_2(H_2O)_2](I^-)\cdot 2H_2O\cdot 1.5DMSO$, which is ferromagnetic, in contrast to the antiferromagnetic parent MOF. In contrast, when the insertion is performed in cyclohexane, the crystals form a framework with the formula $\{[Co^{II}{}_3(pybz)_2(lac)_2]\cdot 2.7I_2\}$ and a conductivity of 7×10^{-6} S cm^{-1}.[118]

Kobayashi *et al.* have developed a redox-active dithiolate-based MOF Cu[Ni(pdt)$_2$] (CuNi) (pdt^{2-} = pyrazine-2,3-dithiolate), which is isostructural to Cu[Cu(pdt)$_2$] (CuCu). In contrast to CuCu, whose framework collapses upon desolvation, CuNi retains its structure upon desolvation, allowing the incorporation of I_2 vapour within the channels of the framework. The resultant I_2@CuNi shows 10^4 times higher conductivity (10^{-4} S cm^{-1} with an activation energy of 490 meV) than the parent CuNi MOF (10^{-8} S cm^{-1}). This might be due to the partial oxidation of the $[Ni^{II}(pdt)_2]$ centres that results in an increase in the charge carriers responsible for the improved conductivity.[119]

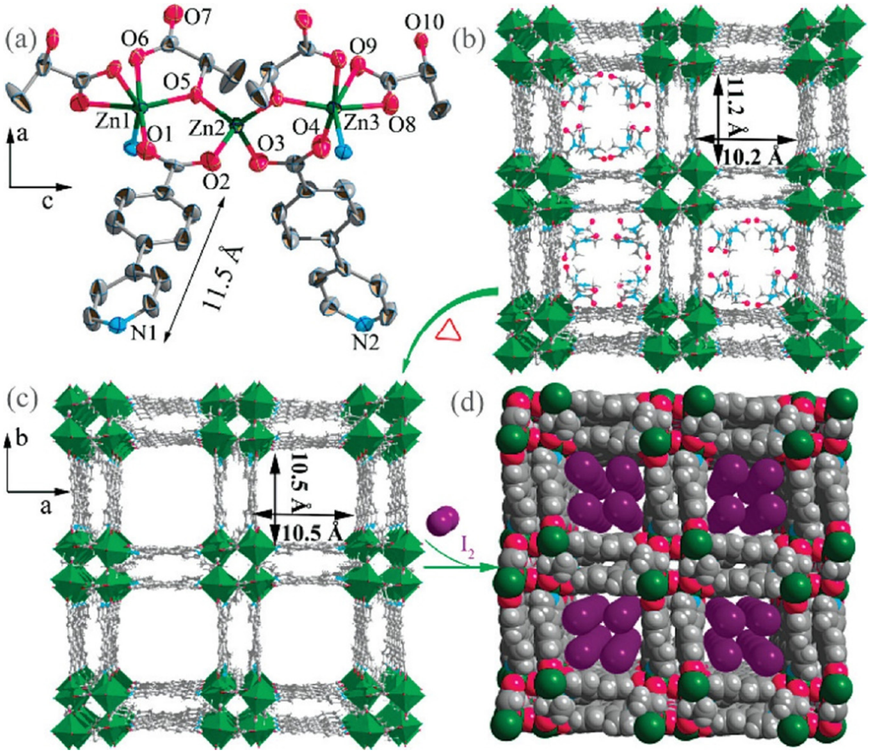

Fig. 14 (a) Coordination environment of Zn atoms in $[Zn_3(\text{DL-lac})_2(pybz)_2]\cdot2.5DMF$ (H-atoms are omitted for clarity). (b) Perspective views of the 3D open framework with 1D channels in $[Zn_3(\text{DL-lac})_2(pybz)_2]\cdot2.5DMF$ with the guest DMF molecules. General colour code: Zn, green; N, blue; O, red; C, gray. (c) The completely desolvated framework of $[Zn_3(\text{DL-lac})_2(pybz)_2]\cdot2.5DMF$, showing the empty channels. (d) Location of the I_2 molecules in the channels of the desolvated framework of $[Zn_3(\text{DL-lac})_2(pybz)_2]\cdot2.5DMF$. The PLATON calculated void space in the desolvated framework of $[Zn_3(\text{DL-lac})_2(pybz)_2]\cdot2.5DMF$ is 43.8%. Reproduced with permission from ref. 117. Copyright 2010, The American Chemical Society.

The I_2 doped MOF $[Cu_6(pybz)_8(OH)_2]\cdot(I_5)\cdot(I_7)$ has been synthesized using the *in situ* template method by Yin *et al.*[120] Structural studies show that the resulting framework contains I_5^- and I_7^- polyiodides within the channels anchored by weak interactions between the polyiodides and the aromatic pore-walls (Fig. 15). Keeping the compound in dry methanol leads to the removal of the polyiodides, leading to the I^--containing framework $[Cu_6(pybz)_8(OH)_2](I)_2\cdot3.5CH_3OH$. The polyiodide-encapsulated MOF shows 10^2 times higher electrical conductivity (8.11×10^{-7} S cm^{-1}) than the iodide: I-@MOF (8.04×10^{-9} S cm^{-1}). These data indicate that the conductivity decreases with decreasing the amount of iodide in the channels. The non-covalent interactions between the polyiodides and the aromatic walls of the MOF provide the charge transport pathway.[120]

Iodine has also been incorporated by Han and co-workers within the thin films of two different Co-MOFs: [Co-NDC] and [Co-BDC], by using two different ligands (NDC = 2,6-napthalenedicarboxylic acid and BDC = 1,4-benzene dicarboxylic acid).[121] Layer-by-layer thin films of the MOFs were prepared on TiO_2 films and iodine incorporation was done by dipping the thin films in a saturated acetonitrile solution of I_2. Both parent MOFs are insulating and iodine incorporation increases both the carrier concentration ($+1.14 \times 10^{11}$ and $+5.48 \times 10^{11}$ cm^{-3}) and mobility (21.2 and 87.6 cm^2 V^{-1} s^{-1}) for both MOF thin-films, respectively. The insulating [Co-NDC] MOF becomes semiconducting with a conductivity value of 1.88×10^{-6} S cm^{-1}.[121] In this case, the enhancement of the conductivity is due to ligand oxidation by I_2 that was confirmed by XPS analysis and by absorption spectroscopy.[122]

The crystal structure of the iodine encapsulated MOF $[Co_3(BDC)_3(H_2bpz)_2]\cdot2DMF\cdot8H_2O$ (H_2BDC = 1,4-benzenedicarboxylic acid, H_2bpz = 3,3′,5,5′-tetra methyl-4,4′-bipyrazole) has been established by Li *et al.* after post-synthetic iodine loading.[123] The parent MOF undergoes a single crystal to single crystal (SCSC) transformation to form the I_2-containing MOF $[Co_3(BDC)_3(H_2bpz)_2]\cdot I_2\cdot2DMF$. The I_2 molecules interact with the host framework through C–H···I hydrogen bonding interactions. I_2@MOF shows 10^3 times higher conductivity (1.56×10^{-8} S cm^{-1}) than the parent MOF (2.5×10^{-11} S cm^{-1}). The authors propose that the n–σ* host–guest charge transfer is the main reason for conductivity enhancement.[123]

Hu *et al.* have measured the electrical conductivity of the MOF $[Tb(Cu_4I_4)(ina)_3(DMF)]$ (ina = isonicotinate) that has two different types of channels (A and B), upon iodine uptake and release. I_2 uptake is carried out by soaking the parent MOF in a saturated I_2 cyclohexane solution for 2 hours while I_2 can be released by heating the I_2@MOF. The parent MOF has a conductivity of 5.72×10^{-11} S cm^{-1} that increases by a factor of 10^7 to a value of 2.16×10^{-4} S cm^{-1} after I_2 uptake. The release of I_2 again decreases the conductivity to 10^{-10} S cm^{-1}. A structural study of the I_2-loaded MOF shows that channel A

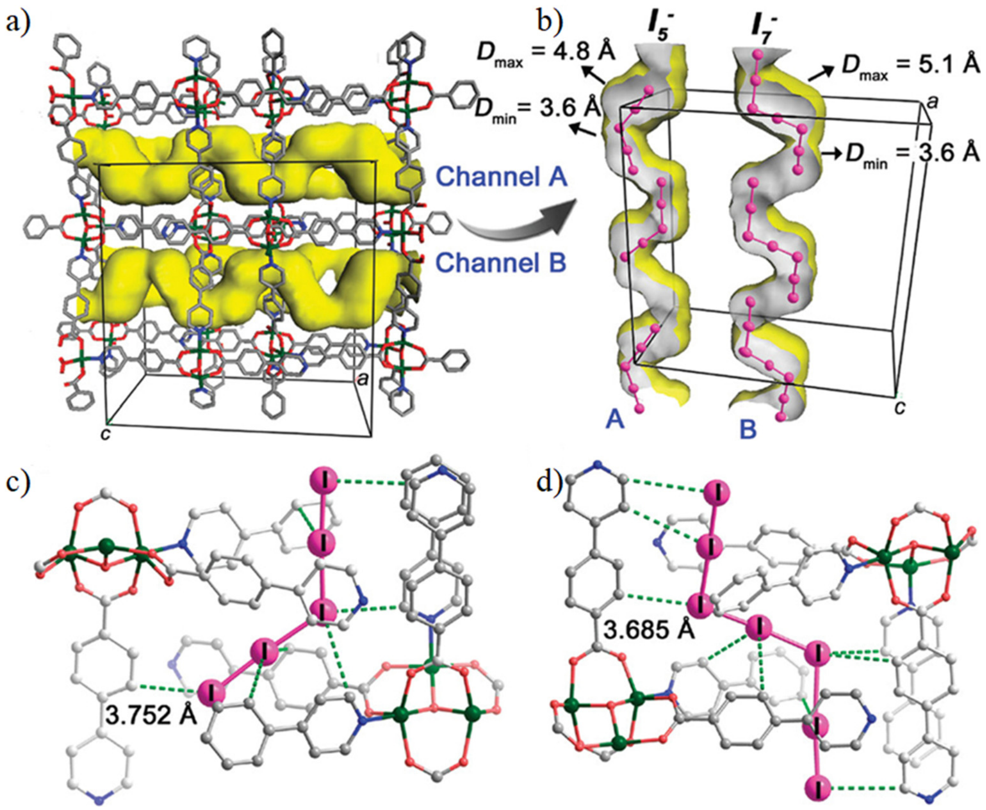

Fig. 15 (a) Perspective view of the S-shaped channels along the *a*-axis in $[Cu_6(pybz)_8(OH)_2]\cdot(I_5)\cdot(I_7)$. (b) Section drawing of the A and B channels in each cell lattice. (c) The environment of I_5^- in channel A; the distances from I atoms to C atoms of phenyl or pyridyl rings are in the range 3.732–3.999 Å. (d) The environment of I_7^- in channel B; the distances from I atoms to C atoms of phenyl or pyridyl rings are in the range of 3.685–4.281 Å. Reproduced with permission from ref. 120. Copyright 2012, The American Chemical Society.

contains half an I_2 molecule per formula unit whereas channel B contains one I_2 molecule. In channel A, the I_2 molecules interact with the aromatic ligands and with the iodides of the Cu_4I_4 moieties to form $I^-\cdots I_2\cdots I^-$ polyiodide chains. On the other hand, the I_2 molecules of channel B interact with the aromatic pore walls only. So, the interaction of $[Cu_4I_4]$ with the guest I_2 molecules forms $[Cu_4I_5]_n$ layers, which is the conducting pathway for the MOF.[124]

The important role of iodine on the conductivity of MOFs was further confirmed by Schröder and co-workers[125] on two different MOFs, $[V_2^{III}(OH)_2(L)]$ and $[V_2^{IV}(O)_2(L)]$ (H_4L = biphenyl-3,3′,5,5′-tetracarboxylic acid), where iodine was incorporated by iodine vapour diffusion after desolvation of the MOF. The crystal structures of the I_2@MOFs were determined by high-resolution synchrotron powder X-ray diffraction. Structural analysis of $I_2@[V_2(OH)_2(L)]$ shows the presence of three I_2 molecules and one I_3^- ion within the channels. The formation of I_3^- implies the oxidation of V^{III} centres. BVS calculation shows that the overall valence is 3.28 for the V centre and the complex is denoted by $I_2@[V^{III}V^{IV}(OH)_2(L)]$. The I_3^- ions are located close to the –OH groups, and there is a strong hydrogen bond between the I_3^- and –OH groups, although the H atom cannot be located from the XRPD data. The I_2 molecules are located near the phenyl rings and are stabilized by intermolecular interactions. In $[V_2^{IV}(O)_2(L)]$, the incorporation of I_2 does not lead to oxidation of the framework and the I_2 molecules interact with each other to form helical chains within the channels of the MOF to form an overall complex formulated as $I_2@[V_2^{IV}(O)_2(L)]$. Electrical conductivity measurements show that the conductivity increases 10^7 times for $[V_2^{III}(OH)_2(L)]$ upon iodine incorporation while it remains almost the same for $[V_2^{IV}(O)_2(L)]$. These data indicate that the host–guest charge transfer interaction enhances the electrical conductivity of the material.[125]

Ballav *et al.* have reported the enhancement of the electrical conductivity of SURMOF (surface-mounted metal–organic framework) thin films of Cu-TCNQ through iodine incorporation. Mercaptoundecanoic acid (MUDA), bearing polar –COOH and –SH head-groups linked together *via* a $-(CH_2)_{10}-$ moiety, was used to form self-assembled monolayers (SAMs) on semiconducting FTO coated on glass and metallic gold. Cu-TCNQ SURMOF thin films were deposited by sinking the SAMs in the solution of copper acetate in EtOH and TCNQ in EtOH. I_2 was incorporated within the channels of the MOF by using iodine vapour. Electrical conductivity measurements show that the iodine-incorporated SURMOF shows 100 times higher conductivity (10^{-3} S cm^{-1}) than the parent MOF itself (10^{-5} S cm^{-1}). In the parent SURMOF, copper is present in its +1 oxidation state while the TCNQ is present as a TCNQ radical anion as suggested by the Raman spectroscopy and EPR studies. The coordination of the TCNQ radical anion with Cu^+ within the parent SURMOF is the reason behind its high conductivity, although a certain amount of the TCNQ radical anion undergoes disproportionation into the TCNQ molecule and the TCNQ dianion. I_2 oxidizes the TCNQ radical anion to the neutral TCNQ molecule with consequent formation of the I_3^- ion but Cu^+ remains unaltered. So, this charge transfer is only ligand oriented and this is the main reason for the enhancement of conductivity.[126]

In a similar manner, the enhancement of the electrical conductivity of the MOF $[Eu_4(BPT)_4(DMF)_2(H_2O)_8]$ (where H_3BPT = biphenyl-3,4′,5-tricarboxylate) through incorporation of iodine was studied by Zhang *et al.* They have observed that the electrical conductivity of the I_2-doped MOF increases with increasing temperature from 25 to 80 °C under anhydrous conditions. Although the MOF loses some amount of doped I_2 on heating, the conductivity increases from 8.27×10^{-7} S cm^{-1} to 2.71×10^{-5} S cm^{-1}. Polyiodide ions, formed within the channels of the MOF, promote the n to σ* transition with high efficiency and this is the reason for the observed conductivity enhancement.[127]

In some cases, the loading of iodine enhances the electrical conductivity of the host MOF only marginally. D'Alessandro and co-workers have reported the enhancement of the electrical conductivity of $[Zn_2(TTFTB)(H_2O)_2]$ (where TTFTB = tetrathiafulvalene tetrabenzoate) through iodine loading by using iodine vapour. Iodine oxidizes the ligand to $TTFTB^{\bullet+}$ with formation of iodide and polyiodides. Such a host–guest charge transfer phenomenon increases the electrical conductivity of the parent MOF from 2.5×10^{-10} S cm^{-1} to 1.6×10^{-9} S cm^{-1}.[128]

In another example, Zuo *et al.* have reported a small improvement in the electrical conductivity of lanthanoid-tetrathiafulvalene-based MOFs through incorporation of iodine within the MOFs. Iodine oxidizes the ligand tetrathiofulvalene (TTF) to $TTF^{\bullet+}$ but the weak enhancement of the conductivity is due to a lack of band formation.[129] In another article, the same group has reported the enhancement in the electrical conductivity of two different 3D MOFs $[Fe(dca)_2]_2[TTF(py)_4]\cdot CH_2Cl_2$ and $[Fe(dca)][TTF(py)_4]\cdot ClO_4\cdot CH_2Cl_2\cdot 2CH_3OH$ having the redox active ligand tetra(4-pyridyl)tetrathiafulvalene (TTF-$(py)_4$) and spin-crossover Fe^{II} centres (dca = dicyanamide). Iodine loading was done by immersing the crystals of the complexes in an I_2 saturated solution in cyclohexane. Single crystal X-ray structural studies of the I_2@MOFs indicate the formation of $TTF^{\bullet+}$ radical cations with consequent reduction of iodine to I_3^- which is also confirmed by XPS and EPR studies. Electrical conductivity measurement shows a 10^3 times increment of conductivity for both cases.[130]

Gordillo *et al.* have developed a semiconducting MOF $[Zn_3(ExTTFTB)_2(H_2O)_4\cdot 6EtOH]$ (where ExTTFTB is an electron-rich π-extended tetrathiafulvalene ligand equipped with four benzoic acid units). The ExTTFTB ligand has a butterfly-like shape and is decorated with four benzoic acid units and forms a porous 3D double-helical MOF by reacting with $Zn(NO_3)_2$. Structural analysis shows that the ExTTFTB ligand is highly constrained with unsymmetrical electron distribution due to the different binding modes of the four carboxylate groups. These distortions critically change the redox behaviour of the ligand. The free ligand shows one two-electron oxidation step to form the planar $ExTTFTB^{2+}$ dication, while the ligand within the MOF undergoes a one-electron oxidation to form the radical cation $ExTTFTB^{\bullet+}$. Iodine was incorporated within the pores of the MOF by placing it in iodine vapour. Electrical conductivity measurement shows that I_2@MOF has 10^4 times higher conductivity (10^{-6} S cm^{-1}) than the parent MOF (10^{-10} S cm^{-1}). EPR studies show that a large amount of ExTTFTB ligand was oxidized to form $ExTTFTB^{\bullet+}$ radical cation upon I_2 loading. The charge transfer interaction between $ExTTFTB^{\bullet+}$ and ExTTFTB forms donor–acceptor chains which act as the charge transport pathway.[131] In another article, the same group demonstrated a 100 times enhancement of the electrical conductivity of the Tb-containing parent MOF (Tb-ExTTFTB) with the same ligand, upon I_2 loading.[132] Similarly, Valente *et al.* have reported a 10^3 times enhancement of the electrical conductivity of a perylene-based MOF through encapsulation of iodine. The perylene-based MOF shows weak electron conduction (10^{-8} S cm^{-1}) while the encapsulation of iodine leads to the formation of I_3^- with consequent oxidation of perylene. Two-probe electrical conductivity measurements on single crystals of the host–guest show an enhanced electrical conductivity value of $\sim 10^{-5}$ S cm^{-1}.[133]

2.2.3 Tetrathiafulvalene (TTF) and derivatives.

Since TTF and its derivatives are π-enriched molecules, they have gained much attention in designing conducting materials in their oxidized state.[134] Even metallic conductivity can be achieved for the charge transfer complex TTF-TCNQ.[135] Since then, much attention has been paid to the synthesis of conductive material combining these molecules with other molecules or lattices to form multifunctional materials. Day and co-workers prepared the first paramagnetic metallic charge transfer complex with bis(ethylenedithio)-tetrathiofulvalene (BEDT-TTF): $(BEDT\text{-}TTF)_3[CuCl_4]\cdot H_2O$ and showed the first evidence of localized and conduction electrons.[136]

One of us has performed extensive research on the incorporation of TTF within the channels of MOFs/PCPs to design conductive materials. In 2000, Coronado, Gómez-García *et al.* showed the presence of magnetoresistance in a host–guest system formed by the *in situ* encapsulation of BEDT-TTF within the interlamellar space of a 2D magnetically ordered framework. The host–guest $(BEDT\text{-}TTF)_3[MnCr(C_2O_4)_3]$ ($C_2O_4^{2-}$ = oxalate dianion) was synthesized by electro-crystallization using tris(oxalate)chromate(III) and Mn^{II} salt in a 2 : 3 ratio in the presence of BEDT-TTF. Structural analysis shows that BEDT-TTF cations form pure pseudohexagonal β-type supramolecular layers within the honeycomb 2D coordination layers of $[MnCr(C_2O_4)_3]^-$. The accumulated charge per BEDT-TTF moiety is +1/3. The material shows magnetic long-range order below 5.5 K with the presence of magnetic hysteresis at 2 K. In plane, four-probe electrical conductivity measurements show the largest room temperature conductivity found in a conductive ec-MOF ($\sim$250 S cm^{-1}). Furthermore, this compound shows a metallic conductivity within the temperature range of 2–300 K.[137] Application of a magnetic field perpendicular to the layers shows the presence of negative magnetoresistance

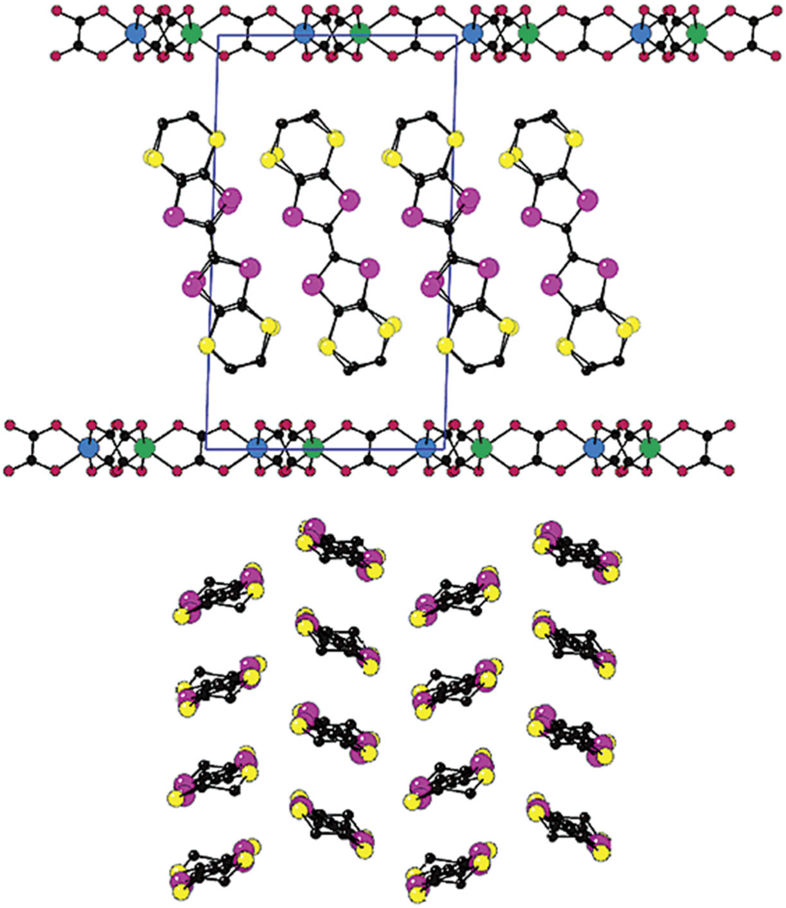

Fig. 16 Representation of the structure of $[BETS]_x[MnCr(ox)_3]\cdot(CH_2Cl_2)$: idealized side view of the alternating layers (up) and top view of the organic layer (down). Reproduced with permission from ref. 138. Copyright 2003, The American Chemical Society.

below 10 K. The same authors reported a similar host–guest framework with the Selenium-substituted organic donor bis(ethylenedithio)-tetraselanafulvalene (BEDT-TSF): $(BEDT\text{-}TSF)_3[MnCr(C_2O_4)_3]$ (Fig. 16).[138] As observed in the previous structure, the (BEDT-TSF) moieties are located within the interlamellar space of the 2D honeycomb layers of $[MnCr(C_2O_4)_3]^-$, and similarly, the average charge on each (BEDT-TSF) moiety is +1/3. The magnetic framework also shows a high room temperature electrical conductivity of 1 S cm^{-1} and a metallic conductivity within the range of 150–300 K. The difference in conductivity is due to the effective distance between the donor moieties.

The same group also prepared the host–guest charge transfer complex formulated as $(BEDT\text{-}TTF)_x[MnRh(C_2O_4)_3]\cdot CH_2Cl_2$ (where $x = 2.526(1)$) by replacing Cr with Rh. The room-temperature electrical conductivity of this compound is 13 S cm^{-1} and shows a metallic behaviour, reaching a very high value of 28 S cm^{-1} at 103 K. The difference in the conductivity value was attributed to small structural differences.[139] The use of other trivalent and divalent metal ions and other TTF-type organic donors gave rise to more than a dozen examples of compounds with magnetic ordering and high electrical conductivities in the range of 0.1–21 S cm^{-1}, which were reported in a series of articles published by Coronado, Gómez-García *et al.*[140–143]

Later Zhang and co-workers encapsulated BEDT-TTF within the interlamellar space of homometallic 2D coordination polymers. An electro-crystallization method was employed to synthesize the framework $(BEDT\text{-}TTF)_3[Cu_2(C_2O_4)_3]\cdot 3H_2O$. Structural analysis shows that each asymmetric unit contains three BEDT-TTF moieties, and they are stacked face-to-face to form 1D stacks along the *a*-axis. These columns are further packed through S···S interactions to form 2D supramolecular layers known as θ^{21}-phase.[144] The donor 2D supramolecular layers are located between the anionic honey-comb coordination layers of $[Cu_2(C_2O_4)_3]^{2-}$. The average formal average charge on each BEDT-TTF molecule is +2/3, although there is an inhomogeneous charge distribution, as confirmed by Raman spectra. Four-probe electrical conductivity measurements show a high room temperature conductivity of ∼4 S cm^{-1}, although it shows a semiconducting behaviour and becomes insulating at low temperatures, due to an inhomogeneous charge distribution.[145]

The same authors prepared another charge transfer complex by incorporating the Se-containing donor BEDT-TSF within the interlayer space of the same 2D homometallic anionic coordination layers using a similar electro-crystallization method.

Similarly, each asymmetric unit contains three BEDT-TSF moieties and they form 2D donor layers through S···S, S···Se and Se···Se interactions. The average formal charge is also +2/3, as confirmed by Raman and EPR spectral analyses. Four probe electrical conductivity measurements show a very high room temperature conductivity of 140 S cm^{-1} and a metallic behaviour from 300 K to 180 K. The conductivity remains approximately constant within the temperature range of 180 to 150 K and below 150 K decreases to a value of 10 S cm^{-1} at 17 K to become insulating below 12 K. The large difference in conductivity value of the BEDT-TTF and BEDT-TSF based structures is due to the larger size and diffused electron density of Se compared to S. Theoretical analysis reveals that overlap integral for BEDT-TSF based structure is twice that of the BEDT-TTF containing material and band dispersion is stronger for the Se-containing compound.[146]

Using a solvothermal synthetic method, Saha *et al.* have very recently prepared another conducting framework by encapsulating TTF within the interlamellar spaces of a 2D framework.[147] Thus, a structure similar to MOF-74, could be prepared by the reaction of the electron acceptor DSNDI (DSNDI = 4,4′-(1,3,6,8-tetraoxobenzo[*lmn*][3,8]phenanthroline-2,7(1*H*,3*H*,6*H*,8*H*)-diyl)bis(2-hydroxy benzoic acid), prepared by reaction between naphthalene dianhydride (NDA) with 4-aminosalicylic acid with zinc salts at 90 °C). The framework contains large hexagonal channels with an average pore size of ∼3.1 nm. The optical bandgap of the host MOF is calculated to be 2.1 eV. The TTF loading was done by soaking the activated material in a TTF solution for 2 days, and the loading was identified by the colour change to brownish. The optical bandgap of the TTF@MOF becomes ∼1 eV. The formation of charge transfer between TTF and MOF was confirmed by the appearance of a new band at 900 nm, and this was also further confirmed by EPR spectroscopy. Such a decrease in the bandgap is due to the intercalation of TTF moieties between electron-deficient DSNDI ligands.[147]

Corma *et al.* showed that the intercalation of TTF in the delaminated 2D zeolite framework ITQ-2 generates stable TTF^{+} radicals within the open cups of the external surface, as demonstrated by EPR measurements.[148]

2.2.4 Fullerenes. These good electron acceptors have become good candidates for designing charge transfer materials by combining them with electron donors.[149] Thus, Goswami *et al.* have incorporated C_{60} within the pores of the insulating Zr-based MOF NU-901. NU-901 is formed by the combination of $[Zr_6(\mu^3\text{-}O)_4(\mu^3\text{-}OH)_4(H_2O)_4(OH)_4]$ nodes and 1,3,6,8-tetrakis(*p*-benzoate)pyrene $(TBAPy)^{4-}$ linkers (Fig. 17). Fullerene was incorporated by soaking the activated MOF within an *o*-dichlorobenzene solution of fullerene for 4 days at 60 °C. C_{60} molecules can

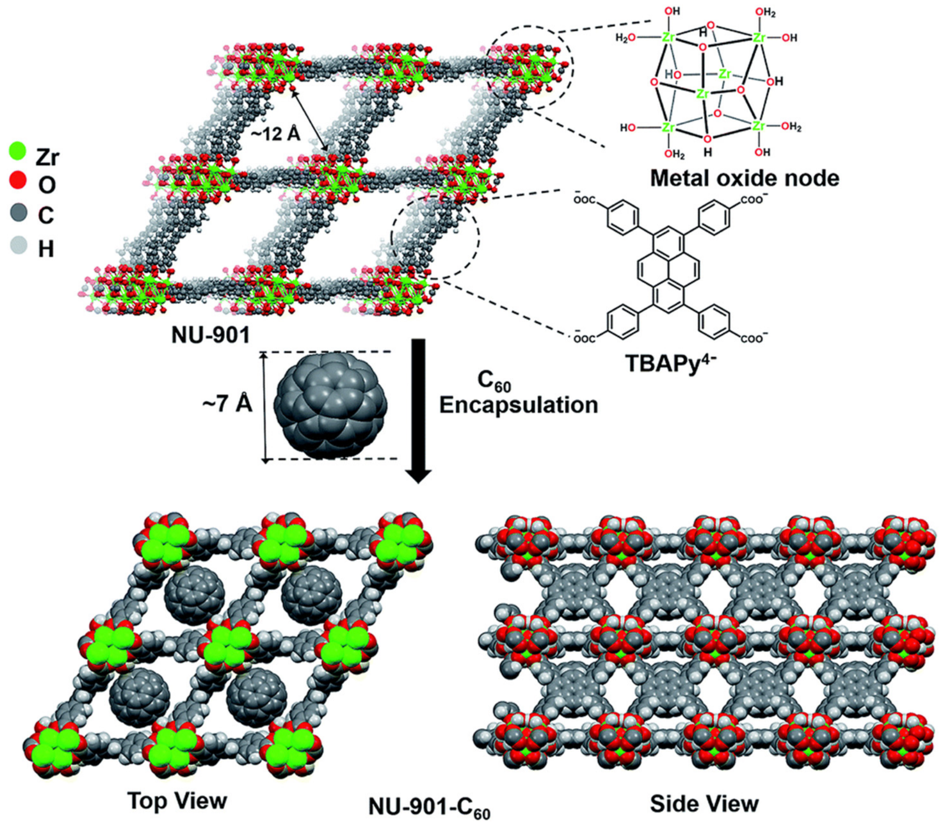

Fig. 17 Immobilization of C_{60} within the rhombus-shaped channels of NU-901. The chemical structures of the individual components of NU-901 are shown. The diameter of C_{60} (7 Å) is well suited for encapsulation in NU-901 with a pore aperture of 12 Å. The top and side views of the composite NU-901-C60 are shown. The top and side views are DFT-optimized structures in the limit of full occupancy of the diamond pores by the fullerene guest, *i.e.*, 1 : 1 occupancy. Reproduced with permission from ref. 91. Copyright 2018, The Royal Society of Chemistry.

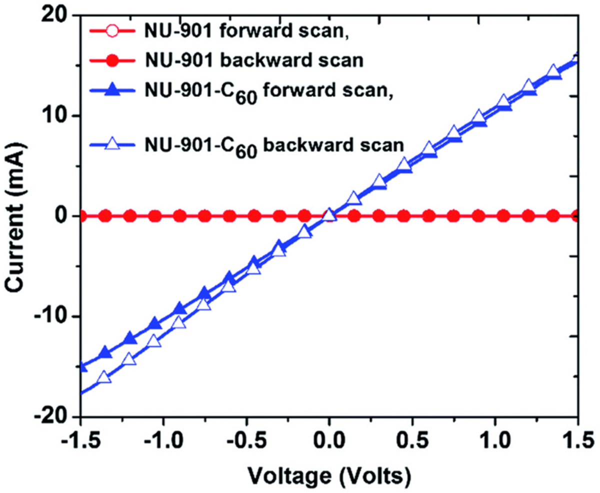

Fig. 18 *I*–*V* plot for pressed pellets of NU-901 and C_{60}@NU-901. The scan was performed from −2 V to 2 V, and the scan rate was 50 mV s^{-1}. Reproduced with permission from ref. 91. Copyright 2018, The Royal Society of Chemistry.

easily penetrate within the channels of the MOF that have a pore aperture of 12 Å, much larger than the diameter of C_{60} (∼7 Å). XRPD and SEM analyses indicate that the encapsulation of C_{60} within the channels does not alter the crystallinity and morphology of the host, and the presence of C_{60} was confirmed by Raman spectroscopy and a naked eye colour change from bright yellow to light brown. The encapsulation reduces the overall porosity of the framework, and the gravimetric analysis indicates the fullerene encapsulation is about 0.6 molecules per node. Geometry optimization using DFT calculations shows that fullerene molecules occupy large rhombus-like pores. Two-probe electrical conductivity measurements on pressed pellets show that C_{60}@NU-901 has 10^{11} times higher conductivity (10^{-3} S cm^{-1}) than the parent MOF (10^{-14} S cm^{-1}) (Fig. 18).[91]

The authors of this study proposed that the charge transfer interaction between the fullerene and the ligand $(TBAPy)^{4-}$ of the framework is responsible for the enhancement of the electrical conductivity. In order to further strengthen it, they also used the electron-rich tetra-amino(phenyl-substituted) based ligand replacing the original $TBAPy^{4-}$ ligand. The synthesized NU-901-amino MOF has a similar structure than the original $(TBAPy)^{4-}$-containing MOF. Intercalation of fullerene in this new MOF NU-901-amino results in a higher conductivity than that observed in C_{60}@NU-901 due to enhanced charge transfer interaction between fullerene and the ligand in NU-901-amino. DFT calculations also show that for the host frameworks, both the valence band maxima and conduction band minima contain contributions from the π-orbitals of the ligand while upon encapsulation of fullerene, the minima of the conduction band is predominantly composed of fullerene molecules. Additionally, the fullerene encapsulation reduces the band gap by 1.2 eV in both cases. Ray and co-workers have shown, theoretically, that the incorporation of hetero-fullerenes within the void space of MOFs may have more impact on the electrical conductivity of MOFs than fullerenes.[150]

A significant conductivity enhancement through encapsulation of C_{60} within a mesoporous tetrathiafulvalene (TTF)-based MOF: $[(TTFTB)_3[(Fe_3O)(H_2O)_2(OH)]_2]$ (where H_4TTFTB = tetrathiafulvalene tetrabenzoic acid) was reported by Mínguez and co-workers.[151] Fullerene loading was done by soaking the activated MOF within an *o*-dichlorobenzene solution of fullerene for 3 days at 60 °C. C_{60}@MOF shows a 100 times higher conductivity (4.7×10^{-9} S cm^{-1}) than the parent MOF (3.7×10^{-11} S cm^{-1}). The authors proposed that the donor–acceptor charge transfer interaction between the C_{60} molecules and TTF-based linkers is the reason behind the enhancement of the electrical conductivity.[151]

Liu *et al.* incorporated C_{60} into two different porous MOFs: [Zn(TPP)] and [Cu(BPDC)] (where TPP = 5,15-bis-(3,4,5-trimethoxyphenyl)-10,20-bis-(4-carboxyphenyl) porphyrinato and BPDC = 4,4′-biphenyl-dicarboxylate). Fullerene-encapsulated MOFs show higher electrical conductivity than the unloaded frameworks. Thus, C_{60}@Zn(TPP) and C_{60}@Cu(BPDC) show conductivities two and four orders of magnitude higher than their parent structures, respectively. This difference is obviously due to different host–guest charge transfer interactions based on the ligand architecture and pore dimensions. Nevertheless, the photo-conducting response of C_{60}@Zn(TPP) is much better than that of C_{60}@Cu(BPDC).[152]

2.2.5 Ferrocene (Fc) and derivatives.

2.2.5 Ferrocene (Fc) and derivatives. Ferrocene (Fc) is one of the simplest organometallic compounds.[153] It consists of a sandwich structure formed by a central iron atom bonded to two cyclopentadiene rings on opposite sides. Due to its several properties such as non-innocent redox behaviour and optical and electrochemical activities, ferrocene and its derivatives are used as guest species or building blocks to design different multifunctional MOFs.[154]

In 1997, Coronado, Gómez-García *et al.* prepared a series of layered magnets with the decamethylferrocenium cation $(FeCp^*_2)^+$ inserted into the interlayer space of oxalate-based 2D honeycomb heterometallic magnets of the type $[M^{II}M^{III}(C_2O_4)_3]^-$ with M^{II} = Mn, Fe, Co, Cr, Ni and Cu and M^{III} = Cr and Fe.[155] The same authors extended the initial work with decamethyl–cobaltocenium $(CoCp^*_2)^+$ and decamethyl–manganocenium $(MnCp^*_2)^+$ with different M^{II} and M^{III} ions, including solid solutions of Cr^{III} and Fe^{III} in different proportions.[156–162]

In 2006, Fischer *et al.* successfully synthesized a Fc-containing MOF where the guest Fc molecules are interpenetrated within the host framework through van der Waals interactions without altering the structure.[163] Later, Fischer and co-workers incorporated Fc within the structure of MIL-53(Al) by grafting 1,1′-ferrocenediyl-dimethylsilane.[164] Heck *et al.* have studied the ferrocene loading within the pores of two different MOFs: $[Cu_2(BDC)_2(dabco)]$ and $[Cu_2(ndc)_2(dabco)]$ (where H_2BDC = 1,4-benzene dicarboxylic acid, ndc = 1,4-naphthalene-dicarboxylate and dabco = 1,4-diazabicyclo-[2.2.2]-octane) by exposing the MOFs to ferrocene vapour. Mössbauer spectroscopic studies indicate that the redox behaviour does not alter after ferrocene loading.[165]

Ferrocene incorporation was also performed by Dragässer *et al.* to enhance the electrical conductivity of thin films of

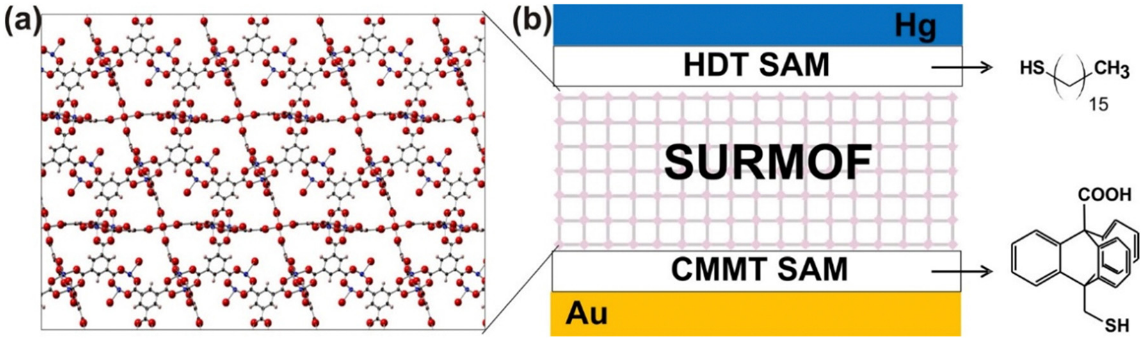

Fig. 19 Scheme of the Hg-based tunnelling junction. (a) Crystal structure of HKUST-1 with [111] orientation with respect to the Au surface. O, C and Cu atoms are coded in red, blue, and black colours, respectively. (b) Contact area between the two electrodes: Hg as the top electrode is passivated with a SAM made of hexadecanethiol ($C_{16}H_{33}$-SH, HDT), whereas the SURMOF grown on a 9-carboxy-10-(mercaptomethyl) triptycene (CMMT) modified Au substrate serves as the bottom electrode. The molecular formulas of HDT and CMMT are presented on the right side. Reproduced with permission from ref. 166. Copyright 2012, The Royal Society of Chemistry.

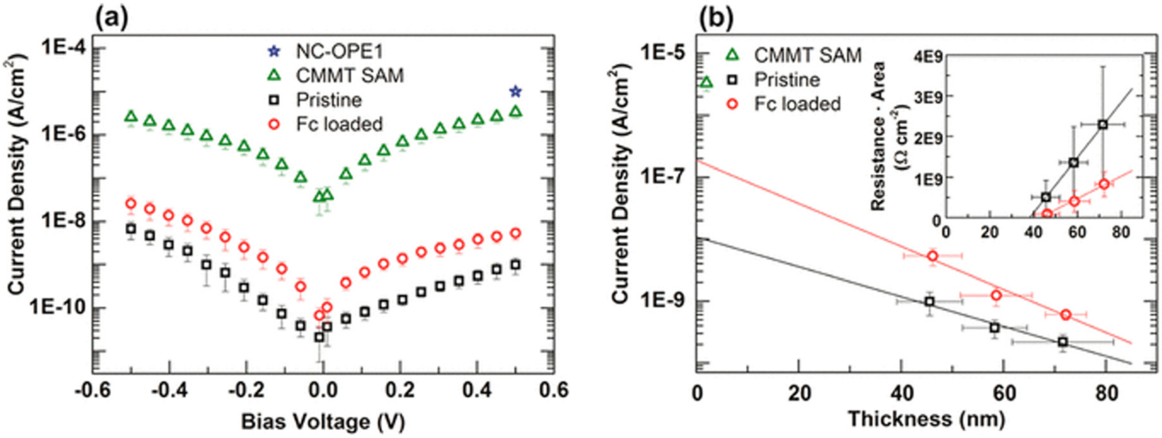

Fig. 20 (a) Current density (logarithmic scale) *vs. V* plot for HKUST-1 SURMOF, prepared by 5 spraying cycles, before (black empty squares) and after (red empty circles) ferrocene loading. Green empty triangles correspond to the CMMT SAM. The blue star represents the current density at a bias voltage of 0.5 V for a nitrile-substituted phenylthiol (NC-OPE1) SAM, which has a comparable thickness to the CMMT SAM and is given for comparison. (b) Current density (logarithmic scale) at 0.5 V *vs.* thickness of HKUST-1 SURMOFs, pristine (black empty squares) and after ferrocene loading (red empty circles). From the slope, the decay factor β has been calculated. A green triangle marks the current density for the CMMT SAM. The inset displays resistance times area *vs.* thickness of HKUST-1 SURMOFs, pristine (empty black squares) and after ferrocene loading (empty red circles). The data are obtained as V J^{-1} at V = 0.5 V. Straight lines show linear fits, corresponding to an ohmic, linear increase in resistance with length. Reproduced with permission from ref. 166. Copyright 2012, The Royal Society of Chemistry.

HKUST-1 MOF (Fig. 19 and 20). Self-assembled monolayers (SAM) of mercaptohexadecanoic acid were prepared on a gold electrode over Si, and thin films of HKUST-1 were prepared by sinking the SAM in solutions of copper(II) acetate and trimesic acid, respectively. Ferrocene loading was done by exposing the thin films in ferrocene vapour. Electrical conductivity measurement shows that the ferrocene@MOF has a conductivity of 2 × 10^{-9} S cm^{-1}, 50 000 times higher than that of ferrocene (10^{-14} S cm^{-1}). Within the pores of HKUST-1, ferrocene undergoes oxidation to ferrocenium $(Fc)^+$ and such charge transfer is the prime reason behind the increment of conductivity.[166] In another article, the same group developed a tunnelling junction by depositing a Hg droplet with passivated hexadecanethiol and observed that the Fc@MOF shows 2.5 times higher conductivity than the parent HKUST-1 MOF (Fig. 19).[167]

Recently, Hupp and co-workers have shown the modulation of the charge transport properties of ferrocene-grafted MOF NU-1000.[168] The carboxylate functionalized ferrocene moieties were grafted at the Zr_6 nodes through coordination of the carboxylate groups to the Zr centres by replacing hydroxide groups and/or water molecules from the node. The Fc-loaded NU-1000 shows efficient charge transport behaviour through oxidation of Fc to Fc^+. In order to control the charge transport properties, the authors introduced β-cyclodextrin (β-CD) molecules within the void spaces of the framework. β-CD has a strong affinity for neutral Fc while very little for Fc^+. They found that with increasing the amount of β-CD, the charge transport efficiency decreases. It is supposed that β-CD molecules encapsulate the grafted Fc moieties and block the charge transport throughout the framework.[168]

2.2.6 Other molecules and molecular entities. Besides the above-mentioned molecules, a few discrete approaches have

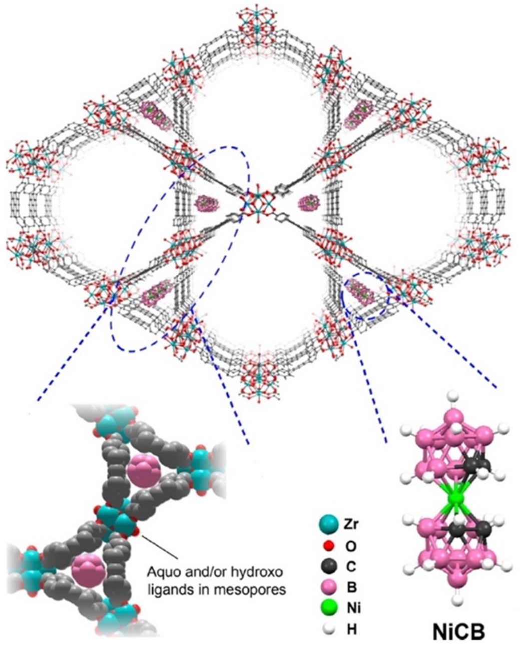

Fig. 21 The crystal structure of NiCB@NU-1000 (100 K; only one orientation of NiCB in the triangular channels is shown for clarity). Triangular channels of NiCB@NU-1000 are also shown in the space-filling model to present the close interaction between NiCB and three surrounding pyrenes. H-atoms have been omitted for clarity. The structure of NiCB is also presented. Reproduced with permission from ref. 169. Copyright 2018, The American Chemical Society.

been done to modulate the electrical conductivity of MOFs by encapsulating other molecules or molecular entities such as cationic methyl viologen (MV), inorganic molecules, O_2, *etc.*

Kung *et al.* have reported the enhancement in electrical conductivity of the porous NU-1000 MOF $[Zr_6(\mu^3\text{-}OH)_8(OH)_8(TBAPy)_2]$ (where H_4TBAPy = 1,3,6,8-tetrakis(*p*-benzoic acid)pyrene) by the encapsulation of electron-deficient $[Ni(dicarbollide)_2]$ (NiCB) (Fig. 21). Theoretical calculations show that the LUMO of NiCB is located in between the valence and conduction bands of NU-1000, and so, they hypothesized that the encapsulation of NiCB can create a charge transfer interaction between NiCB and the pyrene core. Single crystals of NU-1000 were immersed in a DMF solution of NiCB for 3 days with subsequent washing and drying. Structural analysis shows that NiCB molecules are loaded only within the narrow triangular channels while the large hexagonal channels remain empty. Both the XRPD and SEM analyses show that the encapsulation of NiCB does not alter the crystallinity and morphology of NU-1000 MOF. ICP-OES shows that 0.74 ± 0.07 NiCB molecules are loaded per Zr_6 unit. BET measurements show the partial reduction of porosity after guest loading. Electrical conductivity measurements have been done by forming thin films on interdigitated electrodes (IDE). Both parent MOF and NiCB are electrical insulators, but the conductivity of NiCB@MOF is 2.7×10^{-7} S cm^{-1} (Fig. 22). Based on the appearance of the charge transfer band in the UV-vis spectra, the authors suggest that the charge transfer interaction between donor pyrenes and acceptor NiCB is responsible for the enhancement in the electrical conductivity.[169]

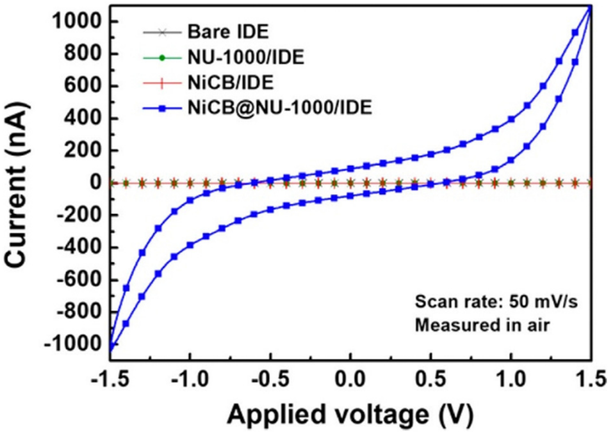

Fig. 22 *I–V* curves of the bare IDE, NU-1000/IDE, NiCB/IDE, and NiCB@NU-1000/IDE. Reproduced with permission from ref. 169. Copyright 2018, The American Chemical Society.

The enhancement of electrical conductivity of host MOFs through encapsulation of π-conjugated guest species was also studied by Guo *et al.*,[92] who attempted to modulate the electrical conductivity of the porous BMOF $[Zn_2(TCPB)(BPDPNDI)]$ (BPDPNDI = *N*,*N'*-bis(4-pyridyl)-2,6-dipyrrolidyl naphthalenediimide and TCPB = 1,2,4,5-tetrakis-(4-carboxy-phenyl)benzene) through encapsulation of multiple organic moieties. (Fig. 23).

In order to measure the electrical conductivity, thin films of the MOF have been prepared on ZnO-coated substrates prepared by spin-coating an EtOH solution of ZnO on FTO and glass slides. The authors observed that during thin-film fabrication, the MOF is selectively deposited on ZnO-coated areas but not on the FTO or glass surfaces. This fact is attributed to the covalent interaction of the tetracarboxylate moieties with the oxide surface. The electrical conductivity was measured by the four-contact method using Au-electrodes. In order to enhance the electrical conductivity, the thin films were immersed in different solutions containing MV^{2+}, 1,5-difluoro-2,4-dinitrobenzene (DFDNB), dinitrotoluene (DNT) or C_{60}. Interestingly, MV^{2+}@BMOF shows a 35 times enhancement of the electrical conductivity (2.3×10^{-5} S cm^{-1}) compared to the parent BMOF (6×10^{-7} S cm^{-1}) (Fig. 24).

For DFDNB@BMOF (3.5×10^{-6} S cm^{-1}) and DNT@BMOF (1.5×10^{-6} S cm^{-1}), there is significant enhancement of the electrical conductivity values but, in contrast, for C_{60}@BMOF, it remains almost constant (4×10^{-7} S cm^{-1}). The authors have proposed that increasing the π-acidity of the guest molecules (MV^{2+} > DFDNB > DNT) increases the donor–acceptor interaction between the host and guest moieties, contributing to the enhancement of the electrical conductivity.[92] The appearance of a charge transfer band in the NIR region confirmed the presence of charge transfer interaction between the BPDPNDI pillars and the intercalated MV^{2+} guests (Fig. 24).

Fischer and co-workers have studied the impact of donor–acceptor charge transfer interactions on the electrical conductivity of two isostructural MOFs: M_2TTFTB, ($TTFTB^{4-}$ = tetrathiafulvalene tetrabenzoate and M = Zn^{2+} and Cd^{2+}) through encapsulation of redox-active tetracyanoethylene (TCNE)

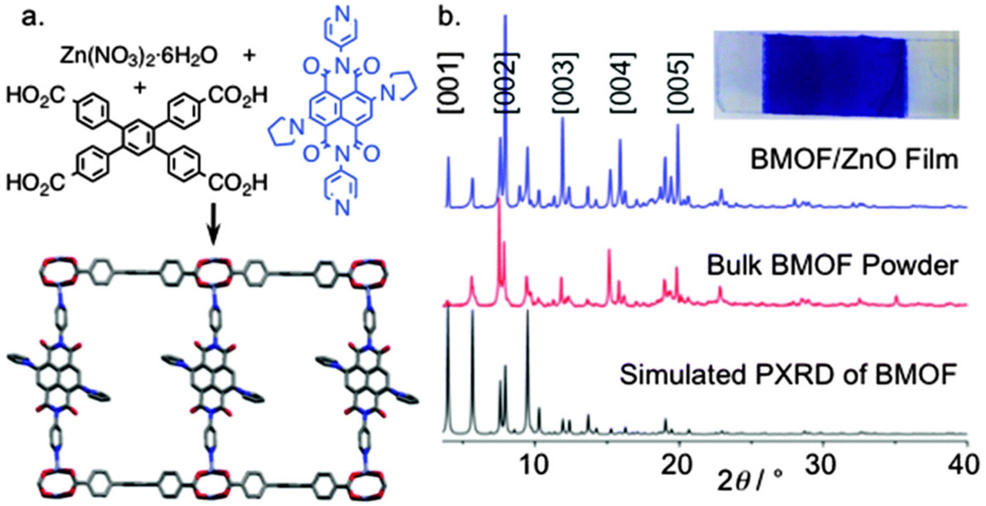

Fig. 23 (a) Solvothermal synthesis and crystal structure of BMOF $[Zn_2(TCPB)(BPDPNDI)]$. (b) XRPD profiles of BMOF. Inset: Photograph of a blue BMOF/ZnO film. Reproduced with permission from ref. 92. Copyright 2016, The Royal Society of Chemistry.

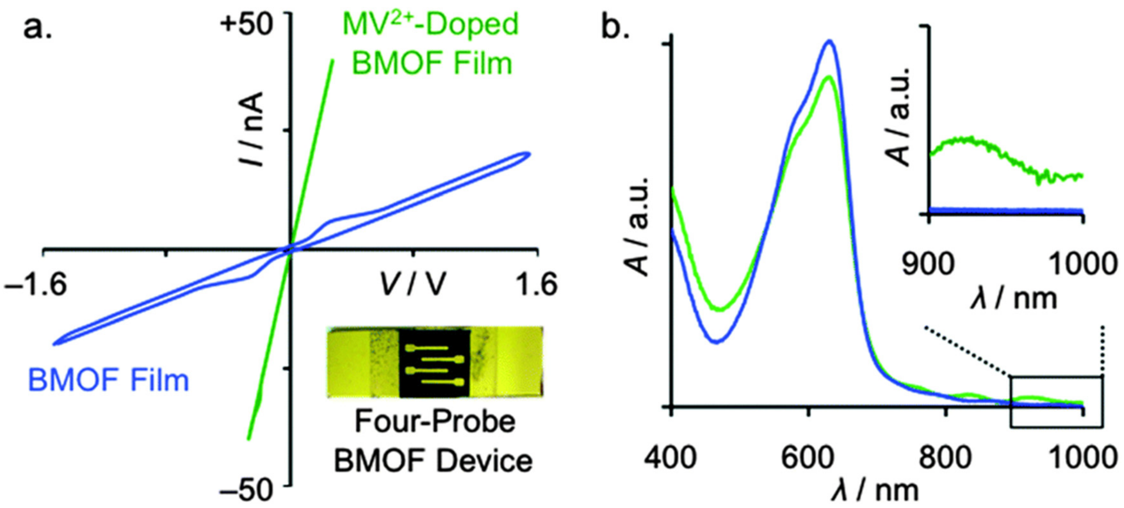

Fig. 24 (a) I–V plot of BMOF/ZnO-glass devices (inset) before (blue line) and after (green line) doping with MV^{2+} for 70 h. (b) Vis-NIR spectra of a BMOF/ZnO film before (blue) and after (green) doping with MV^{2+}. The latter shows new CT bands in the NIR region indicating π-donor/acceptor CT interactions between BPDPNDI ligands and MV^{2+} guests. Reproduced with permission from ref. 92. Copyright 2016, The Royal Society of Chemistry.

(Fig. 25). Both MOFs possess a 3D coordination network with π-stacking interactions among the $TTFTB^{4-}$ moieties forming 1D channels. During the formation of the MOF through metal–ligand self-assembly, the ligand oxidizes and the resultant MOF shows a semiconducting behaviour. Due to the loss of single crystalline nature during activation, the TCNE loading was done by using a powder sample. A number of TCNE@MOFs for both frameworks were prepared by heating homogeneous mixtures of TCNE and MOF samples in different ratios varying both the temperature and the heating period. The loading of TCNE within the MOFs was initially confirmed by the colour change from dark red to black. XRPD and SEM analyses indicate that the incorporation of TCNE does not alter the crystallinity and morphology of the MOFs. Pawley fitting shows that the incorporation of guest TCNE reduces the intensity of the peaks belonging to the π-stacked TTFTB linkers and such a decrease in intensity with increasing the amount of TCNE also clearly dictates the partial oxidation of $TTFTB^{4-}$ moieties. Such encapsulation also reduces the porosity of both frameworks. IR and Raman spectral analyses of TCNE@MOFs clearly show a charge transfer interaction with the formation of $TCNE^{\bullet}$ and $TCNE^{-}$ as well as $TTFTB^{+}$ and $TTFTB^{2+}$. The appearance of such charge transfer is responsible for the increase in the electrical conductivities of TCNE@MOFs when compared with the parent frameworks.[170]

Halogens have also a significant impact on the electrical conductivity of the host MOF structure. Thus, Gupta and co-workers have shown an enhancement of the electrical conductivity of Cu[Cu(pdt)] (pdt = pyrazine-2,3-dithiolate) through encapsulation of bromine. Bromine encapsulation was

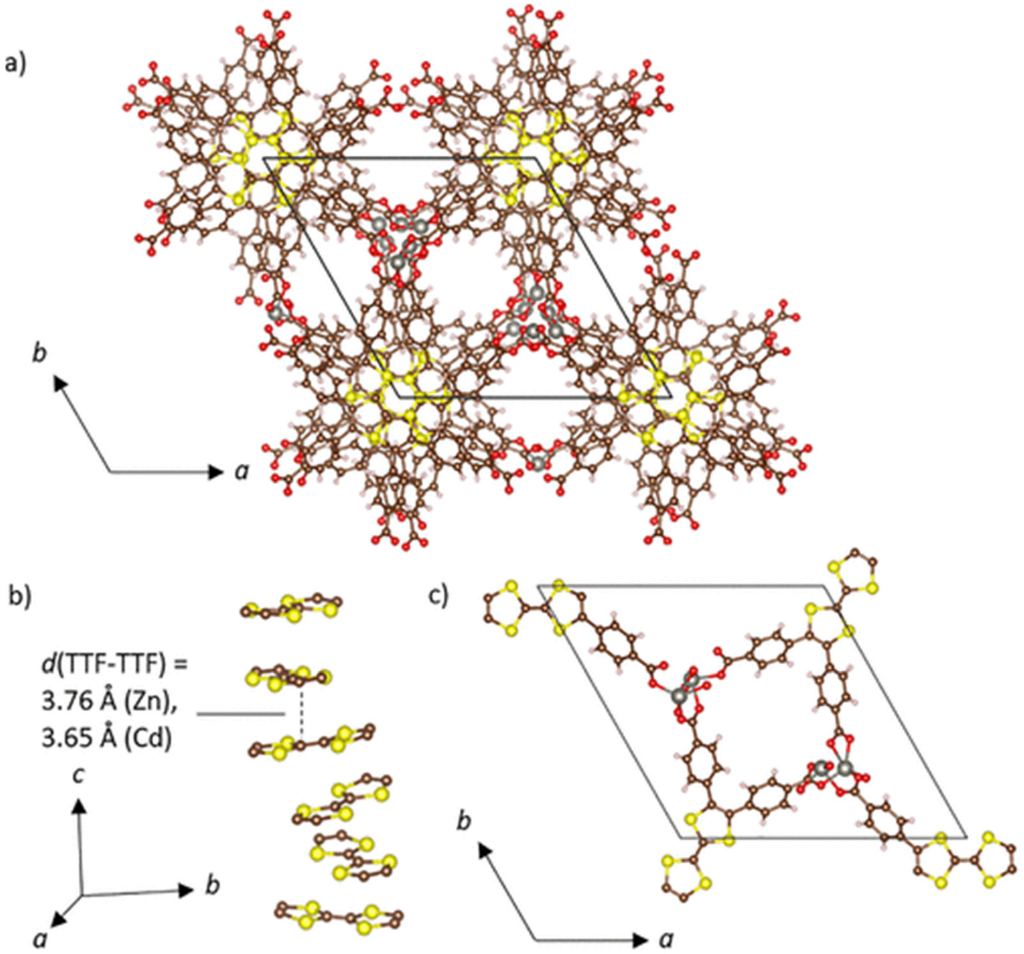

Fig. 25 (a) The crystal structure of isostructural M_2TTFTB (M = Zn, Cd) MOFs along the *c* axis. (b) Infinite helical π-stacks of TTFTB units within M_2TTFTB aligned along the *c*-axis. (c) Illustration of the coordination of TTFTB linkers to the rod-shaped SBUs of corner-sharing ZnO_6 octahedra. Noncoordinating TTFTB benzoate groups are omitted for clarity. Colour code: C = brown, H = white, O = red, S = yellow and M (here Zn) = silver spheres. Reproduced with permission from ref. 170. Copyright 2005, Elsevier.

performed in the vapour phase and caused a simultaneous change in cell dimension as well as oxidation of Cu^{II} to Cu^{III} with formation of $Br_x^-@Cu^{II}[Cu^{II}(pdt)_2]_{1-x}$ $[Cu^{III}(pdt)_2]_x$. The combination of bromine doping as well as redox hopping between Cu^{II} and Cu^{III} centres promotes a 10 times enhancement of the electrical conductivity (measured with the two probe method on pressed pellets) from 1.4×10^{-4} S cm^{-1}.[171]

In another case, Zhang *et al.* have encapsulated $Ru(bpydc)_3^{4-}$ (H_2bpydc = 2,2′-bipyridine-4,4′-dicarboxylic acid) within the channels of three isostructural MOFs $M_3(HITP)_2$ (where M = Co, Ni and Cu; HITP = 2,3,6,7,10,11-hexaiminotriphenylene) by the grafting method. $Ru(bpydc)_3^{4-}$ moieties are bonded to the metal nodes within the host MOFs. Such grafting of the guest coordination complexes enhances the electrical conductivity of the frameworks. The electrochemical impedance analysis shows that the resistance value of $Ru@Ni_3(HITP)_2$/GCE (136.8 Ω) is lower than that of $Ru@Cu_3(HITP)_2$/GCE (346.1 Ω) and $Ru@Co_3(HITP)_2$/GCE (423.9 Ω). Similarly, the electroluminescence of $Ru@Ni_3(HITP)_2$/GCE is higher than that of the other two MOFs.[172]

2.3 Organic polymer-based guests

Following their discovery in 1920,[173] the synthesis of organic polymers, bearing repetitive building blocks, has experienced extraordinary development thanks to their countless applications in many different fields. Since the mid-1990s, controlled polymer synthesis in terms of size, dimension, molecular weight, *etc.* has gained much attention. In this regard, the combination of polymer chemistry with coordination chemistry may create a new generation of novel functional materials. Thus, the integration of polymers within the channels of MOFs has become a major focus in order to combine the novel functionalities of MOFs with the useful properties of polymers.

The encapsulation of polymers within the nano-porous channels of MOFs provides an emerging category of materials with a wide variety of applications. The confined polymer chains are affected by their orientation, conformational arrangement, molecular weight, regularity, polymer composition, *etc.* This host–guest effect is double since, on one side, within the confinement space, polymers show properties different from those of their bulk phases. On the other side, the encapsulation of polymers within the nano-channels of frameworks may have a significant effect on the physical and chemical properties of the host MOF.

Encapsulation of organic conducting polymers has been done using several methods. In most cases, monomers are loaded within the channels of the MOF using an *in situ* synthetic method like a 'ship-in-a-bottle' approach. The small monomers can be easily loaded within the channels of the framework and then different types of polymerization methods like radical, electrochemical, ionic, ring opening methods, *etc.* are applied to form the extended polymeric chains within the channels of the MOF. The so-formed polymeric chains are trapped within the channels and thus cannot be easily released. In some cases, the monomers are loaded by soaking the MOF in the monomers or in a solution of the monomers in different solvents. Subsequently, the loaded guest monomers are converted to polymers. Recently, grafting has emerged as a new method to load the monomers in the MOF. In this case, pre-functionalized MOFs, in both, ligand and metal nodes, interact with a monomer or oligomer having a counter-functional site, facilitating the incorporation of the guest species through strong host–guest interaction within the channels of the framework. The loaded guests can attach to the ligand site by covalent bonding or to the metal site by coordination bonds. These grafted monomers/oligomers can be afterward polymerized within the channels. In a few cases, the polymer chains are directly loaded within the channels of the MOFs. MOFs are soaked in a solution of the polymer or in a melted polymer leading to the direct insertion of the polymer chains within the channels. Such direct insertion becomes feasible due to strong interactions between the polymer chains and the pore walls.

As expected, most of the attempts to increase the electrical conductivity of polymer-doped MOFs have been performed with π-conjugated organic polymers since they are well-known for their electrical conducting properties[174] and their applications in many different electronic devices. Therefore, the incorporation of conducting polymers like PEDOT (polymer of 3,4-ethylenedioxythiophene),[175] polyaniline (PANI),[176] polypyrrole (PPy),[177] polythiophene (PTh),[178] polyacetylene (PA),[179] *etc.* into different MOFs, is expected to increase their carrier density leading to higher conductivities for the guest@MOF materials.

2.3.1 Incorporation of PEDOT.

García, Gómez-García *et al.* reported one of the first attempts to insert PEDOT inside a porous material. Thus, these authors reported the ship-in-a-bottle insertion of PEDOT in Fe^{3+}-exchanged NaX and NaY faujasites.[170] The polymerization was performed by heating at 100 °C the Fe^{3+}-exchanged zeolites with the EDOT monomer inserted inside the channels of faujasite. The polymerization was verified by the development of a green colour, by diffuse reflectance spectroscopy that showed a broad absorption from 550 to 850 nm and by IR spectra. Electrical conductivity studies on thin films show a large enhancement of the conductivity of PEDOT@NaY, which is close to the value of bulk PEDOT and higher than that of pristine NaY faujasite. The high conductivity is attributed to the presence of polarons in the conjugated PEDOT polymer, which was also confirmed by EPR measurements.

Later, Kitagawa *et al.* encapsulated PEDOT within the void space of MIL-101(Cr) in a two-step synthesis: adsorption of the monomer 3,4-ethylenedioxythiophene (EDOT) and then I_2-mediated oxidative polymerization (Fig. 26). The polymerization within the cavities of the parent MOF was characterized by ATR-FTIR, XRPD, MALDI-TOF, X-ray fluorescence (XRF) and adsorption studies. These authors showed that PEDOT@MIL-101(Cr) has 10^8 times higher electrical conductivity (1.1×10^{-3} S cm^{-1}) than the parent MOF ($\sim 10^{-11}$ S cm^{-1}) and, furthermore, that the conductivity of PEDOT@MIL-101(Cr) varies with the amount of loaded polymer. The conductivity of PEDOT@MIL-101(Cr) is also higher than that observed with other polymers, such as polypyrrole and polyaniline, encapsulated within MIL-101(Cr). The authors also showed that PEDOT@MIL-101(Cr) is more conducting than PEDOT encapsulated within La(1,3,5-benzenetricarboxylate). These results demonstrate that the interaction between the polymer and the framework is a key parameter for the enhancement of the electrical conductivity.[180]

Ballav and co-workers have attempted to modulate the charge transport behaviour of the bi-porous insulator UiO-66 MOF through encapsulation of PEDOT and PPy. UiO-66 MOF was immersed in two different solutions of the monomers and the polymerizations were carried out with I_2 and $FeCl_3$ to form UiO-66-PEDOT and UiO-66-PPy, respectively (Fig. 27).[181]

Incorporation of the polymers within the pores of the framework was confirmed by naked eye colour change, absorption

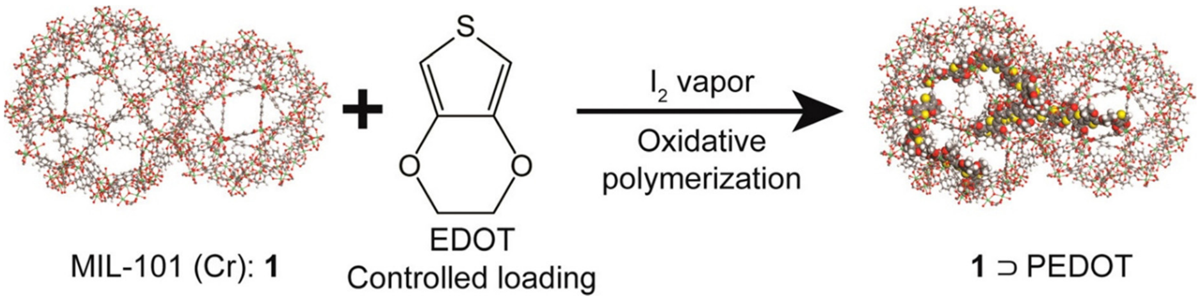

Fig. 26 Schematic image for the preparation of PEDOT@MOF. Reproduced with permission from ref. 180. Copyright 2016, The American Chemical Society.

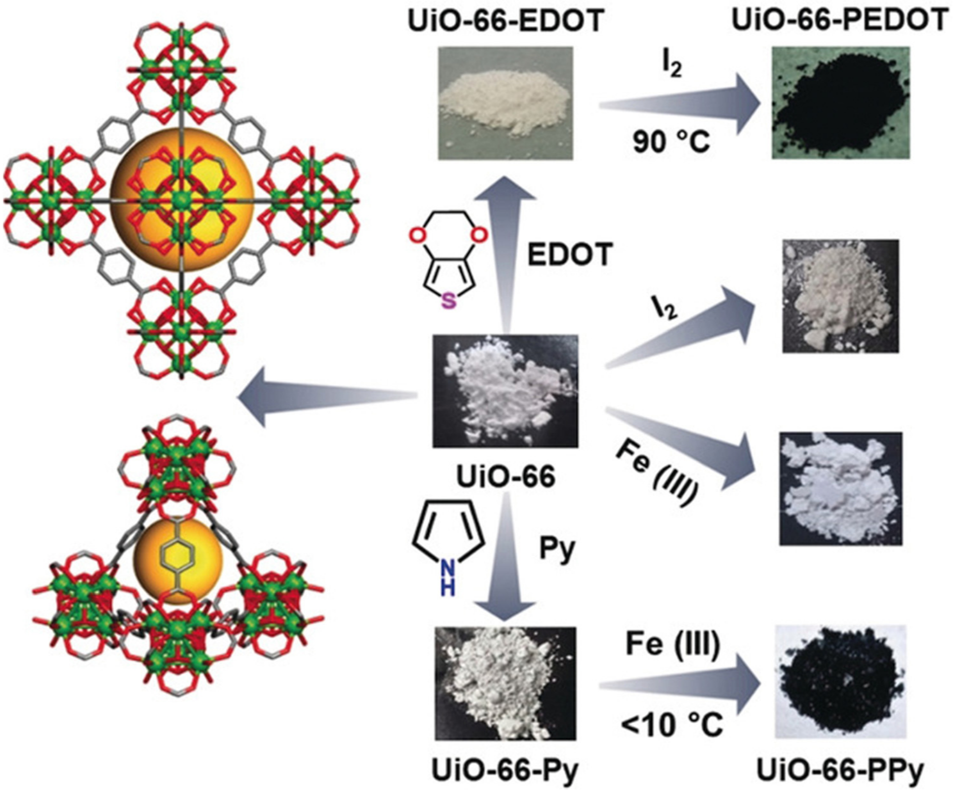

Fig. 27 Reaction scheme for the synthesis of UiO-66-PEDOT and UiO-66-PPy. Left panel: Visualizing two different pores in UiO-66 (colour code: green, zirconium; red, oxygen; gray, carbon; hydrogen is omitted for clarity). Right panel: Optical images of products obtained after each step. Reproduced with permission from ref. 181. Copyright 2019, Wiley and VCH.

spectra, XRPD analysis, TGA, field emission-SEM, energy dispersive X-ray spectroscopy and gas adsorption analysis. XRPD studies show the retention of crystallinity after polymer formation while N_2 sorption analyses indicate that the BET surface area decreases from 1670 m^2 g^{-1} (in UiO-66) to 1150 m^2 g^{-1} (in UiO-66-PPy) and 960 m^2 g^{-1} (in UiO-66-PEDOT). Four-probe electrical conductivity studies show room-temperature conductivity values of 2×10^{-2} S cm^{-1} and 10^{-3} S cm^{-1} for UiO-66-PPy and UiO-66-PEDOT, respectively (Fig. 28).

The authors also measured the electrical conductivity of a physical mixture of UiO-66 with the bulk polymers and observed that their conductivities vary between 10^{-6} and 10^{-7} S cm^{-1}. These conductivity values are also different from bulk PPy and PEDOT polymers. The authors suggested that the enhancement of the electrical conductivity is due to the synergistic interactions between the conjugated polymer and the host framework.[181]

Polymeric chains of PEDOT have also been obtained by Wang *et al.* within the channels of the MOF [Zn_2(1,4-ndc)$_2$(dabco)], (where H_2-1,4-ndc = 1,4-napthalenedicarboxylic acid and dabco = 1,4-diazabicyclo[2.2.2]octane). Electrical conductivity measurements show that PEDOT@MOF is a better electrical conductor than the pristine MOF, and similar to bulk PEDOT.[182]

Saha and co-workers have loaded two different types of conducting polymers (PPy and PEDOT) in the channels of an insulating Zn-dpzNDI MOF (dpzNDI = dipyrazolate-naphthalenediimide) to modulate their electrical conductivities.[183] The MOF contains large pores in the activated form and π-acidic NDI ligands hard to oxidize. A microcrystalline sample of the framework was immersed in a diethyl ether solution of EDOT and then polymerized in the presence of I_2. The polymerization is verified by the naked eye colour change from orange to black. In a similar manner, PPy was loaded into the pores of the same MOF. XRPD studies indicate the retention of crystallinity after polymerization and N_2 adsorption studies indicate that the porosity of PEDOT@MOF (28 m^2 g^{-1}) and PPy@MOF (283 m^2 g^{-1}) is much smaller than that of the parent MOF (1528 m^2 g^{-1}). TGA shows that the polymer-loaded MOFs are stable above 300 °C, in contrast with the bulk polymers that degrade at around 100 °C. Two-probe conductivity measurements show that both PEDOT@MOF and PPy@MOF are semiconductors with room-temperature conductivities of 1.8×10^{-7} and 2.5×10^{-5} S cm^{-1}, respectively. The conductivity of physical mixtures of the MOF with the polymers is lower. This result strongly demonstrates that a co-operative interaction between the MOF and the polymers is responsible for the enhancement of the electrical conductivity.[183]

Recently, Salcedo-Abraira *et al.* synthesized PEDOT@MIL-100(Fe) using a two-step method: adsorption and oxidative polymerization in the presence of $FeCl_3$. They have shown a 100 times increment of the electrical conductivity of the parent MOF upon polymerization of EDOT.[184]

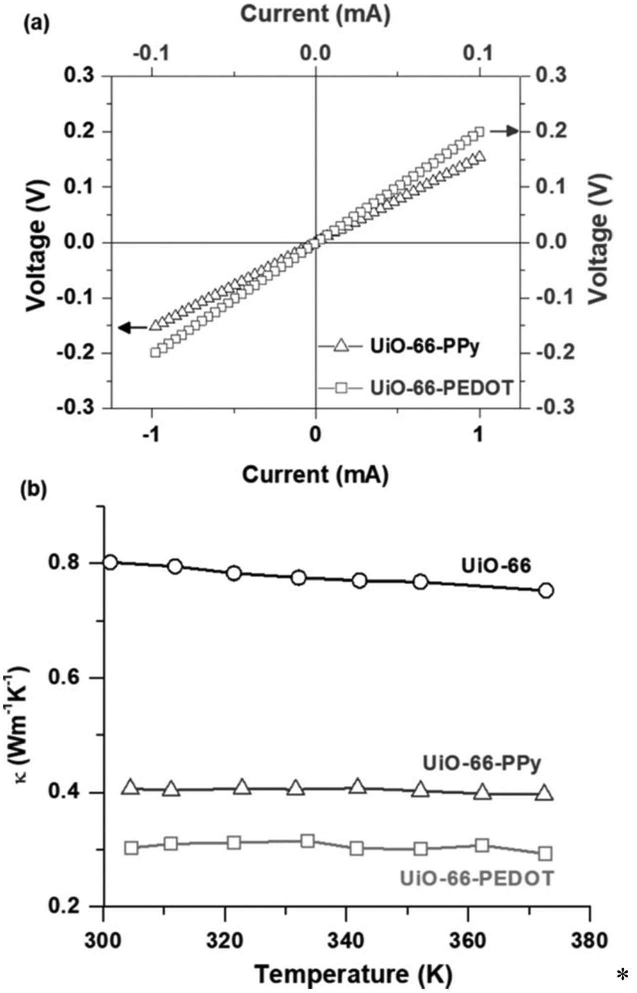

Fig. 28 (a) *I*–*V* plots of UiO-66-PPy (triangles) and UiO-66-PEDOT (squares) recorded with the four-probe configuration. (b) Thermal conductivity as a function of temperature for UiO-66 (circles), UiO-66-PPy (triangles), and UiO-66-PEDOT (squares). Reproduced with permission from ref. 181. Copyright 2019, Wiley and VCH.

PEDOT has also been prepared by Mohmeyer *et al.* on the surface of a Zr-based framework $[Zr(bzpdc)]_n$ (where H_2bzpdc = benzophenone-4,4′-dicarboxylic acid) with a two-dimensional structure and photoreactive free keto-groups. Zr-bzpdc MOF was immersed in EDOT and irradiated by UV LED at a wavelength of 365 nm under Ar to initiate the ketyl radical formation at the keto-group of the bzpdc moiety of the framework. The ketyl radical reacts with the ethylene moiety of EDOT, resulting in the covalent attachment of EDOT to the MOF, leading to the desired polymerization. Polymer formation was identified with the colour change from colourless to dark brownish. XRPD study shows that such grafting does not change the crystalline nature of the framework. Gas adsorption studies indicate a decrease in porosity after polymerization. Electrical conductivity measurements, carried out by the van der Pauw method, indicate that the conductivity increases from 10^{-6} S cm^{-1} in the pristine Zr-bzpdc MOF to 10^{-3} S cm^{-1} after 24 h.[185]

Interestingly, simultaneous enhancement in both electrical conductivity and stability of an insulating and unstable MOF through encapsulation of PEDOT has been reported by Zhang and co-workers. The MOF Ni_2(NDISA) (NDISA = naphthalenediimide *N*,*N*-disalicylate) is insulating in nature ($\sigma = 10^{-10}$ S cm^{-1}) and undergoes structural decomposition upon desolvation. The encapsulation of PEDOT enhances both the stability and the electrical conductivity. The conductivity value becomes $\sim 1.1 \times 10^{-5}$ S cm^{-1} with 22% wt encapsulation and $\sim 10^{-4}$ S cm^{-1} with $\geq$ 33% wt encapsulation of PEDOT.[186]

2.3.2 Incorporation of polypyrrole (PPy).

Oxidative polymerization of pyrrole (Py) to polypyrrole (PPy) within the channels of porous MOFs was performed by Kitagawa and co-workers.[187] Oxidative polymerization of Py within the channels of the MOF $[(Ni(dmen)_2)_2(Fe^{III}(CN)_6)](PhBSO_3)$ (dmen = 1,1-dimethylethylenediamine; $PhBSO_3$ = *p*-phenylbenzenesulfonate) was performed by immersing the MOF within Py. $[Fe(CN)_6]^{3-}$ acts as the oxidizing agent (it reduces to $[Fe(CN)_6]^{4-}$). Polymerization was monitored by visual colour change and IR, UV-Vis and XRPD analyses.[187] These authors also synthesized PPy within the 3D channels of the HKUST-1 MOF by oxidative polymerization in the presence of oxygen at 100 °C.[188] In both cases, they isolated the obtained PPy within the framework after decomposition of the metal–ligand architecture of the MOF.

A huge enhancement of the electrical conductivity through encapsulation of PPy chains within the 1D channels of the MOF $[Zn_3$(D,L-lactate)$_2$(4-pyridylbenzoate)$_2]$ has been reported by Wang *et al.* (Fig. 29).[189] This MOF was immersed in neat Py resulting in the uptake of Py within the channels of the framework. The oxidative polymerization was carried out in the presence of 0.05 M I_2 at −16 °C over 72 hours in hexane solution. The polymerization was monitored by visual colour change and absorption spectroscopy, IR spectra, XRPD and SEM analyses. SEM micrographs of the isolated PPy chains from the MOF show that the chain length of PPy moieties is within the range of 20–30 nm. PPy@MOF shows 10^5 times higher electrical conductivity (10^{-2} S cm^{-1}) than bulk PPy (10^{-7} S cm^{-1}) and 10 times higher than I_2@MOF. Furthermore, these authors have also reported that isolated PPy chains have five times higher electrical conductivity than PPy layers. The improved conductivity in PPy@MOF might be attributed to the cooperative electrical conductivity resulting from the confined PPy molecule chains surrounded by a π-donor type environment[189]

Later, Dhara *et al.* encapsulated PPy within the porous channels of a Cd-MOF (Cd-MOF = $[Cd_2(NDC)(PCA)_2]\cdot G_x$ with H_2NDC = 2,6-naphthalenedicarboxylicacid, HPCA = 4-pyridinecarboxylic acid and G = guest molecules, Fig. 30) through a two-step method.[190] Guest pyrrole (Py) monomer was incorporated into the 1D nanochannels of Cd-MOF and was polymerized to polypyrrole (PPy) with I_2 as an oxidant. The host–guest PPy@Cd-MOF shows 10^9 times higher conductivity (10^{-3} S cm^{-1}) than the Cd-MOF (10^{-12} S cm^{-1}) and 10^4 times higher than I_2@Cd-MOF (10^{-7} S cm^{-1}). Variation of the conductivity with temperature showed a variable range hopping transport mechanism (Fig. 30).

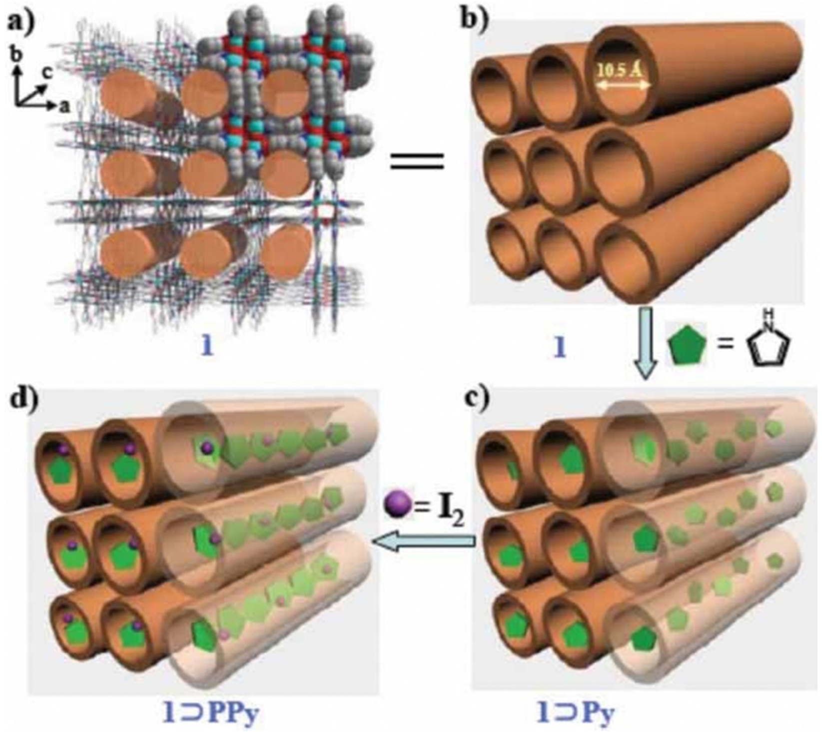

Fig. 29 Schematic illustration for the formation of PPy in the channels of $[Zn_3(\text{D,L-lactate})_2(\text{4-pyridylbenzoate})_2]$ (1). (a) 3-D open framework of the MOF with 1-nm nanochannels. (b) Framework of the MOF. (c) Encapsulation of Py in the channels of the MOF. (d) Polymerization of Py with iodine. Reproduced with permission from ref. 189. Copyright 2011, Wiley and VCH.

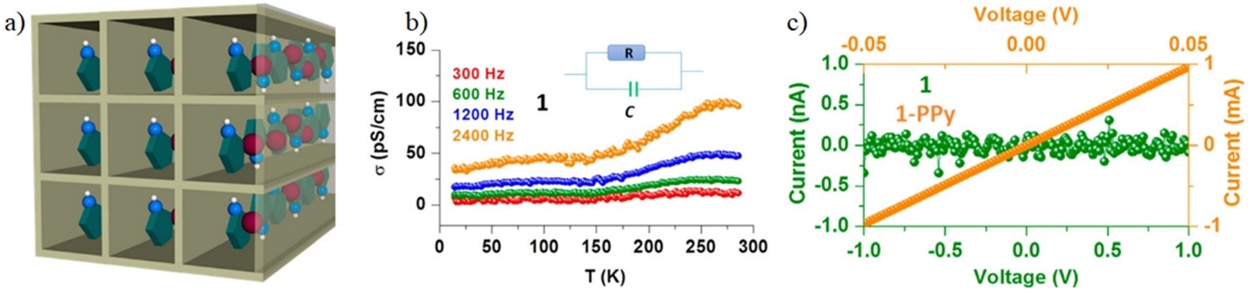

Fig. 30 (a) Schematic incorporation of PPy guest inside the Cd-MOF host, (b) Conductivity *versus* temperature plots obtained from frequency-dependent dielectric measurements of PPy@Cd-MOF (inset: scheme of resistance). (c) Room-temperature *I*–*V* plots of Cd-MOF (green) and PPy@Cd-MOF (orange). Reproduced with permission from ref. 190. Copyright 2016, The American Chemical Society.

The calculated activation energy was ∼0.2 eV. This huge increase in conductivity could be mainly due to non-covalent interaction of guest PPy chains with the host that results in an increase in the electron current across the framework. Hall effect measurement shows n-type semiconductor behaviour of the MOF with high carrier density ($\sim 1.5 \times 10^{17}$ cm^{-3}) and mobility (~ 8.15 cm^2 V^{-1} s^{-1}).[190]

Ppy has also been inserted in zeolitic-imidazolate frameworks in order to prepare conducting ZIF materials. Thus, Jiao and co-workers reported the polymerization of pyrrole in the void space of ZIF-67.[191] Pyrrole monomers are loaded within the pores of the framework by the solvent evaporation method and then polymerization was carried out in the presence of Fe^{3+}. Three different composites were prepared: PZ-1, PZ-2 and PZ-3 with a pyrrole/ZIF mass ratio of 1, 2 and 5, respectively. Unfortunately, the loading of PPy decreases the crystallinity and morphology of the frameworks. Electrical conductivity measurement shows that the conductivity of PZ-3 is 1.5 S cm^{-1}.[191]

PPy has also been inserted in ZIF-67 using a templated synthetic method by Yuan *et al.*[192] Interestingly, the morphology of the pyrrole-loaded ZIFs is dependent on the amount of pyrrole used during the synthesis. When the pyrrole : 2-MIM ratio is 1 : 1 (2-MIM = 2-methylimidazole), the crystal morphology of the synthesized PZ-1 is dodecahedral, similar to pristine ZIF-67. When this ratio is 5 : 1, the morphology of PZ-5 changes to truncated dodecahedra with a total of 18 facets (Fig. 31). The number of newly emerged facets increases continuously with increasing the pyrrole : 2-MIM ratio, and finally, for a 1 : 20

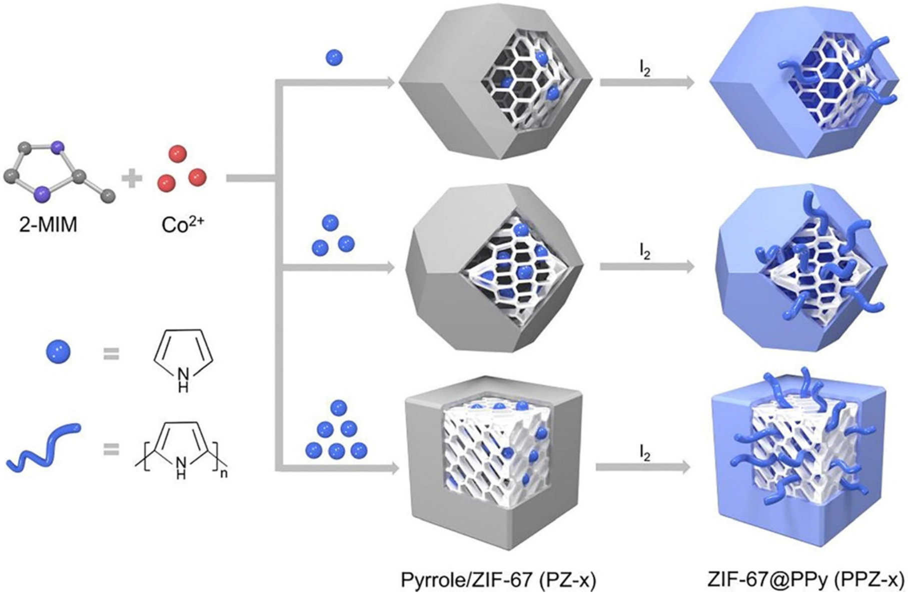

Fig. 31 Schematic illustration of the modulation of ZIF-67 crystal morphology by pyrrole and the formation of polymer-reinforced ZIF-67 using I_2 as the polymerization initiator. Reproduced with permission from ref. 192. Copyright 2021, Elsevier.

ratio, the morphology becomes cubic and remains cubic for any ratio above 1 : 20.

The as-obtained samples of PZ-*x* were then re-dispersed into an I_2-containing methanol solution to polymerize the pyrrole monomers (PPZ-*x*). Polymerization was monitored using absorption spectroscopy, XRPD analysis and gas adsorption studies. The specific surface area and pore volume of the activated ZIF-67 (1555.5 $m^2\ g^{-1}$ and 0.797 $cm^3\ g^{-1}$) decrease to 992.1 $m^2\ g^{-1}$ and 0.510 $cm^3\ g^{-1}$, respectively, for PPZ-20. Four probe conductivity measurements (Fig. 32) show that PPZ-20 has a conductivity value of 0.51 S cm^{-1}, nine orders of magnitude higher than that of the pristine ZIF-67 MOF (4.5×10^{-10} S cm^{-1}) but one order of magnitude lower than pure PPy (6.2 S cm^{-1}).[192]

Xin and co-workers showed that PPy@MOF (where MOF = $[Zr_6O_{16}H_{18}][TCPP\text{-}Co]_2$ and H_2-TCPP = tetrakis(4-carboxyphenyl)porphyrin) has a higher conductivity (1.08×10^{-9} S cm^{-1}) than the parent MOF (3.9×10^{-10} S cm^{-1}).[93] In some cases, conductive PPy-loaded MOFs have also been used for electrocatalytic applications. Thus, Fang and co-workers reported the enhancement of the electrical conductivity of a 3D porous MOF: $\{H_2TCPP[AlOH]_2(DMF_3(H_2O)_2)\}$ (where H_2TCPP = 5,10,15,20-tetrakis(4-carboxyphenyl)porphyrin) through incorporation of PPy within the pores of the framework. Furthermore, the resultant PPy@MOF shows an excellent CO_2 reduction capacity.[193]

Very recently, Vello and co-workers have encapsulated PPy within thin films of HKUST-1. The SURMOF of HKUST-1 was fabricated on SiO_2/Au electrodes through nanomembrane

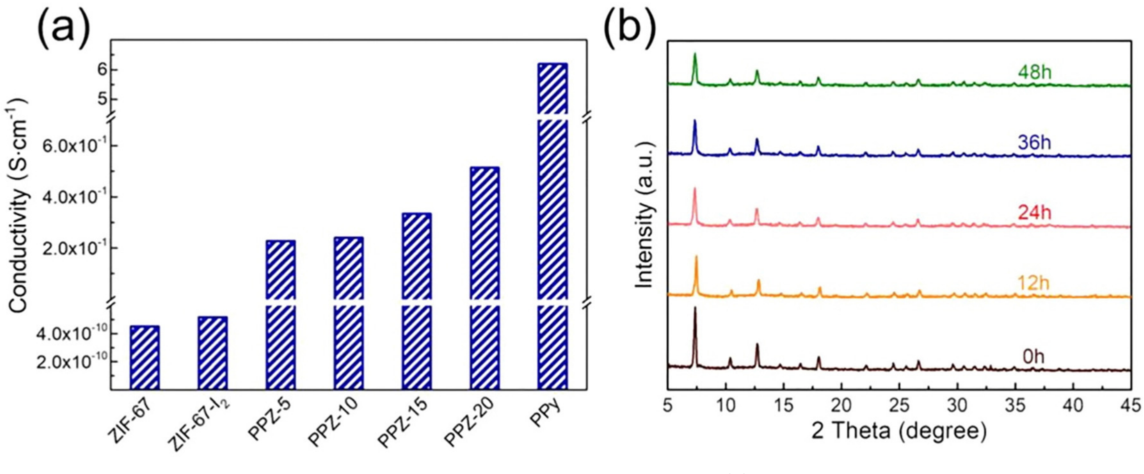

Fig. 32 (a) Electrical conductivity of PPZ-*x* and comparison with ZIF-67, ZIF-67-I_2 and PPy. (b) Time-lapse XRD patterns of PPZ-20 immersed in water from 0 to 48 h. Reproduced with permission from ref. 192. Copyright 2021, Elsevier.

origami technology. The monomers of Py were encapsulated in the vapour phase within the porous channel of HKUST-1 in the SiO_2/Au/HKUST-1/Au devices followed by *in situ* polymerization to obtain PPy@HKUST-1. The successful encapsulation was monitored by XRPD analysis, Raman spectroscopy, AFM and elemental characterizations. *I–V* measurement clearly indicates the enhancement of electrical conductivity of the heterojunctions. The conductivity value varies from 2×10^{-8} to 5×10^{-8} S cm^{-1} with the temperature increasing from 180 to 300 K.[194]

2.3.3 Incorporation of polyaniline (PANI). Polyaniline formation from aniline monomers takes place in the presence of strong acidic medium (1 M HCl solution), and therefore, the incorporation and formation of PANI@MOFs requires MOFs stable in strong acidic solutions.

Shao *et al.* have developed a composite PANI@MIL-101(Cr) by two-step methods: adsorption of aniline within the MOF and then polymerization (Fig. 33). At lower concentrations, the polymers are encapsulated within the pores of the MOF; at higher concentrations, the polymer grows on the surface of MOF particles. IR spectra clearly indicate that N–H groups on the polymeric chains are coordinated with the coordinatively unsaturated Cr(III) centres in addition to the presence of $\pi\cdots\pi$/N–H$\cdots\pi$ interactions. SEM and XRPD studies indicate that the morphology and XRD patterns do not change significantly at low polymer loadings although, upon high loadings, substantial changes occur. N_2 adsorption analysis indicates that the BET surface area of PANI@MIL-101(Cr) is much smaller than the pristine MIL-101(Cr) due to the filling of the pores of the MOF with PANI. These authors have also shown the continuous enhancement of electrical conductivity by increasing the amount of encapsulated PANI within the pores, with a maximum value of 0.55 S cm^{-1} for 20% loading.[94]

Later, they prepared another ec-MOF by encapsulating PANI within a UiO-66 MOF under similar conditions. The electrical conductivity of PANI@UiO-66 is higher than that of PANI itself while the MOF acts as an insulator.[195] Lin *et al.* also prepared a composite material of PANI and UiO-66 with the PANI chains located within the channels as well as on the surface of the material. Conductivity measurements show that the resultant PANI@UiO-66 compound has an electrical conductivity of 2.17×10^{-4} S cm^{-1}.[196]

In another example, Xu *et al.* incorporated doped PANI within the hexagonal channels of three different Co-based MOFs: Co-MOF, Co-MOF-Br and Co-MOF-Ag.[197] Co-MOF was synthesized by reacting $CoCl_2$ with 5,5′-(1*H*-2,3,5-triazole-1,4-diyl)diisophthalic acid (H_4L) and pyrazin-2-amine ($Pz\text{-}NH_2$). The structural study shows that the MOF contains two different types of channels: hexagonal and triangular (Fig. 34). The hexagonal channels are filled with free Co^{2+} ions and deprotonated anionic ligands. Single-crystal to single-crystal transformations have been observed for Co-MOF by using two different salts, 1-ethylpyridinium bromide (EtpyBr) or $AgNO_3$, replacing the Co^{2+} ions and the anionic ligands in the pores.

All three MOFs were loaded with doped PANI by immersion in DMF solutions. Four probe electrical conductivity measurements show very high similar conductivity values for PANI@Co-MOF,

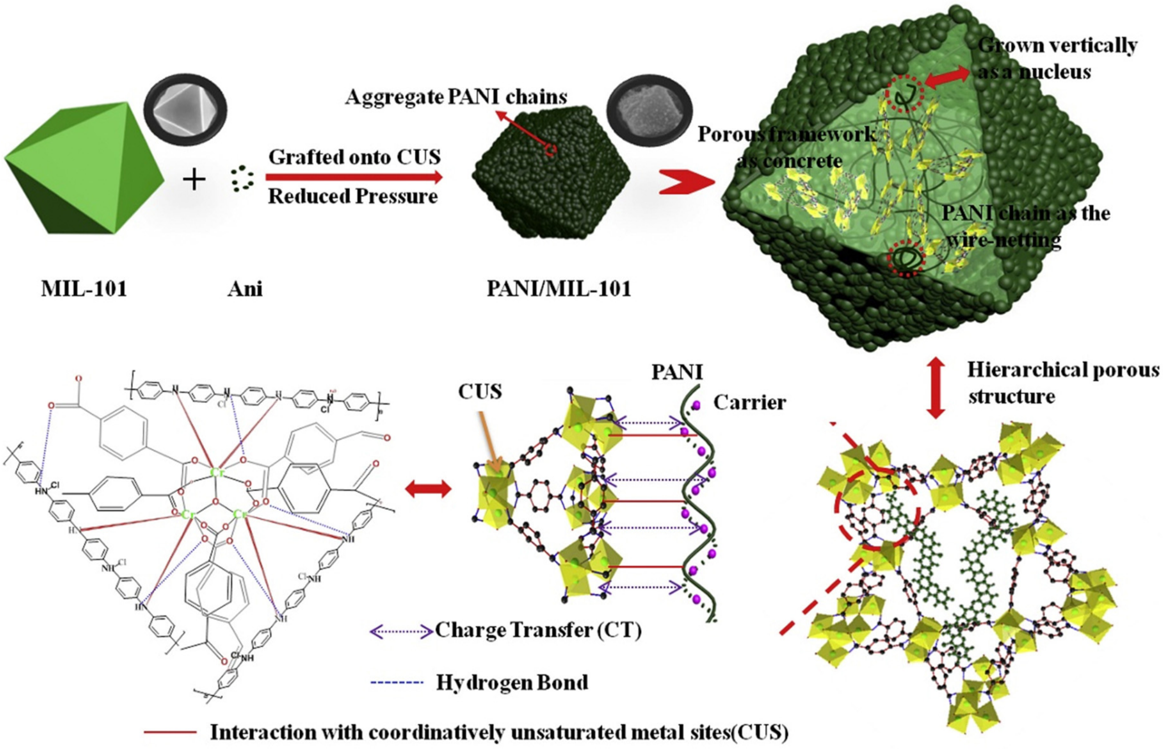

Fig. 33 Schematic illustration of the fabrication process and the interaction between PANI and MIL-101(Cr). Reproduced with permission from ref. 94. Copyright 2018, Elsevier.

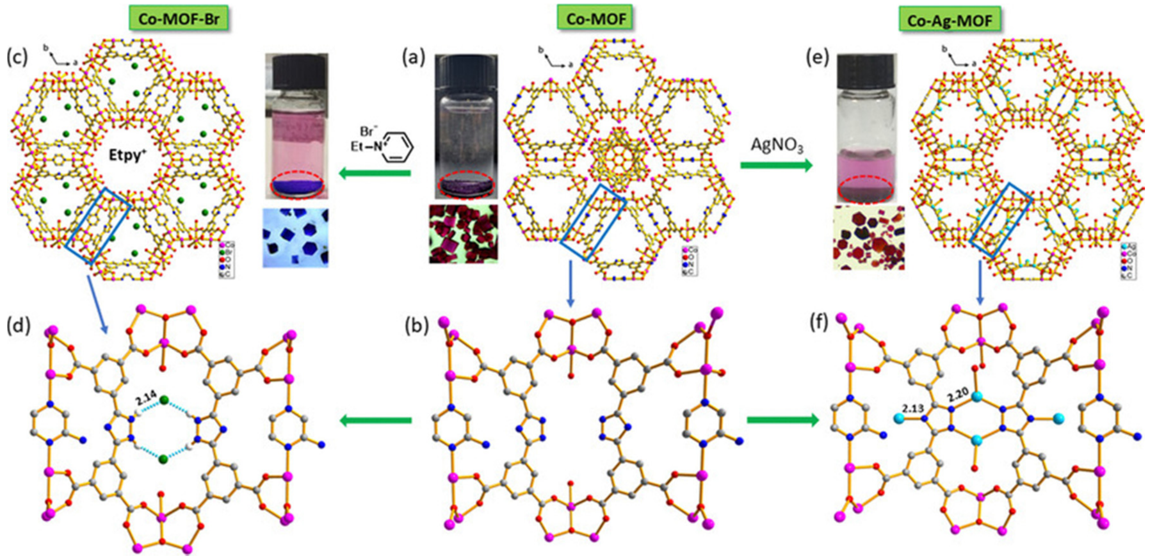

Fig. 34 (a), (c) and (e) Crystal structures of Co-MOF, Co-MOF-Br and Co-Ag-MOF and photographs of solutions and crystals before and after metathesis with EtpyBr and $AgNO_3$. (b), (d) and (f) The change of connection mode of L_4@, Pz-NH_2, SBU1 and SBU2 in MOFs through SC–SC transformation. All H atoms are omitted for clarity. Reproduced with permission from ref. 197. Copyright 2021, Wiley & VCH.

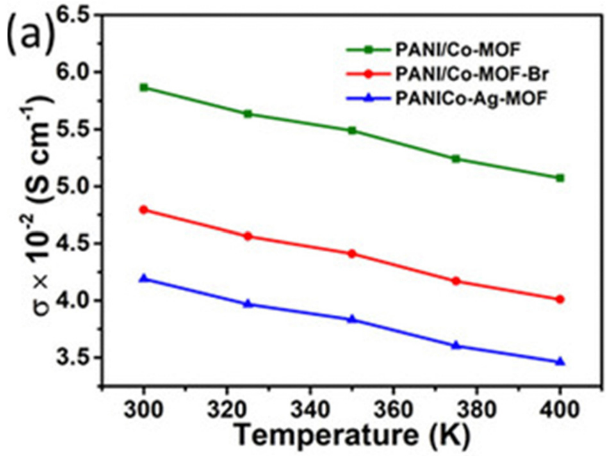

Fig. 35 Variable-temperature conductivity of PANI@CoMOF, PANI@Co-MOF-Br and PANI@Co-Ag-MOF. Reproduced with permission from ref. 197. Copyright 2021, Wiley & VCH.

PANI@Co-MOF-Br and PANI@Co-MOF-Ag (5.9×10^{-2}, 4.8×10^{-2} and 4.2×10^{-2} S cm^{-1} at 300 K, respectively, Fig. 35).[197]

2.3.4 Incorporation of polythiofene (PTh) and derivatives.

Kitagawa *et al.* polymerized thiophene within the 1D channels of the porous 3D MOF $[La(BTB)]_n$ (where BTB = 1,3,5-benzenetrisbenzoate).[198] The MOF contains 1D nanochannels along the crystallographic *c*-axis with dimensions 10.7×10.7 $Å^2$. Vapour adsorption method has been employed for the loading of monomers of 2,2′:5′,2″-terthiophene, (TTh) within the channels (Fig. 36). Oxidative polymerization was done in the presence of iodine vapour at high temperature to form the composite PTTh@MOF. Polymerization has been controlled through the TTh : MOF ratio. XRPD study shows that there is no substantial change of peak positions upon polymerization but the intensity of the peaks is reduced. Both the SEM and energy dispersive spectroscopy indicate that the polymers are present within the channels of the MOF and the adsorption analysis shows that the PTTh@MOF has very low void space compared to the parent MOF. Molecular dynamics (MD) simulations show that single and double chains are formed within the channels at low concentrations while at higher concentrations, tri- and tetra-chains are also formed. The polymeric chains within PTTh@MOF·30 (formed by using a w/w TTh : MOF ratio of 30) are assembled by interchain π· · ·π interactions. Electrical conductivities of the polyterthiophene-loaded MOFs and of the pristine framework have been measured by flash-photolysis time-resolved microwave conductivity (FP-TRMC) which allows evaluation of the intrinsic charge transport of PTTh chains. Upon excitation by a laser pulse of wavelength of 355 nm, the conductivity of the PTTh@MOF samples increases rapidly compared to the parent MOF. The charge carrier mobility of PTTh@MOF·15 (formed by using w/w Th : MOF ratio of 15) is 0.04 cm^2 V^{-1} s^{-1}. The mobility reaches a maximum of 0.3 cm^2 V^{-1} s^{-1} for PTTh@MOF·30. The authors suggested that the π-orbital overlap has a key effect for such enhancement of conductivity.[198]

Polythiophene chains have been prepared by Hupp and co-workers within the porous channels of NU-1000 MOF by using *p*-thio acid, a building block synthesized by multi-step organic synthesis, composed of five thiophene molecules and a carboxylic acid group connected by an aliphatic chain.[199] The *p*-thio acid precursor was inserted within the channels of the NU-1000 MOF by a post-synthetic method thanks to the interaction of the carboxylate groups that coordinate the metal ions of the Zr_6 unit by replacing coordinated water molecules and hydroxide groups (Fig. 37). The incorporation of *p*-thio-acid within the MOF was characterized by XRPD and adsorption analyses. Polymerization of the coordinated pentathiophene

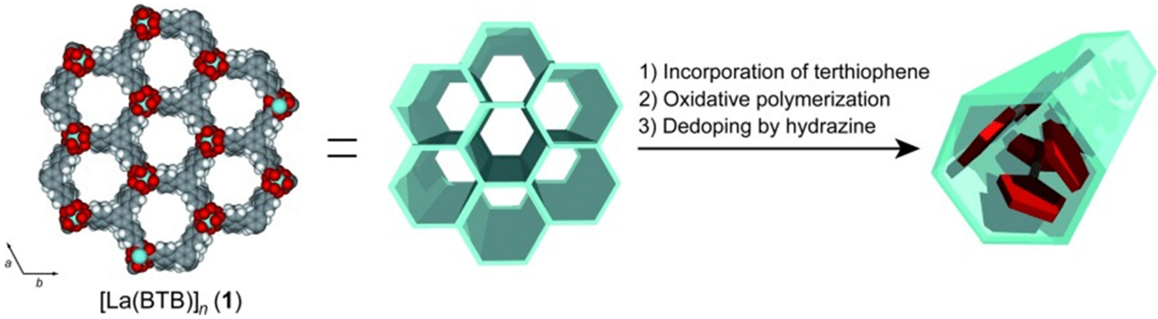

Fig. 36 Synthetic strategy for the confinement of unsubstituted polythiophene (PTh) within the 1D channels of the MOF. Reproduced with permission from ref. 198. Copyright 2016, Wiley & VCH.

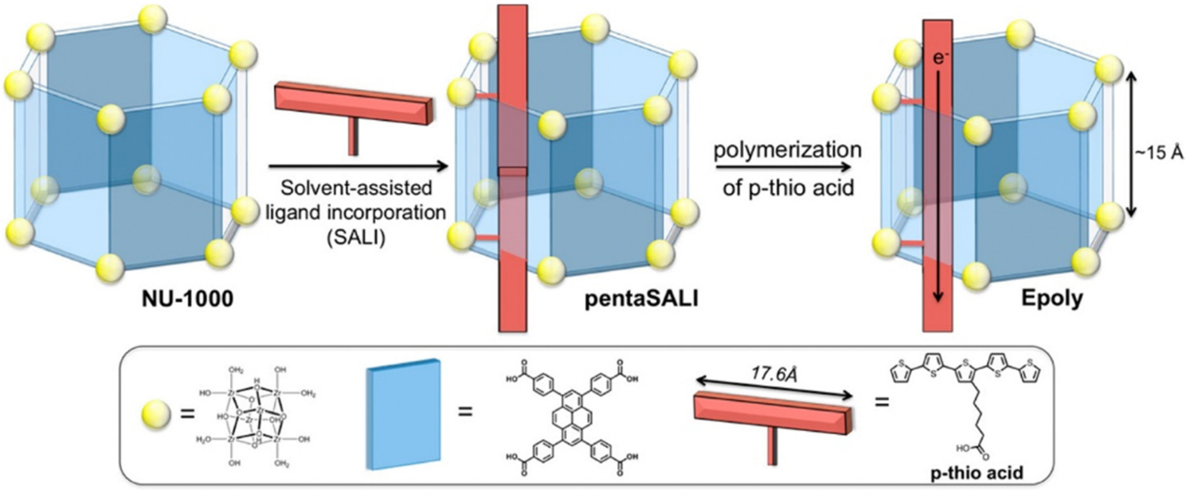

Fig. 37 Schematic representation of the synthesis of the PTh@NU-1000 MOF. Reproduced with permission from ref. 199. Copyright 2017, The American Chemical Society.

moieties within the channels was performed by electropolymerization with a concomitant change of colour to green. The change in electrical conductivity was measured by AC impedance analysis. NU-1000 MOF having pentathiophene moieties shows a low conductivity of $\sim 10^{-9}$ S cm^{-1}, while after polymerization, the conductivity increases two orders of magnitude, up to 1.3×10^{-7} S cm^{-1}.[199]

2.3.5 Incorporation of polyacetylene (PA). Polyacetylene has the highest electrical conductivity among organic conducting polymers. This fact, together with the small size of acetylene and the possibility of inserting it in the gas phase, makes PA one of the best-conducting polymers to be inserted in porous materials. One of the first examples was reported by García, Gómez-García *et al.*, who reported the insertion of PA (and polypropyne) in a porous material as mordenite (Ni^{2+}-exchanged) and a mesoporous material as MCM-41. The insertion and polymerization of acetylene and propyne were performed by putting the activated porous materials into an atmosphere of the monomer at ambient pressure and different temperatures up to 300 °C. Diffuse reflectance UV-vis spectra confirm the presence of both polymers. Elemental analysis showed that the polymer content increases with increasing the polymerization temperature and is higher for MCM-41 than for mordenite, as expected, given the higher pore volume of MCM-41. In order to dope the conducting polymers formed inside mordenite, the Ni^{2+}-exchanged mordenite was treated with H_2 gas at 750 °C to reduce the Ni^{2+} centres to Ni(0). These Ni(0) centres should act as reducing agents to dope PA and polypropyne in order to increase the polaron density and the electronic conductivity. The presence of polarons in the conducting polymers was confirmed using EPR spectroscopy.[200]

To date, only Ruben and co-workers have attempted to incorporate PA within the pores of MOFs *via* potentiostatic electro-polymerization (EP) (Fig. 38 and 39). They electro-polymerized PA using 1-hexyne within the 1D channels of SURMOF [$Cu_2(BDC)_2$] (where H_2BDC = benzene-1,4-dicarboxylic acid and SURMOF = surface-mounted metal–organic framework). Initially, SURMOF of Cu-BDC has been deposited on Au@SiO_2 substrates functionalized by MHDA-SAM (mercaptohexadecanoic acid self-assembled monolayer). A layer-by-layer (LBL) technique is used to obtain monolithic, oriented films with channels within the MOF layer running parallel to the surface. After complete deposition, the thin films were immersed in a dry dichloromethane solution of 1-hexyne. The guest loading

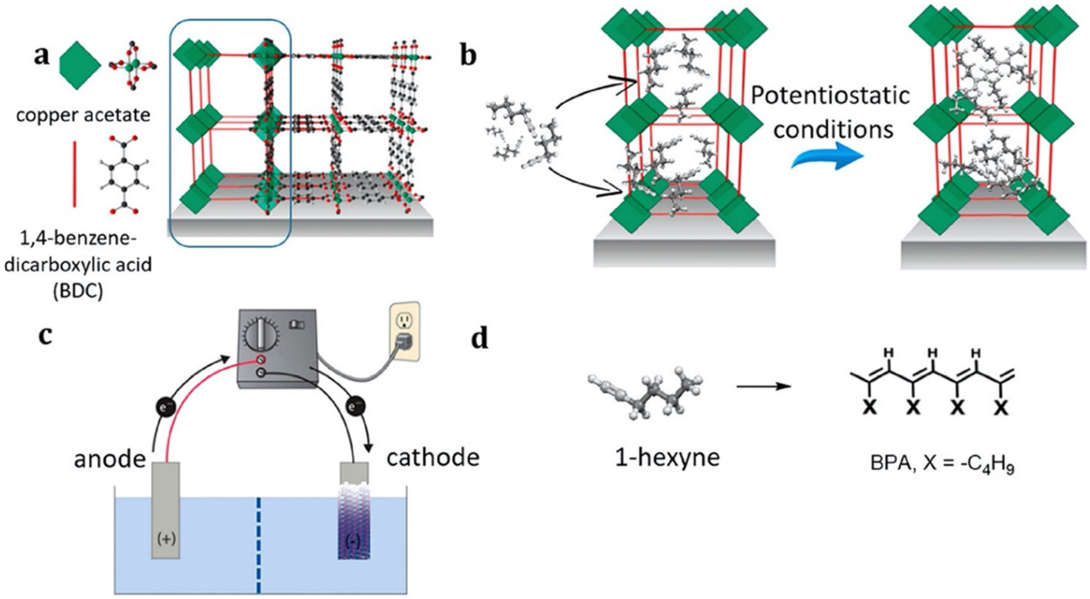

Fig. 38 Schematic presentation of the use of Cu(BDC) SURMOF-2 as working electrodes in an electrochemical cell. (a) Side view of Cu(BDC) crystal structure grown along the [001] direction on an MHDA SAM. O = red, Cu = green and C = black. (b) Scheme showing the encapsulation of alkyne monomer and the polymer formation inside the nanochannels of SURMOF-2. (c) Schematic representation of the electrochemical cell. (d) Scheme of polymerization of monosubstituted alkyne (1-hexyne, C_6H_{10}). Reproduced with permission from ref. 201. Copyright 2020, The American Chemical Society.

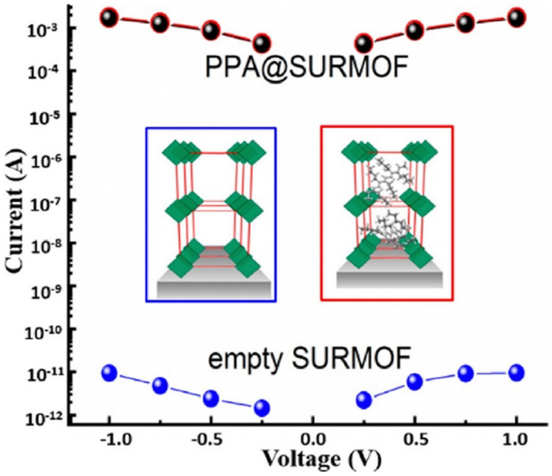

Fig. 39 Current–voltage curves before (blue) and after (black) infiltration with 1-hexyne and potentiostatic electro-polymerization (EP). The red data points, virtually identical with the black points, were measured after 3 months after EP where the sample was stored in pure argon at room temperature. Reproduced with permission from ref. 201. Copyright 2020, The American Chemical Society.

was monitored by Raman spectroscopy as the loading generated two characteristic Raman peaks at 2930 cm^{-1} (assigned to the C–H bond of butyl chains) and 2330 cm^{-1} (assigned to the C–C triple bond stretches). After loading, the electropolymerization was performed by keeping 1-hexyne-loaded thin films in a dry dichloromethane solution of 0.1 M tetrabutylammonium hexafluorophosphate (TBAHFP) as a supporting electrolyte.

The IR peak at 1631 cm^{-1} is characteristic of the conjugated C═C units within PA and is attributed to the formation of polymeric chains. Raman bands between 1260 and 1600 cm^{-1} are due to *trans*-polyacetylene (C═C stretching). XRPD, focused ion beam (FIB), SEM, energy dispersive X-ray spectroscopy (EDX) and matrix-assisted laser desorption/ionization (MALDI) analyses clearly demonstrate the polymerization of 1-hexyne molecules to form polyacetylene chains within the pores of the framework. Electrical conductivity measurements show that the conductivity of PA@SURMOF is 9.8 × 10^{-4} S cm^{-1} whereas for the SURMOF, it is only 6 × 10^{-12} S cm^{-1}. So, the polymerization in the pores has increased the electrical conductivity by 8 orders of magnitude due to both intrachain and interchain charge transport.[201]

The above-mentioned examples of modification of the conductivity of MOFs by insertion of different types of guests are summarized in Tables 1–3.

3. Fabrication of MOF thin films

For the applications of MOFs in electronic and optoelectronic devices, the fabrication of MOF thin films on conducting substrates is highly desirable.[203,204] The fruitful integration can be achieved by establishing strong contacts between the MOFs and the substrates. However, most of the MOFs are synthesized as crystalline powders, hindering their use in device fabrication. Most of the inorganic–organic hybrid MOFs are not as thermally stable as inorganic materials and are not soluble in organic solvents, in contrast to organic compounds. These differences preclude the use of well-established techniques

Table 3 Organic polymer based guest-promoted enhancement of electrical conductivity of MOFs

MOF	Guest	Method	σ_{MOF} (S cm^{-1})	$\sigma_{\text{Guest@MOF}}$ (S cm^{-1})	σ mechanism	Ref.
MIL-101(Cr)	PEDOT + I_2	PSM	10^{-11}	1.1×10^{-3}	CP	180
UiO-66	PEDOT	PSM	Insulator	2×10^{-2}	CP	181
Zn-dpzNDI	PEDOT	PSM	10^{-14}	1.8×10^{-7}	CP	183
$[Zr(bzpdc)]_n$	PEDOT	PSM	10^{-6}	10^{-3}	CP	185
$(\{Zn_3(\text{D,L-lactate})_2(\text{4-pyridylbenzoate})_2\}_n)$	PPy	PSM	—	10^{-2}	CP	189
$[Cd(NDC)_{0.5}(PCA)]\cdot G_x$	PPy	PSM	10^{-12}	10^{-3}	CP	190
ZIF-67	PPy	PSM	—	1.5	CP	191
$[Zr_6O_{16}H_{18}][TCPP\text{-}Co]_2$	PPy	PSM	3.9×10^{-10}	1.08×10^{-9}	CP	93
ZIF-67	20% PPy	PSM	4.5×10^{-10}	0.51	CP	192
UiO-66	PPy	PSM	Insulator	10^{-3}	CP	181
Zn-dpzNDI	PPy	PSM	10^{-14}	2.5×10^{-3}	CP	183
UiO-66	20% PANI	PSM	Insulator	0.55	CP	195
Co-MOF	PANI	PSM	—	5.9×10^{-2}	CP	197
Co-MOF-Br	PANI	PSM	—	4.8×10^{-2}	CP	197
Co-MOF-Ag	PANI	PSM	—	4.2×10^{-2}	CP	197
NU-1000	PTh	GRAF	10^{-9}	1.3×10^{-7}	CP	199
$[Cu_2(BDC)_2]n$	PA	PSM	6×10^{-12}	9.8×10^{-4}	CP	201

PSM = post-synthetic method; GRAF = grafting; CP = conduction pathway.

for thin film fabrication.[205,206] It is highly important to understand the interfacial interactions and the charge transport mechanism between the substrate and the thin film.[206] In order to do so, the first step involves the deposition of thin films on the surface of the substrate. The most important parameters of the deposited thin films are thickness, composition, morphology, crystallinity, homogeneity, robustness, orientation, *etc.* for their real-world applications.[207] Since the properties of thin films may be different from those of the bulk MOFs, the complete characterization of the thin film is also required.[206,207] However, the quality of the thin films may vary with the method of deposition.[208,209] Thus, it is necessary to gain proper knowledge of the thin film fabrication method. Another important criterion for developing thin films is the proper choice of the substrate. Different materials like silicon, silica, silicon nitride, gold, aluminium, graphite, copper, indium tin oxide (ITO), fluorine-doped indium tin oxide (FTO), *etc.* have been chosen for this purpose. In some cases, functionalization of substrates like self-assembled monolayer (SAM) formation or polymer coating has been performed to form uniform thin films. There are also a few reports of thin film fabrication using extrinsically conducting MOFs, and, therefore, we describe examples of thin film fabrication of MOFs using both intrinsically and extrinsically conducting MOFs.

To date, different methods have been developed for depositing MOF thin films on solid substrates, but it is difficult to use only a particular method for all types of MOFs. Several review articles have highlighted this topic.[203–209] Here, we attempt to provide a better understanding of thin film methods to find out the most suitable ones applicable for extrinsically conducting MOFs. We have classified all the methods to fabricate thin films of MOFs into two categories: (a) liquid phase and (b) gas phase.

3.1 Liquid phase processing

Here, the solutions of either pre-synthesized MOF or MOF precursors are used for the thin film fabrication.

3.1.1 Thin film fabrication with pre-synthesized MOFs. Pre-synthesized MOFs are used to fabricate thin films using different methods: (a) exfoliation, (b) bottom up and (c) drop casting.

3.1.1.1 (a) Exfoliation. Liquid phase exfoliation has been done by ultrasonication or ball milling to prepare dispersed thin layers of 2D metal–organic frameworks and coordination polymers very easily, and thus, it is well-accepted to delaminate many types of layered frameworks.[210] In this method, a very small amount of sample (∼1–2 mg) is dispersed in a solvent and then delaminated through exfoliation using ultrasonication. The obtained delaminated nano-/micro-flakes are dried by solvent evaporation from the suspension and collected. For the thin film fabrication, the suspension can be drop-cast or spin-coated on the substrate or the obtained dried thin flakes redisperse in the same or a different solvent and drop-cast on the substrate. The thin films can then be characterized using AFM to analyse the thickness, surface roughness and side flake dimensions. Despite the easy synthesis of nano-flakes and thin film fabrication, this method does not lead to the formation of uniform flakes. Although this method allows the preparation of thin flakes of 2D MOFs, device fabrication with these exfoliated 2D flakes remains a challenge, probably due to the difficulty of transferring and attaching the flakes onto different substrates. Suárez-García *et al.* have reported the delamination of the spin crossover (SCO) 2D metal–organic framework $[Fe(L1)_2](ClO_4)_2$ (where L1 = tris(2-(1*H*-tetrazol-1-yl)ethyl)-amine ligand) (Fig. 40).[211]

Very good-shaped crystals of this 2D MOF were chosen for the exfoliation and dispersed in different solvents such as water, methanol (MeOH), ethanol (EtOH), dimethylformamide (DMF), acetone ($(CH_3)_2CO$), chloroform ($CHCl_3$), toluene (Tol) and tetrahydrofuran (THF) for sonication at room temperature in an ultrasound bath for 4, 6 and 12 h. The exfoliation is monitored by the Tyndall effect. The samples are monitored by dynamic light scattering (DLS) analysis. After 12 h, only the vial containing water showed successful delamination of the layered crystal. Afterwards, the vial was placed in an orbital shaker for 24 h for the correct separation and to increase the

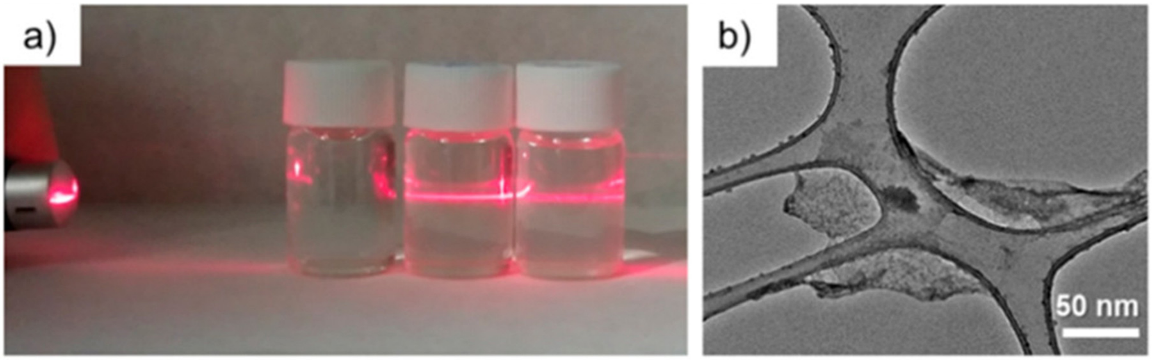

Fig. 40 Morphological characterization of the flakes of the SCO MOF $[\mathrm{Fe(L1)_2}](\mathrm{ClO_4})_2$. (a) Tyndall effect demonstration of the colloidal suspension in water. From left to right: the red laser beam remains invisible through the first vial, which contains $[\mathrm{Fe(L1)_2}](\mathrm{ClO_4})_2$ before exfoliation. The scattered laser beam can be observed through the colloidal suspension of flakes immediately (in water, second vial) and a few weeks (in water/ethanol mixture, third vial) after exfoliation; (b) transmission electron microscopy (TEM) image of a single flake, a few hundred nanometres width, obtained after transferring a drop of the same colloidal suspension to the grid. Reproduced with permission from ref. 211. Copyright 2018, the American Chemical Society.

exfoliation yield obtaining a final colloidal suspension that is stable for at least one week without any precipitation and/or colour change. The delaminated thin film of the MOF can be deposited on the Si-wafer by drop casting or spin coating of the colloidal solution on the Si-wafer and dried under an argon flow. The dried 2D flakes were further used to measure the spin-crossover behaviour which is similar to the bulk compound.[211]

Zeng *et al.* have exfoliated the anionic 2D MOF $\mathrm{Eu(dfdmt)_2}$ (where dfdmt = 2,5-difluoro-3,6-dimercaptoterephthalate) into ultrathin and few-layer nanosheets by simple ball-milling. An AFM study indicates that the thickness of the delaminated 2D films is about 0.84 nm for each layer and the lateral dimensions are 324 and 476 nm. HRTEM images reveal the crystalline thin morphology of the flakes with distinct lattice fringes of the thin films. The stability of the delaminated thin films was characterized using XRPD analysis and FT-IR spectroscopy.[212]

Using ultrasounds with different solvents, Benmansour *et al.* have shown that it is possible to exfoliate anilato-based mixed-valent $\mathrm{Fe^{II}/Fe^{III}}$ highly conducting 2D MOFs into nanosheets of a few monolayers ($\sim$7 nm).[213]

3.1.1.2 (b) Bottom-up deposition. In this method, a substrate is dip-coated into colloidal solutions/suspensions of micro-/nano-sized MOF particles to deposit the thin films on the surface of the substrate. This method is also known as chemical solution deposition (CSD) as the solution contains *meta*-stabilized MOF particles. The obtained thin films are characterized using XRPD analysis to check their homogeneity and surface topography by AFM and TEM studies. Interestingly, this method leads to the formation of a homogeneous thin film fabrication and also the thickness of the thin films can be controlled by repetition of the coating process. One of the major obstacles is the formation of a metastable state of the MOFs in solution, and thus, it has been used in rare cases. Horcajada and co-workers have deposited the thin film of MIL-89 $\{[\mathrm{Fe_3OCl(muconate)_3}]\cdot n\mathrm{Solv}\}$ on a silicon wafer by this method.[214] Initially, they prepared a colloidal solution of MIL-89 NPs by heating the orange mixture of iron(III) acetate and *trans*-muconic acid in ethanol at 60 °C for 10 min which led to a rapid increase of viscosity and cloudiness of the solution. Afterwards, the side-polished silicon wafer was dip-coated within the cooled colloidal solution for 2 min and then dried at room temperature. The film thickness can be improved through multiple deposition under the same conditions.[214] These authors have also obtained thin films of other MOFs such as MIL-101 $[\mathrm{Cr_3OF(BDC)_2(H_2O)_2}]_2$ and ZIF-8 $[\mathrm{Zn(Cu_4H_5N_2)_2}]$ with this method. This method allows for the preparation of thin films with controlled size of the MOF particles.[215,216]

3.1.1.3 (c) Spin coating. The solvothermally synthesized MOF particles can be directly deposited by spin coating a suspension of a MOF in a volatile solvent on the surface of a substrate. The MOF powder is dispersed in a highly volatile solvent, homogenized by sonication and then the suspension is drop-cast on the substrate through the spin coating method. In most cases, a binder is mixed with the MOF particles before drop-casting to improve the adhesion of the MOF particles to the surface. This is one of the oldest methods for the fabrication of thin films and has attracted significant attention for the low cost and simplicity but the formation of a uniform distribution on the surface is questionable. Wong and co-workers have studied the photocatalytic water splitting behaviour of the MOF $[\mathrm{La(TTCA)(H_2O)}]\cdot\mathrm{DMF}\cdot\mathrm{H_2O}$ ($\mathrm{TTCA^{3-}}$ = triphenylene-2,6,10-tricarboxylate, DMF = *N*,*N*-dimethyl formamide) by depositing thin films of it on an ITO substrate using Nafion as the binder.[217] Similarly, Horiuchi *et al.* have also deposited thin films of MIL-101(Fe) on FTO glass substrates with Nafion as a binder and studied the photocatalytic activity.[218] In some cases, other additives like polymeric binders are used for this purpose. Campbell and co-workers have fabricated HKUST-1 membranes with polyimide P84 by mixing HKUST-1 microcrystals with a solution of the polymer with polymer : HKUST ratio of 5 : 1 and then this mixture was cast on the polypropylene non-woven sheets to obtain thin films of thickness $\sim$250 μm.[219]

3.1.2 *In situ* growth of thin films from mother solutions. The solvothermal method is the most useful technique to synthesize diverse classes of MOFs and thus several research groups have attempted to grow MOF thin films directly from mother solutions of precursors. In this method, precursors are dissolved in a solvent or mixed solvent and treated solvothermally for initial nucleation and then the substrate is immersed in the solution, although in some cases, the substrate is immersed directly into the solution of precursors. Upon heating, MOF thin films were grown rapidly on the substrate or in the solution which can be seen as the crystals on the surface of the substrate. Nevertheless, the major problem of this method is that such direct crystallization leads to both homogeneous and heterogeneous growth of the thin film layers and the MOF particles are randomly oriented on the substrate. Albeit, this easy, efficient and low-cost deposition method has been often used for the preparation of MOF thin films, although it is difficult to control the thickness of the thin films as well as their uniformity.

Ho and co-workers have synthesized thin films of MOF-525 by immersing an FTO doped glass substrate in a solution of precursors H_4TCPP, benzoic acid, and zirconyl chloride, octahydrate in a two-step method (Fig. 41).[220]

The synthesis of the thin film was monitored by XRPD analysis. SEM images reveal that the cubic MOF particles are very uniform, with sizes in the range of 500–1000 nm and that there is a strong adhesion between the MOF particles and the substrate. These authors have demonstrated that the MOF particles remain identical after post-metalation by immersing the thin films into solutions of Co and Zn salts. Energy dispersive X-ray (EDX) spectroscopic analysis clearly identifies the uniform distribution of Zn or Co ions within the particles. They have also demonstrated that the charge diffusion is easier in the parent MOF than post-metalated MOFs as evidenced by cyclic voltamperometry (CV) analysis.[220]

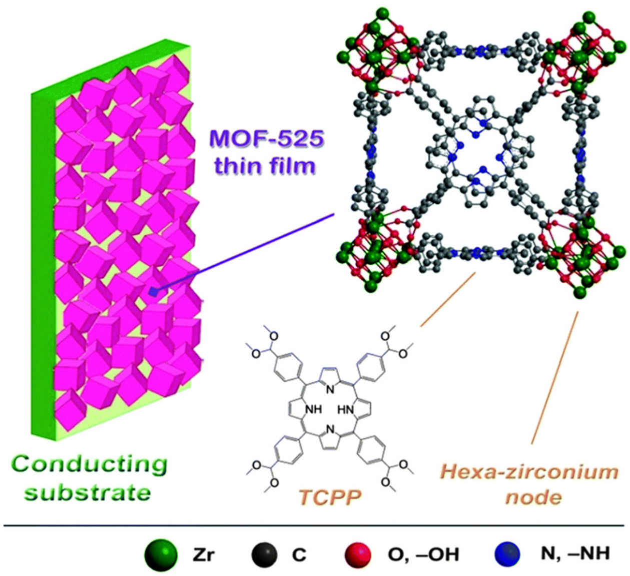

Fig. 41 MOF-525 crystal structure and schematic representation of its solvothermally grown thin film. For simplicity, hydrogen atoms are not shown. Reproduced with permission from ref. 220. Copyright 2015, the Royal Society of Chemistry.

Thin films of MOF-5 on ZnO-coated FTO glass substrates have been prepared by Wang *et al.* using a solvothermal method by soaking the substrate in a DMF solution of $Zn(NO_3)_2$ and terephthalic acid.[221] An attempt with bare FTO was unsuccessful. The formation of a thin film was characterized by XRD and SEM analyses. Tb^{3+} doping was done by soaking the thin films in DMF solutions of $Tb(NO_3)_3$ for 3 days and was characterized by XRD, SEM, EDS and ICP analyses. SEM micrographs clearly show the strong attachment between the MOF particles and the substrate. These doped MOF-5 thin films act as a good luminescent material.[221]

Recently, Saha and co-workers have developed thin films of a porphyrin-based MOF, namely ZnTCPP (TCPP = tetrakis(4-carboxyphenyl)porphyrin) on ZnO-coated FTO glass slides. DMF:ethanol solution of $Zn(NO_3)_2$, TCPP and DMBPY were solvothermally treated at 80 °C for 2 h for initial nucleation, and then, the substrate was immersed in the solution and consequently solvothermally treated at 80 °C for another 30 min. An XRD study shows that the thin films were grown in the [100] direction in contrast to the [001] direction of bulk crystallization. These authors have suggested that the ZnO surface facilitates the thin film fabrication by capturing TCPP struts through –COOH groups and thus directing the film growth vertically on the surface. SEM images revealed that the densely packed rectangular slab-like crystals are vertically oriented on the surface and the thickness is ~10 μm (Fig. 42). Afterwards, these authors encapsulated C_{60} within the void space of the MOF by soaking the thin films in a saturated solution of C_{60} in toluene for seven days. The fullerene-doped ZnTCPP thin films show weaker solar cell photoconversion activity than that of the undoped MOF.[222]

3.1.3 Electrochemical synthesis of MOF thin films.

There are three different electrochemical methods namely: (a) electrophoretic, (b) anodic and (c) cathodic methods for the deposition of MOF thin films (Fig. 43). Mild synthetic conditions, facile and controlled synthesis, *etc.* have made these electrochemical methods highly interesting to fabricate MOF thin films. Such electrochemical methods are highly attractive due to the fact that the thickness and size of the thin film can be controlled by an external voltage. However, these methods also suffer from several problems related to common electrochemical studies.

3.1.3.1 (a) Electrophoretic method (EPD). The underlying principle of this method is to use the partial charge present on the surface of the MOFs. The defects at the surface of the MOF crystallites due to missing metal ions or linkers create partial charges at the surface. Under an applied voltage, the MOF particles move towards the electrodes following the charge at the surface. In the electrophoretic method, two electrodes are immersed in a solution containing the MOF as a colloidal suspension. On applying a fixed voltage between the two electrodes, the partial charge on the surface drives the MOF particles towards the oppositely charged electrodes, where they

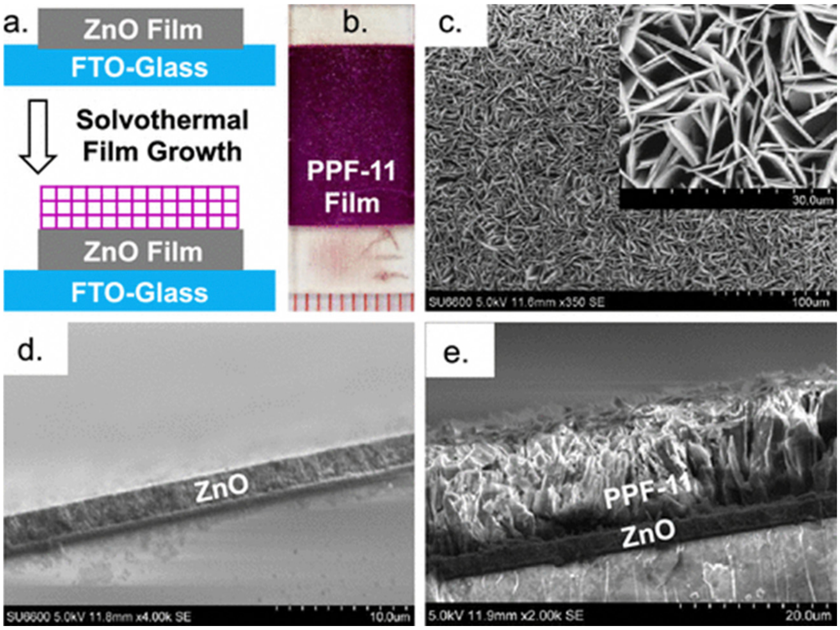

Fig. 42 (a) Schematic diagram outlining the solvothermal growth of the PPF-11 film. (b) A photograph of a solvothermally grown PPF-11/ZnO film. (c) Scanning electron microscopy (SEM) images of a PPF-11/ZnO film showing densely packed crystals aligned uniformly on the surface. Cross-sectional-SEM images of (d) a 2.5 μm thick annealed ZnO film and (e) a solvothermally grown 10 μm thick PPF-11 film on the ZnO layer. Reproduced with permission from ref. 222. Copyright 2019, The American Chemical Society.

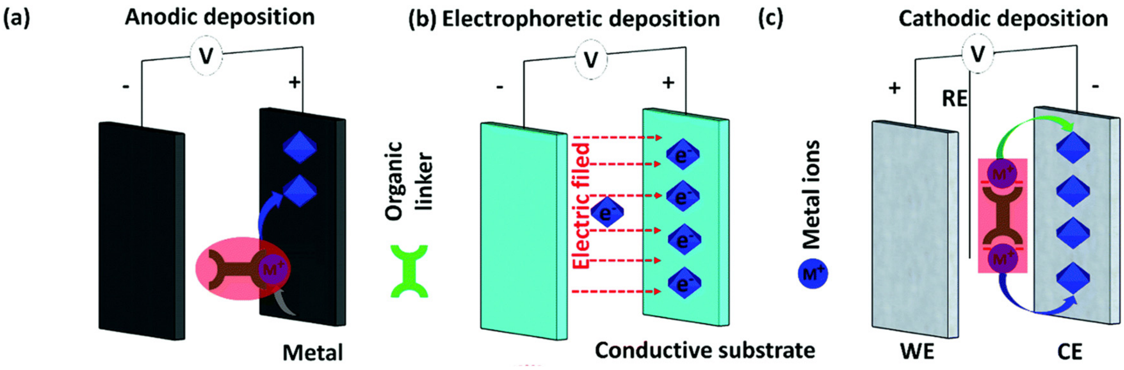

Fig. 43 Schematic representation of the electrochemical fabrication of MOF thin films with (a) anodic deposition, (b) electrophoretic deposition and (c) cathodic deposition. Reproduced with permission from ref. 204. Copyright 2017, the Royal Society of Chemistry.

deposit and form thin films. Hupp and co-workers have employed this method to deposit thin films of four different MOFs: NU-1000, UiO-66, HKUST-1 and MIL-53.[223] Two FTO electrodes were immersed in toluene solutions of UiO-66 and NU-1000 MOF particles, and then a fixed voltage was applied with different time periods. SEM micrographs indicate that the accumulation on the electrode surface by the MOF particles increases with time of electrophoresis, forming a film of 4–5 μm thickness after 3 h (Fig. 44). The authors have established that the thin films of NU-1000 MOF obtained by this method act as a reversible redox couple similar to NU-901 containing a redox pyrene core. These authors have also developed a micropatterned MOF thin film by combining photolithography with EPD through the consecutive formation of layers of insulating photoresist material, then patterning the photoresist layer by photolithography, later EPD on the bare FTO part and finally removal of the photoresist material.[223] Hupp *et al.* have also prepared thin films of ferrocene derivatized NU-1000 MOF using a similar method and measured their redox behaviour.[224]

Zhang and co-workers have developed thin films of ZIF-67 using a similar electrophoretic method by varying the applied voltage from 20 to 60 V to prepare thin films of 1–7 μm thickness within one minute. Later, they converted these MOF thin films into Co_9S_8 thin films which are further utilized for the degradation of vanillin.[225] Recently, Hupp and co-workers have studied the diffusion behaviour of different alkanes with chain length C5–C16 using thin films of ZIF-8 obtained by this

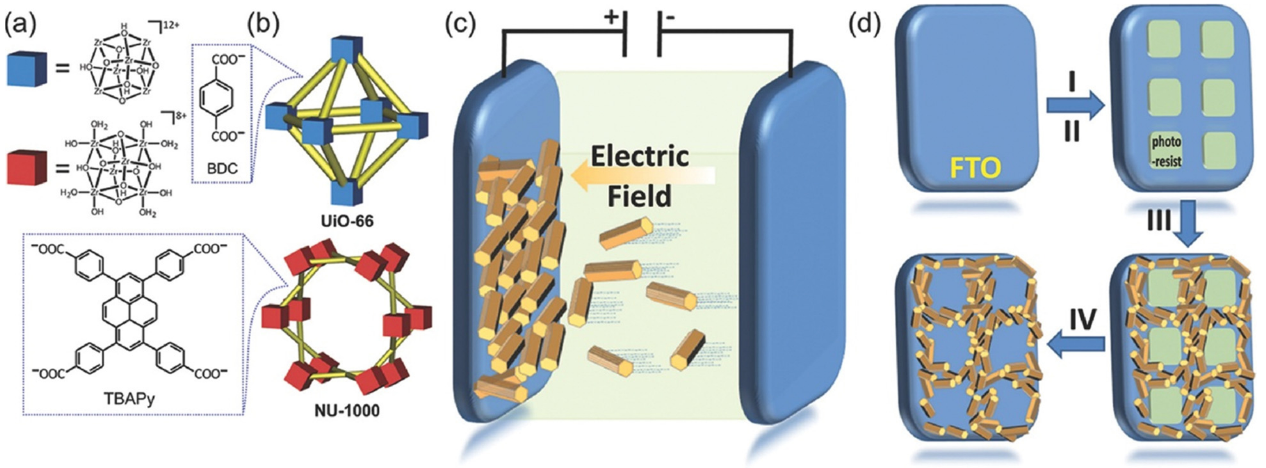

Fig. 44 (a) Components of UiO-66 and NU-1000: Zr-containing nodes (blue for UiO-66 and red for NU-1000) and organic linkers. (b) Illustration of the crystal structures of UiO-66 and NU-1000 MOFs. (c) A scheme illustrating the MOF EPD film growth, showing the attraction of charged MOF particles towards an oppositely charged electrode using an applied electric field. (d) Illustration of the patterning of the MOF EPD film procedure: (I) spin coating a layer of photoresist on a bare FTO substrate, (II) using photolithography to create patterned squares of photoresist, (III) deposition of MOF particles on the conductive exposed FTO areas using EPD, and (IV) removal of the remaining photoresist squares to obtain the desired pattern. Reproduced with permission from ref. 223. Copyright 2014, Wiley & VCH.

method. They have established that the thin films obtained using the EPD method are more porous and allow faster diffusion of alkanes than the thin films obtained using *in situ* solvothermal methods.[226] Nevertheless, there is no report on guest encapsulation within the void space of MOF thin films obtained by this method. Cao and co-workers have developed thin films of Ln^{3+}-doped UiO-66 MOF and have shown their temperature-sensing behaviour.[227] In another article, Cao and co-workers have developed thin films of Tb-BTC, Eu-BTC and $Eu_{0.5}Tb_{0.5}$-BTC MOF (where H_3BTC = trimesic acid) by EPD method. In these frameworks, BTC ligands show three different binding modes: bidentate, monodentate and free carboxylate groups that create some charges on the surface that have been utilized for EPD. The thin films were used for detection of Cr^{3+} and nitrobenzene in the solution phase as well as nitrobenzene in the gas phase.[228]

3.1.3.2 (b) Anodic deposition. In anodic deposition, a metal electrode is used as the source of the cations and immersed in the solution containing the organic ligand. On applying voltage, the metal oxidizes, generating cations that react with the ligands to generate small MOF particles that grow on the surface of the anode. In some cases, the metal is coated on the surface of non-metallic substrates to be used as an anode. The size of the synthesized MOF particles is dependent on the applied voltage. Increasing the voltage increases the release of cations from the anode, reducing the thickness of the coating. In 2006, Muller and co-workers synthesized a series of MOFs by an electrochemical method using bulk powders.[229] Ameloot and co-workers have developed thin films of HKUST-1 by the same method with varying voltages on a copper electrode by immersing two different electrodes in a solution of trimesic acid and methyltributylammonium methyl sulphate (MTBS) as the electrolyte (Fig. 45). The film growth was monitored by XRD and SEM analyses. The SEM micrographs reveal that the size of the synthesized particles can be tuned by modifying the synthetic conditions.[230] Later, they have patterned thin film fabrication on the substrate during electrochemical deposition of HKUST-1.[231]

Campagnol *et al.* have deposited thin films of MIL-100(Fe) and HKUST-1 by anodic deposition method at high temperatures (110–190 °C) and pressures. They have found that the HKUST-1 particles are formed with an unusual cubic morphology. They have also synthesized MIL-100(Fe) without using any harsh chemicals like strong acid (HF) and conductive salts.[232] Schäfer *et al.* have studied the mechanism of thin film formation for HKUST-1 with the anodic deposition method. They have established that the thin film formation proceeds in two steps: (a) Cu is first oxidized to Cu_2O in the presence of O_2 and then Cu_2O is further oxidized to Cu^{II}-BTC in the presence of the linker at the cuprite–electrolyte interface.[233] Several other research groups have attempted to synthesize a number of MOFs like ZIF-8, MIL-100(Al) and so on. Stassen and co-workers observed the thin film deposition of UiO-66 MOFs on both the anode and cathode.[234] Recently, Hauser and co-workers have synthesized thin films of four different Cu and Zn MOFs, both 2D and 3D, by immersing metal-coated ITO electrodes in the ligand solutions (Fig. 46).[235]

3.1.3.3 (c) Cathodic deposition. The cathodic deposition method was first developed by Dinca and co-workers for the thin film fabrication of MOF-5. They used a three-electrode cell where both the working and counter electrodes are used as chemical separators and electron pools but do not participate in the MOF formation. The basic principle of this deposition method is the deprotonation of the organic ligands by reaction with the metal ions near the cathode and this can be done by the electrochemical reduction of oxo-anions like nitrate,

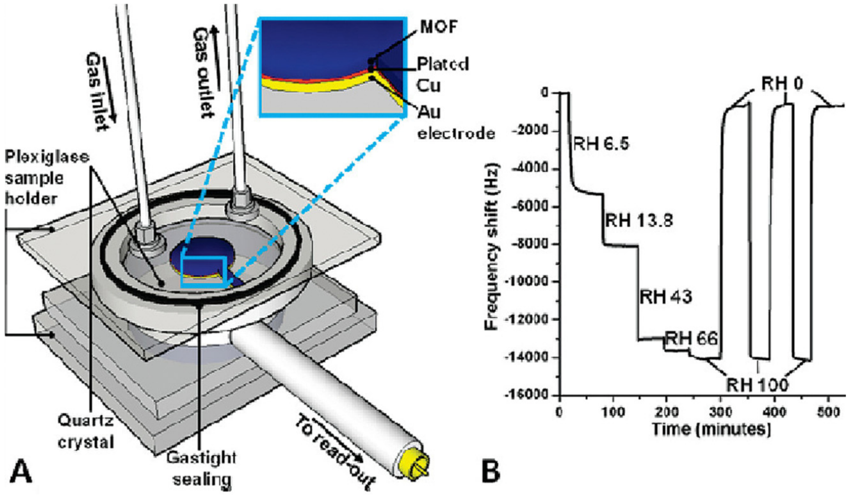

Fig. 45 Electrochemically grown [$Cu_3(BTC)_2$] coatings in QCMB measurement of water adsorption. (A) Schematic representation of the setup. (B) Signal upon adsorption of water from nitrogen streams at different RH values illustrating reversibility and reproducibility. Reproduced with permission from ref. 230. Copyright 2009, The American Chemical Society.

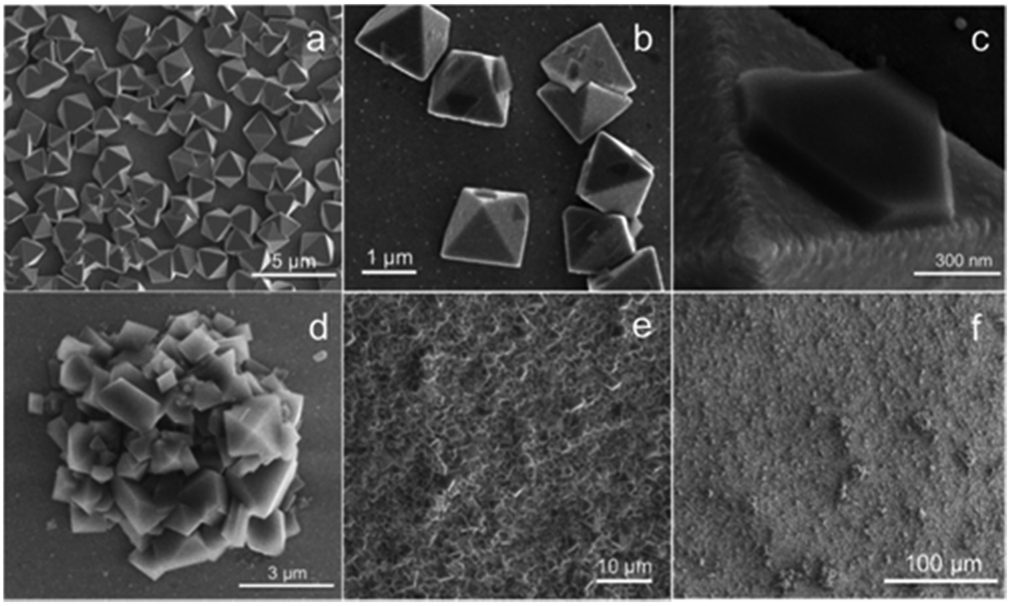

Fig. 46 SEMs of HKUST-1 grown on Cu-ITO at 0.75 V: (a) copper octahedra grown by electrodeposition on ITO (−1.0 V for 90 s). (b) and (c) the beginning of HKUST-1 growth on Cu octahedra after 2 min. (d) An isolated copper octahedron covered by MOF crystals after 50 min of growth. (e) Typical film coverage after 50 min of growth. (f) A 0.1 mm^2 section of film illustrating the relative smoothness and continuity of the HKUST-1 film after 50 min of growth. Reproduced with permission from ref. 235. Copyright 2010, The American Chemical Society.

perchlorate *etc.* which consequently produces large amounts of hydroxide ions near the cathode. These hydroxide ions deprotonate the organic ligands for the synthesis of the MOF. For the electrochemical synthesis, $Zn(NO_3)_2$, H_2BDC (1,4-benzenedicarboxylic acid), $(NBu_4)PF_6$ electrolyte was dissolved in 100 : 1 DMF–water mixture and a flexible transparent polymer (FTP) electrode was immersed in the solution. A constant potential of 1.6 V was applied for 15 min for the deposition of MOF-5 on the electrode. During the electrochemical reaction, NO_3^- was reduced to NO_2^- with subsequent deprotonation of the H_2BDC ligands with formation of hydroxide ligands through deprotonation of water in the solution.[236] Later, Liu and co-workers prepared thin films of $[Eu(HBPTC)(H_2O)_2]\cdot 2DMF$ (BPTC = benzophenone-3,3′,4,4′-tetracarboxylate) by a cathodic deposition method.[227] In this case, they used anhydrides or esters of the ligand with the assumption that increasing hydroxide ion concentration may hydrolyse esters into acids. In the electrochemical cell, enzophenone-3,3′,4,4′-tetracarboxylic dianhydride (BTDA) and $Eu(NO_3)_3$ were dissolved in DMF with graphite rod (anode) and FTO (cathode).

Applying a current density of 0.4 mA cm^{-2} for 10 minutes leads to the deposition of thin films on the cathode. They have used these thin films for the luminescence-based detection of carbonate anions in aqueous solution.[237] They have also developed thin films of a number of Ln-MOFs by this method and studied their light-emitting behaviour.[238] Wang and co-workers have synthesized thin films of terbium succinate by this approach and used them for sensing copper ions in aqueous solution.[239]

3.1.4 Interfacial method. In the interfacial method, both the reactants *i.e.*, metal ions and ligands, are taken into two different immiscible media that were put together to form the thin film at the interface. There are basically two different methods developed for the interfacial synthesis of MOF thin films: (a) liquid–liquid and (b) liquid–gas. We also discuss the Langmuir–Blodgett thin film fabrication technique, which is a special case of liquid–gas interfacial synthesis. The main limitation of these methods is the uncontrolled growth of the thin films at the interfacial layer.

3.1.4.1 (a) Liquid–liquid interfacial method. In this method, two different immiscible liquids are used to dissolve both the metal ions and organic ligands, respectively. Then, one solution is layered over the other and the thin film is formed at the interface of the two solutions. The interface between the two immiscible liquids has been used as a template for thin film formation. Ameloot and co-workers have introduced this technique for the formation of a thin film of HKUST-1.[240] Classical HKUST-1 synthesis is done by using two different solvents such as water and ethanol. They have replaced ethanol with octanol to dissolve trimesic acid (H_3BTC) and used water to dissolve the copper salt. Both solutions were layered to obtain thin films at the interface. They have also synthesized thin films of ZIF-8 using a similar method. In the same report, they also prepared hollow spheres of HKUST-1 by dispersing the aqueous phase/solution as droplets in an octanol solution. To obtain monodisperse droplets, the aqueous phase was transported through a tapered capillary tube into the co-flowing organic phase. The hollow spheres are formed at the interface when these droplets are moved through the hydrophobic tube and then collected in ethanol. SEM micrographs show that the diameter of such hollow spheres is ∼375 μm.[240]

Kambe and co-workers have developed thin films of $Ni_3(BHT)$ (BHT = benzenehexathiolate) following a similar liquid–liquid interfacial method by using $Ni(OAc)_2$ with NaBr (Na^+ acts as a charge compensating counter ion) in the aqueous layer with BHT in DCM. SEM analysis shows that the layers are monolithic in nature with a size of ∼100 μm and a thickness of 1–2 μm (Fig. 47).[241] In another example, Huang *et al.* have developed thin films of Cu-BHT 2D MOF with the same method.[242] They observed that, during growth, the thin films change from transparent to opaque. SEM micrographs indicate that the thin

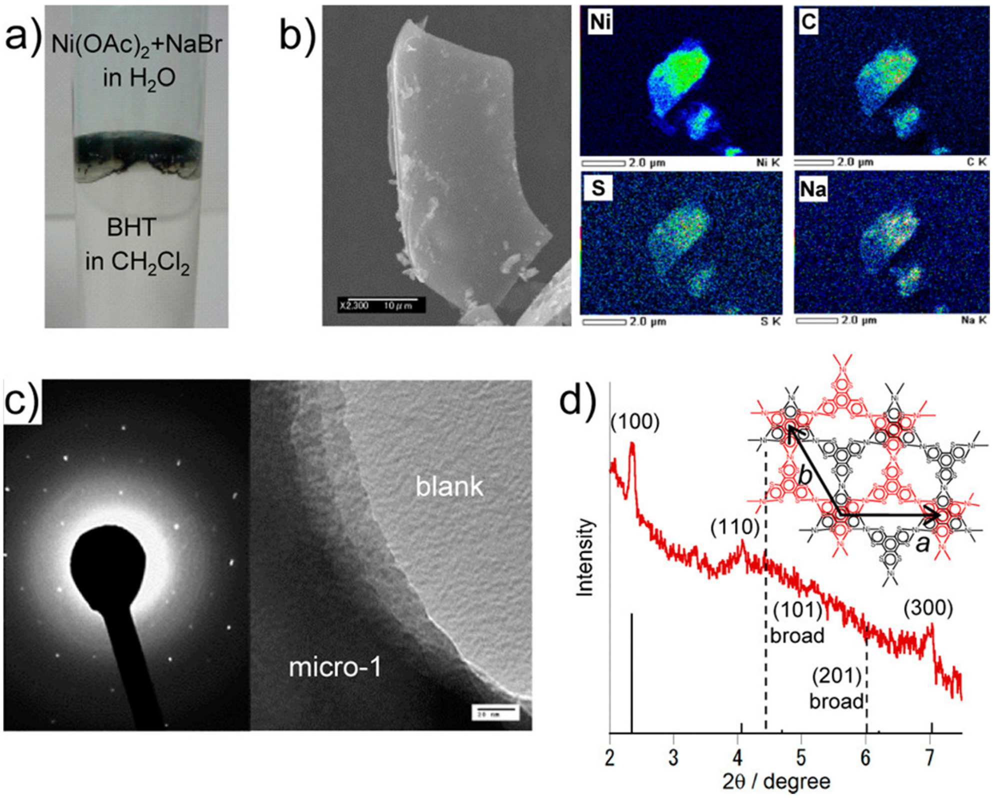

Fig. 47 Synthesis and characterization of micro-1. (a) Photograph focusing on the water–CH_2Cl_2 interface holding micro-1. (b) (left) FE-SEM image and (right) elemental mapping of Ni, S, C, and Na performed using SEM–EDS. (c) (left) SAED pattern and (right) HRTEM image. (d) Experimental (red curve) and simulated (black sticks) XRPD patterns. Reproduced with permission from ref. 241. Copyright 2013, The American Chemical Society.

films have different morphology on both sides. The upper side is flat and shows no cracks while the other side is highly rough due to the random orientation of the platelike nanosheets. SEM images also show that the thickness of the films is ∼200 nm.[242] Recently, Chen and co-workers have synthesized thin films of 2D MOFs, Ag_3(BHT) and Au_3(BHT), using a similar liquid–liquid interface method.[243] Several other research groups have utilized this method to develop thin films of different MOFs.

Bai and co-workers have developed a spray assisted liquid–liquid interface method to prepare a 2D thin film of Cu(BDC) (BDC = 1,4-benzenedicarboxylic acid) MOF by spraying a DMF–acetonitrile solution (1 : 2) of copper salt on the surface of a DMF–acetonitrile (2 : 1) solution of H_2BDC with a flow rate of 1 μL s^{-1}. The thin film formation was completed after spraying 50 μL. SEM images show that the size of the obtained thin films is ∼200 nm, and the thickness is 0.25–5.55 μm. They have studied the catalytic performance of the thin films for the reduction of 4-nitrophenol to 4-aminophenol.[244]

3.1.4.2 (b) Gas–liquid interfacial method. In this method, the thin films are synthesized at the gas–liquid interface. In 2013, Kambe and co-workers attempted to synthesize thin films of Ni_3(BHT) by a gas–liquid interfacial reaction for the first time.[241] They sparged an ethyl acetate solution of benzenehexathiol on the surface (77.5 cm^2) of an aqueous solution of $Ni(OAc)_2$ (50 mM) and NaBr (10 mM) using a micro-syringe. The thin film formation was continued for two hours. Scanning probe microscopy (SPM) measurements were used to determine the structure. An AFM study reveals that the thickness of the layer is ∼0.6 nm which is equivalent to the graphene layer on the substrate. The SPM study revealed that the Ni-BHT thin film has a hexagonally ordered monolayer structure.[241]

In 2013, Makiura *et al.* synthesized a crystalline, uniform and large-scale thin film of NAFS-13 using a gas–liquid interfacial reaction. In the first step, they spread the molecular building block 15,10,15,20-tetrakis(4-carboxyphenyl)-porphyrinato-palladium(II) (PdTCPP) in ethanol medium on the surface of an aqueous layer and then an aqueous solution of $Cu(NO_3)_2$ was slowly injected in the aqueous solution. The chemical reaction between the metal nodes with the carboxylate groups of the PdTCPP building blocks forms a thin layer of the 2D MOF NAFS-13. The slow injection of metal ions makes it feasible to grow the flakes in a microscopic level with a very smooth surface.[245]

Later, Wu and co-workers developed thin films of semiconductive 2D MOF $Ni_3(HITP)_2$ (HATP = 2,3,6,7,10,11-hexaaminotriphenylene) and fabricated an electronic device as a field effect transistor. They observed the formation of thin layers of the 2D MOF on the water surface on heating the aqueous solution of the precursors with trimethylamine to 60 °C. The hydrophobic metal–organic layers float on the water surface. Within 3 min, the film thickness reached 100 nm and the colour of the thin film deepened with increasing thickness to dark violet blue (Fig. 48).[246] They have transferred the thin

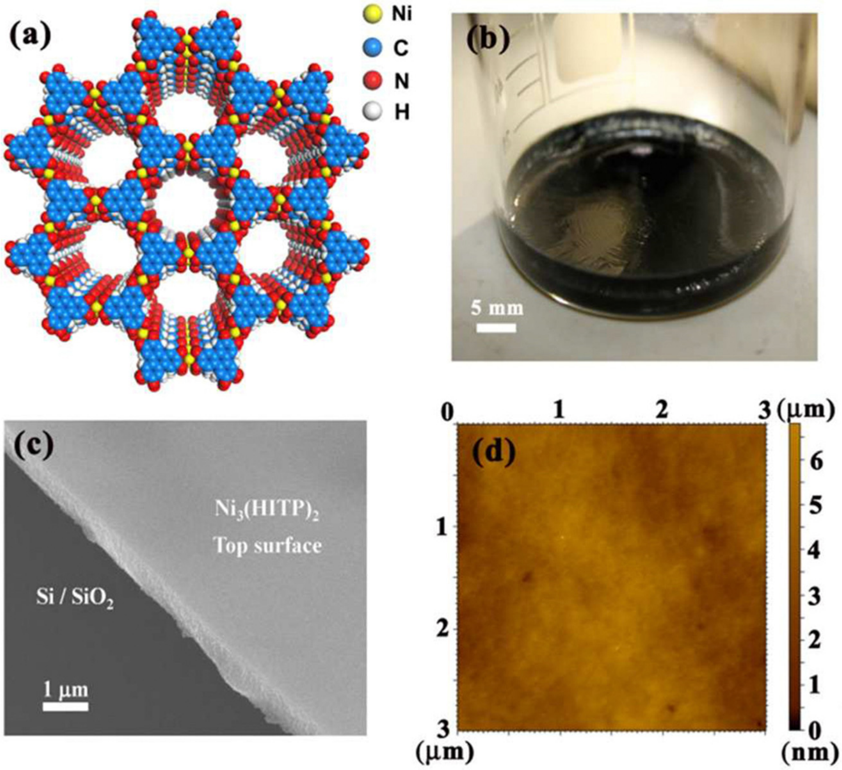

Fig. 48 (a) Crystal structure of $Ni_3(HITP)_2$. (b) Photograph of a $Ni_3(HITP)_2$ membrane formed at the air–liquid interface. (c) SEM and (d) AFM images of the top surface of a $Ni_3(HITP)_2$ membrane. Reproduced with permission from ref. 246. Copyright 2017, The American Chemical Society.

films on SiO_2/Si wafer substrates and then patterned Au electrodes are deposited on the top to form the porous FET.

3.1.4.3 (c) Langmuir–Blodgett deposition. In 2010, H. Kitagawa and co-workers developed thin films of the 2D MOF NFAS-1 using the Langmuir–Blodgett technique.[247] This technique allows the growth of a monolayer at the liquid–air interface and to transfer it easily to a substrate. These authors prepared a chloroform/methanol solution of [Co(TCPP)] (TCPP = 5,10,15,20-tetrakis(4-carboxyphenyl)porphyrin) and pyridine that was spread on $CuCl_2{\cdot}2H_2O$ in water medium to form a Langmuir film on the surface. The chemical reaction between CoTCPP and copper leads to the formation of a paddle-wheel-based 2D coordination polymer with the apical positions occupied by pyridyne moieties which allow the 2D layers to assemble by interlayer $\pi\cdots\pi$ interactions. The 2D metal–organic thin films were then transferred onto Si substrates and stacked by a sequential layer-by-layer growth procedure to form thin films of any desired thickness. Growth of thin films was monitored by absorption and X-ray photoelectron spectroscopy while detailed crystallinity, homogeneity and orientation were studied by XRD analysis. The thickness of the thin film is 20 nm after 20 cycles of deposition on the substrate. θ-Scan shows that the 2D layers are parallel to each other but they are tilted at an angle of 0.3°.[247]

Kitagawa *et al.* have also prepared thin films of another 2D MOF: NAFS-2, with a similar method using a non-metalated porphyrin: 5,10,15,20-tetrakis(4-carboxyphenyl)porphyrin (H_2TCPP) as a building to form the 2D layered MOF in the absence of pyridine (Fig. 49). The water molecules coordinate to the copper centres within the dinuclear paddle-wheel units. Here, the tilting angle is 3° and the authors suggested that this is due to the absence of stacking interactions between the layers.[248]

3.1.5 Liquid phase epitaxy (LPE). Wöll and co-workers have developed this method for the fabrication of MOF thin films, and it is the most useful technique for this purpose.[204] The most important requirement for this method is the functionalization of the substrate. The substrate functionalization can be done by the deposition of SAMs (self-assembled monolayers) on the surface of the substrate. Organic chain-like molecules having two different functional groups on both ends are generally used for the SAMs. For substrate functionalization, the anchoring group of the molecule is allowed to react with the substrate to form the attachment. For example, gold substrates can be functionalized with organic molecules having thiol anchoring groups. After attachment, the end group of the organic moiety, which may vary from inert to barely attainable to highly polar, remains free for further use. It is also possible to modify the ending group. Thus, aldehydes can be oxidized to carboxylic acids. Thanks to the ordered arrangement of the ending groups of the functional SAMs, it is possible to prepare ordered thin films of MOFs on the substrate. The most important characteristic of these methods is that the obtained thin films are strongly attached to the substrate through chemical bonds. Here, we will discuss the main three MOF deposition methods on SAMs-functionalized substrates.

3.1.5.1 (a) Solvothermal synthesis. In this method, the SAM-functionalized substrates are immersed in a solution of the reactants for the growth of MOF thin films by solvothermal treatment. However, the relatively lower thermal stability of most SAMs on the substrates makes it difficult for practical use.[249] In this

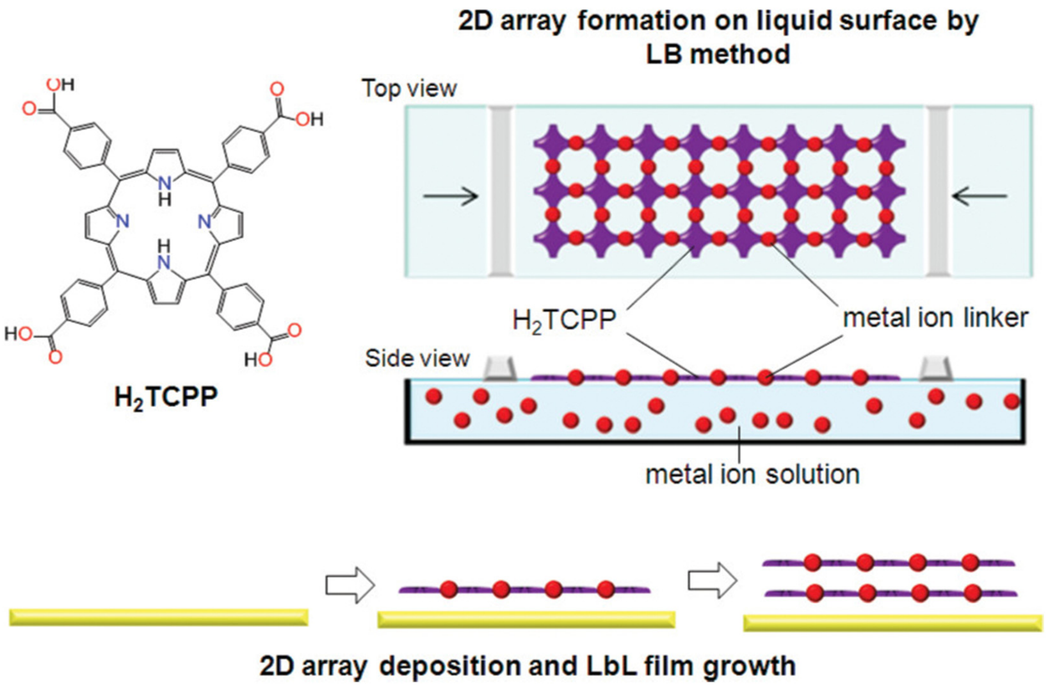

Fig. 49 Schematic illustration of the representative assembly processes of NAFS-2 by combined Langmuir–Blodgett/layer-by-layer (LB-LbL) nanofilm growth technique. Reproduced with permission from ref. 248. Copyright 2011, The American Chemical Society.

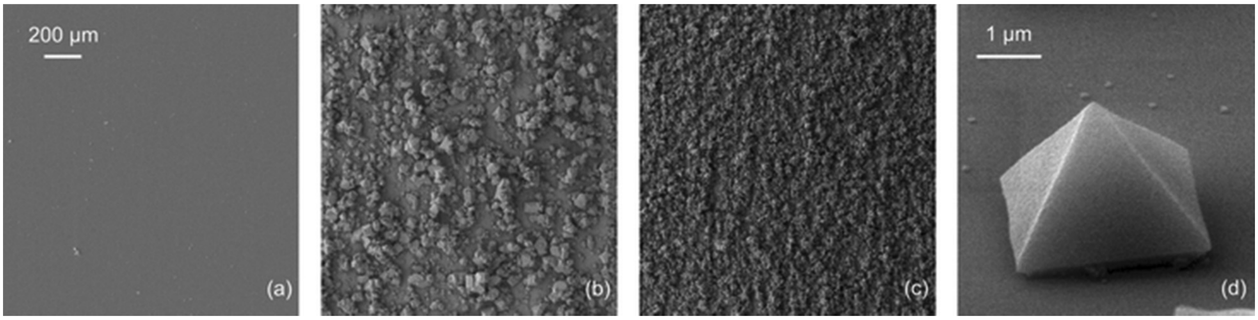

Fig. 50 SEM images of [$Cu_3(btc)_2$] coatings on (a) bare SiO_2, (b) Al_2O_3 (sapphire) and (c) ALD-Al_2O_3. (d) Single pyramidal crystal of [$Cu_3(btc)_2$] grown on *c*-plane sapphire. No crystal growth takes place on the SiO_2 surface whereas densely packed obviously polycrystalline agglomerated [$Cu_3(btc)_2$] microcrystals were formed on sapphire and ALD-Al_2O_3. Reproduced with permission from ref. 250. Copyright 2007, Royal Society of Chemistry.

regard, thermally stable robust alkylsiloxane-based SAMs can be used to functionalize the substrate. Zacher *et al.* modified SiO_2 substrates by reacting them with 10-undecenyltrichlorosilane and oxidizing the ending group to form carboxylic acids which have been further used to form thin films of HKUST-1 and [$Zn_2(BDC)_2(DABCO)$] (dabco = 1,4-diazabicyclo[2.2.2]) by directly immersing the SAM functionalized substrate into reactant solutions for solvothermal treatment (Fig. 50).[250]

3.1.5.2 (b) Crystallization from aged mother solution. In this method, the mother solution, after almost complete crystallization by the solvothermal method, is used for further thin film fabrication with the idea that the solution can form new crystallites. Hermes and co-workers have prepared a thin film of MOF-5 by this method on SAM-functionalized substrates.[251]

3.1.5.3 (c) Layer by layer (LBL) growth. In this method, as the first step, the substrate is functionalized with SAMs and the ending group of the SAMs is exposed to metal and ligand solutions alternatively. Such external control over the reaction process allows thickness-control of the thin films which is almost impossible for other processes mentioned here.

Shekhah *et al.* attempted to synthesize thin films of MOF for the first time using this LBL method.[252] As the first step, the Au substrate was reacted with 16-mercaptohexadecanoic acid (MHDA) to functionalize the substrate. Then, the SAM-functionalized substrate with carboxylic ending groups was allowed to react with a zinc(II) acetate solution, removed from the solution and washed. Afterwards, it was reacted with a solution of the BTC ligand. XPS, Infrared reflection Absorption Spectroscopy (IRRAS) and Near edge X-ray absorption fine structure spectroscopy (NEXAFS) indicate the absorption of BTC ligands on the surface. When functionalized SAM was reacted with BTC in the absence of Zn(II) ions, there was no absorption of BTC. AFM micrographs show that the thickness of the metal–organic layer is ∼1.6 nm. The thickness of the deposited layer increases with the number of cycles (Fig. 51).[252]

These authors also formed a thin film of HKUST-1.[253] In this case, they functionalized a gold substrate with 16-mercaptohexadecanoic acid (MHDA) and 11-mercaptoundecanol (MUD).

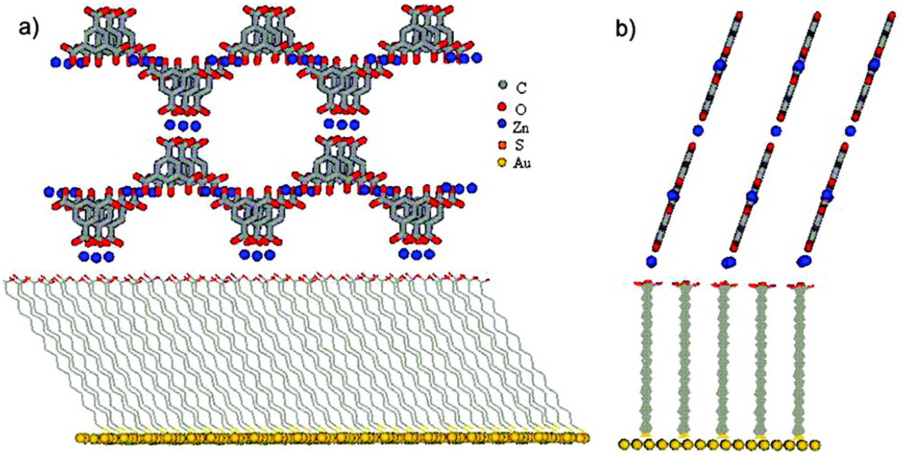

Fig. 51 (a) Proposed model (front view) for the layer-by-layer growth of the BTC ligand on the MHDA SAM obtained by repeated immersion cycles in solutions of $Zn(OAc)_2$ and BTC. (b) Side view showing that the layers are tilted with respect to the surface normal. For clarity, the model simplifies the assumed structural complexity of the carboxylic acid coordination modes (*i.e.*, mono and bidentate) and the likely presence of additional species such as water molecules at the Zn(II) centre of the MOF layers. Reproduced with permission from ref. 252. Copyright 2007, American Chemical Society.

The SAM-functionalized substrate with carboxylic groups was reacted sequentially with copper(II) acetate and H_3BTC and monitored by *in situ* surface plasmon resonance (SPR) spectroscopy. Both, the SPR and IR spectral analyses show that the deposition of the HKUST-1 MOF from the sub-monolayer to the multilayer proceeds with a sequential reaction of metal ions and ligands. XRPD data collected for the thin films obtained after 40 cycles of sequential deposition showed the formation of highly crystalline oriented thin films with crystal growth along the [100] direction. These authors also observed that the thin film formation was unsuccessful in the presence of copper(II) nitrate and suggested that the presence of a paddle wheel cluster in copper(II) acetate is a primary requirement for the formation of a HKUST-1 thin film by this process.

3.1.6 Substrate seed epitaxy. In this method, a solid substrate is used as the metal source to grow MOF thin films. Zhao and co-workers have deposited thin films of $[Al_2(OH)_2TCPP]$ on Ag-nano clusters. In the first step, they deposited Ag-NCs (NCs = nanoclusters) on silicon substrates by using a colloidal solution of octahedral Ag-NCs obtained by reducing $AgNO_3$ with 1,5-pentanediol under heating. Then, alumina was deposited on the Ag-NCs by simply heating at 60 °C the precursors trimethylaluminum and water at a deposition rate of 0.1 nm per cycle. Then, the alumina-coated substrate was reacted with H_4TCPP dissolved in DMF by heating at 140 °C in a microwave reactor. They have established that the alumina layer with a thickness of < 3 nm can be converted into MOF completely (Fig. 52).[254]

Falcaro and co-workers have utilized $Cu(OH)_2$ nanobelts as a sacrificial layer to form thin films of the Cu(BDC) MOF and of the 3D MOF $[Cu_2(BDC)_2(DABCO)]$. Initially, they synthesized $Cu(OH)_2$ nanotubes on the surface of Si wafers and observed that the nano-tubes were located perpendicular to the Si-wafer. Then, these nano-tubes were reacted with a saturated ethanolic solution of H_2BDC at room temperature. SEM micrographs show that triangular crystals of Cu(BDC) were grown orthogonally to the nano-tubes. Then, they used 2D nano-belts of $Cu(OH)_2$ and similarly reacted with BDC and form 2D layers of Cu-BDC MOF on the surface. Finally, they reacted $Cu(OH)_2$ nano-belts with BDC and DABCO at 60 °C to form thin films of the porous 3D MOF $[Cu_2(BDC)_2(DABCO)]$. The formation of thin films was proven by XRD and SEM analyses and the porosity of the thin film of 3D MOF was measured by N_2 adsorption analysis.[255]

3.2 Gas phase processing

In order to avoid solvent interference in the morphology and/or quality of thin films; recently, gas phase thin film fabrication has become a major research focus in conductive MOFs. Gas phase fabrication proceeds through three different steps: (a) vaporization of the metal ions and ligands, (b) transport of the vapours and (c) deposition.[256] To date, three different types of gas phase processing have been developed: (i) physical vapour deposition (PVD), (ii) chemical vapour deposition (CVD), and (iii) atomic layer deposition (ALD). These processes are very new in the field of thin film fabrication of MOFs and will require further studies for the development of optimal conditions.

3.2.1 Physical vapour deposition (PVD). It proceeds without any chemical reaction. The MOF is evaporated and then deposited on the substrate. The low thermal stability of MOFs is the main drawback of this method and thus it has only been used in very rare cases. Müller-Buschbaum *et al.* prepared thin layers of 100–500 nm thickness of a non-porous europium(II) imidazolate MOF by using a femtosecond laser beam under ultra-high-vacuum conditions on a sapphire substrate at room temperature.[257] The thin film was characterized by XRPD, XPS, SEM and EDAX studies. The thin film also shows turquoise emission like the parent MOF. Later Lotsch and co-workers deposited the thin film of ZIF-8 zinc-2-methylimidazolate using femtosecond pulsed-laser deposition on sapphire substrate. They demonstrated that thin film fabrication of ZIF-8 was successful in the presence of polyethylene glycol as a vehicle while pristine ZIF-8, without a transporting agent, was unsuccessful. After thin film fabrication, the excess polyethylene glycol can be removed with ethanol (Fig. 53).[258] In another report, Dinu and co-workers prepared thin films of ZIF-8 by matrix-assisted pulsed laser evaporation (MAPLE) using different laser fluences on a Si substrate. SEM analysis showed that the thickness of the MOF thin films was dependent on the laser fluence rate.[259]

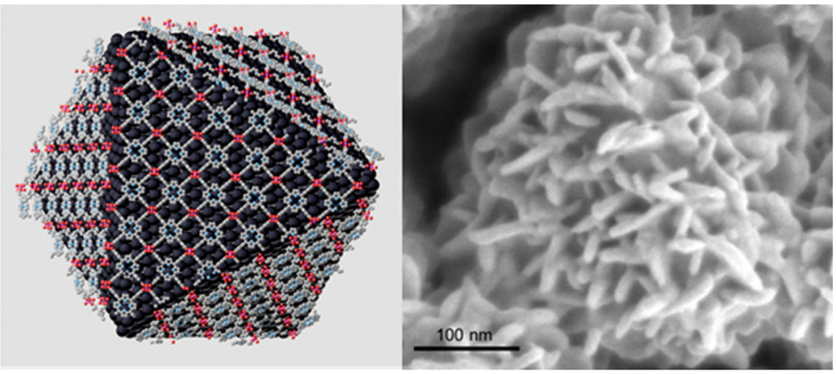

Fig. 52 Schematic diagram of synthesized MOF thin films on Ag-NC. Reproduced with permission from ref. 254. Copyright 2017, The American Chemical Society.

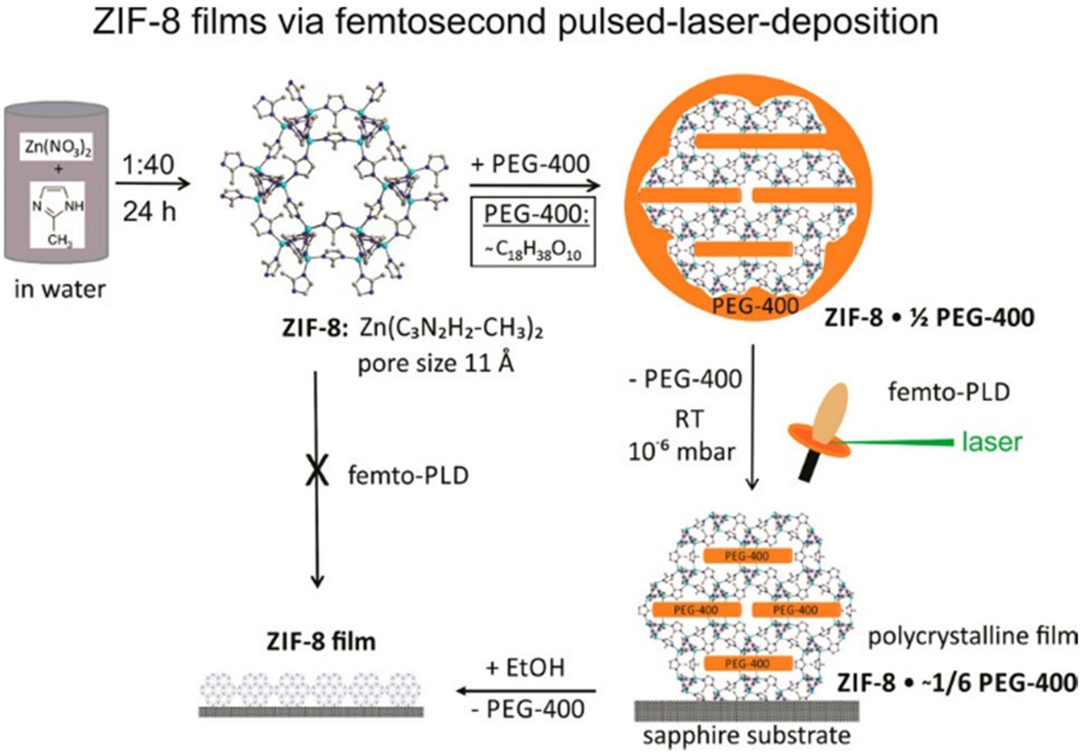

Fig. 53 Scheme of the steps used for the ZIF-8 film preparation *via* the femtosecond pulsed-laser-deposition technique. Reproduced with permission from ref. 258. Copyright 2017, The American Chemical Society.

3.2.2 Chemical vapour deposition (CVD). CVD consists of the chemical reaction between the precursor, in gas phase, with the substrate to form a uniform thin film with controlled thickness. It involves the deposition of a metallic precursor with the desired thickness by a gas–solid reaction between organic components and metallic species without hampering the physical properties of the obtained MOF thin film. Ameloot and co-workers have developed the first thin film of ZIF-8 by a two-step method: (a) Atomic layer deposition (ALD, see below) was employed to develop a ZnO thin film of thickness 3–15 nm and (b) a chemical reaction between 2-methylimidazole vapour with the ZnO thin film at 100 °C for 30 min. MOF formation was confirmed by XRPD, ATR-IR, EDAX, surface area measurement studies and so on. Interestingly, TEM analyses indicate the complete transformation of ZnO layers of thickness less than 10 nm into ZIF-8 films.[260] The same group has also prepared a thin film of highly porous MAF-8 [$Zn(eIm)_2$] (where eIm = 2-ethylimidazolate) in a similar 2-step approach. They have observed that the synthesized MAF-8 nanocrystals are larger due to formation of a porous structure, although complete conversion cannot be achieved in this case (Fig. 54).[261] They demonstrated that the thinner ZnO layers are converted at a faster rate. Several other groups have also used the same technique to develop thin films of MOFs.[262]

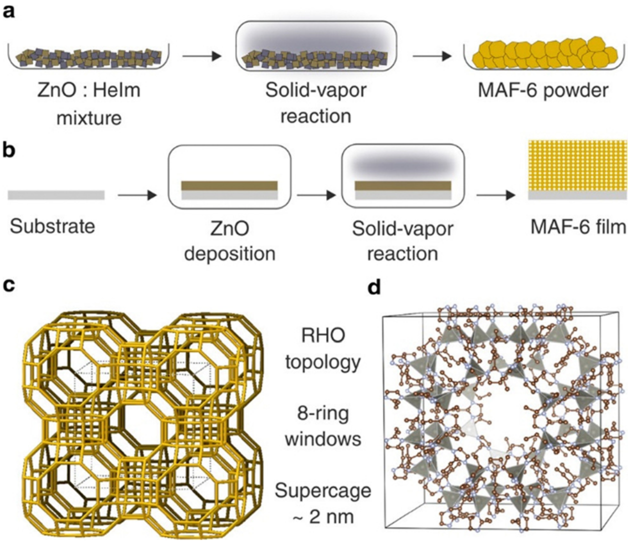

Fig. 54 Large-pore MAF-6 from the reaction between ZnO and 2-ethylimidazole vapour. (a) Schematic representation of the CVD powder synthesis. (b) Schematic representation of the film CVD. (c) MAF-6 RHO topology, showing the super-cages connected through octagonal prisms and (d) cubic unit cell of MAF-6. Reproduced with permission from ref. 261. Copyright 2020, The American Chemical Society.

3.2.3 Atomic layer deposition (ALD). This is an important technique in gas-phase thin film fabrication. It involves the chemical reaction between the precursors in the gas phase to form monolayers or sub-monolayers of thin films on the substrate. Salmi and co-workers attempted to fabricate a thin film of the MOF by reacting $Zn(OAc)_2$ with 1,4-benzenedicarboxylic acid in the vapour phase within the temperature range of 225–350 °C. These authors observed that the obtained thin film on the silicon substrate is amorphous, although it crystallized under a humid atmosphere (relative humidity 60%) at room temperature for 12 h. An XRPD study reveals that the obtained thin film is equivalent to MOF-5 while, in contrast, MOF-5 is unstable in the presence of moisture.[263] Later, Karppinen *et al.* fabricated thin films of paddlewheel MOF-2 copper(II) terephthalate by reacting Cu(thd)$_2$ (thd = 2,2,6,6-tetramethyl-3,5-heptanedione) with terephthalic acid on a Si-substrate in the presence of N$_2$ as the carrier gas. They have observed that the thin film formation is temperature-dependent.[264] These authors also prepared thin films of Ca-TP (TP = 1,4-benzenedicarboxylate) by the gas phase reaction between Ca(thd)$_2$ and terephthalic acid on Si substrates within a large temperature range of 190–420 °C. Additionally, they measured the mechanical properties of the thin films (Fig. 55).[265] Lausand and co-workers have deposited thin films of UiO-66 by reacting ZrCl$_4$ with 2-amino-1,4-benzenedicarboxylic acid (ABDC) at 265 °C in the presence of acetic acid.[266]

3.3 Other methods

There are several other methods reported for the synthesis of thin films of MOFs which include seed-assisted growth, sono-chemical, ultrasonic, microwave, electrospray, hot pressing, *etc.*

3.3.1 Seed assisted growth. Ranjan and co-workers have synthesized a thin film of multi-porous metal-organic frameworks on surface-modified porous alumina by this method. In the first step, they modified the alumina substrate with polyethyleneimine (PEI) attached to the surface. Then, the crystals obtained by the solvothermal method were crushed into sub-micrometre crystals which were then layered on the PEI-modified substrate. This seed-containing substrate was placed in the mother solution containing the precursors for secondary growth under solvothermal conditions.[267]

3.3.2 Sono-chemical method. Abuzalat group prepared thin films of four different MOFs: Cu-BTC, Cu-BDC, ZIF-8 and MOF-5 by the sono-chemical method (Fig. 56).[268]

In this case, initially, they oxidized the Cu and Zn metal substrates in the presence of NaOH to form Cu(OH)$_2$ nanotubes and Zn(OH)$_2$ nanostrands after 30 min and 60 min of oxidation, respectively. Then, these oxidized substrates are further reacted with the ligand in an ultrasonic bath with a frequency of 40 kHz and a power of 100 W for different time periods. The temperature of the reaction solution increases with the time of sonication. The synthesized MOF films were further characterized by XRPD, IR and SEM analyses which clearly demonstrate the formation of thin films of the MOFs.

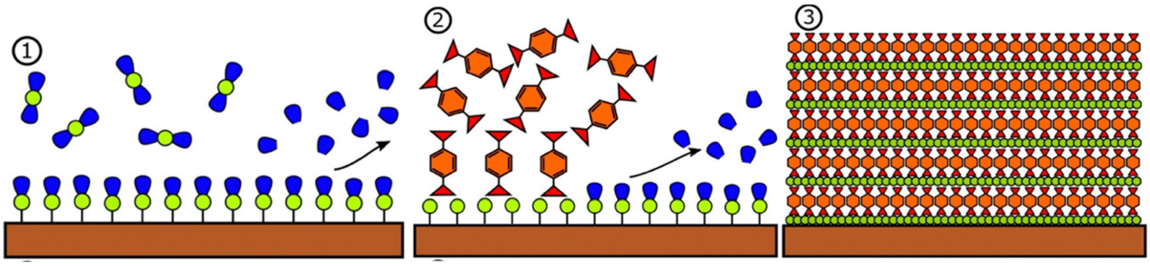

Fig. 55 Schematics of the ALD/MLD process for inorganic–organic coordination network thin films, where the process consists of inert-gas-separated pulses of (1) metal (here Ca(thd)$_2$) and (2) organic (here TPA) precursors to yield (3) a monolayer of the hybrid material (here Ca-TP). The film thickness is solely determined by the selected number of repetitions of steps (1) and (2). Reproduced with permission from ref. 265. Copyright 2016, The American Chemical Society.

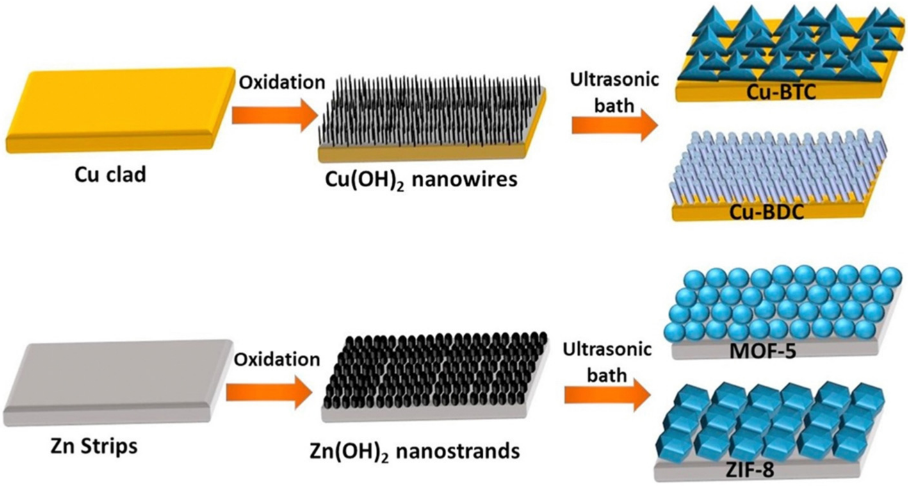

Fig. 56 Schematic illustration of the two-step method for the different thin MOF film fabrication. Reproduced with permission from ref. 268. Copyright 2018, Elsevier.

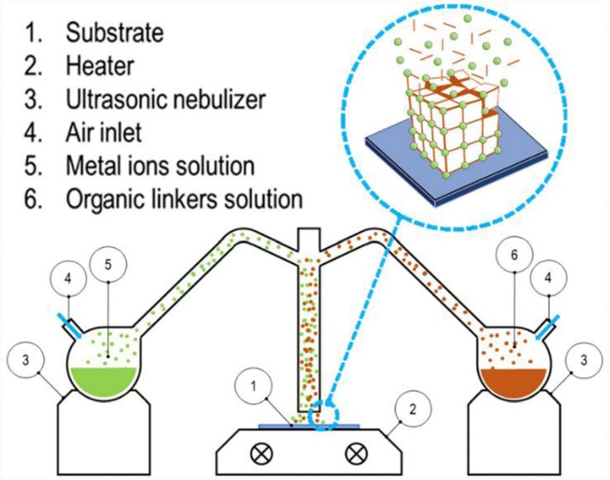

Fig. 57 Scheme of the ultrasonic spray deposition system. Reproduced with permission from ref. 269. Copyright 2019, Elsevier.

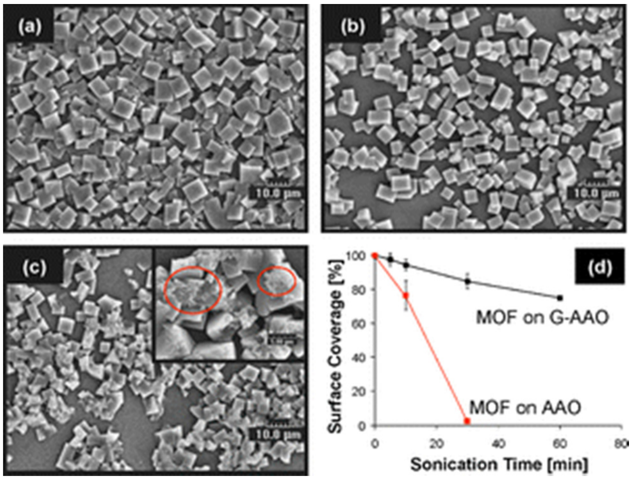

Fig. 58 Binding strength of MOF-5 crystals on G-AAO and AAO under sonication: SEM images of MOF-5 films on G-AAO treated under sonication for (a) 0 min (as-prepared), (b) 10 min and (c) 60 min and time-dependent surface coverages (d). The coverage data were obtained by examining the image contrast between MOF crystals and substrates using Adobe Photoshop. The data were normalized to the initial coverages. Reproduced with permission from ref. 270. Copyright 2008, The Royal Society of Chemistry.

3.3.3 Ultrasonic spray method. Thin films of the luminescent MOF $Tb_2(BDC)_3$ (H_2BDC = 1,4-benzenedicarboxylic acid) on glass substrates have been prepared by this method.[269] In this method, isolated DMF solutions of both the ligand and the metal ions are transported to a gas flux and then the mixture is deposited on a heated glass substrate (Fig. 57). The solvents are instantly evaporated to form the thin film of the MOF. The MOF formation was monitored by XRD, IR and SEM analyses.[269]

3.3.4 Microwave synthesis. Yoo and co-workers prepared thin films of MOF-5 by microwave-assisted synthesis on three different substrates: anodized aluminium oxide (AAO), amorphous carbon-coated-AAO (C-AAO) and graphite-coated-AAO (G-AAO) (Fig. 58). In this method, the substrates are mounted vertically on a DMF solution containing the precursors and are treated under microwave irradiation (500 W) for 5–30 seconds to grow MOF-5 crystals on the surface of the substrates. These authors observed that the thickness of the formed thin films on coated substrates is larger than on the bare substrate, which may be due to the fact that the conductive surfaces allow rapid growth under microwave heating. The formation of a thin film was further characterized by XRPD and SEM analyses. These authors also studied the binding strength of the MOF nanoparticles on the substrate by ultrasonication method. They found that the attachment of MOF-5 particles is stronger with the conductive substrates than with the bare ones.[270]

3.3.5 Electrospray method. Thin films and membranes of ZIF-8 were prepared by Fan and co-workers by this method.[271] In the first step, they prepared nano-crystals of ZIF-8 by reacting $Zn(NO_3)_2$ with 2-methylimidazole *via* a solvothermal method. Then, the obtained ZIF-8 microcrystals were suspended in methanol with 12% wt polyvinylpyrrolidone to form a low-viscosity uniform solution suitable for electrospray. This solution was loaded in a syringe and sprayed on a SiO_2 substrate under an applied voltage of 12 kV at a distance of 15 cm to synthesize uniform fibres. The formation of a ZIF-8 membrane was characterized using XRPD, SEM and gas adsorption analyses. The ZIF-8 membrane-decorated SiO_2 substrate was further used for the secondary growth of the ZIF-8 crystals by immersing the substrate within a solution of the precursors and treating solvothermally.[271] Later, Melgar and co-workers synthesized thin films of ZIF-7 by this method. Here, they prepared two different solutions of metal ions ($Zn(NO_3)_2$) and ligands (sodium formate and benzimidazole) in DMF, mixed them, and used the resulting solution for electrospray in a metal capillary using a syringe at a flow rate of 0.5 to 2 mL h^{-1} on alumina substrates under an applied voltage of 5–12 kV. The thickness of the membranes can be controlled by adjusting the amount of precursor solution.[272]

3.3.6 Hot pressing method. In this method, the precursors, metal ions and ligands, are placed on the substrate and then pressed while heating to favour the direct coordination between the metal ions and ligands to form the coordination network. Under these conditions, the attachment between the MOF and the substrate becomes strong for further applications. Chen and co-workers have spread a mixture of $Zn(OAc)_2$, 2-methylimidazole and poly ethylene glycol on a carbon cloth within an aluminium foil. The resulting fully covered substrate was heated at 200 °C for 10 minutes. SEM micrographs show that the size of ZIF-8 microcrystals is ∼100 nm. These authors have also prepared a number of different carboxylate and imidazole-based MOFs like Cd-MOF, Co-MOF, ZIF-67, ZIF-9, MOF-5, and Ni-ZIF-8 on carbon cloths using this hot and pressing method (Fig. 59).[273]

4. Applications of extrinsically conducting MOFs

Conductive MOFs, at the conjunction of organic semiconductors and inorganic metallic conductors, have aroused much attention as multifunctional materials due to their large surface

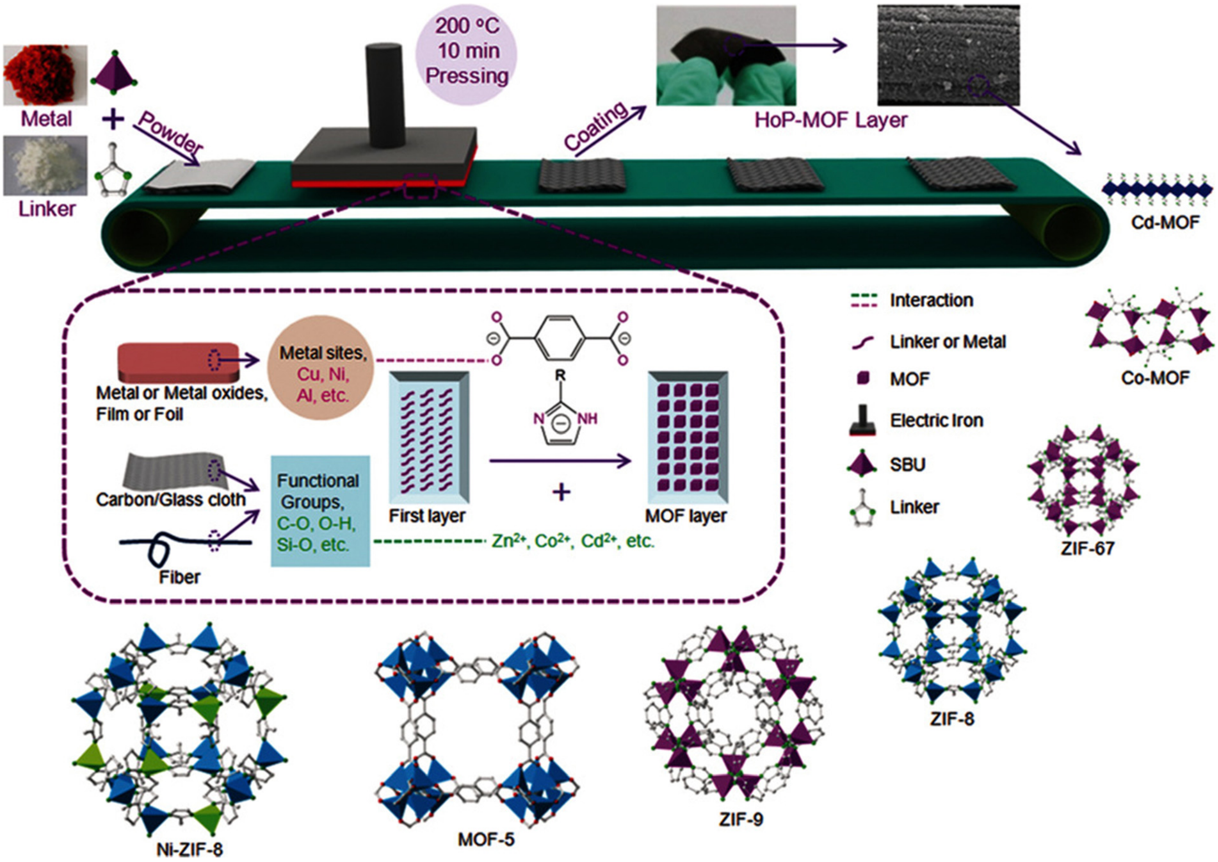

Fig. 59 Schematic presentation of the hot-pressing (HoP) method for MOF coating. SBU = secondary building unit. Reproduced with permission from ref. 273. Copyright 2016, The Royal Society of Chemistry.

area, tuneable structure and moderate-to-high charge transport properties. To date, conductive MOFs are used for different applications such as sensing, electrocatalysis, photoconductivity, charge storage, *etc.* Here, we briefly summarize the applications of ec-MOFs in these relevant fields.

4.1 Electrocatalysis

Large surface area and high porosity with an easily accessible large number of transition metal sites with labile exchangeable coordination sites make these conductive MOFs high potential electrocatalysts. Several review articles have covered this topic.[30,31,68,274,275] Herein, we only focus on the electrocatalytic applications of guest@MOFs.

4.1.1 Hydrogen evolution reaction (HER). The rapid growth of human civilization and the danger of using fossil fuel stocks are urgently demanding alternative and sustainable sources of energy. Molecular hydrogen, with a high energy density per mass unit, has become one of the major energy vectors in the near future.[276] Although there are several methods of producing molecular hydrogen, electrocatalytic hydrogen evolution from water splitting is considered as one of the most efficient and clean methods.[277,278] Pt-group metals are considered as the most efficient catalysts but the scarcity of these precious metals limits their practical applications.[279] Different homo- and heterogeneous catalysts have been developed for the electrocatalytic HER reaction.[280] MOFs, with high surface area, uniform pore size distribution and easily accessible numerous active metal sites, have shown promising electrocatalytic HER activity, and this topic has been reviewed by several research groups. Herein, we will discuss only the special cases in which guest-encapsulated MOFs are used for electrocatalytic HER activity.

Dai and co-workers studied the electrochemical HER activity of a MoS_x encapsulated UiO-66-NH_2 MOF $[Zr_6(O)_4(OH)_4(ATP)_6]$ (ATP = 2-aminoterephthalate).[281] *In situ* reaction between the MOF ingredients with $(NH_4)_2MoS_4$ leads to the formation of the MoS_x@UiO-66 structure. TEM micrographs clearly demonstrate the formation of NPs of MoS_x (with an average size of 0.64 nm) within the UiO-66 nanocrystals of size ~33 nm. Porosity measurements using N_2 adsorption reveal that such encapsulation reduces both the void space and pore diameter which clearly demonstrates the incorporation of MoS_x NPs within the void space of the MOF. An IR study shows the presence of $p\cdots\pi$ interaction between the sulphur atoms of the MoS_x NPs with the benzene ring of the ligands in the MOF. MoS_x@UiO-66 shows excellent HER activity with an onset potential of ~125 mV and a cathodic current of 10 mA cm^{-2} at an overpotential of 200 mV with excellent durability (Fig. 60). Theoretical mechanistic analysis reveals that the MoS_x NPs act as an electron pool for the reduction of protons on the electrode surface.[281]

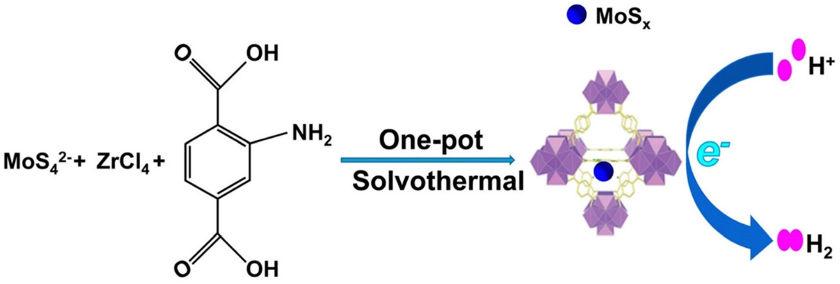

Fig. 60 Schematic presentation on the encapsulation of MoS$_x$ within the void space of Zr-MOF. Reproduced with permission from ref. 281. Copyright 2016, The American Chemical Society.

In another article, Peng and co-workers have shown the electrochemical HER activity of noble metal nanoparticles (Ru, Ir and Pd) encapsulated MOFs.[282] The spontaneous reduction reaction between Ru^{3+} and the Ni atoms of the Ni-foam produces Ru-NPs and Ni^{2+}, and these Ni^{2+} ions react with terephthalates to form the MOF architecture. Both SEM and HRTEM micrographs directly demonstrate the formation of Ru-NPs@Ni-MOF, and the ICP study shows that the content or Ru is 2.3% wt; XPS and XAFS analyses identify the presence of interactions between the metal atoms of the NPs with the oxygen atoms of the terephthalate ligands present in the Ni-MOF. Ru-NPs@Ni-MOF shows excellent HER activity with an overpotential of 22 mV to reach 10 mA cm^{-2} current density in 1 M KOH with very high durability over 24 h. Theoretical calculations reveal that the optimized adsorption-free energy of water and hydrogen due to interfacial bond-induced electron redistribution is responsible for such excellent HER activity.[282]

4.1.2 Oxygen evolution reaction (OER). Water oxidation or OER is a key step in different energy and storage-related technologies like water splitting into hydrogen and oxygen, metal–air batteries *etc.*[283] OER is a four-electron and kinetically sluggish process since it requires a high overpotential to overcome it.[284] To date, different noble metals (mainly Pt-group metals) and their oxides (RuO_2 and IrO_2) are used to overcome high overpotential but their high cost, scarcity and easy poisoning restrict their broad applications.[285] Several types of MOFs have been designed for this purpose and a number of review articles have been published on this topic, although there are only a few scattered examples of guest-encapsulated MOFs operating as OER catalysts.

Gao and co-workers reported the OER activity of a post-metalated 3D MOF [Th-BPYDC] (BPYDC = [2,2′-bipyridine]-5,5′-dicarboxylate) with metal(II) chlorides. The free bipyridyl groups can react and bind with different metal chlorides ($CoCl_2$, $NiCl_2$ and $CuCl_2$) to encapsulate the metal salts within its architecture. Simulated structural analysis shows that the Co/Ni/Cu metal centres are in 4-coordinated square planar conformation with MN_2Cl_2 coordination sphere (Fig. 61(a) and (b)). XANES (X-ray absorption near edge structure) spectroscopy reveals the +2 oxidation state of the guest metal ions within the exceptionally stable Th(VI)-BPYDC MOF. The $CoCl_2$@Th-BPYDC MOF structure shows excellent OER activity with an overpotential of 388 mV at 10 mA cm^{-2} current density in 0.1 M $HClO_4$ electrolyte, which is much lower than $NiCl_2$@Th-BPYDC (482 mV) and $CuCl_2$@Th-BPYDC (646 mV) and comparable to IrO_2 (Fig. 61(c) and (d)). This catalyst also shows excellent stability for this electrochemical reaction. Theoretical analysis reveals that during acidic HER, the coordinated chloride atoms rotate and facilitate the binding and activation of the substrate.[286]

In another work, Zhang and co-workers embedded CoFeO$_x$ nanoparticles within the 2D layers of a Co–imidazolate framework using an *in situ* method.[287] The formation of CoFeO$_x$ nanoparticles within the structure of the Co–Im framework was demonstrated using XRPD, FE-SEM and TEM analyses. These metal-oxide NP-embedded 2D MOFs can be easily exfoliated by ultrasonication while the parent MOF is inert towards ultrasonication. ICP-OES study shows that the amount of Fe within the MOF is 4.14%. An XRPD study reveals that the inter-layer gap between the 2D layers increases during exfoliation and as a result, the porosity also increases from 11.2 m^2 g^{-1} to 98.6 m^2 g^{-1}. A TEM study shows that the thickness of the exfoliated 2D layers is about 3 nm. Such metal oxide-embedded 2D MOF has shown excellent OER activity with a very low overpotential of 232 mV at 10 mA cm^{-2} current density with good stability.[287]

Luo *et al.* have shown a significant enhancement of the electrocatalytic OER activity of Ni-HHTP by encapsulation of ferrocene methylamine (Fc-NH_2).[288] Given the pore diameter of the Ni-HHTP framework, they attempted to encapsulate different types of ferrocene derivatives like Fc, Fc-COOH, Fc-$(COOH)_2$ and Fc-NH_2 but successful encapsulation was only achieved for Fc-NH_2, through protonation, based on electrostatic host–guest interactions. Several samples were prepared by varying the amount of Fc-NH_2 concentration and the reaction time. The encapsulation was characterized using XRPD, HRTEM, XPS and EDXS analyses. The electrocatalytic OER activity reveals that the Fc-NH_3^+@Ni-HHTP (Fc content ∼0.011 mmol mL^{-1}) shows better electrocatalytic OER activity with an overpotential of 482 mV at 10 mA cm^{-2}.[288]

4.1.3 Oxygen reduction reaction (ORR). This reaction, in which oxygen is reduced *via* either $2e^-$ or $4e^-$ pathways, is one of the key processes in fuel cells and metal–air batteries.[289] The electrocatalytic ORR suffers from sluggish kinetics and also pH dependence. The ORR proceeds through a four proton-four electron transfer to transform O_2 into water as well as through a

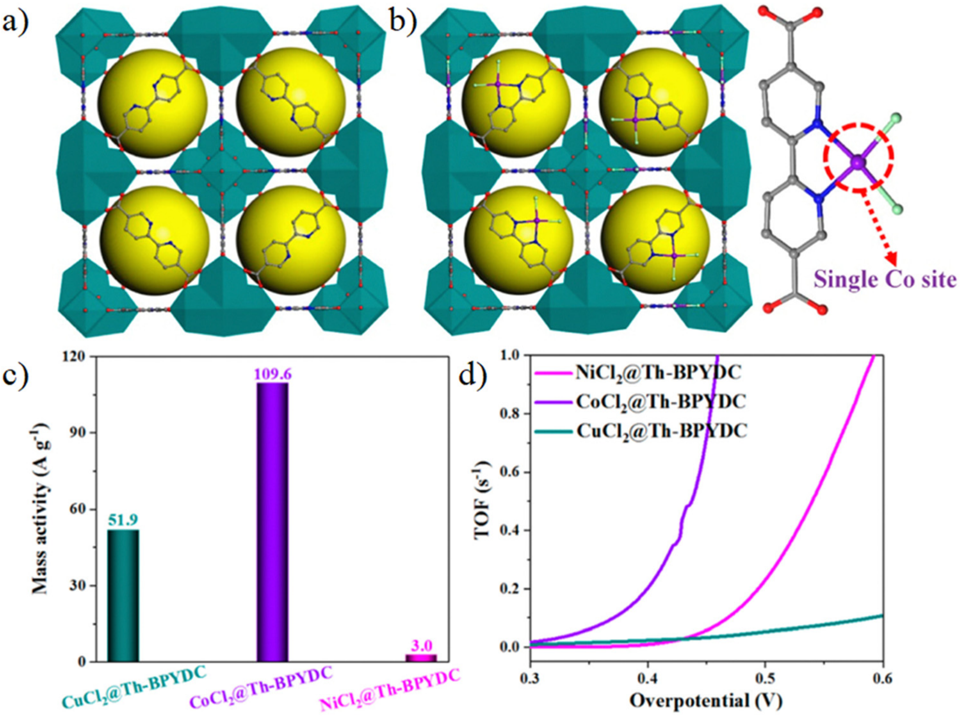

Fig. 61 Crystal structure of (a) Th-BPYDC and (b) $CoCl_2$@Th-BPYDC. (c) Mass activities normalized to the metal mass of catalysts (d) TOF plot. Reproduced with permission from ref. 286. Copyright 2016, The American Chemical Society.

less-efficient two proton-two electron pathway to produce H_2O_2.[290] Significant attention has been given to design MOF-based ORR catalysts to replace the benchmark Pt.

Miao and co-workers have reported the ORR activity of Co–salen encapsulated MOF MIL-100(Cr).[291] The encapsulation of the cobalt–salen complex was done by a multistep method in which the pre-synthesized MOF particles are dispersed in a solution of cobalt acetate for immobilization of metal ions within the MOF and then reacted with the H_2 salen ligand. The encapsulation was monitored by XRPD, IR and UV analyses. N_2 adsorption studies reveal that the overall porosity of the parent MOF decreases from 1293 $m^2\ g^{-1}$ to 820 $m^2\ g^{-1}$ due to encapsulation. This cobalt–salen@MIL-100(Cr) has shown electrocatalytic ORR activity at a potential of −0.21 V at a pH of 6.84. It also shows excellent durability for the four-electron reduction from oxygen to water as evidenced by chronocoulometry.[291]

Patra *et al.* immobilized both laccase and ABTS (2,2′-azino-bis(3-ethylbenzothiazoline-6-sulfonic acid)) within the MIL-100(Fe). This material also shows electrocatalytic ORR activity with high current density and excellent stability over a long period.[292]

Cho *et al.* modified Cu-BTC MOF with CuS-NPs both on the surface and in the void space. Several samples were prepared by varying the amount of CuS. The presence of CuS within and on the Cu-BTC MOF particles enhances its electrical conductivity over 10^9 times. The CuS@Cu-BTC MOF (28% wt) shows significant electrocatalytic ORR activity with an onset potential of 0.91 V and a kinetic current density of 11.3 mA cm^{-2} at 0.55 V *vs.* RHE *via* a four electron reduction pathway.[293] In another article, Si *et al.* encapsulated Pt-NPs within the porous conducting $[Ni_3(HITP)_2]$ framework and the obtained Pt@$[Ni_3(HITP)_2]$ shows excellent ORR activity.[294]

4.1.4 CO_2 reduction reaction (CO_2RR). Utilization of aerial CO_2 as a feedstock to produce value-added chemicals like methane, methanol, ethane, *etc.* is currently a very attractive way for energy storage and conversion.[295,296] The reduced product may vary from carbon monoxide, formic acid, methane, methanol, ethanol, oxalate, ethylene,… depending on the reaction conditions.[297] The CO_2RR is thermodynamically and kinetically challenging due to the high stability of carbon dioxide. Therefore, multiple proton-coupled electron transfer is an attractive approach.[298] On the other hand, proton reduction is also a competitive reaction in water. Several MOFs have been used for the electrochemical reduction of CO_2 but the extrinsically conducting MOFs are used in very rare cases.

Kung and co-workers have studied the electrochemical CO_2 reduction capacity of CuNPs-loaded MOF NU-1000.[299] Thin films of the MOF were prepared by soaking FTO-coated glass substrates within the reagents *via* a solvothermal method (Fig. 62). The obtained thin films were further soaked in a solution of Cu(dmap) (dmap = dimethylamino-2-propoxide) to incorporate them within the void space of the MOF and were then reduced with hydrogen gas. Such encapsulation changes the colour of the films to green and reduces the porosity substantially. ICP-OES indicates that 4.0 Cu atoms are deposited per Zr_6 unit of the MOF and they are located between each Zr_6 cluster of the framework. The CuNP-loaded NU-1000 MOF

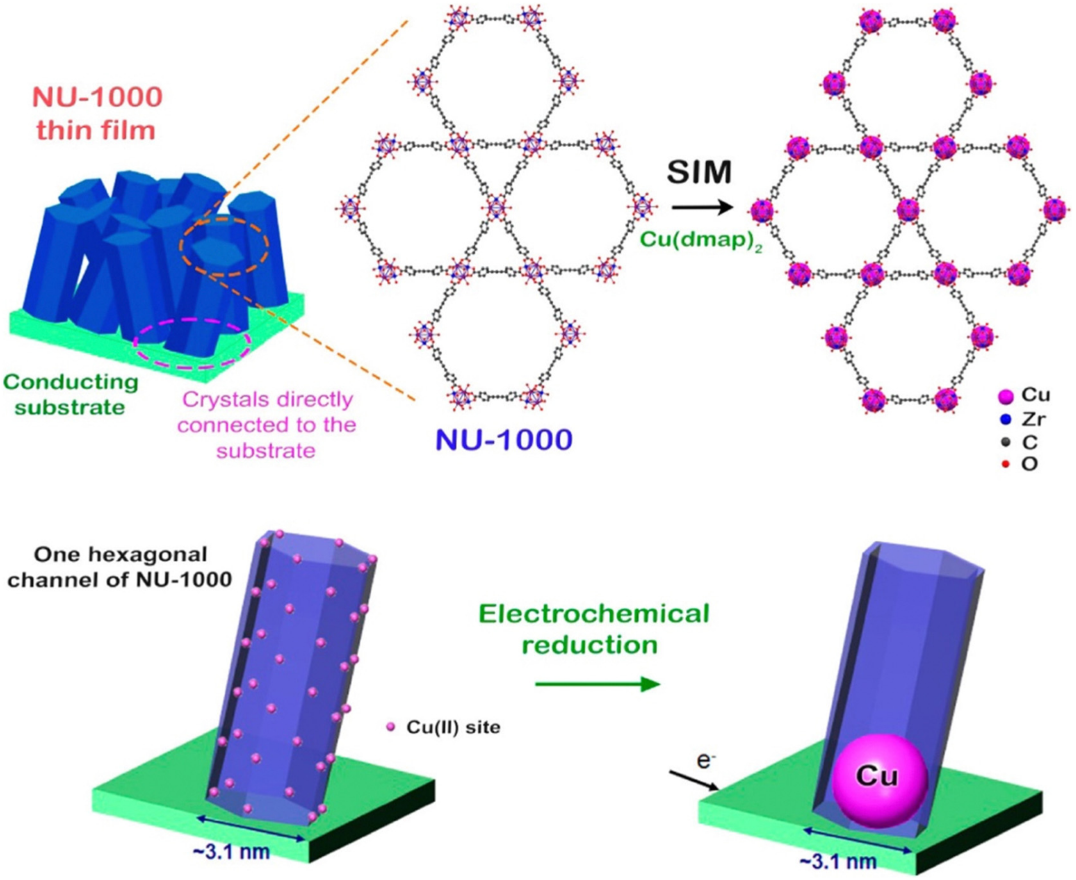

Fig. 62 Schematic representation of the solvothermal deposition in MOF (SIM) to install single-site Cu(II) into the NU-1000 thin film and the electrochemical reduction of Cu(II) to generate metallic Cu nanoparticles. For simplicity, hydrogen atoms are not shown in the structure. Reproduced with permission from ref. 299. Copyright 2017, The American Chemical Society.

shows electrochemical CO_2 reduction to CO with an onset potential of −0.82 V with a faradaic efficiency (FE) of ~31%.[299]

Yan *et al.* reported the enhancement of electrochemical CO_2 reduction to ethylene by encapsulation of metal-porphyrins (M-TCPP where M = Fe, Co and Ni; and TCPP = tetrakis(4-carboxyphenyl)porphyrin) within HKUST-1.[300] The successful one-step encapsulation was characterized by XRPD, IR, SEM, TEM, XPS and elemental analyses. The electrochemical CO_2 reduction by HKUST-1 results in the production of ethylene with FE of 16.85% at a potential of −1.27 V while for the Fe-TCPP@HKUST-1 the FE is 33.42% at a potential of −1.17 V. The other two materials Ni-TCPP@HKUST-1 and Co-TCPP@HKUST-1 show almost similar activity as the Fe-TCPP-encapsulated MOF. These authors proposed that the encapsulated M-TCPP moieties supply the intermediate CO towards the Cu-centres of HKUST-1 to promote C–C coupling for ethylene production.[300]

In another article, Xin and co-workers have shown the electrocatalytic CO_2 reduction by a polypyrrole-loaded MOF-545-Co. PPy@MOF-545-Co shows a large current density of 32 mA cm^{-2} at −1.1 V, a much higher current density than that of PPy@MOF-545 and MOF-545-Co. The faradaic efficiency for CO production is 98% at −0.8 V. These authors propose that the PPy moieties within the MOF facilitate the electron transfer during CO_2 reduction.[301]

4.1.5 Nitrogen reduction reaction (NRR). Electrochemical nitrogen reduction is an attractive approach for the activation of the highly inert N_2 molecule.[302] Some metal catalysts have shown promising results thanks to their strong binding capacity and high electrical conductivity. He and co-workers have shown the electrocatalytic nitrogen reduction to ammonia by an Au-NP-encapsulated MOF.[303] The thiol-functionalized dicarboxylic ligand (3,3′-bis(mercapto)biphenyl-*p*,*p*′-dicarboxylic acid) was used to construct a 3D MOF with Zn^{2+} ions. Structural analysis shows that caged-shaped disulphide trimers are generated *in situ* in the resulting MOF. The highly stable MOF is used as a matrix to form Au NPs within the void space by chemical reduction of $KAuCl_4$ with $NaBH_4$. The synthesized AuNPs@MOF was further coated with a hydrophobic layer using organo-silicone and then used for electrocatalytic NRR. The AuNPs@MOF shows an outstanding electrocatalytic NRR performance under ambient conditions, with a highest NH_3 yield of 49.5 μg h^{-1} mg$_{cat}$$^{-1}$ and a faradaic efficiency of 60.9% in water.[303]

4.1.6 Substrate conversion. Electrochemical oxidation, reduction, conversion and decomposition of different substrates has become a major topic of research. Behara and co-workers have shown the electrochemical decomposition of PET to terephthalic acid using a 1D MOF.[304] Deng and co-workers have studied the electrochemical oxidation of hydrazine by a series of Pt nano-particle encapsulated MOFs (UiO-66/67/68) synthesized by *in situ* reduction of H_2PtCl_6.[305] Conductivity measurement studies reveal that the encapsulation of Pt-NPs enhances the electrical conductivity of MOFs and that Pt@UiO-66 has the highest conductivity of the three MOFs. The electrocatalytic oxidation of hydrazine was studied by cyclic voltammetry in 0.1 M phosphate buffered saline solution (pH = 7.00) using Pt@UiO-66 as the catalyst. Pt-NP encapsulated MOFs show a significant increase in electrocatalytic current compared to the parent MOFs. The synergy between the Pt-NPs and MOFs provides a fast electron transfer and also a large surface area with many active sites for efficient electrochemical oxidation. The oxidation current for Pt@UiO-66 is 128.9 μA, which is much higher than that for Pt@UiO-67 and Pt@UiO-68. These authors have also studied the effect of the amount of Pt-NPs loaded within the MOFs by varying the amount of H_2PtCl_6 used in the reaction media and observed that 0.6 mL of H_2PtCl_6 is the best one to prepare the most efficient Pt@UiO-66 MOF at pH = 7.0. Mechanistic studies revealed that hydrazine undergoes four-electron oxidation in the presence of Pt@UiO-66 whereas with Pt@UiO-67 and Pt@UiO-68 it undergoes two- and three-electron oxidations:[305]

$$N_2H_4 + 4H_2O \xrightarrow{\text{Pt@UiO-66}} N_2 + 4H_3O^+ + 4e^-$$

$$N_2H_4 + 2.5H_2O \xrightarrow{\text{Pt@UiO-67}} 0.5N^{3-} + 0.5NH_3 + 2.5H_2O + 2e^-$$

Cyclic voltammetry was used by Wang and co-workers for the electrochemical oxidation of acetaminophen (AP) by a Au-NP-loaded ZIF-L.[306] Au-NP@ZIF-L/GCE shows an increase in oxidation current compared to bare GCE and ZIF-L/GCE. The synergy between high electrical conductivity and porosity of ZIF is the main driving force for such oxidation. AuNP@ZIF provides a favourable environment for transferring species in solution and is beneficial for accelerating electron transfer between the electrode and AP. The oxidation peak current also increases with increasing the scan rate, suggesting a diffusion-controlled process. The oxidation peak shifts to negative values with increasing pH which clearly indicates that protons take part in the electrochemical oxidation of AP.[306]

4.2 Electronic sensing

Electronic sensors are analytical devices that show the presence of a particular analyte or their existence above a certain concentration by transducing different electronic parameters like resistivity, capacitance, *etc.*[307] Several important parameters like technical simplicity, easy fabrication, cost-effectiveness, sensitivity and selectivity make these electronic sensors highly attractive in analytical research.[308] The chemical tuneability of MOFs provides an enormous opportunity to tune the electrochemical performance and recognition behaviour of the fabricated devices. The inherent void space can also accommodate different analytes, and the large surface area of MOFs facilitates their interaction with the metal centres or with the organic building blocks. Again, the easy fabrication of MOF thin films in electronic devices also boosts their application in sensing devices.[309] To date, different methods like chemiresistive, chemicapacitive, impedance, Kelvin probe, FET, *etc.* have been adopted for this purpose.[310–312] A number of MOFs and MOF composites with other conducting substances have been developed for sensing various types of analytes: gases, ions, toxic molecules and biomolecules. Several reviews have already been published on this topic which include either pristine MOF or MOF composite as the sensing electronic platform but there is no review that highlights the sensing properties of extrinsically conducting MOFs. Here, we discuss some sensing behaviour of extrinsically conducting MOFs by classifying analytes into different categories.

4.2.1 Gas molecules. Kung and co-workers have shown the sensing capacity of molecular hydrogen (H_2) of a SnO_2-loaded NU-1000 MOF followed by the electrochemical sensing behaviour of SnO_2-based nanobelts/nanowires.[75] The nanoclusters of SnO_2 within NU-1000 show significant enhancement of electrical conductivity in the presence of H_2 (5% in N_2) with repeatability more than 1000 times. The response times are 400 s and 5–10 s for 5% H_2 and air, respectively. This device shows more rapid sensing of hydrogen in air rather than other SnO_2-based sensor devices at room temperature. The long response time to hydrogen (5% in N_2) may be attributed to the slow dissociation of H_2 due to the lack of dissociation catalysts. In the presence of oxygen, Sn ions undergo oxidation to form tin ions which act as the sensing platform.[75]

Shiozawa *et al.* have shown the chemiresistive sensing of Ar by TCNQ-doped Co-MOF-74. Co-MOF is insulating in nature and the encapsulation of TCNQ increases its conductivity. This porous TCNQ@MOF-74 shows Ar absorption behaviour and a decrease of the resistance of the framework with increasing the amount of Ar.[313] Kim and co-workers reported the highly selective sensing of NO_2 by Pt@$Cu_3(HHTP)_2$ MOF thin-film.[314] Also Koo *et al.* developed Pt@$Cu_3(HHTP)_2$ and Pd@$Cu_3(HHTP)_2$ for NO_2 sensing.[315]

Zheng and co-workers developed thin films of $[Cu_3(HHTP)_2]$ by the vapour phase layer-by-layer method. The obtained thin films were used for the detection of H_2 and NH_3.[316] Very recently, Lim *et al.* have developed nanoparticles of HKUST-1 on Laser-Induced Graphene (LIG) sheets. The obtained HKUST-1@LIG has shown chemresistive sensing towards NO_2.[317]

4.2.2 Inorganic molecule sensing. Dong *et al.* have reported hydrogen peroxide sensing by AgNPs doped ZIF-67 MOF in an alkaline medium with electroreduction of H_2O_2. Upon the addition of 3 mM H_2O_2, the current of ZIF-67/GCE increases which clearly indicates the electroreduction of H_2O_2. The presence of AgNPs within ZIF-67 also increases the electrical conductivity and decreases the reduction potential. Similarly, the reduction peak current increases and reduction potential decreases with increasing the concentration of NaOH. The response time is 3 s and the detection limit is 1.5 μM. The authors have further used these devices for real sample analysis.[106]

Vilian *et al.* have shown electrochemical nitrite ion detection by PdNPs@MIL-101(Cr) due to the electro-oxidation of nitrite ions. In the presence of nitrite ions, the CV of the electrochemical device shows an irreversible anodic peak at 0.904 V with a peak current of 120 nA which indicates the oxidation of nitrite. Under optimal conditions, the oxidation current increases linearly with increasing nitrite concentration from 5 to 150 nM and the detection limit is 1.3 nM. A pH-dependent electrocatalytic study also reveals that pH = 7 is the most suitable condition for electro-oxidation. The peak current also increases with the scan rate in the range of 0.01–0.1 V s^{-1} and the anodic peak potential shifts to more positive values. These authors have further used PdNPs@MIL-101(Cr) for nitrite ion detection in sausage and pickle samples.[102]

4.2.3 Bio-sensing. Meng and co-workers reported the electrochemical glucose detection using ZIF-67 and AgNP@ZIF-67.[105] The CV shows that ZIF-67/GCE has two pairs of redox peaks in the absence of glucose. The first pair of redox peaks appear at 0.2 V due to the reversible redox process between Co^{II} and Co^{III} and another redox peak at 0.42 V is due to the Co^{III}/Co^{IV} process. After addition of 2000 μm glucose, the anodic peak current increases, indicating that ZIF-67 has electrocatalytic oxidation behaviour of glucose and this electrocatalytic oxidation is carried out by the couple $[Co^{IV}(mim)_2(OH)_2]/[Co^{III}(mim)_2(OH)]$ rather than $[Co^{III}(mim)_2(OH)]/[Co^{II}(mim)_2]$. Encapsulation of AgNPs within the void space of ZIF-67 increases the electrical conductivity as well as the oxidation peak current. This electro-oxidation is also dependent on the OH^- ions present in ZIF-67. Thus, the current density increases with increasing the concentration of NaOH from 0.001 to 0.1 M. The response time also decreases with increasing the amount of guest AgNPs. This device also shows excellent selectivity for glucose over other biomolecules like uric acid, ascorbic acid and acetaminophen.[105]

Bhardwaj *et al.* have studied the conductometric detection of prostate cancer antigen by TCNQ-doped HKUST-1 MOF. The slow diffusion of TCNQ into the pores of HKUST-1 MOF increases its electrical conductivity from 10^{-14} S cm^{-1} to 7.3×10^{-4} S cm^{-1}. The physical absorption of antibodies on the surface of TCNQ@HKUST-1 leads to the decrease of conductance of the thin film by a factor of almost three (2.7×10^{-5} S cm^{-1}). The antibody-decorated TCNQ-doped HKUSTE-1 thin film was used to detect antigens in the concentration range of 0.01–150 ng mL^{-1}. With increasing concentration of PSA (prostate cancer antigen), the electrical conductivity of the device decreases which is attributed to the antibody–antigen interaction.[318] Selvam *et al.* developed a composite material by mixing SeS_2@Co-MOF with Au@PANI. The material was used for electroanalytical sensing of patulin mycotoxin.[319] In another article, Ma *et al.* reported the electrochemical glucose (Glu) sensing by Cu@Co-MOF with rapid current response, low interferences and high stability and repeatability to Glu detection.[320]

4.3 Charge storage

Electrochemical energy storage has gained much interest in the field of conducting porous MOFs for their high charge storage densities, fast charging processes, large number of cycles and large surface areas.[321,322]

4.3.1 Supercapacitors. Electrochemical supercapacitors, mainly electrical double-layer capacitors and pseudo-capacitors, are considered as the new generation for clean energy storage devices with several advanced features like fast charging/discharging, high power density and long cycle life.[28] In electric double-layer capacitors (EDLC), the basic principle relies on the storage/release of energy by adsorbing/desorbing electrolyte ions in the double layers at the electrode–electrolyte interface to obtain a high capacitance value. In pseudo-capacitors, the redox behaviour of the electrolyte ions at the surface of the electrode promotes charge storage. Porous MOFs with abundant metal ions as easily accessible active sites can act as pseudo-capacitors while the inherent void space allows the penetration of electrolytes for the formation of electric double layers.[28,29] The low electrical conductivity of most MOFs is the main drawback of their use in supercapacitors. Insertion of guest species within the void space, *i.e.*, extrinsically conducting MOF has become a major focus for this purpose recently.

Kung and co-workers have shown the pseudo-capacitance behaviour of NiCB@NU-1000 MOF (CB = bis(dicarbollide)). Redox behaviour of thin films of NU-1000, NiCB@NU-1000, manganese oxide deposited by atomic layer deposition in MOF (AIM) on NU-1000 (Mn-AIM@NU-1000) and Mn-AIM-NiCB@NU-1000 was explored using cyclic voltammetry. The initial three samples show negligible charge storage behaviour while the specific conductance value of Mn-AIM-NiCB@NU-1000 is 270 F $g_{MnO_2}{}^{-1}$.[169]

Wang and co-workers have encapsulated polypyrrole (Ppy) within the pores of the Keggin polyoxometalate $PMo_{12}O_{40}{}^{3-}$ (PMo_{12})-based MOFs, NENU-5. The composite of NENU-5 with Ppy shows a high specific capacitance (5147 mF cm^{-2}) larger than pure NENU-5 MOF. These authors prepared a symmetric supercapacitor with PPy@NENU-5 that shows an aerial capacitance of 1879 mF cm^{-2}.[323] Liu and co-workers have used the same NENU-5 to prepare a composite with PPy to study the charge storage property.[324] In another report, Wei and co-workers have developed another composite of $PMo_{12}V_2$-encapsulated MOF HKUST-1 with reduced graphene oxide to study the charge storage properties. This composite shows a reversible capacity of 1075 mAh g^{-1} and a capacity retention of nearly 100% at both 2000 and 3000 mA g^{-1} for over 400 cycles.[325]

Shao and co-workers have reported a large charge storage capacity of PANI@UiO-66. The CV study shows that the current density increases with the scan rate and a maximum specific conductance value of 1084 F g^{-1} is obtained at a current density of 0.5 A g^{-1}. This PANI@UiO-66 MOF showed 84% of capacitance retention after 3500 galvanostatic charge–discharge (GCD) cycles. They also developed an advanced flexible solid-state supercapacitor device with PANI@UiO-66. This flexible symmetric supercapacitor shows a large specific capacitance of 886 F g^{-1} at a current density of 0.5 A g^{-1}. The framework also shows high stability with 91% retention of specific capacitance after 5000 GCD cycles.[195]

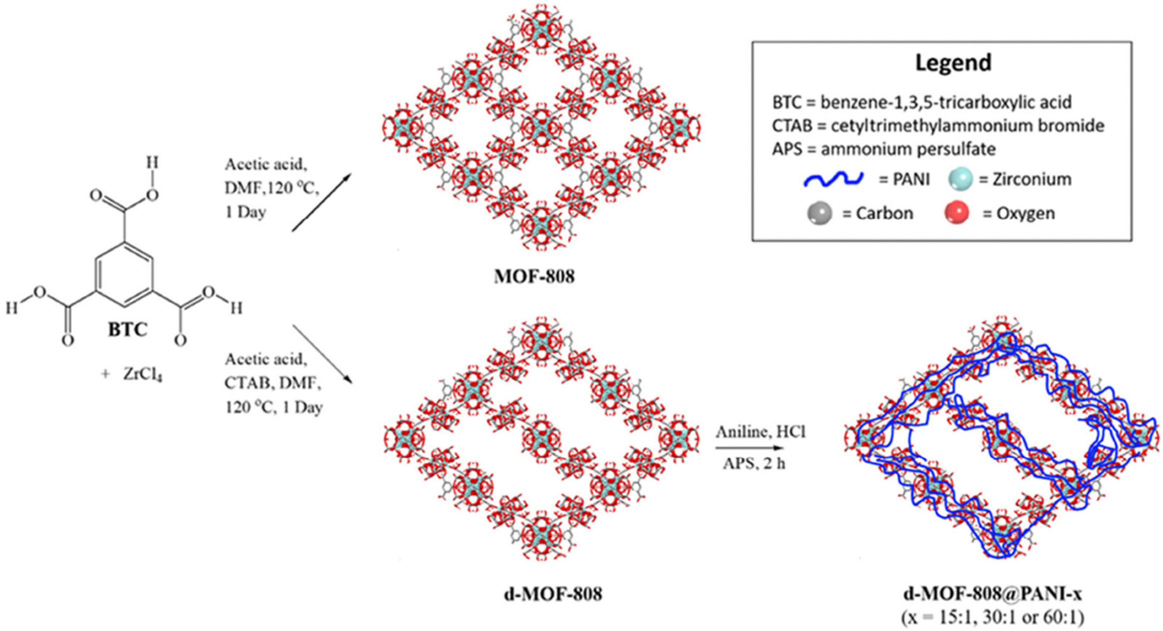

Fig. 63 Synthetic route to prepare MOF-808, d-MOF-808 and d-MOF-808@PANI-15:1, 30:1, and 60:1. Reproduced with permission from ref. 326. Copyright 2017, The American Chemical Society.

Ferhi and co-workers reported the charge storage capacity of another polyaniline-encapsulated MOF. They have observed that PANI@d-MOF-808 (defective zirconium MOF 808) with a polymer : MOF ratio of 60 : 1 shows the maximum capacitance behaviour (Fig. 63). The highest specific capacitance value obtained is 188 F g^{-1} at 30 mV s^{-1} in 1 M KOH with ∼100% retention of capacitance after 10 000 cycles.[326]

Zheng and co-workers have shown the electrochemical capacitance behaviour of Cu_{2+1}@Cu-MOF/Cu-foam.[327] They prepared Cu_{2+1}@Cu-MOF by a two-step method: in the first step, $Cu(OH)_2$ nano-rods were grown on the surface of copper foam and in the second step, these nano-rods were reacted with *p*-phthalic acid at 350 °C. At high temperatures, these $Cu(OH)_2$ nano-rods are reduced to $Cu_{2+1}O$ while some of them react with *p*-phthalic acid to form Cu-MOF. The obtained $Cu_{2+1}O$@Cu-MOF shows an enhanced capacitance value (∼2.5 F cm^{-2} at 2.0 mA cm^{-2}) compared to $Cu(OH)_2$/Cu-foam and Cu_{2+1}/Cu-foam (∼0.8 and ∼0.9 F cm^{-2} at 2.0 mA cm^{-2}, respectively). This supercapacitor shows a high energy density of 38.3 W h kg^{-1} at a power density of 824.6 W kg^{-1} with 90% capacitance retention after 5000 cycles.[327]

In another report, Wang *et al.* have shown a very high capacitance value of 1197 F g^{-1} at a current density of 1 A g^{-1} of PANI@MIL-101 with good cyclic stability of 81% retention even after 10 000 cycles.[94]

Recently, Tsai *et al.* have shown a significant enhancement of the charge storage capacity of the 2D MOF Zr-BTB (where BTB = 1,3,5-tri(4-carboxyphenyl)-benzene) through encapsulation of PANI.[328] They used a sulfonate-based ligand to spatially separate the polymeric chains of PANI thanks to the electrostatic interaction between the aniline unit and the negatively charged sulfonate groups. Initially, they grafted the sulfonate-based ligand on the metal nodes of 2D Zr-BTB-SO_3. Afterward, PANI was encapsulated through *in situ* polymerization. The resulting PANI@MOF shows a specific capacitance of 515 F g^{-1} at a charge–discharge current of 0.5 mA cm^{-2}, which is much higher than those achieved by the pristine PANI (230 F g^{-1}), PANI@ZrBTB (137 F g^{-1}) and the physical mixture of PANI and ZrBTB-SO_3 (130 F g^{-1}).[328]

4.3.2 Li-ion battery (LIB). Recently, LIBs have gained much attention as charge storage devices based on the 'back and forth' movement of Li^+ ions between the anode and cathode.[329] Several research groups have introduced Li^+ ions within the void space of MOFs through ion exchange. Guo *et al.* have shown LIB application of a MOF following the Li^+ ion diffusion with a modest specific capacity (631 mA h g^{-1} at 0.2 A g^{-1}) and ∼81% retention of capacity after 500 cycles.[330] In another example, Yan and co-workers have reported LIB application of MOF [Cu-HHTQ] (HHTQ = 2,3,7,8,12,13-hexahydroxytricycloquinazoline) with a specific capacity of 657 mA h g^{-1} at 600 mA g^{-1} with a retention of capacity of ∼82% after 200 cycles.[331]

4.3.3 Lithium sulphur battery (LSB). Recently, LSB applications of conductive MOFs have become a major focus of research based on their unique porous structure to encapsulate sulphur/polysulfides, easy diffusion of electrolytes along with high charge carrying behaviour, reduced dissolution of polysulfides, *etc.*[321,322] Cai and co-workers have shown LSB application of the porous 2D MOF $[Ni_3(HATP)_2]$ through encapsulation of sulphur.[332] They developed a composite of S@Ni-HATP with CNTs as a cathode material. The material shows a high storage capacity of 1302.9 mA h g^{-1} with a high retention after 300 cycles. Based on the high conductivity of the S@Ni-HATP, mutual cooperation between MOF and CNTs and movement of ions through the channels of the MOF, it shows extraordinary LSB performance. Following the high electrical conductivity and polysulfide adsorption behaviour of the Ni-HHTP framework, Wang *et al.* have studied its LSB application by growing Ni-HHTP particles on carbon paper (CP). The obtained cathode material Ni-HHTP@CP shows a high capacitance of 892 mA h g^{-1}.[333]

4.4 Photo-conductivity

Photoconductivity is a useful property for applications such as solar cells, photo-electrocatalysis *etc.* In a photoconductive material, upon light excitation, electrons will jump from the valence band to the conduction band by creating holes in the valence band. In order to develop a photoconductive MOF, a donor–acceptor pair is required.[203] So, to design an extrinsically photo-conducting MOF, a donor–acceptor pair should be formed within a host MOF. There are two different possibilities: either the MOF acts as a donor and the guest as an acceptor or *vice versa*. Liu and co-workers have studied the photoconductivity of thin films of three different MOFs upon C_{60} encapsulation.[152] They have prepared thin films of C_{60}@Cu-BPDC (BPDC = biphenyl-dicarboxylate), C_{60}@ZnTPP (TPP = 5,15-bis-(3,4,5-trimethoxyphenyl)-10,20-bis(4-carboxyphenyl)-porphyrine) and C_{60}@ZnDAP (DAP = 10,20-bis(4-carboxyphenyl)-5,15-diazaporphyrine) with the LBL technique. Two-probe conductivity measurements show that Cu-BPDC (2×10^{-13} Sm^{-1}) shows an enhancement of 4 orders of magnitude due to encapsulation of C_{60}. However, the enhancement of conductivity is less than 10% for C60@Cu-BPDC upon illumination. C_{60}@ZnTPP shows a conductivity value of $\sim 1.5 \times 10^{-11}$ S cm^{-1} while the parent MOF has a conductivity value of 1.5×10^{-13} S cm^{-1} and the conductivity value rises by 100 times upon illumination with light of 455 nm (Fig. 64).

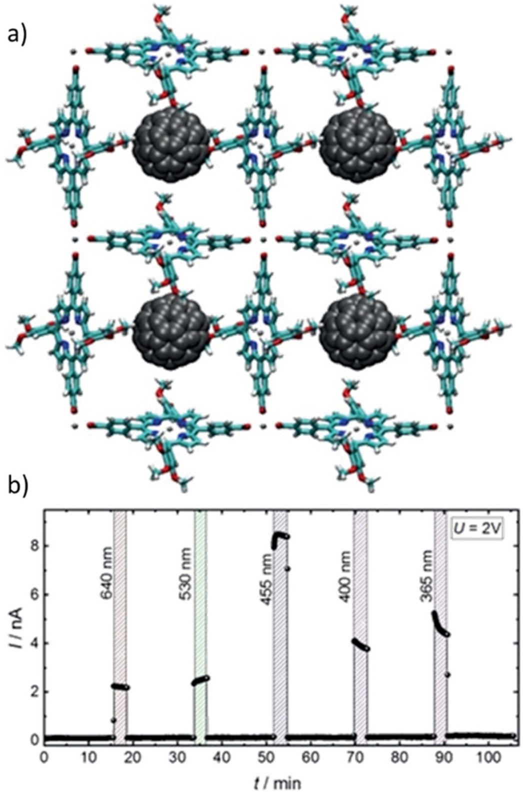

Fig. 64 (a) The structure of C_{60}@Zn(TPP). O = red, Zn = dark grey, N = blue and H = white. For clarity, C in the MOF scaffold is shown in cyan, and C of fullerene is grey. (b) The DC current I at a voltage of 2 V is measured while the sample is irradiated with light of 640 nm, 530 nm, 455 nm, 400 nm and 365 nm wavelength. The current without light irradiation is 0.11 nA. Reproduced with permission from ref. 152. Copyright 2019, Wiley & VCH.

This difference is obviously due to the cooperative charge transfer between the donor porphyrin and the acceptor C_{60} moieties. The related MOF C_{60}@ZnDAP also shows a 100 times enhancement of the electrical conductivity upon excitation with 455 nm wavelength. This different photoelectric behaviour of these porphyrin-based MOFs is due to their different electronic structure. In order to explain the photoconductive behaviour of these MOFs, these authors have performed quantum mechanical calculations which reveal that the LUMO of TPP is lower in energy than in the C_{60}@ZnTPP MOF and this facilitates both the direct and photo-induced electron transfers between porphyrin and C_{60}. Upon excitation, the Soret band of the porphyrin was activated to generate electron–hole pairs and promote their transfer by hampering their recombination and electron back transfer. Han and co-workers have shown the photoconductive behaviour of AgNC@Rb-CD-MOF. AgNC@MOF shows 10^4 times enhancement of the electrical conductivity upon illumination to reach 2.15×10^{-7} S cm^{-1}.[73] They have established that direct optical excitation and an indirect thermal excitation contribute to the overall enhancement of the electrical conductivity upon illumination and also proposed a tunnelling mechanism for charge transport. Hu *et al.* have shown the photoconductive behaviour of the MOF $[\mathrm{Tb(Cu_{4I4})(INA)_3(DMF)}]$ after iodine adsorption.[124] Upon illumination with a Xe lamp, the photocurrent increases from 3.8 to 5.8 μA.

Some of these guest-encapsulated photoconductive MOFs may also be used for photovoltaic cells to convert solar light into electricity. Lee *et al.* have shown the photovoltaic activity of thin films of two different MOFs, Co-BDC (H_2BDC = 1,4-benzene dicarboxylic acid) and Co-NDC (NDC = 2,6-naphthalenedicarboxylate).[122] Thin films of these MOFs are prepared *via* layer-by-layer and iodine was loaded by soaking the thin films within an iodine saturated acetonitrile solution. Absorption spectroscopy confirms the encapsulation of iodine as well as oxidation of Co^{2+} to Co^{3+}. Such iodine encapsulation converts these two insulating MOFs to semiconductors. Co-NDC shows better conductivity than Co-BDC due to the encapsulation of a larger number of iodine molecules. Both iodine-doped MOFs are used as light-harvesting sensitizers in a TiO_2-based photovoltaic cell. The Co-NDC MOF has a power conversion efficiency of 1.12%.[122] In another article, Zhang and co-workers reported the solar cell activity of a polyoxometalate-encapsulated MOF.[325] The MOF [Fe(BDC)(4,4′-bpy)] was used to encapsulate $H_3PW_{12}O_{40}$ Keggin POMs inside the MOF. This MOF shows an optical response with $\lambda_{\max} \sim 750$ nm. The photovoltaic performance of the POM@MOF modified ZnO photoanode shows better performance than bare ZnO. The power conversion efficiency is ∼0.073%.

4.5 Photocatalysis

Some of the conducting MOFs are also used for photocatalytic applications like CO_2 reduction, water splitting *etc.* Yuan *et al.* have studied the photocatalytic CO_2 reduction behaviour of PPy-loaded ZIF-67.[334] Due to high electrical conductivity, high aqueous stability and large surface area, PPy@ZIF-67 is used as a co-catalyst for CO_2 reduction under visible light in the presence of $[Ru(bpy)_3]^{2+}$ as a photosensitizer. Under these catalytic reaction conditions, PPy@ZIF-67 produces CO and H_2 with a CO selectivity of 63%. The encapsulated PPy acts as an electron harvester and transporter for the photogenerated electron from the photosensitizer to the metal nodes. Upon excitation at 500 nm, $[Ru(bpy)_3]^{2+}$ shows the characteristic emission peak at 606 nm, which is quenched by the presence of the co-catalyst PPy@ZIF-67. The weak interactions between PPy and $[Ru(bpy)_3]^{2+}$ enable a more efficient electron transfer within the MOF.[334]

In another article, Fang *et al.* have shown a similar photocatalytic CO_2 reduction of PPy@Al-PMOF-Cu. Porphyrin moieties with Al-PMOF were post-metalated with copper and then pyrrole monomers were encapsulated within the void space. Oxidative polymerization to form PPy was done within the void space and confirmed by TEM, XRPD and IR studies. Such encapsulation of PPy reduces porosity but enhances electrical conductivity. Photocatalytic CO_2 reduction to CO (90 μmol g^{-1} h^{-1}) was obtained by using triethanolamine as the sacrificial agent under visible light irradiation. The porphyrin moiety acts as a photosensitizer, PPy as an electron transporter and the Cu sites as the catalytic active centres.[193]

4.6 Other applications

Xu *et al.* have shown thermoelectric properties of PANI-loaded MOFs by measuring the temperature dependence of their Seebeck coefficients.[197] The Seebeck coefficients for all the PANI-loaded MOFs (PANI@Co-MOF, PANI@Co-MOF-Br and PANI@Co-Ag-MOF) increase with temperature and all show a p-type thermoelectric behaviour. PANI@Co-MOF-Br has the highest Seebeck coefficient (66.5 μV K^{-1} at 400 K), much higher than PANI@Co-MOF (46.3 μV K^{-1}) and PANI@Co-Ag-MOF (59.5 μV K^{-1}). They have observed that this trend is different from the electrical conductivity of MOFs due to the coupling effect and the mobility and carrier concentration.[197] Jiao and co-workers have reported the electromagnetic absorption (EMA) of PPy@ZIF by evaluating the reflection loss (RL) value. They have observed that the electromagnetic absorption is also dependent on the electrical conductivity of the samples. The higher the electrical conductivity, the higher the absorbance. Pure ZIFs have low EMA performance but it improves with the introduction of PPy within the channels. PZ-3 containing 5% of PPy shows the maximum EMA performance and this can also be tuned by the sample thickness and the frequency of the electromagnetic radiation. The maximum EMA performance for PZ-3 is −49 dB with a sample thickness of 2.9 nm.[191] Prasoon and co-workers have shown a diode-like behaviour of thin films of TCNQ-doped Cu-BTEC MOF with a rectification ratio of $\sim 10^5$.[335] Liu and co-workers have shown the photothermal energy storage behaviour of PPy composite with ODA@Cr-MIL-101-NH_2 (ODA = 1-octadecanol). The photothermal conversion and storage efficiency of ODA@MOF/PPy-6% reaches values as high as 88.3%.[336]

5. Summary and outlook

During the last two decades, MOFs have become a major research topic thanks to their interesting properties such as ultrahigh surface area, tuneable structure, gas and solvent sorption, size-selective heterogeneous catalysis, sensing, *etc.* The development of intrinsically conductive MOFs for multiple applications combining electronic properties and structure-based functionalities is hindered by the limited choice of electroactive organic ligands and metal ions to construct these MOFs. In this scenario, the encapsulation of electroactive guest species within the void space of MOFs has gained much attention due to the endless possibilities of guest species and host–guest interactions. A large number of electroactive species can be used as guests to design ec-MOFs by generating mobile charge carriers, host–guest charge transfer interactions or individual conductive pathways. Although significant progress has been made in this field, there are still several limitations such as device fabrication, stability, mechanical properties, *etc.* In conducting MOFs, the formation of efficient charge transport pathways is the main requisite for the development of highly conductive materials. Based on this conducting pathway, MOFs and PCPs can be classified into two categories: intrinsically (ic-MOFs) and extrinsically conducting MOFs (ic-MOFs). The main differences between both types of conducting MOFs can be grouped in different aspects as (i) design, (ii) synthesis, (iii) structural studies and (iv) conductivity studies.

(i) Design: in ic-MOFs, the charge transport depends on the metal–ligand backbone of the framework. Different strategies have been adopted to design ic-MOFs including metal–ligand overlap (use of soft donor-based ligands), redox hopping (use of mixed-valence metal ions), extended organic conjugation (use of highly conjugated ligands) and redox-active radical-based ligands. Thus, the design of ic-MOFs is critically dependent on the metal ions and ligands. However, the limited choice of electroactive ligands, compared to general MOFs, strongly reduces the design possibilities.

In contrast, in ec-MOFs, the charge transport depends on the guest and host–guest interactions. The guests can conduct electrons on their own (as organic conducting polymers) within the void space of the host MOF. In other cases, host–guest interactions create new charge transport pathways within the guest@MOF structure through π-interaction, redox hopping, metal–guest interactions, *etc.* Here, the large number of possible guests and host–guest interactions provide almost infinite opportunities to design ec-MOFs.

(ii) Synthesis: ic-MOFs are generally synthesized by *in situ* methods through direct mixing of the chemical components under solvo- or hydrothermal conditions by self-assembly of organic ligands and metal ions. Additionally, some post-synthetic modification can be done by metal ions or organic ligands exchange while keeping the basic MOF architecture.

In contrast, ec-MOFs are very rarely obtained by *in situ* methods. In most cases, the guest encapsulation is done *via* the post-synthetic methods. The encapsulated guest species remain either in the void space or grafted to the metal ions or to the ligands. Such post-synthetic encapsulation leads to the non-homogeneous distribution of guests within the host structure. So, the synthesis of ec-MOF is somewhat a bigger challenge compared to ic-MOFs.

(iii) Structural analysis. For the intrinsically conducting frameworks, the detailed structural information enables the rational development of such materials by simply using mixed-valence metal ions, conjugated ligands with an adequate metal–ligand overlap, *etc.* In contrast, for extrinsically conducting materials, there is little crystallographic evidence of the host–guest interactions and their contributions to the charge transport phenomena of the resultant host–guest materials. However this host–guest interaction has already shown a high potential to enhance the electrical conductivity by several orders of magnitude. Unfortunately, in most cases, the inclusion of guests within the regular confinement spaces of the frameworks reduces the crystallinity of the host and precludes the single crystal X-ray structure determination.

(iv) Conductivity studies. The electrical conductivity of MOFs is measured either on single crystals or on microcrystalline powders. Single crystals of ec-MOFs are very rare as the post-synthetic encapsulation of guest species within the pores of MOFs reduces the single crystalline nature. Therefore, the electrical conductivity of ec-MOFs is measured mostly on pressed pellets or thin films. In the case of ic-MOFs, there are more reports on single-crystal electrical conductivity measurement. The electrical conductivity measurement using pressed pellets or thin films of MOFs is less reliable than single crystal measurements due to the influence of grain-boundary effects. Although for real-world applications, devices can be prepared by using MOF thin films, in order to get a deep understanding of the structure-properties relationships, we need accurate structural and electrical studies.

The maximum electrical conductivity reported to date for ic-MOFs is 1580 S cm^{-1} for the MOF Cu-BHT (BHT = benzenehexathiolate), measured on thin films by D. Zhu *et al.*[242] whereas the maximum electrical conductivity reported to date for an ec-MOF is 250 S cm^{-1}, measured on single crystals of a BEDT-TTF donor–acceptor charge-transfer based MOF reported by Coronado, Gómez-García *et al.*[137]

In this review, we have focused on these guest-containing extrinsically conducting materials. We have classified the guests into three categories: (a) metal-based guest, (b) molecule-based guest and (c) organic conducting polymers. For the reported examples, we have discussed: (i) the guest loading process within the pores/channels of the MOFs and PCPs, (ii) the structural modifications after guest loading (when data is available), (iii) the (most times huge) change in the electrical conductivity and (iv) the charge transport pathway and mechanisms proposed. The review of these extrinsically conducting MOFs shows the following conclusions:

(a) Metal-based dopants: the dopants (metal ions, metal nanoclusters and metal oxides) are incorporated into the MOFs *via* post-synthetic techniques. The incorporation of metal ions can be done by simple intercalation. This method usually maintains the crystallinity and allows the study of the crystal structure of the intercalated material. Structural studies show that the metal ions are mainly located around the ligand donor sites of the framework and, accordingly, the electrical conductivity is obtained thanks to a charge transport hopping mechanism. The metal nanoclusters (MNCs) are usually loaded by intercalation of metal ions followed by a reduction to form metal nanoparticles. The reduction can be done by either incorporating a secondary reducing agent or by the MOF itself, although this chemical reaction decreases the crystalline nature of the frameworks. The enhancement of the electrical conductivity is due to the easy charge transport through the MNCs within the MNC@MOFs by the hopping mechanism. Metal-oxide encapsulated within MOFs is very rare and is performed by post-synthetic methods. The highest conductivity value obtained with this strategy is 1.8×10^{-2} S cm^{-1}, reported for a MOF with Cd^{2+} ions encapsulated.[73]

(b) Molecules and molecular entities: different molecules and molecular entities have been loaded within the void space of many different MOFs and PCPs by both, templated and post-synthetic methods. The incorporated guest molecules enhance the electrical conductivity either by developing an alternative pathway of charge transport or by host–guest charge transfer interactions. In some cases, the incorporation of guest molecules may increase the conductivity more than one million times, as in TCNQ@HKUST-1, where metal–guest coordination interactions provide the pathway for electron transport and show almost 10^7 times enhancement of the electrical conductivity. For iodine, TTF-type donors, fullerene, ferrocene, *etc.*, the appearance of donor–acceptor charge transfer interactions with the host framework may also lead to an increase of several orders of magnitude of the electrical conductivity. The host–guest $(\mathrm{BEDT\text{-}TTF})_3[\mathrm{MnCr}(\mathrm{C_2O_4})_3]$ framework shows the highest conductivity in this category (250 S cm^{-1}).[137] For this category of host–guest structures, the electrical conductivity value varies depending on the guest, the host as well as the host–guest interactions.

(c) Organic conducting polymers: polymerization of different conducting organic polymers within the channels of the frameworks is usually done in two steps: loading of monomers within the pores and then polymerization. Loading of monomers or molecular fragments can be done by both template and post-synthetic methods. The loaded monomers interact with the MOFs either by weak interactions or forming covalent or coordination bonds with the ligands or metals of the framework. The polymerization can be performed by different mechanisms such as oxidative polymerization, radical polymerization, electro-polymerization, *etc.*, depending on the monomer and MOF. The charge transport for most of the polymer-encapsulated frameworks is due to the extended π-conjugated polymeric chains, interchain π-interactions as well as polymer–host interactions. In most cases, these frameworks with encapsulated organic conducting polymers show moderate conductivity in the range of 10^{-4} to 10^{-2} S cm^{-1} with a maximum reported conductivity of 1.5 S cm^{-1} for PPy encapsulated in ZIF-67.[191] In all cases, the electrical charge transport occurs through the encapsulated organic polymer, although the role of host–guest interaction is non-negligible.

The design of conducting host–guest structures, through encapsulation of different electroactive guest species within the cavities and channels of porous materials, is an area of growing interest. Despite the intense efforts performed in the last decades, there are still several challenges that need to be addressed for further development:

1. **Structural aspects and rational design**: the advance of single crystal X-ray crystallography has enabled the establishment of the structure–property relationships for different assembled materials like MOFs, PCPs and COFs and their rational design. Thanks to the knowledge of crystal engineering, material chemists have designed and modulated the structure of these materials to obtain the desired properties. Nevertheless, the lack of precise crystallographic information in many guest@MOFs precludes the rational design to build highly conducting guest encapsulated frameworks. Some guest@MOFs formed by template-assisted methods may allow the precise determination of the crystal structure but, in most cases, guest encapsulation within pre-synthesized frameworks using post-synthetic methods, reduces the crystallinity. The formation of conducting polymeric chains within the channels of MOFs is the best example of such loss of crystallinity of the frameworks. Therefore, the synthesis of high-quality single crystals of guest@MOFs, remains one of the most important challenges in conducting MOF chemistry, especially in polymer-encapsulated frameworks. The use of Rietveld analysis of XRPD data and neutron diffraction data, pair distribution function analysis *etc.*, may also be helpful to resolve the crystal structure of homogeneous, single-phase microcrystalline guest@MOF samples.

2. **Host–guest interactions**: rational design of conducting MOFs through appropriate encapsulation of guests within the cavities of host frameworks is strongly dependent on the host–guest interaction. The lack of precise crystallographic information limits the analysis of these host–guest interactions. Therefore, the synthesis of single crystals of guest@MOFs and their structural determination constitutes a key step to studying and understanding the host–guest interactions that govern the conductivity, in order to improve the electrical properties of these porous materials.

3. **Homogeneous distribution of the guests**: one of the major challenges in this field is the lack of homogeneous loading of the guest molecules within the channels of the MOFs. Homogeneous loading of guest molecules within the channels of MOFs is only achieved by template-assisted synthetic methods, since guest-loading through post-synthetic methods usually leads to an inhomogeneous distribution of the guests within the channels. The presence of pores that are much larger than the guests may lead to the disordered accumulation of guests within the channels as well as the chance to increase the leaching. Therefore, the choice of complementary hosts and guests for the homogeneous encapsulation of the guests within the channels of the hosts constitutes a very challenging task in this field. Thus, the proper structural analysis is the primary criterion for the rational design and further development of this field. The introduction of similar guests with identical geometrical parameters within a single MOF may also highlight the host–guest interactions. Theoretical calculations may also predict the ideal candidates of host and guest to design ec-MOFs. Advanced simulations and molecular modelling could assist in the synthesis by optimizing proper building blocks towards predesigned structures with predefined functionalities and host–guest interactions.

4. **Mechanistic studies**: although in some cases high electrical conductivities at room temperature have been obtained (up to 250 S cm^{-1}), most of the conducting host–guest materials behave as semiconductors. In fact, only very few are metallic and no superconducting host–guest MOF has been reported to date. The development of metallic conductors and superconductors constitutes, therefore, a very appealing challenge. A possible way to achieve these goals maybe the incorporation of charge transfer active guest species within the cavities of highly conducting MOFs containing highly conjugated ligands and mixed-valence metal ions. These features are expected to facilitate the electron delocalization and lead to metallic or even superconducting MOFs with electron delocalization through the guest, through the MOF or even through both. Nevertheless, such development requires a deep understanding of the charge transfer mechanisms as well as the charge carrier mobility and a control of both. Such mechanistic studies with ec-MOFs have been done in very rare cases.

5. **Identify charge carriers and their properties**: the electrical conductivity of a material is determined by the charge carrier density and charge carrier mobility. Only in very few examples, these studies have been performed. Therefore, more studies to identify the charge carriers (electrons or holes) and determine their properties (density and mobility) as well as the conduction mechanisms are needed. These studies are expected to contribute to a better understanding of the key parameters that control the electron delocalization mechanisms and, therefore, the electrical properties of these guest@MOFs. Further, in-depth analysis is highly necessary to identify the charge transfer mechanism.

6. **Control over the charge transport**: one of the major advantages of the design of guest-mediated conducting MOFs is that their conductivity can be tuned by changing the amount of guest loading. Only a few studies have been done to modulate the electrical conductivity of MOFs by controlling the loading of guests, and, therefore, there is still a lot of work to be done in this direction. This work is expected to lead to the easy control and modulation of the electrical properties of these guest@MOFs materials by simply changing the nature and amount of the guest. The final aim is the synthesis of guest-

dependent conducting materials at will. Furthermore, these materials may tune their electrical conductivity by gas or ionic absorption in solution, rendering them as ideal candidates for the preparation of gas and ionic sensors.

7. **Thin film fabrication**: for advanced applications, it is highly necessary to deposit defect-free and homogeneous thin films of conductive MOFs on different substrates. Thickness, coverage, roughness, orientation, homogeneous distribution over the substrate and crystallinity after fabrication, are the important parameters of a MOF thin film. Following their many potential applications, several research groups have developed different thin film fabrication methods and explored their applications. Still, there are several challenges to be addressed for further development: (a) Improvement of the thin films quality and thickness, their homogeneity at the surface, orientation, low defect density, *etc.* There is no ideal method to reach these goals and, therefore, extensive research should be done to address this issue. (b) Stability and adhesion of the MOF particles to the substrate is also important for device performance. The growth of MOF thin films on functionalized substrates may be a good choice to increase the stability and adhesion. (c) Control over defects, as defects may have an important influence on the properties and functionality of thin films of conductive MOFs. Defects can disrupt the charge transport behavior in the thin film although they can promote the electrocatalytic and electrochemical sensing properties. So, it is important to understand the relationship between defects and the charge transport properties. (d) Mechanistic studies of the growth process of thin film should be performed to improve their synthetic methods. Theoretical analysis is also an important aspect. Besides, the thermal, chemical and mechanical stabilities of the thin films are also crucial for practical applications.

Several thin film fabrication methods are well-known for conducting MOFs with each method having its own advantages and limitations. Here, we have summarized the thin film fabrication methods of ec-MOFs and pointed out their challenges and possible solutions. For the fabrication of ec-MOFs, synthesized by *in situ* methods, it is highly challenging to control the leaching of weakly bonded guest species from the host MOF. So, it is more convenient to fabricate the thin film of the host MOF on the substrate and then encapsulate the guest species.[60] Such guest encapsulation has also several challenges. A thin film of the host MOF should interact with the guest present in any solvent – so there will be a chance of solvent interference. Solvent molecules may penetrate within the void space of the MOFs. The use of non-coordinating and volatile solvents may be a good choice to avoid solvent interference. Vapor-phase guest encapsulation can also be done by chemical vapor adsorption. The next challenge may arise from the accumulation of guest species at the pore window of the host MOF which may block further encapsulation of guests. Similarly, non-homogeneous distribution is also a big challenge for ec-MOF fabrication. The next issue may arise from the stability of the host framework during encapsulation. It is important to note that the host MOF structure can change or collapse during thin film fabrication. Under such circumstances, the guest loading will be different from the theoretical prediction or even zero loading may be found. So, it is highly important to characterize the host MOF after fabrication as well as after guest loading. After guest encapsulation, it is necessary to measure the electrical conductivity of the guest@MOF thin film to point out the host–guest interactions and the differences from the bulk phase. More studies of the mechanism of guest encapsulation, host–guest interaction and their effects on the electrical conductivity of the guest@MOF thin films are needed. The complete characterization of the thin films of the MOFs before and after encapsulation of the guests is also necessary.

8. **Patterning**: the patterning of conductive MOF thin films is another necessary step for their integration in electronic devices. The control over the position of MOF thin films on the surface of the substrate has paramount importance in exploring the applications of MOF thin films in sensors and microelectronics. Here, the problem is that MOFs are usually grown as microparticles or as single crystals and patterning of MOF thin films is challenging. Several methods have been adopted for the successful patterning of MOF thin films including: (a) masking the substrate and functionalizing the desired area for the preferential growth of the MOF thin film, (b) patterned deposition of chemical components of MOFs and then growth, and (c) lithographic technique. Photolithography is also an important area of research in MOF patterning. There are several challenges to be addressed including the development of an ideal technique that should be fast, easy, cheap, while allowing the control of the thickness, position, size and crystal orientation. Another important parameter is the adhesion of the MOF particles on the substrate, mechanical properties and durability. For the ec-MOFs, the guest moieties can be encapsulated within the void space after patterning the thin films of the host MOF.

9. **Applications**: the main aim of electrically conductive MOF research is the development of novel functional materials for applications in electrocatalysis, chemiresistive sensing, charge storage, photovoltaics, photocatalysis, *etc.*

Electrocatalysis: the design of efficient and cheap electrocatalysts for the energy-related applications like electrocatalytic HER, OER, ORR, CO_2RR, NRR, *etc.* is important to find an alternative and sustainable source of energy to control fossil fuel consumption. The suitable electrocatalysts must have the following properties: high electrical conductivity, easily accessible and homogeneously distributed active sites, optimized pore dimension for efficient mass transfer, stability under the electrocatalytic reaction conditions and durability. To date, several ec-MOFs have been reported with electrocatalytic applications containing diverse types of guest species like metal ions, metal oxides, metal chalcogenides, inorganic molecular catalysts and others. However, their catalytic activity and stability are still questionable. For electrocatalytic applications, thin film fabrication of MOFs on the electrode surface is the primary criterion – such thin film fabrication improves the electrical conductivity but decreases the number of active sites due to the necessity of Nafion-like binders. Most of the MOFs are not stable in the solution phase under acidic/basic conditions while both media are required for many electrocatalytic studies. Therefore, it is important to characterize the MOFs after the electrocatalytic experiments. In several cases, MOFs are attached to the electrode surface through non-covalent interactions, limiting the durability of the catalysts. Detailed studies of the mechanism of these electrocatalytic processes using ec-MOFs are also required. Theoretical study may provide some insights on this topic. Following the high efficiency of single-atom catalysts, it will be desirable to incorporate catalytically active single atoms as the guest species within the host MOFs to study their activity. The confined space of MOFs may provide extra stability to the single atoms within the MOF structure. Highly efficient molecular catalysts can also be incorporated within the MOFs to design ec-MOF-based electrocatalysts. Further, the design of bimetallic host–guest MOFs through encapsulation of different metallic species within an MOF will also be a fruitful strategy. Substrate conversion is also another hot topic in electrocatalysis that has gained attention very recently. In summary, there are many aspects to improve on ec-MOF-based electrocatalytic applications.

Charge storage: several ec-MOFs have been studied for different types of charge storage applications such as supercapacitors, Li-ion batteries and Li–S batteries. However, the design of highly conducting MOFs to prepare supercapacitors is still at its initial stage. The ideal supercapacitor should possess the following characteristics: metallic conductivity, easily accessible and enriched active sites, high specific capacitance, large surface area, optimized porosity, high chemical and physical stability, durability during operation and cost-effectiveness. To date, not only the electrical conductivity of MOFs is far lower than metallic behavior but also the specific capacity is much smaller than the desired value (around 1000 F g^{-1}). Moreover, structural stability and high cost further hinder their use. Again, further studies with ec-MOFs are needed for potential supercapacitor applications. MOFs with encapsulated alkali metal ions and poly-sulfides are important for the development of metal-ion and sulfur-based batteries. The unique properties of such devices are generally high porosity, controlled uptake and release of guest metal ions, reversible redox behavior, prolonged stability, high storage capacity, large charge–discharge cycling behavior, durability, *etc.* The number of studies conducted with ec-MOFs for battery applications is still very limited. Some of the challenges that should be addressed are the device fabrication with powdered samples of the ec-MOFs and the diffusion of guest moieties through the channels of the framework.

Electrochemical sensors: conducting MOFs are highly promising materials for sensing different types of analytes (gases, ions, molecules, liquids, biomolecules,...) due to their tunable porosity, large surface area, chemically functionalized pores, functionalized organic ligands and strong sensor–analyte interactions. Research on MOF-based sensors has increased rapidly with the inclusion of electronic properties in the frameworks. The development of highly conductive MOFs and the advantages of chemiresistive sensing devices based on them, such as ease of fabrication and integration, low power consumption, *etc.*, has stimulated the development of these devices. The most important characteristics of a sensing material are sensitivity, selectivity, stability, reliability and reproducibility. Although significant progress has been made in this field (several ec-MOFs are used for sensing different analytes), still there are several drawbacks. For the integration of devices, the most important part is the formation of thin films, an area which is already in progress. High selectivity and sensitivity can be achieved through rational design. Various studies have revealed that mixed metal MOFs are very promising as electrochemical sensors and, therefore, the encapsulation of different metallic species within host MOF structures may be a good strategy to achieve these properties. Furthermore, no mechanistic analysis of electrochemical sensing devices has been reported. Computational studies may help to identify the potential ec-MOF candidates for the selective identification of particular analytes as well as highlight their mechanism. Finally, it is worth mentioning that there are many other different applications of ec-MOFs such as photocatalysis, photoconductivity, magnetoresistance, *etc.* Nevertheless, these studies are at the very initial stages, and they should be explored in the near future. Despite the multiple challenges above mentioned, we believe that further study will provide more opportunities to explore the multiple applications of ec-MOFs.

10. **Commercialization**: although commercialization is not the only goal of scientific research, patenting and real-world applications of a material boost the scientific community. The finding of possible commercialization of a material attracts interest from different and multiple technological directions. It is also obvious that real-world applications require multiple, coherent and interdisciplinary actions. The commercial success, gross profit and benefit for society will be the main target for such commercialization.

In MOF chemistry, the initial targets were to develop suitable MOFs for adsorption and separation of gases, (several patents have been granted) and scale up of some MOF-based materials is also in process for industrial applications. Very recently, the exploration of conductive MOFs has become a prime focus for their unique electronic applications and thus we hope to see real-world applications of conductive MOFs very soon. The self-assembly of metal ions and organic ligands provides an opportunity to overlap their inherent properties along with newly evolved structure-related functionalities. Additionally, the encapsulation of electroactive guest species within the void space of MOFs further allows modulation of the electronic and other properties of the host MOF in a controlled manner. The major obstacle is the lack of complete structural information in most cases. Theoretical calculations may provide insight and help to find the most suitable candidates for this purpose. One of the major concerns for real-world application of MOFs is the formation of thin films, which can be used in optoelectronic devices, bio-sensing, electrocatalysis, *etc.* There are several methods for thin film fabrication of ec-MOFs, although this field is still in its infancy. Here, we present the first attempt to summarize and highlight thin film fabrication of ec-MOFs. Furthermore, chemical stability, mechanical flexibility, durability and other properties should be analyzed thoroughly for practical applications. Thus, we believe that the coherent strategy from various fields like synthetic chemistry (for the synthesis), engineering (device fabrication), characterization of thin films (solid state physics), material integration, *etc.* can provide a better understanding of real-world applications of ec-MOFs.

11. **Future generation materials**: encapsulation of different guest species within the void space of MOFs to tune their electrical conductivity, most probably, will become one of the hottest research topics in materials science within the next few years. We also look forward to see some interesting examples of conducting MOFs, particularly ec-MOFs in highly relevant applications for future technologies like:

Dual conducting MOFs: very recently, dual conducting materials, *i.e.*, simultaneous electronic and protonic conductors, have gained much attention for various applications (like CO_2RR, OER, *etc.*) where proton-coupled electron transfer is the main step. In this regard, the encapsulation of electroactive guest species within the void space of proton-conducting MOFs or *vice versa* will be a good strategy for designing dual-conducting MOFs.

Tuning conductivity by external stimuli. Further control over the electronic conductivity of guest@MOFs through external physical stimuli such as light, heat, *etc.*, or even chemical ones (such as gasses, solvents…) may also lead to the construction of advanced electronic materials, sensors and opto-electronic switches.

Quantum computing. The design of electrically conducting MOF in combination with ferromagnetic behavior may provide a pathway to develop spintronic devices for their applications in quantum computation.

Biomedical applications. The encapsulation of electroactive drug molecules within the host framework may also allow the controlled release of the guest drug molecules at the targeted site under a particular bias voltage – this may be fascinating in biomedical research.

Motor. We wish to see the development of MOF motors, rotors and machines using ec-MOFs. Under external stimuli like voltage, light, pressure, *etc.*, the encapsulated guest moieties may show rudimentary motions like shuttle, rotor, motor, *etc.* following the perfect host–guest interaction and structure.

In conclusion, MOF chemistry has grown rapidly as advanced functional materials over the last two decades. To date, more than 90 000 MOFs have been reported with tunable structural topology, chemical versatility, inherent porosity, large surface areas, *etc.* and diverse applications. The poor charge transport properties hinder the use of these MOFs in electronic applications like electrocatalysis, chemiresistive sensing, photovoltaics, *etc.* The design and synthesis of electronically conductive MOFs with enhanced electron transport properties have gained significant attention in the last decade. These electrically conductive MOFs can be classified as ic-MOF and ec-MOF, depending on the conducting entity (the host or the guest, respectively). Following the structural details, ic-MOFs have gained much attention for rational design although the limited choice of electroactive ligands has become a major problem for further development. In contrast, ec-MOFs show many more possibilities given the huge number of electroactive guest species and the many different possible host–guest interactions. However, ec-MOFs lack, in most cases, detailed structural information and the synthetic methods present some drawbacks such as low guest insertion, non-homogeneous guest distribution, guest-leaching, *etc.* Additionally, there are not adequate scientific guidelines to measure and report the electrical conductivity, device fabrication, measurement conditions, charge transport mechanistic analysis, transport pathway, *etc.* Although thin film fabrication of ec-MOFs is the main requirement for their integration into electronic devices, still there is no ideal technique for the preparation of high quality, defect-free thin films of ec-MOFs. The detailed characterization of these thin films is also required. In the last decade, the research on ec-MOFs has seen significant growth due to their significant electronic applications in electrocatalysis, chemiresistive sensing, charge storage, and so on. Still, we look forward to further advances in this field including: (i) the rational synthesis of improved ec-MOFs based on synergistic and cooperative host–guest interactions, (ii) the complete characterization of these ec-MOFs, (iii) the improvement of the methods for thin films and devices preparation and (iv) more in-depth theoretical studies to facilitate and guide the synthesis of better conductive MOFs and help to understand, not only the electron transport mechanism but also the other properties of these MOFs. These advances will lead to a new generation of (multi)functional materials and conductive MOFs in the near future.

Abbreviations

MOF	Metal–organic framework
PCP	Porous coordination polymer
TCNQ	7,7,8,8-Tetracyanoquinodimethane
TTF	Tetrathiafulvalene
PEDOT	Poly(3,4-ethylenedioxythiophene)
PANI	Polyaniline
PPy	Polypyrrole
PTh	Polythiofene
PA	Polyacetylene
PTC	1,2,3,4,5,6,7,8,9,10,11,12-Perthiolated coronene
H_4dobdc	2,5-Dihydroxy-benzene-1,4-dicarboxylic acid
EC	Ethylene carbonate
DEC	Diethyl carbonate
^{i}Pr	Isopropyl
UiO	University of Oslo
H_2OBA	4,4′-Oxybisbenzoic acid
PSM	Post-synthetic modification
MNCs	Metal nano-clusters
CD	Cyclodextrin
NU	Northwestern University
PDA	Polydopamine
Hmim	2-Methylimiazole
TEM	Tunnelling electron microscope

XRPD	X-ray powder diffraction
NP	Nanoparticle
ZIF	Zeolitic imidazolate framework
amd	Bis(*N*,*N*′-di-i-propylacetamidinato)
DED	Difference electron density
BET	Brunauer–Emmett–Teller
H$_3$BTC	Benzene-1,3,5-tricarboxylic acid
HKUST	Hong-Kong University of Science and Technology
H$_3$TATAB	4,4′,4″-((1,3,5-Triazine-2,4,6-triyl)tris(azane diyl))-tribenzoic acid
DL-lac	Lactate
pybz	4-Pyridine benzoate
pdt^{2-}	Pyrazine-2,3-dithiolate
NDC	2,6-Napthalenedicarboxylic acid
H$_2$BDC	1,4-Benzenedicarboxylic acid
H$_2$bpz	3,3′,5,5′-Tetra methyl-4,4′-bipyrazole
INA	Isonicotinate
H$_4$L	Biphenyl-3,3′,5,5′-tetracarboxylic acid
MUDA	Mercaptoundecanoic acid
EPR	Electron paramagnetic resonance
H$_3$BPT	Biphenyl-3,4′,5-tricarboxylate
DMF	*N*,*N*′-Dimethylformamide
TTFTB	Tetrathiafulvalene tetrabenzoate
dca	Dicyanamide
XPS	X-Ray photoelectron spectroscopy
BEDT-TTF	Bis(ethylenedithio)-tetrathiofulvalene
BEDT-TSF	Bis(ethylenedithio)-tetraselanafulvalene
TBAPy	1,3,6,8-Tetrakis(*p*-benzoate)pyrene
DFT	Density functional theory
H$_4$TTFTB	Tetrathiafulvalene tetrabenzoic acid
TPP	5,15-Bis-(3,4,5-trimethoxyphenyl)-10,20-bis-(4-carboxyphenyl) porphyrinato
BPDC	4,4′-Biphenyl-dicarboxylate
Fc	Ferrocene
FeCp$^{*}{}_2{}^{+}$	Decamethylferrocenium cations
ndc	1,4-Napthalenedicarboxylate
dabco	1,4-Diazabicyclo-[2.2.2]-octane
HDT	Hexadecanethiol
CMMT	9-Carboxy-10-(mercaptomethyl) triptycene
H$_4$TBAPy	1,3,6,8-Tetrakis(*p*-benzoic acid)pyrene
NiCB	[Ni(dicarbollide)$_2$]
IDE	Interdigitated electrodes
BPDPNDI	*N*,*N*′-Bis(4-pyridyl)-2,6-dipyrrolidyl naphthalenediimide
TCPB	1,2,4,5-Tetrakis-(4-carboxy phenyl)benzene
MV^{2+}	Methyl viologen
DFDNB	1,5-Difluoro-2,4-dinitrobenzene
DNT	Dinitrotoluene
TTFTB^{4-}	Tetrathiafulvalene tetrabenzoate
TCNE	Tetracyanoethylene
MIL	Matérial Institut Lavoisier
dpzNDI	Dipyrazolate-naphthalenediimide
H$_2$bzpdc	Benzophenone-4,4≤-dicarboxylic acid
dmen	1,1-Dimethylethylenediamine
PhBSO$_3$	*p*-Phenylbenzenesulfonate
H$_2$NDC	2,6-Napthalenedicarboxylicacid
HPCA	4-Pyridinecarboxylic
H$_2$-TCPP	Tetrakis((4-carboxyphenyl)porphyrin)
BTB	1,3,5-Benzentrisbenzoate
SURMOF	Surface-mounted metal–organic framework
MHDA	Mercaptohexadecanoic acid
SAM	Self-assembled monolayer
TBAHFP	Tetrabutylammonium hexafluorophosphate
FIB	Focused ion beam
SEM	Scanning electron microscope
EDX	Energy dispersive X-ray spectroscopy
MALDI	Matrix-assisted laser desorption/ionization
EP	Electro-polymerization

Author contributions

The manuscript was written through the contributions of both authors.

Data availability

No primary research results, software or code have been included and no new data were generated or analysed as part of this review.

Conflicts of interest

The authors declare no competing financial interest.

Acknowledgements

R. S. is the beneficiary of the grant (Z21-070) for the requalification of the Spanish University system from the Ministry of Universities of the Government of Spain, modality "Maria Zambrano" financed by the European Union. This study forms part of the Advanced Materials program and was supported by the Spanish MCIN with funding from European Union Next-Generation EU (PRTR-C17.I1) and the Generalitat Valenciana (project MFA-2022-057). We also thank the Grant PID2021-125907NB-I00 funded by MCIN/AEI/10.13039/501100011033 and by "ERDF A way of making Europe" and project CIPROM-2022-060 from the Generalitat Valenciana, for financial support.

References

1 H. Li, M. Eddaoudi, M. O'Keeffe and O. M. Yaghi, *Nature*, 1999, **204**, 276–279.
2 H. Furukawa, K. E. Cordova, M. O'Keeffe and O. M. Yaghi, *Science*, 2013, **341**, 1230444.
3 S. Kitagawa, R. Kitaura and S.-I. Noro, *Angew. Chem., Int. Ed.*, 2004, **43**, 2334–2375.
4 H.-C. Zhou, J. R. Long and O. M. Yaghi, *Chem. Rev.*, 2012, **112**, 673–674.
5 K. K. Tanabe and S. M. Cohen, *Chem. Soc. Rev.*, 2011, **40**, 498–519.

6 R.-B. Lin, S. Xiang, H. Xing, W. Zhou and B. Chen, *Coord. Chem. Rev.*, 2019, **378**, 87–103.

7 K. Sumida, D. L. Rogow, J. A. Mason, T. M. McDonald, E. D. Bloch, Z. R. Herm, T.-H. Bae and J. R. Long, *Chem. Rev.*, 2012, **112**, 724–781.

8 D. Alezi, Y. Belmabkhout, M. Suyetin, P. M. Bhatt, J. Weselinski, V. Solovyeva, K. Adil, I. Spanopoulos, P. N. Trikalitis, A.-H. Emwas and M. Eddaoudi, *J. Am. Chem. Soc.*, 2015, **137**, 13308–13318.

9 Q. Qian, P. A. Asinger, M. J. Lee, G. Han, K. M. Rodriguez, S. Lin, F. M. Benedetti, A. X. Wu, W. S. Chi and Z. P. Smith, *Chem. Rev.*, 2020, **120**, 8161–8266.

10 M. Yoon, R. Srirambalaji and K. Kim, *Chem. Rev.*, 2012, **112**, 1196–1231.

11 L. E. Kreno, K. Leong, O. K. Farha, M. Allendorf, R. P. V. Duyne and J. T. Hupp, *Chem. Rev.*, 2012, **112**, 1105–1125.

12 S. Mallakpour, E. Nikkhoo and C. M. Hussain, *Coord. Chem. Rev.*, 2002, **451**, 214262.

13 A. Dutta, Y. Pan, J.-Q. Liu and A. Kumar, *Coord. Chem. Rev.*, 2021, **445**, 214074.

14 G. S. Papaefstathiou and L. R. MacGillivray, *Coord. Chem. Rev.*, 2003, **246**, 169–184.

15 G. Chakraborty, I.-H. Park, R. Medishetty and J. J. Vittal, *Chem. Rev.*, 2021, **121**, 3751–3891.

16 B. Seoane, S. Castellanos, A. Dikhtiarenko, F. Kapteijn and J. Gascon, *Coord. Chem. Rev.*, 2016, **307**, 147–187.

17 D. Jiang, C. Huang, J. Zhu, P. Wang, Z. Liu and D. Fang, *Coord. Chem. Rev.*, 2021, **444**, 214064.

18 R. Custelcean, *Chem. Sci.*, 2021, **12**, 12518–12528.

19 Z. Wang and S. M. Cohen, *Chem. Soc. Rev.*, 2009, **38**, 1315–1329.

20 S. Mandal, S. Natarajan, P. Mani and A. Pankajakshan, *Adv. Funct. Mater.*, 2021, **31**, 2006291.

21 P. Deria, J. E. Mondloch, O. Karagiaridi, W. Bury, J. T. Hupp and O. K. Farha, *Chem. Soc. Rev.*, 2014, **43**, 5896.

22 Y. K. Hwang, D.-Y. Hong, J.-S. Chang, S. H. Jhung, Y.-K. Seo, J. Kim, A. Vimont, M. Daturi, C. Serre and G. Férey, *Angew. Chem., Int. Ed.*, 2008, **47**, 4144–4148.

23 Z. Ji, T. Li and O. M. Yaghi, *Science*, 2020, **369**, 674–780.

24 X.-T. Liu, B.-B. Qian, D.-S. Zhang, M.-H. Yu, Z. Chang and X.-H. Bu, *Coord. Chem. Rev.*, 2023, **476**, 214921.

25 S. Yang, V. V. Karve, A. Justin, I. Kochetygov, J. Espín, M. Asgari, O. Trukhina, D. T. Sun, L. Peng and W. L. Queen, *Coord. Chem. Rev.*, 2021, **427**, 213525.

26 L. Chen, R. Luque and Y. Li, *Chem. Soc. Rev.*, 2017, **46**, 4614–4630.

27 C. H. Sharp, B. C. Bukowski, H. Li, E. M. Johnson, S. Ilic, A. J. Morris, D. Gersappe, R. Q. Snurr and J. R. Morris, *Chem. Soc. Rev.*, 2021, **50**, 11530–11558.

28 M. Majumder, M. S. Santosh, R. Viswanatha, A. K. Thakur, D. P. Dubal and K. Jayaramulu, *Energy Storage Mater.*, 2021, **37**, 396–416.

29 G. Xu, C. Zhu and G. Gao, *Small*, 2022, **18**, 2203140.

30 C. A. Downes and S. C. Marinescu, *ChemSusChem*, 2017, **10**, 4374–4392.

31 L. Liu, Q. Xu and Q.-L. Zhu, *Adv. Energy Sustainability Res.*, 2021, **2**, 2100100.

32 C.-S. Liu, J. Li and H. Pang, *Coord. Chem. Rev.*, 2020, **410**, 213222.

33 N. B. Shustova, A. F. Cozzolino, S. Reineke, M. Baldo and M. Dinca, *J. Am. Chem. Soc.*, 2013, **135**, 13326–13329.

34 L. Sun, M. G. Campbell and M. Dincă, *Angew. Chem., Int. Ed.*, 2016, **55**, 3566–3579.

35 L. S. Xie, G. Skorupskii and M. Dincă, *Chem. Rev.*, 2020, **120**, 8536–8580.

36 M. D. Allendorf, R. Dong, X. Feng, S. Kaskel, D. Matoga and V. Stavila, *Chem. Rev.*, 2020, **120**, 8581–8640.

37 R. Murase, B. Ding, Q. Gu and D. M. D'Alessandro, *Philos. Trans. R. Soc., A*, 2019, **377**, 20180226.

38 M. Hmadeh, Z. Lu, Z. Liu, F. Gandara, H. Furukawa, S. Wan, V. Augustyn, R. Chang, L. Liao, F. Zhou, E. Perre, V. Ozolins, K. Suenaga, X. Duan, B. Dunn, Y. Yamamto, O. Terasaki and O. M. Yaghi, *Chem. Mater.*, 2012, **24**, 3511–3513.

39 Y. Cui, J. Yan, Z. Chen, J. Zhang, Y. Zou, Y. Sun, W. Xu and D. Zhu, *Adv. Sci.*, 2019, **6**, 1802235.

40 X. Huang, H. Li, Z. Tu, L. Liu, X. Wu, J. Chen, Y. Liang, Y. Zou, Y. Yi and J. Sun, *J. Am. Chem. Soc.*, 2018, **140**, 15153–15156.

41 S. S. Park, E. R. Hontz, L. Sun, C. H. Hendon, A. Walsh, T. Van Voorhis and M. Dincă, *J. Am. Chem. Soc.*, 2015, **137**, 1774–1777.

42 R. W. Day, D. K. Bediako, M. Rezaee, L. R. Parent, G. Skorupskii, M. Q. Arguilla, C. H. Hendon, I. Stassen, N. Gianneschi and P. Kim, *ACS Cent. Sci.*, 2019, **5**, 1959–1964.

43 J. A. DeGayner, I.-R. Jeon, L. Sun, M. Dincă and T. D. Harris, *J. Am. Chem. Soc.*, 2017, **139**, 4175–4184.

44 J. Cui and Z. Xu, *Chem. Commun.*, 2014, **50**, 3986–3988.

45 A. J. Clough, J. M. Skelton, C. A. Downes, A. A. De La Rosa, J. W. Yoo, A. Walsh, B. C. Melot and S. C. Marinescu, *J. Am. Chem. Soc.*, 2017, **139**, 10863–10867.

46 X. Huang, S. Zhang, L. Liu, L. Yu, G. Chen, W. Xu and D. Zhu, *Angew. Chem., Int. Ed.*, 2018, **57**, 146–150.

47 R. Dong, Z. Zhang, D. C. Tranca, S. Zhou, M. Wang, P. Adler, Z. Liao, F. Liu, Y. Sun, W. Shi, Z. Zhang, E. Zschech, S. C. B. Mannsfeld, C. Felser and X. Feng, *Nat. Commun.*, 2018, **9**, 2637.

48 L. E. Darago, M. L. Aubrey, C. J. Yu, M. I. Gonzalez and J. R. Long, *J. Am. Chem. Soc.*, 2015, **137**, 15703–15711.

49 J. A. DeGayner, I.-R. Jeon, L. Sun, M. Dincă and T. D. Harris, *J. Am. Chem. Soc.*, 2017, **139**, 4175–4184.

50 J. Y. Choi and J. Park, *ACS Appl. Electron. Mater.*, 2021, **3**, 4197–4202.

51 X.-N. Wang, P. Zhang, A. Kirchon, J.-L. Li, W.-M. Chen, Y.-M. Zhao, B. Li and H.-C. Zhou, *J. Am. Chem. Soc.*, 2019, **141**, 13654–13663.

52 C. F. Leong, P. M. Usov and D. M. D'Alessandro, *MRS Bull.*, 2016, **41**, 858–864.

53 G. Zhang, L. Jin, R. Zhang, Y. Bai, R. Zhu and H. Pang, *Coord. Chem. Rev.*, 2021, **439**, 213915.

54 P. Zhou, J. Lv, X. Huang, Y. Lu and G. Wang, *Coord. Chem. Rev.*, 2023, **478**, 214969.

55 D. M. D'Alessandro, *Chem. Commun.*, 2016, **52**, 8957–8971.
56 I. Stassen, N. Burtch, A. Talin, P. Falcaro, M. Allendorf and R. Ameloot, *Chem. Soc. Rev.*, 2017, **46**, 3185–3241.
57 M. Ko, L. Mendecki and K. A. Mirica, *Chem. Commun.*, 2018, **54**, 7873–7891.
58 C.-W. Kung, P.-C. Han and C.-H. Chuang, *APL Mater.*, 2019, **7**, 110902.
59 J.-S. M. Lee, K.-I. Otake and S. Kitagawa, *Coord. Chem. Rev.*, 2020, **421**, 213447.
60 M. D. Allendorf, M. E. Foster, F. Léonard, V. Stavila, P. L. Feng, F. P. Doty, K. Leong, E. Y. Ma, S. R. Johnston and A. A. Talin, *J. Phys. Chem. Lett.*, 2015, **6**, 1182–1195.
61 P. Mani, N. Mandal, M. Roopesh, H. Gopalakrishnan, A. Datta and S. Mandal, *J. Mater. Chem. C*, 2020, **8**, 4836.
62 W.-H. Li, W.-H. Deng, G.-E. Wang and G. Xu, *EnergyChem*, 2020, **2**, 100029.
63 T. Kitao, Y. Zhang, S. Kitagawa, B. Wang and T. Uemura, *Chem. Soc. Rev.*, 2017, **46**, 3108.
64 J. Calbo, M. J. Golomb and A. Walsh, *J. Mater. Chem. A*, 2019, **7**, 16571–16597.
65 L. Ding, Z.-D. Yu, X.-Y. Wang, Z.-F. Yao, Y. Lu, C.-Y. Yang, J.-Y. Wang and J. Pei, *Chem. Rev.*, 2023, **123**, 7421–7497.
66 N. F. Mott, *Philos. Mag.*, 1969, **19**, 835.
67 A. J. Clough, N. M. Orchanian, J. M. Skelton, A. J. Neer, S. A. Howard, C. A. Downes, L. F. J. Piper, A. Walsh, B. C. Melot and S. C. Marinescu, *J. Am. Chem. Soc.*, 2019, **141**, 16323–16330.
68 S. Lin, P. M. Usov and A. J. Morris, *Chem. Commun.*, 2018, **54**, 6965.
69 B. M. Wiers, M.-L. Foo, N. P. Balsara and J. R. Long, *J. Am. Chem. Soc.*, 2011, **133**, 14522–14525.
70 R. Ameloot, M. Aubrey, B. M. Wiers, A. P. Gmora-Figueroa, S. N. Patel, N. P. Balsara and J. R. Long, *Chem. – Eur. J.*, 2013, **19**, 5533–5536.
71 D. K. Panda, K. Maity, A. Palukoshka, F. Ibrahim and S. Saha, *ACS Sustainable Chem. Eng.*, 2019, **7**, 4619–4624.
72 F. Rouhani, F. Rafizadeh-Masuleh and A. Morsali, *J. Am. Chem. Soc.*, 2019, **141**, 11173–11182.
73 S. Han, S. C. Warren, S. M. Yoon, C. D. Malliakas, X. Hou, Y. Wei, M. G. Kanatzidis and B. A. Grzybowski, *J. Am. Chem. Soc.*, 2015, **137**, 8169–8175.
74 M. A. Gordillo, P. A. Benavides, K. Ma and S. Saha, *ACS Appl. Nano Mater.*, 2022, **5**, 13912–13920.
75 C.-W. Kung, A. E. Platero-Prats, R. J. Drout, J. Kang, T. C. Wang, C. O. Audu, M. C. Hersam, K. W. Chapman, O. K. Farha and J. T. Hupp, *ACS Appl. Mater. Interfaces*, 2018, **10**, 30532–30540.
76 C. J. Pedersen, *Angew. Chem., Int. Ed.*, 1998, **27**, 1021.
77 J. W. Steed, D. R. Turner and K. J. Wallace, *Core Concepts in Supramolecular Chemistry and Nanochemistry*, John Wiley and Sons, West Sussex, UK, 2007.
78 J.-M. Lehn, *Supramolecular Chemistry-Concepts and Perspectives*, Wiley-VCH, Weinheim, Germany, 1995.
79 R. D. Mukhopadhyay, G. Das and A. Ajayaghosh, *Nat. Commun.*, 2018, **9**, 1987.
80 C. Marti-Gastaldo, D. Antypov, J. E. Warren, M. E. Briggs, P. A. Chater, P. V. Wiper, G. J. Miller, Y. Z. Khimyak, G. R. Darling, N. G. Berry and M. J. Rosseinsky, *Nat. Chem.*, 2014, **6**, 343–351.
81 R. Haldar, R. Matsuda, S. Kitagawa, S. J. George and T. K. Maji, *Angew. Chem., Int. Ed.*, 2014, **53**, 11772–11777.
82 T. Haraguchi, K. Otsubo, O. Sakata, A. Fujiwara and H. Kitagawa, *J. Am. Chem. Soc.*, 2016, **138**, 16787–16793.
83 W. Yang, W. Liang, L. A. O'Dell, H. D. Toop, N. Maddigan, X. Zhang, A. Kochubei, C. J. Doonan, Y. Jiang and J. Huang, *JACS Au*, 2021, **1**, 2172–2181.
84 H. Meng, C. Zhao, Y. Li, M. Nie, C. Wang and T. Wang, *Nanoscale*, 2018, **10**, 3291–3298.
85 G. W. Gokel, W. M. Leevy and M. E. Weber, *Chem. Rev.*, 2004, **104**, 2723–2750.
86 A.-M. Caminade and J. P. Majoral, *Chem. Rev.*, 1994, **94**, 1183–1213.
87 B. W. Purse and J. Rebek Jr., *Proc. Natl. Acad. Sci. U. S. A.*, 2005, **102**, 10777–10782.
88 R. Nag and C. P. Rao, *Chem. Commun.*, 2022, **58**, 6044.
89 A. A. Talin, A. Centrone, A. C. Ford, M. E. Foster, V. Stavila, P. Haney, R. A. Kinney, V. Szalai, F. E. Gabaly, H. P. Yoon, F. Léonard and M. D. Allendorf, *Science*, 2014, **343**, 66–69.
90 A. Sengupta, S. Datta, C. Su, T. S. Herng, J. Ding, J. J. Vittal and K. P. Loh, *ACS Appl. Mater. Interfaces*, 2016, **8**, 16154–16159.
91 S. Goswami, D. Ray, K.-I. Otake, C.-W. Kung, S. J. Garibay, T. Islamoglu, A. Atilgan, Y. Cui, C. J. Cramer, O. K. Farha and J. T. Hupp, *Chem. Sci.*, 2018, **9**, 4477–4482.
92 Z. Guo, D. K. Panda, K. Maity, D. Lindsey, T. G. Parker, T. E. Albrecht-Schmitt, J. L. Barreda-Esparza, P. Xiong, W. Zhou and S. Saha, *J. Mater. Chem. C*, 2016, **4**, 894–899.
93 Z. Xin, J. Liu, X. Wang, K. Shen, Z. Yuan, Y. Chen and Y.-Q. Lan, *ACS Appl. Mater. Interfaces*, 2021, **13**, 54959–54966.
94 Q. Wang, L. Shao, Z. Ma, J. Xu, Y. Li and C. Wang, *Electrochim. Acta*, 2018, **281**, 582–593.
95 C. H. Hendon, D. Tiana and A. Walsh, *Phys. Chem. Chem. Phys.*, 2012, **14**, 13120–13132.
96 S. T. Meek, J. A. Greathouse and M. D. Allendorf, *Adv. Mater.*, 2011, **23**, 249–267.
97 S. K. Bhardwaj, N. Bhardwaj, R. Kaur, J. Mehta, A. L. Sharma, K.-H. Kim and A. Deep, *J. Mater. Chem. A*, 2018, **6**, 14992–15009.
98 T. Kitao, Y. Zhang, S. Kitagawa, B. Wang and T. Uemura, *Chem. Soc. Rev.*, 2017, **46**, 3108–3133.
99 K. Leong, M. E. Foster, B. M. Wong, E. D. Spoerke, D. V. Gough, J. C. Deaton and M. D. Allendorf, *J. Mater. Chem. A*, 2014, **2**, 3389.
100 H. Ma, X. Li, T. Yan, Y. Li, Y. Zhang, D. Wu, Q. Wei and B. Du, *Biosens. Bioelectron.*, 2016, **79**, 379–385.
101 D. T. Sun, N. Gasilova, S. Yang, E. Oveisi and W. L. Queen, *J. Am. Chem. Soc.*, 2018, **140**, 16697–16703.
102 A. T. E. Vilian, B. Dinesh, R. Muruganantham, S. R. Choe, S.-M. Kang, Y. S. Huh and Y.-K. Han, *Microchim. Acta*, 2017, **184**, 4793–4801.
103 L. Wang, T. Meng, Y. Fan, C. Chen, Z. Guo, H. Wang and Y. Zhang, *J. Colloid Interface Sci.*, 2018, **524**, 1–7.

104 M. Deng, X. Bo and L. Guo, *J. Electroanal. Chem.*, 2018, **815**, 198–209.

105 W. Meng, Y. Wen, L. Dai, Z. He and L. Wang, *Sens. Actuators, B*, 2018, **260**, 852–860.

106 Y. Dong, C. Duan, Q. Sheng and J. Zheng, *Analyst*, 2019, **144**, 521–529.

107 S. Saha, K. S. Anantharam, N. Hassan, A. Ugale, K. Tarafder and N. Ballav, *Nano Lett.*, 2023, **23**, 9326–9332.

108 Y. Singh, *AIP Conf. Proc.*, 2018, **1953**, 080036.

109 C. Schneider, D. Ukaj, R. Koerver, A. A. Talin, G. Kieslich, S. P. Pujari, H. Zuilhof, J. Janek, M. D. Allendorf and R. A. Fischer, *Chem. Sci.*, 2018, **9**, 7405–7412.

110 K. Thürmer, C. Schneider, V. Stavila, R. W. Friddle, F. Léonard, R. A. Fischer, M. D. Allendorf and A. A. Talin, *ACS Appl. Mater. Interfaces*, 2018, **10**, 39400–39410.

111 S. K. Bhardwaj, A. L. Sharma, N. Bhardwaj, M. Kukkar, A. A. Gill, K.-H. Kim and A. Deep, *Sens. Actuators, B*, 2017, **240**, 10–17.

112 S. Jung, L. Huelsenbeck, Q. Hu, S. Robinson and G. Giri, *ACS Appl. Mater. Interfaces*, 2021, **13**, 10202–10209.

113 H. Shiozawa, B. C. Bayer, H. Peterlik, J. C. Meyer, W. Lang and T. Pichler, *Sci. Rep.*, 2017, **7**, 2439.

114 Q.-Q. Huanga, Y.-J. Lina, R. Zheng, W.-H. Deng, C. Kashi, P. N. Kumar, G.-E. Wang and G. Xu, *Inorg. Chem. Commun.*, 2019, **105**, 119–124.

115 P. Sindhu and N. Ballav, *Inorg. Chem.*, 2023, **62**, 10887–10891.

116 T. Dohi and Y. Kita, *Oxidising Agents*, 2014, ch. 16.

117 M.-H. Zeng, Q.-X. Wang, Y.-X. Tan, S. Hu, H.-X. Zhao, L.-S. Long and M. Kurmoo, *J. Am. Chem. Soc.*, 2010, **132**, 2561–2563.

118 M.-H. Zeng, Z. Yin, Y.-X. Tan, W.-X. Zhang, Y.-P. He and M. Kurmoo, *J. Am. Chem. Soc.*, 2014, **136**, 4680–4688.

119 Y. Kobayashi, B. Jacobs, M. D. Allendorf and J. R. Long, *Chem. Mater.*, 2010, **22**, 4120–4122.

120 Z. Yin, Q.-X. Wang and M.-H. Zeng, *J. Am. Chem. Soc.*, 2012, **134**, 4857–4863.

121 D. Y. Lee, E.-K. Kim, N. K. Shrestha, D. W. Boukhvalov, J. K. Lee and S.-H. Han, *ACS Appl. Mater. Interfaces*, 2015, **7**, 18501–18507.

122 D. Y. Lee, I. Lim, C. Y. Shin, S. A. Patil, W. Lee, N. K. Shrestha, J. K. Lee and S.-H. Han, *J. Mater. Chem. A*, 2015, **3**, 22669–22676.

123 G.-P. Li, K. Zhang, H.-Y. Zhao, L. Hou and Y.-Y. Wang, *ChemPlusChem*, 2017, **82**, 716–720.

124 Y.-Q. Hu, M.-Q. Li, Y. Wang, T. Zhang, P.-Q. Liao, Z. Zheng, X.-M. Chen and Y.-Z. Chen, *Chem. – Eur. J.*, 2017, **23**, 8409–8413.

125 X. Zhang, I. Silva, R. Fazzi, A. M. Sheveleva, X. Han, B. F. Spencer, S. A. Sapchenko, F. Tuna, E. J. L. McInnes, M. Li, S. Yang and M. Schröder, *Inorg. Chem.*, 2019, **58**, 14145–14150.

126 S. Rana, R. Rajendra, B. Dhara, P. K. Jha and N. Ballav, *Adv. Mater. Interfaces*, 2016, **3**, 1500738.

127 Z. Hao, G. Yang, X. Song, M. Zhu, X. Meng, S. Zhao, S. Song and H. Zhang, *J. Mater. Chem. A*, 2014, **2**, 237–244.

128 C. F. Leong, C.-H. Wang, C. D. Ling and D. M. D'Alessandro, *Polyhedron*, 2018, **154**, 334–342.

129 J. Su, T.-H. Hu, R. Murase, H.-Y. Wang, D. M. D'Alessandro, M. Kurmoo and J.-L. Zuo, *Inorg. Chem.*, 2019, **58**, 3698–3706.

130 H.-Y. Wang, J.-Y. Ge, C. Hua, C.-Q. Jiao, Y. Wu, C. F. Leong, D. M. D'Alessandro, T. Liu and J.-L. Zuo, *Angew. Chem., Int. Ed.*, 2017, **56**, 5465–5470.

131 M. A. Gordillo, P. A. Benavides, D. K. Panda and S. Saha, *ACS Appl. Mater. Interfaces*, 2020, **12**, 12955–12961.

132 M. A. Gordillo, P. A. Benavides, C. McMillen and S. Saha, *Mater. Adv.*, 2022, **3**, 6157–6160.

133 G. Valente, M. Esteve-Rochina, A. Paracana, A. Rodríguez-Diéguez, D. Choquesillo-Lazarte, E. Ortí, J. Calbo, M. Ilkaeva, L. Mafra, M. A. Hernández-Rodríguez, J. Rocha, H. Alves and M. Souto, *Mol. Syst. Des. Eng.*, 2022, **7**, 1065.

134 C. Rovira, *Chem. Rev.*, 2004, **104**, 5289–5317.

135 D. Canevet, M. Sallé, G. Zhang, D. Zhang and D. Zhu, *Chem. Commun.*, 2009, 2245–2269.

136 S. Benmansour and C. J. Gómez-García, *Magnetochemistry*, 2021, **7**, 93.

137 E. Coronado, J. R. Galán-Mascarós, C. J. Gómez-García and V. Laukhin, *Nature*, 2000, **408**, 447–449.

138 A. Alberola, E. Coronado, J. R. Galán-Mascarós, C. Giménez-Saiz and C. J. Gómez-García, *J. Am. Chem. Soc.*, 2003, **125**, 10774–10775.

139 E. Coronado, J. R. Galán-Mascarós, C. J. Gómez-García, E. Martínez-Ferrero and S. Smaalen, *Inorg. Chem.*, 2004, **43**, 4808–4810.

140 A. Alberola, E. Coronado, J. R. Galan-Mascaros, C. Gimenez-Saiz, C. J. Gómez-García and F. M. Romero, *Synth. Met.*, 2003, **133**, 509–513.

141 A. Klehe, V. Laukhin, P. A. Goddard, J. A. Symington, J. Aghassi, J. Singleton, E. Coronado, J. R. Galán-Mascarós, C. J. Gómez-García and C. Gimenez-Saiz, *Synth. Met.*, 2003, **133–134**, 549–551.

142 A. Alberola, E. Coronado, J. R. Galán-Mascarós, C. Giménez-Saiz, C. J. Gómez-García, E. Martínez-Ferrero and A. Murcia-Martínez, *Synth. Met.*, 2003, **135**, 687–689.

143 E. Coronado, J. R. Galán-Mascarós, C. J. Gómez-García, E. Martínez-Ferrero and S. Van Smaalen, *Inorg. Chem.*, 2004, **43**, 4808–4810.

144 U. Geiser, H. H. Wang, K. M. Donega, B. A. Anderson, J. M. Williams and J. F. Kwak, *Inorg. Chem.*, 1986, **25**, 401–402.

145 B. Zhang, Y. Zhang and D. Zhu, *Chem. Commun.*, 2012, **48**, 197–199.

146 B. Zhang, Y. Zhang, Z. Wang, S. Gao, Y. Guo, F. Liu and D. Zhu, *CrystEngComm*, 2013, **15**, 3529–3535.

147 Z. Guo, D. K. Panda, M. A. Gordillo, A. Khatun, H. Wu, W. Zhou and S. Saha, *ACS Appl. Mater. Interfaces*, 2017, **9**, 32413–32417.

148 A. Corma, V. Fornes, M. S. Galletero, H. García and C. J. Gómez-García, *Phys. Chem. Chem. Phys.*, 2001, **3**, 1218–1222.

149 B. M. Illescas and N. Martín, *C. R. Chim.*, 2006, **9**, 1038–1050.

150 D. Ray, S. Goswami, J. Duan, J. T. Hupp, C. J. Cramer and L. Gagliardi, *Chem. Mater.*, 2021, **33**, 1182–1189.

151 M. Souto, J. Calbo, S. Mañas-Valero, A. Walsh and G. Mínguez-Espallargas, *Beilstein J. Nanotechnol.*, 2019, **10**, 1883–1893.

152 X. Liu, M. Kozlowska, T. Okkali, D. Wagner, T. Higashino, G. Brenner-Weiß, S. M. Marschner, Z. Fu, Q. Zhang, H. Imahori, S. Bräse, W. Wenzel, C. Wöll and L. Heinke, *Angew. Chem., Int. Ed.*, 2019, **58**, 9590–9595.

153 S. Kaur, M. Kaur, P. Kaur, K. Clays and K. Singh, *Coord. Chem. Rev.*, 2017, **343**, 185–219.

154 Z. Huang, H. Yu, L. Wang, X. Liu, T. Lin, F. Haq, S. Z. Vatsadze and D. A. Lemenovskiy, *Coord. Chem. Rev.*, 2021, **430**, 213737.

155 M. Clemente-Leon, E. Coronado, J. R. GalanMascaros and C. J. Gómez-García, *Chem. Commun.*, 1997, 1727–1728.

156 E. Coronado, J. R. Galán-Mascarós, C. J. Gómez-García and J. M. Martínez-Agudo, *Adv. Mater.*, 1999, **11**, 558–561.

157 E. Coronado, J. R. Galán-Mascarós, C. J. Gómez-García and R. Burriel, *J. Magn. Magn. Mater.*, 1999, **196–197**, 558–560.

158 E. Coronado, J. R. Galan-Mascaros and C. J. Gómez-García, *Mol. Cryst. Liq. Cryst.*, 1999, **334**, 679–691.

159 E. Coronado, J. R. Galán-Mascarós, C. J. Gómez-García, J. Ensling and P. Gütlich, *Chem. – Eur. J.*, 2000, **6**, 552–563.

160 E. Coronado, M. Clemente-León, J. R. Galán-Mascarós, C. Giménez-Saiz, C. J. Gómez-García and E. Martínez-Ferrero, *J. Chem. Soc., Dalton Trans.*, 2000, 3955–3961.

161 E. Coronado, J. R. Galán-Mascarós, C. J. Gómez-García and J. M. Martínez-Agudo, *Synth. Met.*, 2001, **122**, 501–507.

162 E. Coronado, J. R. Galán-Mascarós, C. Giménez-Saiz, C. J. Gómez-García, J. M. Martínez-Agudo and E. Martínez-Ferrero, *Polyhedron*, 2003, **22**, 2381–2386.

163 S. Hermes, F. Schröder, S. Amirjalayer, R. Schmid and R. A. Fischer, *J. Mater. Chem.*, 2006, **16**, 2464–2472.

164 M. Meilikhov, K. Yusenko and R. A. Fischer, *J. Am. Chem. Soc.*, 2009, **131**, 9644–9645.

165 R. Heck, O. Shekhah, O. Zybaylo, P. G. Weidler, F. Friedrich, R. Maul, W. Wenzel and C. Wöll, *Polymers*, 2011, **3**, 1565–1574.

166 A. Dragässer, O. Shekhah, O. Zybaylo, C. Shen, M. Buck, C. Wöll and D. Schlettwein, *Chem. Commun.*, 2012, **48**, 663–665.

167 J. Liu, T. Wächter, A. Irmler, P. G. Weidler, H. Gliemann, F. Pauly, V. Mugnaini, M. Zharnikov and C. Wöll, *ACS Appl. Mater. Interfaces*, 2015, **7**, 9824–9830.

168 I. Hod, O. K. Farha and J. T. Hupp, *Chem. Commun.*, 2016, **52**, 1705–1708.

169 C.-W. Kung, K. Otake, C. T. Buru, S. Goswami, Y. Cui, J. T. Hupp, A. M. Spokoyny and O. K. Farha, *J. Am. Chem. Soc.*, 2018, **140**, 3871–3875.

170 V. Fornés, H. García, C. J. Gómez-García and E. Peris, *Chem. Phys. Lett.*, 2005, **415**, 271–273.

171 S. Gupta, H. Tanaka, T. Sato, S. Ye, B. K. Breedlove, H. Iguchi and H. Takaishi, *Inorg. Chem.*, 2022, **61**, 4414–4420.

172 J. Zhang, S. Guo, Y. Yang, W. Liang, M. Lu, X. Zhang, H. Xiao, Y. Li, R. Yuan and D. Xiao, *Biosens. Bioelectron.*, 2023, **227**, 115157.

173 H. Staudinger, *Ber. Dtsch. Chem. Ges. B*, 1920, **53**, 1073–1085.

174 S. Begum, Z. Hassan, S. Brase and M. Tsotsalas, *Langmuir*, 2020, **36**, 10657–10673.

175 M. N. Gueye, A. Carella, J. Faure-Vincent, R. Demadrille and J.-P. Simonato, *Prog. Mater. Sci.*, 2020, **108**, 100616.

176 B. Wessling, *Synth. Met.*, 1998, **93**, 143–I54.

177 S. Raman and A. R. Sankar, *J. Mater. Sci.*, 2022, **57**, 13152–13178.

178 T. P. Kaloni, P. K. Giesbrecht, G. Schreckenbach and M. S. Freund, *Chem. Mater.*, 2017, **29**, 10248–10283.

179 H. Shirakawa, *Angew. Chem., Int. Ed.*, 2001, **40**, 2574–2580.

180 B. L. Ouay, M. Boudot, T. Kitao, T. Yanagida, S. Kitagawa and T. Uemura, *J. Am. Chem. Soc.*, 2016, **138**, 10088–10091.

181 A. Jadhav, K. Gupta, P. Ninawe and N. Ballav, *Angew. Chem., Int. Ed.*, 2019, **59**, 2215–2219.

182 T. Wang, M. Farajollahi, S. Henke, T. Zhu, S. R. Bajpe, S. Sun, J. S. Barnard, J. S. Lee, J. D. W. Madden, A. K. Cheetham and S. K. Smoukov, *Mater. Horiz.*, 2017, **4**, 64–71.

183 A. Khatun, A. Yadav, S. Zhang and S. Saha, *Mater. Today Chem.*, 2002, **24**, 100981.

184 P. Salcedo-Abraira, A. Santiago-Portillo, P. Atienzar, P. Bordet, F. Salles, N. Guillou, E. Elkaim, H. García, S. Navalon and P. Horcajada, *Dalton Trans.*, 2019, **48**, 9807–9817.

185 A. Mohmeyer, A. Schaate, B. Hoppe, H. A. Schulze, T. Heinemeyer and P. Behrens, *Chem. Commun.*, 2019, **55**, 3367–3370.

186 S. Zhang, W. Zhang, A. Yadav, J. Baker and S. Saha, *Inorg. Chem.*, 2023, **62**, 18999–19005.

187 N. Yanai, T. Uemura, M. Ohba, Y. Kadowaki, M. Maesato, M. Takenaka, S. Nishitsuji, H. Hasegawa and S. Kitagawa, *Angew. Chem., Int. Ed.*, 2008, **47**, 9883–9886.

188 T. Uemura, Y. Kadowaki, N. Yanai and S. Kitagawa, *Chem. Mater.*, 2009, **21**, 4096–4098.

189 Q.-X. Wang and C.-Y. Zhang, *Macromol. Rapid Commun.*, 2011, **32**, 1610–1614.

190 B. Dhara, S. S. Nagarkar, J. Kumar, V. Kumar, P. K. Jha, S. K. Ghosh, S. Nair and N. Ballav, *J. Phys. Chem. Lett.*, 2016, **7**, 2945–2950.

191 Y. Jiao, J. Li, A. Xie, F. Wu, K. Zhang, W. Donga and X. Zhu, *Compos. Sci. Technol.*, 2019, **174**, 232–240.

192 X. Yuan, Q. Mu, S. Xue, Y. Su, Y. Zhu, H. Sun, Z. Deng and Y. Peng, *J. Energy Chem.*, 2021, **60**, 202–208.

193 X. Fang, S. Lei, Z. Feng and J. Ou, *ChemElectroChem*, 2023, **10**, e202201147.

194 T. P. Vello, L. G. S. Albano, T. C. dos Santos, J. C. Colletti, C. V. S. Batista, V. F. C. Leme, T. C. dos Santos, M. P. D. C. Miguel, D. Henrique, S. de Camargo and C. C. B. Bufon, *Nano Micro Small*, 2024, **20**, 2305501.

195 L. Shao, Q. Wang, Z. Ma, Z. Ji, X. Wang, D. Song, Y. Liu and N. Wang, *J. Power Sources*, 2018, **379**, 350–361.

196 C.-C. Lin, Y.-C. Huang, M. Usman, W.-H. Chao, W.-K. Lin, T.-T. Luo, W.-T. Whang, C.-H. Chen and K.-L. Lu, *ACS Appl. Mater. Interfaces*, 2019, **11**, 3400–3406.

197 W. Xu, Y. Zhao, H. Wang, H. Wang, F. Pan, R. Xu and H. Hou, *Chem. – Eur. J.*, 2021, **27**, 5011–5018.

198 M. W. A. MacLean, T. Kitao, T. Suga, M. Mizuno, S. Seki, T. Uemura and S. Kitagawa, *Angew. Chem., Int. Ed.*, 2016, **55**, 708–713.

199 T. C. Wang, I. Hod, C. O. Audu, N. A. Vermeulen, S. T. Nguyen, O. K. Farha and J. T. Hupp, *ACS Appl. Mater. Interfaces*, 2017, **9**, 12584–12591.

200 M. S. Galletero, M. Alvaro, H. García, C. J. Gómez-García and A. K. Lay, *Phys. Chem. Chem. Phys.*, 2002, **4**, 115–120.

201 S. Klyatskaya, A. B. Kanj, C. Molina-Jirón, S. Heidrich, L. Velasco, C. Natzeck, H. Gliemann, S. Heissler, P. Weidler, W. Wenzel, C. C. B. Bufon, L. Heinke, C. Wöll and M. Ruben, *ACS Appl. Mater. Interfaces*, 2020, **12**, 30972–30979.

202 D. Ukaj, H. Bunzen, J. Berger, G. Kieslich and R. A. Fischer, *Chem. Mater.*, 2021, **33**, 2532–2542.

203 Z. Zhuang and D. Liu, *Nano-Micro Lett.*, 2020, **12**, 132.

204 J. Liu and C. Woll, *Chem. Soc. Rev.*, 2017, **46**, 5730–5770.

205 C. Crivello, S. Sevim, O. Graniel, C. Franco, S. Pané, J. Puigmartí-Luis and D. Muñoz-Rojas, *Mater. Horiz.*, 2021, **8**, 168–178.

206 M. D. Allendorf, R. Dong, X. Feng, S. Kaskel, D. Matoga and V. Stavila, *Chem. Rev.*, 2020, **120**, 8581–8640.

207 I. Stassen, N. Burtch, A. Talin, P. Falcaro, M. Allendorf and R. Ameloot, *Chem. Soc. Rev.*, 2017, **46**, 3185–3241.

208 X. Mu, W. Wang, C. Sun, J. Wang, C. Wang and M. Knez, *Adv. Mater. Interfaces*, 2021, **8**, 2002151.

209 V. Rubio-Giménez, S. Tatay and C. Martí-Gastaldo, *Chem. Soc. Rev.*, 2020, **49**, 5601–5638.

210 M. Zhao, Q. Lu, Q. Ma and H. Zhang, *Small Methods*, 2017, **1**, 1600030.

211 S. Suárez-García, N. N. Adarsh, G. Molnár, A. Bousseksou, Y. García, M. M. Dîrtu, J. Saiz-Poseu, R. Robles, P. Ordejón and D. Ruiz-Molina, *ACS Appl. Nano Mater.*, 2018, **1**, 2662–2668.

212 Q. Zeng, L. Wang, Y. Huang, S.-L. Zheng, Y. He, J. He, W.-M. Liao, G. Xu, M. Zeller and Z. Xu, *Chem. Commun.*, 2020, **56**, 3645–3648.

213 S. Benmansour, A. Abherve, P. Gómez-Claramunt, C. Vallés-García and C. J. Gómez-García, *ACS Appl. Mater. Interfaces*, 2017, **9**, 26210–26218.

214 P. Horcajada, C. Serre, D. Grosso, C. Boissière, S. Perruchas, C. Sanchez and G. Férey, *Adv. Mater.*, 2009, **21**, 1931–1935.

215 A. Demessence, P. Horcajada, C. Serre, C. Boissière, D. Grosso, C. Sanchez and G. Férey, *Chem. Commun.*, 2009, 7149–7151.

216 A. Demessence, C. Boissiere, D. Grosso, P. Horcajada, C. Serre, G. Férey, G. J. A. A. Soler-Illiac and C. Sanchez, *J. Mater. Chem.*, 2010, **20**, 7676–7681.

217 Y.-N. Gong, T. Ouyang, C.-T. Hea and T.-B. Lu, *Chem. Sci.*, 2016, **7**, 1070–1075.

218 Y. Horiuchi, T. Toyao, K. Miyahara, L. Zakary, D. D. Van, Y. Kamata, T.-H. Kim, S. W. Leed and M. Matsuoka, *Chem. Commun.*, 2016, **52**, 5190–5193.

219 J. Campbell, G. Székely, R. P. Davies, D. C. Braddock and A. G. Livingston, *J. Mater. Chem. A*, 2014, **2**, 9260–9271.

220 C.-W. Kung, T.-H. Chang, L.-Y. Chou, J. T. Hupp, O. K. Farha and K.-C. Ho, *Chem. Commun.*, 2015, **51**, 2414–2417.

221 Y. Wang, F. Zhang, Z. Fang, M. Yu, Y. Yang and K.-L. Wong, *J. Mater. Chem. C*, 2016, **4**, 8466–8472.

222 M. A. Gordillo, D. K. Panda and S. Saha, *ACS Appl. Mater. Interfaces*, 2019, **11**, 3196–3206.

223 I. Hod, W. Bury, D. M. Karlin, P. Deria, C.-W. Kung, M. J. Katz, M. So, B. Klahr, D. Jin, Y.-W. Chung, T. W. Odom, O. K. Farha and J. T. Hupp, *Adv. Mater.*, 2014, **26**, 6295–6300.

224 I. Hod, W. Bury, D. M. Gardner, P. Deria, V. Roznyatovskiy, M. R. Wasielewski, O. K. Farha and J. T. Hupp, *J. Phys. Chem. Lett.*, 2015, **6**, 586–591.

225 H. Han, X. Yuan, Z. Zhang and J. Zhang, *Inorg. Chem.*, 2019, **58**, 3196–3202.

226 C. O. Audu, D. Chen, C.-W. Kung, R. Q. Snurr, S. T. Nguyen, O. K. Farha and J. T. Hupp, *Langmuir*, 2021, **37**, 9405–9414.

227 J.-f Feng, S.-Y. Gao, T.-f Liu, J. Shi and R. Cao, *ACS Appl. Mater. Interfaces*, 2018, **10**, 6014–6023.

228 J.-f Feng, X. Yang, S.-y Gao, J. Shi and R. Cao, *Langmuir*, 2017, **33**, 14238–14243.

229 U. Müller, H. Pütter, M. Hesse, H. Wessel, M. Schubert, J. Huff and M. Guzmann, WO 2005/049892, 2006.

230 R. Ameloot, L. Stappers, J. Fransaer, L. Alaerts, B. F. Sels and D. E. De Vos, *Chem. Mater.*, 2009, **21**, 2580–2582.

231 R. Ameloot, L. Pandey, M. V. der Auweraer, L. Alaerts, B. F. Selsa and D. E. De Vos, *Chem. Commun.*, 2010, **46**, 3735–3737.

232 N. Campagnol, T. V. Assche, T. Boudewijns, J. Denayer, K. Binnemans, D. De Vos and J. Fransaer, *J. Mater. Chem. A*, 2013, **1**, 5827–5830.

233 P. Schäfer, M. A. van der Veenb and K. F. Domke, *Chem. Commun.*, 2016, **52**, 4722–4725.

234 I. Stassen, M. Styles, T. V. Assche, N. Campagnol, J. Fransaer, J. Denayer, J.-C. Tan, P. Falcaro, D. D. Vos and R. Ameloot, *Chem. Mater.*, 2015, **27**, 1801–1807.

235 J. L. Hauser, M. Tso, K. Fitchmun and S. R. J. Oliver, *Cryst. Growth Des.*, 2019, **19**, 2358–2365.

236 M. Li and M. Dincă, *J. Am. Chem. Soc.*, 2011, **133**, 12926–12929.

237 H. Liu, H. Wang, T. Chu, M. Yu and Y. Yang, *J. Mater. Chem. C*, 2014, **2**, 8683–8690.

238 H. Liu, T. Chu, Z. Rao, S. Wang, Y. Yang and W.-T. Wong, *Adv. Opt. Mater.*, 2015, **3**, 1545–1550.

239 Z. Wang, H. Liu, S. Wang, Z. Rao and Y. Yang, *Sens. Actuators, B*, 2015, **220**, 779–787.

240 R. Ameloot, F. Vermoortele, W. Vanhove, M. B. J. Roeffaers, B. F. Sels and D. E. De Vos, *Nat. Chem.*, 2011, **3**, 382–387.

241 T. Kambe, R. Sakamoto, K. Hoshiko, K. Takada, M. Miyachi, J.-H. Ryu, S. Sasaki, J. Kim, K. Nakazato, M. Takata and H. Nishihara, *J. Am. Chem. Soc.*, 2013, **135**, 2462–2465.

242 X. Huang, P. Sheng, Z. Tu, F. Zhang, J. Wang, H. Geng, Y. Zou, C.-A. Di, Y. Yi, Y. Sun, W. Xu and D. Zhu, *Nat. Commun.*, 2015, **6**, 7408.

243 I.-F. Chen, C.-F. Lu and W.-F. Su, *Langmuir*, 2018, **34**, 15754–15762.

244 X.-J. Bai, D. Chen, L.-L. Li, L. Shao, W.-X. He, H. Chen, Y.-N. Li, X.-M. Zhang, L.-Y. Zhang, T.-Q. Wang, Y. Fu and W. Qi, *ACS Appl. Mater. Interfaces*, 2018, **10**, 25960–25966.

245 R. Makiura and O. Konovalov, *Sci. Rep.*, 2013, **3**, 2506.
246 G. Wu, J. Huang, Y. Zang, J. He and G. Xu, *J. Am. Chem. Soc.*, 2017, **139**, 1360–1363.
247 R. Makiura, S. Motoyama, Y. Umemura, H. Yamanaka, O. Sakata and H. Kitagawa, *Nat. Mater.*, 2010, **9**, 565–571.
248 S. Motoyama, R. Makiura, O. Sakata and H. Kitagawa, *J. Am. Chem. Soc.*, 2011, **133**, 5640–5643.
249 D. Käfer, G. Witte, P. Cyganik, A. Terfort and C. Wöll, *J. Am. Chem. Soc.*, 2006, **128**, 1723–1732.
250 D. Zacher, A. Baunemann, S. Hermes and R. A. Fischer, *J. Mater. Chem.*, 2007, **17**, 2785–2792.
251 S. Hermes, F. Schröder, R. Chelmowski, C. Wöll and R. A. Fischer, *J. Am. Chem. Soc.*, 2005, **127**, 13744–13745.
252 O. Shekhah, H. Wang, T. Strunskus, P. Cyganik, D. Zacher, R. Fischer and C. Wöll, *Langmuir*, 2007, **23**, 7440–7442.
253 O. Shekhah, H. Wang, D. Zacher, R. A. Fischer and C. Wöll, *Angew. Chem. Int. Ed.*, 2009, **48**, 5038–5041.
254 Y. Zhao, N. Kornienko, Z. Liu, C. Zhu, S. Asahina, T.-R. Kuo, W. Bao, C. Xie, A. Hexemer, O. Terasaki, P. Yang and O. M. Yaghi, *J. Am. Chem. Soc.*, 2015, **137**, 2199–2202.
255 P. Falcaro, K. Okada, T. Hara, K. Ikigaki, Y. Tokudome, A. W. Thornton, A. J. Hill, T. Williams, C. Doonan and M. Takahashi, *Nat. Mater.*, 2017, **16**, 342–348.
256 I. Stassen, D. De Vos and R. Ameloot, *Chem. – Eur. J.*, 2016, **22**, 14452–14460.
257 D. Fischer, L. V. Meyer, M. Jansen and K. Mller-Buschbaum, *Angew. Chem., Int. Ed.*, 2014, **53**, 706–710.
258 D. Fischer, A. von Mankowski, A. Ranft, S. K. Vasa, R. Linser, J. Mannhart and B. V. Lotsch, *Chem. Mater.*, 2017, **29**, 5148–5155.
259 O. L. Rose, A. Bonciu, V. Marascu, A. Matei, Q. Liu, L. Rusen, V. Dinca and C. Z. Dinu, *Nanomaterials*, 2021, **11**, 1367.
260 I. Stassen, M. Styles, G. Grenci, H. V. Gorp, W. Vanderlinden, S. D. Feyter, P. Falcaro, D. De Vos, P. Vereecken and R. Ameloot, *Nat. Mater.*, 2016, **15**, 304–310.
261 T. Stassin, I. Stassen, J. Marreiros, A. J. Cruz, R. Verbeke, M. Tu, H. Reinsch, M. Dickmann, W. Egger, I. F. J. Vankelecom, D. E. De Vos and R. Ameloot, *Chem. Mater.*, 2020, **32**, 1784–1793.
262 M. Choe, J. Y. Koo, I. Park, H. Ohtsu, J. H. Shim, H. C. Choi and S. S. Park, *J. Am. Chem. Soc.*, 2022, **144**, 16726–16731.
263 L. D. Salmi, M. J. Heikkilä, E. Puukilainen, T. Sajavaara, D. Grosso and M. Ritala, *Microporous Mesoporous Mater.*, 2013, **182**, 147–154.
264 E. Ahvenniemi and M. Karppinen, *Chem. Commun.*, 2016, **52**, 1139–1142.
265 E. Ahvenniemi and M. Karppinen, *Chem. Mater.*, 2016, **28**, 6260–6265.
266 K. B. Lausund, V. Petrovic and O. Nilsen, *Dalton Trans.*, 2017, **46**, 16983–16992.
267 R. Ranjan and M. Tsapatsis, *Chem. Mater.*, 2009, **21**, 4920–4924.
268 O. Abuzalat, D. Wong, M. Elsayed, S. Park and S. Kim, *Ultrason. Sonochem.*, 2018, **45**, 180–188.
269 J. U. Balderas, D. Navarro, V. Vargas, M. M. Tellez-Cruz, S. Carmona and C. Falcony, *J. Lumin.*, 2019, **212**, 322–327.
270 Y. Yoo and H.-K. Jeong, *Chem. Commun.*, 2008, 2441–2443.
271 L. Fan, M. Xue, Z. Kang, H. Li and S. Qiu, *J. Mater. Chem.*, 2012, **22**, 25272.
272 V. M. A. Melgar, H. T. Kwon and J. Kim, *J. Membr. Sci.*, 2014, **459**, 190–196.
273 Y. Chen, S. Li, X. Pei, J. Zhou, X. Feng, S. Zhang, Y. Cheng, H. Li, R. Han and B. Wang, *Angew. Chem., Int. Ed.*, 2016, **55**, 3419–3423.
274 B. Zhu, D. Wen, Z. Liang and R. Zou, *Coord. Chem. Rev.*, 2021, **446**, 214119.
275 C. Li, X. Sun, Y. Yao and G. Hong, *Mater. Today Nano*, 2021, **13**, 100105.
276 Q. Lu, Y. Yu, Q. Ma, B. Chen and H. Zhang, *Adv. Mater.*, 2016, **28**, 1917.
277 M. Fang, G. Dong, R. Wei and J. C. Ho, *Adv. Energy Mater.*, 2017, **7**, 1700559.
278 I. Roger, M. A. Shipman and M. D. Symes, *Nat. Rev. Chem.*, 2017, **1**, 0003.
279 Y. Yan, J. Lin, T. Xu, B. Liu, K. Huang, L. Qiao, S. Liu, J. Cao, S. C. Jun, Y. Yamauchi and J. Qi, *Adv. Energy Mater.*, 2022, **12**, 2200434.
280 Y. Wang, H. Lv, L. Sun, F. Jia and B. Liu, *Adv. Energy Mater.*, 2022, **12**, 2201478.
281 X. Dai, M. Liu, Z. Li, A. Jin, Y. Ma, X. Huang, H. Sun, H. Wang and X. Zhang, *J. Phys. Chem. C*, 2016, **120**, 12539–12548.
282 L. Deng, F. Hu, M. Ma, S.-C. Huang, Y. Xiong, H.-Y. Chen, L. Li and S. Peng, *Angew. Chem., Int. Ed.*, 2021, **60**, 22276–22282.
283 M. G. Walter, E. L. Warren, J. R. Mckone, S. W. Boettcher, Q. Mi, E. A. Santori and N. S. Lewis, *Chem. Rev.*, 2010, **110**, 6446.
284 D. Furlong, D. Yates, T. Healy and S. Trasatti, *Electrodes of Conductive Metallic Oxides, Part B*, Elsevier, Amsterdam, 1981, p. 367.
285 C. C. McCrory, S. Jung, I. M. Ferrer, S. M. Chatman, J. C. Peters and T. F. Jaramillo, *J. Am. Chem. Soc.*, 2015, **137**, 4347.
286 Z. Gao, Y. Lai, L. Gong, L. Zhang, S. Xi, J. Sun, L. Zhang and F. Luo, *ACS Catal.*, 2022, **12**, 9101–9113.
287 W. Zhang, Y. Wang, H. Zheng, R. Li, Y. Tang, B. Li, C. Zhu, L. You, M.-R. Gao, Z. Liu, S.-H. Yu and K. Zhou, *ACS Nano*, 2020, **14**, 1971–1981.
288 W. Luo, L. Tang, X. Wang, S.-J. Lin and Z. Cai, *ACS Appl. Nano Mater.*, 2023, **6**, 22406–22415.
289 N. Zion, A. Friedman, N. Levy and L. Elbaz, *Adv. Mater.*, 2018, **30**, 1800406.
290 S. Chatterjee, K. Sengupta, B. Mondal, S. Dey and A. Dey, *Acc. Chem. Res.*, 2017, **50**, 1744–1753.
291 P. Miao, G. Li, G. Zhang and H. Lu, *J. Energy Chem.*, 2014, **23**, 507–512.
292 S. Patra, S. Sene, C. Mousty, C. Serre, A. Chaussé, L. Legrand and N. Steunou, *ACS Appl. Mater. Interfaces*, 2016, **8**, 20012–20022.
293 K. Cho, S.-H. Han and M. P. Suh, *Angew. Chem., Int. Ed.*, 2021, **60**, 22276–22282.

294 X. Si, H. Zhao, B. Yi, L. Zhou, Y. Ling, Y. An, Y. Wang, H. K. Lee, C.-K. Tsung, Y. Ma and L.-Y. Chou, *Nanoscale*, 2022, **14**, 9655–9660.

295 H. Liu, H. Wang, Q. Song, K. Küster, U. Starke, P. A. van Aken and E. Klemm, *Angew. Chem., Int. Ed.*, 2022, **61**, e202117058.

296 F. N. Al-Rowaili, A. Jamal, M. S. Ba Shammakh and A. Rana, *ACS Sustainable Chem. Eng.*, 2018, **6**, 15895–15914.

297 Y. Liu, S. Li, L. Dai, J. Li, J. Lv, Z. Zhu, A. Yin, P. Li and B. Wang, *Angew. Chem., Int. Ed.*, 2021, **60**, 16409–16415.

298 T. Yan, J.-H. Guo, Z.-Q. Liu and W.-Y. Sun, *ACS Appl. Mater. Interfaces*, 2021, **13**, 25937–25945.

299 C.-W. Kung, C. O. Audu, A. W. Peters, H. Noh, O. K. Farha and J. T. Hupp, *ACS Energy Lett.*, 2017, **2**, 2394–2401.

300 T. Yan, J.-H. Guo, Z.-Q. Liu and W.-Y. Sun, *ACS Appl. Mater. Interfaces*, 2021, **13**, 25937–25945.

301 Z. Xin, J. Liu, X. Wang, K. Shen, Z. Yuan, Y. Chen and Y.-Q. Lan, *ACS Appl. Mater. Interfaces*, 2021, **13**, 54959–54966.

302 R. Schlogl, *Angew. Chem., Int. Ed.*, 2003, **42**, 2004–2008.

303 H. He, Q.-Q. Zhu, Y. Yan, H.-W. Zhang, Z.-Y. Han, H. Sun, J. Chen, C.-P. Li, Z. Zhang and M. Du, *Appl. Catal., B*, 2022, **302**, 120840.

304 S. Behera, S. Dinda, R. Saha and B. Mondal, *ACS Catal.*, 2023, **13**, 469–474.

305 M. Deng, X. Bo and L. Guo, *J. Electroanal. Chem.*, 2018, **815**, 198–209.

306 L. Wang, T. Meng, Y. Fan, C. Chen, Z. Guo, H. Wang and Y. Zhang, *J. Colloid Interface Sci.*, 2018, **524**, 1–7.

307 M. G. Campbell and M. Dincă, *Sensors*, 2017, **17**, 1108.

308 W.-T. Koo, J.-S. Jang and I.-D. Kim, *Chem*, 2019, **5**, 1938–1963.

309 C.-S. Liu, J. Li and H. Pang, *Coord. Chem. Rev.*, 2020, **410**, 213222.

310 M. D. Allendorf, R. Dong, X. Feng, S. Kaskel, D. Matoga and V. Stavila, *Chem. Rev.*, 2020, **120**, 8581–8640.

311 Y.-M. Jo, Y. K. Jo, J.-H. Lee, H. W. Jang, I.-S. Hwang and D. J. Yoo, *Adv. Mater.*, 2023, 2206842.

312 V. N. Palakollu, D. Chen, J.-N. Tang, L. Wang and C. Liu, *Microchim. Acta*, 2022, **189**, 161.

313 H. Shiozawa, B. C. Bayer, H. Peterlik, J. C. Meyer, W. Lang and T. Pichler, *Sci. Rep.*, 2017, **7**, 2439.

314 J.-O. Kim, W.-T. Koo, H. Kim, C. Park, T. Lee, C. A. Hutomo, S. Q. Choi, D. S. Kim, I.-D. Kim and S. Park, *Nat. Commun.*, 2021, **12**, 4294.

315 W.-T. Koo, S.-J. Kim, J.-S. Jang, D.-H. Kim and I.-D. Kim, *Adv. Sci.*, 2019, **6**, 1900250.

316 R. Zheng, Z.-H. Fu, W.-H. Deng, Y. Wen, A.-Q. Wu, X.-L. Ye and G. Xu, *Angew. Chem., Int. Ed.*, 2022, **61**, e202212797.

317 H. Lim, H. Kwon, H. Kang, J. E. Jang and H.-J. Kwon, *Nat. Commun.*, 2023, **14**, 3114.

318 S. K. Bhardwaj, A. L. Sharma, N. Bhardwaj, M. Kukkar, A. A. S. Gill, K.-H. Kim and A. Deep, *Sens. Actuators, B*, 2017, **240**, 10–17.

319 S. P. Selvam, A. N. Kadam, K. R. Maiyelvaganan, M. Prakash and S. Cho, *Biosens. Bioelectron.*, 2021, **187**, 113302.

320 Z.-Z. Ma, Y.-S. Wang, B. Liu, H. Jiao and L. Xu, *Chemosensors*, 2022, **10**, 416.

321 T. Wang, H. C. Chen, F. Yu, X. S. Zhao and H. Wang, *Energy Storage Mater.*, 2019, **16**, 545–573.

322 T. Wang, J. Lei, Y. Wang, L. Pang, F. Pan, K. J. Chen and H. Wang, *Small*, 2022, **18**, 2203307.

323 H.-N. Wang, M. Zhang, A.-M. Zhang, F.-C. Shen, X.-K. Wang, S.-N. Sun, Y.-J. Chen and Y.-Q. Lan, *ACS Appl. Mater. Interfaces*, 2018, **10**, 32265–32270.

324 Y.-Z. Liu, W. Yao, H.-M. Gan, C.-Y. Sun, Z.-M. Su and X.-L. Wang, *Chem. – Eur. J.*, 2019, **25**, 16617–16624.

325 T. Wei, M. Zhang, P. Wu, Y.-J. Tang, S.-L. Li, F.-C. Shen, X.-L. Wang, X.-P. Zhou and Y.-Q. Lan, *Nano Energy*, 2017, **34**, 205–214.

326 N. Ferhi, B. D. Assresahegn, C. Ardila-Suarez, N. Dissem, D. Guay and A. Duong, *ACS Appl. Energy Mater.*, 2022, **5**, 1235–1243.

327 K. Zheng, H. Tan, L. Wang, J. Liu, M. Ding and D. Jia, *Adv. Mater. Interfaces*, 2021, **8**, 2002145.

328 M.-D. Tsai, Y.-L. Chen, J.-W. Chang, S.-C. Yang and C.-W. Kung, *ACS Appl. Energy Mater.*, 2023, **6**, 11268–11277.

329 Z. Wu, J. Xie, Z. J. Xu, S. Zhang and Q. Zhang, *J. Mater. Chem. A*, 2019, **7**, 4259–4290.

330 L. Guo, J. Sun, W. Zhang, L. Hou, L. Liang, Y. Liu and C. Yuan, *ChemSusChem*, 2019, **12**, 5051–5058.

331 J. Yan, Y. Cui, M. Xie, G.-Z. Yang, D.-S. Bin and D. Li, *Angew. Chem., Int. Ed.*, 2021, **60**, 24467–24472.

332 D. Cai, M. Lu, L. Li, J. Cao, D. Chen, H. Tu, J. Li and W. Han, *Small*, 2019, **15**, 1902605.

333 S. Wang, F. Huang, Z. Zhang, W. Cai, Y. Jie, S. Wang, P. Yan, S. Jiao and R. Cao, *J. Energy Chem.*, 2021, **63**, 336–343.

334 X. Yuan, Q. Mu, S. Xue, Y. Su, Y. Zhu, H. Sun, Z. Deng and Y. Peng, *J. Energy Chem.*, 2021, **60**, 202–208.

335 A. Prasoon, B. Dhara, D. Roy, S. Rana, S. Bhand and N. Ballav, *Chem. Sci.*, 2019, **10**, 10040–10047.

336 P. Liu, M. Huang, X. Chen, Y. Gao, Y. Li, C. Dong and G. Wang, *Interdiscip. Mater.*, 2023, **2**, 423–433.